Heterogeneously catalyzed reactions over newly developed SCR DeNOx catalysts

Heterogen katalysierte Reaktionen an neu entwickelten SCR-DeNOx-Katalysatoren

Von der Fakultät Energie-, Verfahrens- und Biotechnik der Universität Stuttgart

zur Erlangung der Würde eines Doktors

der Ingenieurwissenschaften (Dr.-Ing.) genehmigte Abhandlung

vorgelegt von

Tobias Schwämmle

aus Calw

Hauptberichter: Prof. Dr. techn. G. Scheffknecht

Mitberichter: Prof. Dr.-Ing. habil. H. Köser, Universität Magdeburg

Tag der mündlichen Prüfung: 25.02.2022

Institut für Feuerungs- und Kraftwerkstechnik der Universität Stuttgart
2022

Acknowledgements

The work presented in this thesis has been conducted during my time at the Institute of Combustion and Power Plant Technology (IFK) of the University of Stuttgart. The main research activities were carried out in the framework of the publicly funded research projects “DENOPT” (Optimisation of SCR-DeNOx Catalysts Performance related to Deactivation and Mercury Oxidation) and the “successor” project “DEVCAT” (Development of High Performance SCR-Catalysts Related to Different Fuel Types). The financial support from the European Union’s Research Fund for Coal and Steel (RFCS) of the projects “DENOPT” (grant number: RFCR-CT-2007-00008) and “DEVCAT” (grant number: RFCR-CT-2010-00012) is greatly acknowledged. Moreover, the collaboration with experts from IBIDEN Porzellanfabrik Frauenthal GmbH (today: Ceram Austria GmbH), EnBW Energie Baden-Württemberg AG, E.ON New Build & Technology GmbH (today: Uniper SE), Enel Ingegneria e Ricerca S.p.A. and Recom Services GmbH within the projects and also further bilateral industrial partners is highly appreciated.

I would like to express my deepest gratitude to Prof. Dr. techn. Günter Scheffknecht for providing the unique infrastructure at the IFK, supervising my research work during my time at the institute and finally his advice during the process of finishing this thesis. Special thanks go to Prof. Dr.-Ing. habil. Heinz Köser of the University of Magdeburg, whose research during the last decades in the field of SCR catalysts I followed closely and who finally undertook the secondary report of my dissertation.

During my time at the (former) Department for “Fuels and Flue Gas Cleaning” (BuR), I worked together with different heads of the department who deserve my sincerest thanks: Dr.-Ing. Kevin Brechtel, who enabled me the start into the topic on “his special way”, Prof. Dr.-Ing. Barna Heidel, who really lived the positive synergies in our flue gas cleaning works and finally Barbara Sophia Klein for the freedom in my scientific work and the discussions. I thank also my fellow colleagues at the IFK for the collaboration, critical discussions and suggestions and especially Vladimir Stack Lara for allaying me the fear from mercury and laboratory glass in the beginning of my scientific work. I would also like to thank the team of the “Laboratory for Fuels, Ashes and Slag” led by Wolfgang Ross† for their support by numerous analyses. Finally, additional thanks go to the workshop and administrative team of the IFK for their support, especially Ursula Docter and Antje Radszuweit and last but not least Dieter Straub for the first positive contacts to the work at the IFK years ago.

I thank the numerous students who supported portion of the experimental work in the framework of their student theses under my supervision. Special thanks go to Andreas

Pospiech, Fabian Bertsche, Ivana Čačić, Martin Frank, Robin Laube, Stefan Schöller, Anahit Ahmadian, Nico Güldner, Christian Dörr, Lisa Koch, Katharina Blum, Uzo Edoka, Marc Schmid, Ida Masoomi, Anna Lelickens and Karin Schreiber.

Finally, I would like to thank my father Traugott and my mother Marta who made it possible for me to study at the university and who supported me on this long way. In addition, I thank my brother Jochen for his support and encouragement. Last but not least, very special thanks go to my girlfriend Bettina for her motivation, support and patience during the long time of genesis of this work and to my daughter Lisa and my son Fabian for their understanding.

Aalen, July 2022

Tobias Schwämmle

Contents

List of symbols, indices and acronyms

List of symbols

Symbol	Unit	Meaning
α	-	NH_3/NO ratio
a_{ch}; b_{ch}	mm	clear width of the catalyst
A_{ch}	m^2	catalyst surface area exposed to flow
AV	m/h	area velocity
β	mg/m^3, $\mu g/m^3$	mass concentration
B	-	channel shape factor
D	m	diameter
D	m^2/s	diffusion coefficient
D_{NO}	cm^2/s	molecular diffusion coefficient of NO
H	J/mol	enthalpy
h	J·s	Planck constant
κ_{23}	%	SO_2/SO_3 conversion
$\kappa_{Hg0/Hg2+}$	%	Hg oxidation
k	-	constant (unspecified)
k_{23}	1/h	SO_2/SO_3 reaction rate constant
K_{23}	m/h	SO_2/SO_3 conversion coefficient
k_{Bo}	J/K	Boltzmann constant
K_{Hg}	m/h	Hg oxidation activity
K_{NOx}	m/h	DeNOx activity
L	m	length
LV	m/s	linear velocity
M	g/mol	molar mass
η(α)	%	NO reduction
n	-	number
P3	m/h	performance indicator (considering all three relevant reactions at SCR catalysts)
R	m	radius
$\tilde{R}$	J/(mol·K)	universal gas constant
Re	-	Reynolds number
S	J/(mol·K)	entropy
Sc	-	Schmidt number
S_C	m^2	surface of the catalyst
T	K	absolute temperature (Kelvin)
V_C	m^3	catalyst volume
$\dot{V}_{dry}$	m^3/h (STP, dry)	flue gas flow rate (at STP, dry)
$\dot{V}_{wet}$	m^3/h (STP, wet)	flue gas flow rate (at STP, wet)

List of indices

Indice	Meaning
ads	adsorbed
ch	channel
des	desorbed
E	entrance
g	gas, gaseous
hyd	hydraulic
in	inlet
NO	Nitrogen oxide
out	outlet
ox	oxidized
red	reduced

List of chemical compounds

Formula	Name
Al_2O_3	aluminum oxide
Br	bromine
$CaSO_4 \cdot 2\ H_2O$	gypsum
CeO_2	cerium oxide
CH_3Hg^+	methyl mercury
Cl/Cl_2	chlorine / chlorine (molecular form)
CO	carbon monoxide
FeS	iron sulfide
H_2O	water
HCl	hydrogen chloride
HBr	hydrogen bromide
Hg / Hg^0	mercury (elemental)
Hg^{2+}	mercury (oxidized)
$HgCl_2$	mercury chloride
Hg_2Cl_2	mercury chloride (calomel)
Hg^P	particulate-bound mercury
HgS	mercury sulfide (cinnabar)
Hg^{tot}	total mercury (Hg^0 + Hg^{2+})
La_2O_3	lanthanum oxide
M	reaction partner (unspecified)
Me	metal (unspecified)
MnO_2	manganese oxide
MoO_3	molybdenum(VI)oxide
NO	nitrogen monoxide
NO_2	nitrogen dioxide
NO_x	nitrogen oxides
N_2	nitrogen
N_2O	dinitrogen monoxide
NH_3	ammonia
NH_4HSO_4	ammonium bisulfate
$(NH_4)_2SO_4$	ammonium sulfat
O_3	ozone
OH	hydroxyl radical
Pd	palladium
Pt	platinum
SiO_2	silica oxide
SO_2	sulfur dioxide
SO_3	sulfur trioxide
SO_x	sulfur oxides (sum of SO_2 and SO_3)
SO_3^{2-}	sulfite
SO_4^{2-}	sulfate
SO_x	sulfur oxides
TiO_2	titanium dioxide (*titania*)
V	vanadium
V_2O_5	vanadium(V)oxide (*vanadia*)
WO_3	tungsten(VI)oxide
ZSM-5	zeolithe socony mobil-5

List of acronyms and abbreviations

Abbreviation	Name
abs.	absolute
absorb.	absorption
approx.	approximately
BAT	best available techniques
BET	Brunauer-Emmett-Teller (surface area analysis)
BImSchG	Bundes-Immissionsschutzgesetz (Federal Immission Control Act)
BImSchV	Verordnung zur Durchführung des Bundes-Immissionsschutzgesetzes (Federal Immission Control Ordinance)
BJH	Barrett, Joyner, Halenda (pore size distribution)
BP	British Petroleum
BREF	best available techniques reference documents
BTU	British thermal unit
CAA	clean air act
CFD	computational fluid dynamics
CVAA	cold vapor atomic absorption
EDX	energy disperse X-ray spectroscopy
EPA	United States Environmental Protection Agency
ESP	electrostatic precipitator
EU	European Union
FGD	flue gas desulfurization
GWh	gigawatt hour
HC	honeycomb (catalyst)
HE	heat exchanger
ICP-OES	inductively coupled plasma - optical emission spectrometry
ID	induced draught
IEA	International Energy Agency
impr.	impregnated
lb	pound
LCP	large combustion plant
MACT	maximum achievable control technologies
MATS	Mercury and Air Toxic Standard
maf	moisture and ash free
MFC	mass flow controller
MW	megawatt
n.d.	not detected
NDIR	non-dispersive infrared light absorption
NDUV	non-dispersive ultraviolet light absorption
ORP	oxidation redox potential
pc.	piece
PFA	perfluoroalkoxy alkane
POG	process optimisation guidance
PM	particulate matter
ppb	parts per billion
ppm	parts per million
PT	plate (catalyst)

Abbreviation	Name
PTFE	polytetrafluoroethylene
RACT	reasonably available control technology
ref.	reference / referred to
RH	reheater
SCR	selective catalytic reduction
SEM	scanning electron microscopy
SI	international system of units (fr.: *Système international d'unités*)
SNCR	selective non-catalytic reduction
STP	standard temperature and pressure (273.15 K, 1013.25 mbar)
TA Luft	Technische Anleitung zur Reinhaltung der Luft (Technical Instructions on Air Quality Control)
TBtu	trillion British thermal units
UNFCC	United Nations Framework Convention on Climate Change
UNEP	United Nations Environment Programme
US	United States
UV	ultraviolet
VGB	Technische Vereinigung der Großkraftwerksbetreiber (Technical association of the large-scale power plant operators)
vs.	versus
w/o	without
wt.	weight
yr	year
XRF	X-ray fluorescence

Abstract

Catalysts for selective catalytic reduction (SCR) can, in addition to the reduction of NOx, also contribute to the oxidation of elemental mercury (Hg^0) as well as to the undesired conversion of SO_2 to SO_3. By placing the catalysts in the high-dust configuration, oxidized mercury (Hg^{2+}) can then be separated in downstream wet flue gas desulfurization units, allowing mercury to be removed efficiently from the flue gas.

The aim of this work is to show how mercury oxidation can be increased by newly developed SCR catalysts, which influences there are on Hg oxidation, and which mechanisms lie behind the three reactions over the SCR catalysts. The research with parameters derived from the experiences and conditions in power plant operation is carried out in synthetic flue gas in laboratory micro-reactors as well as in a lab-scale firing system under real flue gas conditions. The research forms a comprehensive examination of all reactions relevant in power plant operation with conventional as well as newly developed SCR catalysts. As a benchmark of the catalysts regarding all reactions, the performance indicator P3 is introduced.

The research is mainly conducted with standard SCR catalysts as reference and newly developed, modified honeycomb SCR catalysts, and supplemented by tests on plate-type SCR catalysts. In this research, modifications in the active component (V, Cu, Fe, Mn, Ce), of the promoters (W, Mo) as well as modifications of the base materials are studied. Through the dedicated application of the promoter molybdenum and modifications of the base material, a significant and clear increase in catalyst performance (high values of P3) can be achieved. An increased wall thickness of the catalyst also leads to an increase in Hg oxidation; however, the SO_2/SO_3 conversion is increased in parallel.

Examinations on the influences of the flue gas on the oxidation of Hg show a strong effect of the halogen content (HCl, HBr) in the flue gas. Likewise, the sulfation of the catalysts has a positive effect on the reactions over the catalysts. A parallel DeNOx reaction in the catalyst with the addition of NH_3 and the presence of CO in flue gas inhibits Hg oxidation as well as SO_2/SO_3 conversion.

The oxidation of Hg over SCR catalysts seems to proceed according to an Eley-Rideal or Mars-Maessen mechanism: mercury adsorbs on the SCR catalyst and reacts with weakly adsorbed hydrogen halide or hydrogen halide species from the gas phase. The Hg adsorption and release can be correlated with the catalyst composition. The Deacon reaction might bring an additional contribution, but does not seem to be exclusively responsible for the measured effects.

Kurzfassung

Katalysatoren zur selektiven katalytischen Reduktion (SCR) können neben der NO_x-Reduktion auch zur Oxidation des elementaren Quecksilbers (Hg^0) sowie zur unerwünschten SO_2/SO_3-Konversion beitragen. Durch die high-dust Schaltung des Katalysators kann dann in nachgeschalteten nassen Rauchgasentschwefelungsanlagen oxidiertes Quecksilber (Hg^{2+}) abgeschieden und damit Quecksilber effizient aus dem Rauchgas entfernt werden.

In dieser Arbeit soll aufgezeigt werden, wie die Quecksilberoxidation durch neu entwickelte SCR-Katalysatoren gesteigert werden kann, welche Einflüsse auf die Quecksilberoxidation bestehen und welche Mechanismen hinter den drei Reaktionen am SCR-Katalysator stecken. Die Untersuchungen mit Parametern abgeleitet aus den Erfahrungen und Bedingungen im Kraftwerksbetrieb finden sowohl im synthetischen Rauchgas im Labor-Mikro-Reaktor als auch in einer Laborfeuerung im realen Rauchgas statt. Sie stellen eine umfassende Betrachtung aller im Kraftwerksbetrieb relevanten Reaktionen an konventionellen als auch neu-entwickelten SCR-Katalysatoren dar. Als Vergleichsgröße der Katalysatoren hinsichtlich aller Reaktionen wird der Leistungsindikator P3 eingeführt.

Die Untersuchungen werden hauptsächlich an Standard-SCR-Katalysatoren als Referenz und an neu entwickelten, modifizierten SCR-Waben-Katalysatoren durchgeführt und durch Untersuchungen von SCR-Plattenkatalysatoren ergänzt. Dabei werden Modifikationen hinsichtlich der Aktivkomponente (V, Cu, Fe, Mn, Ce), des Promoters (W, Mo) sowie des Grundmaterials betrachtet. Insbesondere durch gezielten Einsatz des Promoters Molybdän und durch Modifikationen des Grundmaterials kann -verglichen mit der Referenz- eine deutliche Steigerung der Katalysatorperformance (hohe Werte für P3) erreicht werden. Größere Wandstärken des Katalysators wirken sich ebenfalls steigernd auf die Hg-Oxidation aus, jedoch wird ebenfalls die SO_2/SO_3-Konversion erhöht.

Untersuchungen zu den Einflüssen des Rauchgases auf die Hg-Oxidation zeigen einen starken Effekt des Halogengehalts (HCl, HBr) im Rauchgas auf die Quecksilberoxidation. Ebenfalls wirkt sich die Sulfatisierung des Katalysators positiv auf die Reaktionen am Katalysator aus. Inhibierend auf die Quecksilberoxidation und die SO_2/SO_3-Konversion wirken hingegen die parallele Entstickungsreaktion am Katalysator durch NH_3-Zugabe sowie CO im Rauchgas.

Die Hg-Oxidation an SCR-Katalysatoren scheint gemäß dem Eley-Rideal- oder dem Mars-Maessen-Mechanismus abzulaufen: Quecksilber adsorbiert am SCR-Katalysator und reagiert mit schwach adsorbiertem Halogenwasserstoff oder Halogenwasserstoff aus der Gasphase. Die Hg-Adsorption und Freisetzung kann mit der Katalysatorzusammensetzung und Hg-Oxidation korreliert werden. Die Deacon-Reaktion kann einen zusätzlichen Beitrag liefern, ist jedoch nicht alleinig für die beobachteten Effekte verantwortlich.

1 Introduction

The global demand for energy has been continuously increasing during the last centuries. Although there has been a rise in renewable energy utilization in the last decade, the combustion of fossil fuels still plays an important role. The primary energy consumption by fuel in 2018 is depicted in figure 1-1 according to the numbers of BP [1]. It shows coal as the second-largest primary energy source globally.

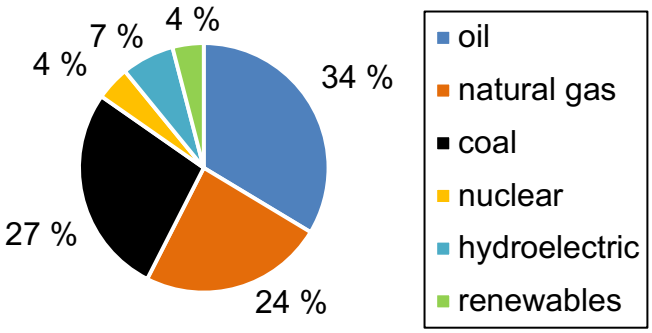

Figure 1-1: Primary energy consumption by fuel in 2018 [1]

A growth of the share of coal in the global energy mix of more than 25% since the beginning of this century was recorded by the International Energy Agency (IEA) in 2015 [2]. In 2019, the report by the IEA showed a rise in global coal use for the second straight year in 2018 after a decrease from the 2014 peak [3]. Although there is a trend toward low-carbon energy options and scenarios show a reduction in overall coal demand, there are regions like Asia in which the demand for electricity is increasing. In Asia, many new coal-fired power plants have been constructed during the last years in order to satisfy their demand for electricity and development. This leads to an increase in coal demand in this region according to the discussed scenarios [3].

However, the combustion of coal is associated with emissions of various pollutants. Particulate matter (PM), nitrogen oxides (NO_x), sulfur dioxide (SO_2) and mercury (Hg) are emitted after combustion – to name just the most prominent ones. These pollutants lead above all to respiratory illnesses and irritations in human beings and thus to premature deaths. Additionally, sulfur oxides (SO_x) and NO_x emissions have direct effects on plants and vegetation and furthermore, acid rain is formed from SO_x and NO_x, leading to indirect effects in nature [4].

The reduction of particulate emissions started in the 1960s and 1970s in central Europe via the installation of particulate removal technologies, e.g. electrostatic precipitators (ESPs). The effects of acid rain and respiratory health effects led to the installation of flue gas desulfurization (FGD) units in the early 1980s to reduce the sulfur dioxide emissions.

Finally, driven by the development in Japan, in the mid-1980s the selective catalytic reduction (SCR) catalyst was introduced in European power plants in order to further reduce the environmental effects of power plant operation. Figure 1-2 shows the development of the atmospheric emissions from the energy sector in Germany starting from 1990.

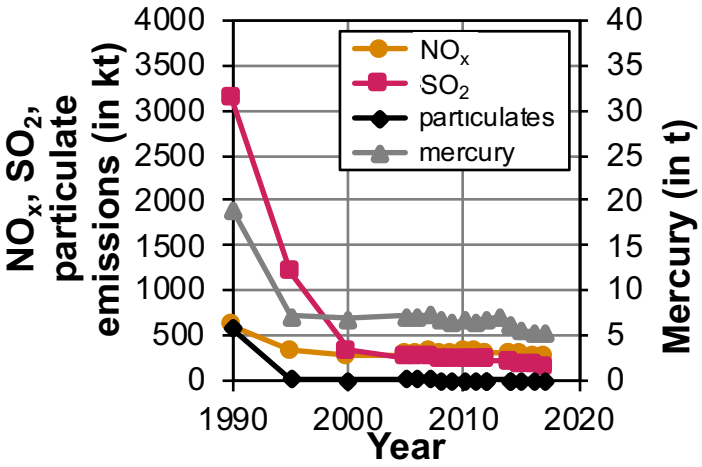

Figure 1-2: Development of the emissions from the energy sector in Germany [5]

The development outlined above is clearly visible in figure 1-2. The steep decrease in emissions from 1990 to 1995 can on the one hand be explained by the closing down of many industrial plants in the former German Democratic Republic and on the other hand by the installing of air quality control systems in the energy sector, which led to an improved ambient air quality in Germany. Whereas the emission of "classical" pollutants like particulates, NO_x and SO_x had been focused on in the past, recently, emissions of heavy metals and especially mercury have been addressed. As can be seen in figure 1-2, a significant amount of about 5 t of mercury is emitted by the energy sector in Germany annually [5].

1.1 Mercury as a global pollutant

Mercury (Hg^0) is a chemical element with a molecular mass of 200 g/mol and a relatively high vapor pressure compared to other metals of 0.180 Pa (at 20°C). It is the only metal which is liquid at standard conditions (STP). In addition to the elemental form with the oxidation state 0, mercury also occurs in the oxidation states +1 and +2. These compounds are clearly distinguishable in their physical and chemical properties as well as in their behavior in the environment.

The chemical mercury compounds in nature can be distinguished as:

- Elemental mercury (Hg^0)

- Inorganic oxidized mercury compounds (e.g. $HgCl_2$, Hg_2Cl_2 (calomel), HgS (cinnabar))
- Organic mercury compounds (e.g. methyl-mercury CH_3Hg^+)

Since mercury is contained in some mineral ores, it is naturally released through the degassing of mineral material, especially through geogenic activities like volcanic eruptions. Natural fires of biomass also lead to a release of mercury into the atmosphere. However, a significant proportion of mercury emissions of about 20% are anthropogenic. According to a report by the United Nations Environment Programme (UNEP) [6] for the year 2010, anthropogenic mercury emissions were calculated as 1,960 t/yr with an uncertainty range of 1,000 to 4,000 t/yr. These numbers are similar to the previous reports about man-made mercury emissions in 2000 by Pacyna and Pacyna [7], who reported numbers of 2,200 t/yr, and the Arctic Monitoring and Assessment Programme report of 2008 [8], calculating anthropogenic mercury emissions of 2,200 to 2,700 t/yr. However, the studies name different sources as the main cause of anthropogenic mercury emissions. The reports before 2013 cite the combustion of coal as the biggest source of anthropogenic mercury emissions, but in the newer reports, artisanal and small-scale gold mining is responsible for the highest mercury emissions to the atmosphere. Further anthropogenic emissions include cement production, chlorine-alkali electrolysis, and primary ferrous and non-ferrous metal production. For the emissions of mercury from these sources, three forms of mercury are relevant:

- Gaseous elemental mercury (Hg^0)
- Gaseous divalent oxidized mercury (Hg^{2+})
- Particulate-bound mercury (Hg^P)

Of these, gaseous elemental mercury forms the most common species in anthropogenic as well as in natural emissions to the atmosphere [6]. In the literature, global atmospheric mercury concentrations are given as 1.4 ng/m³ in Ireland and 1.6 ng/m³ at a monitoring station in Germany [9]. The average gaseous elemental mercury concentration in the US was measured as 1.2 to 2.1 ng/m³ [10]. Values in Asia were determined to be the highest in the northern hemisphere with values of 2.7 ng/m³ in Shanghai [11] and much higher values in other regions [6].

The annual mercury emissions mentioned above are an input to the global mercury cycle in which chemical as well as biochemical processes play a role. Gravity force leads to the deposition of particulate-bound mercury (Hg^P) very close to the source site. Due to the relatively high water solubility of Hg^{2+}, the emissions of this species are washed out by rain. Gaseous elemental mercury stays in the atmosphere for a long time until it is finally oxidized by O_3, Br/BrO- or OH- radicals and also washed out [6]. Especially in aquatic ecosystems, dissolved mercury is methylated to the organic mercury compound mono-

methylmercury (CH_3Hg^+) by biochemical mechanisms in bacteria. This mercury compound is highly toxic. It is bioaccumulated and concentrated through the food chain in aquatic ecosystems [12]. Especially in the arctic region, the contribution of anthropogenic mercury emissions to mercury concentrations in animals was calculated to be as high as 92% [13]. Studies have shown that especially in the polar bear, mercury concentrations in the hair have increased tremendously over the last 200 years, e.g. from 1.4 µg/g in 1890 to 4.9 µg/g in 2000 [13], since arctic polar bears are at the top of the food chain. In their predecessor in the food chain, the ringed seal, the mercury concentration increased by a factor of eight over the last 100 years to a value of 0.004 µg/g in the teeth [14]. So, relatively low concentrations of mercury – either methyl- or inorganic mercury compounds – can lead to high concentrations in animals at the top of the food chain, which also includes humans like the Inuit, who eat a lot of fish [15], [16].

Figure 1-3 shows the global mercury cycle with natural as well as anthropogenic mercury sources. As sinks, depositions to land and oceans are to be named, as previously described, by the washing out of oxidized mercury. Via transportation within natural water cycles in rivers and lakes, it finally arrives in the ocean, which forms a huge mercury storage and which is also the source from which the bioaccumulation of mercury in the food chain starts. The ocean also forms the biggest source of natural mercury re-emission into the air due to the chemical reactions as shown in simplified form in figure 1-3.

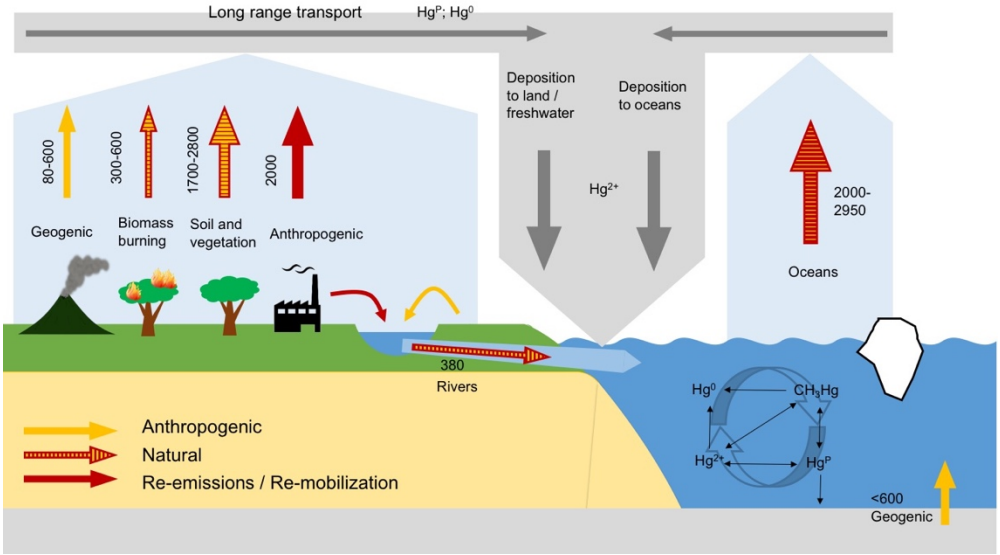

Figure 1-3: The global mercury cycle - natural and anthropogenic mercury emissions, numbers in t/year (figure adapted and modified from [6])

Especially in the arctic region, due to the reaction with bromine in the atmosphere supported by ultraviolet light, high amounts of mercury are deposited as oxidized mercury. It is then fixed in the ice crust. Melting of the ice crust leads to a release of mercury to the atmosphere [6]. Research [17] has also shown an influence of the El Niño Southern Oscillation on mercury concentration in the troposphere, which is explained by emissions from biomass burning.

1.2 Legal regulations

1.2.1 Development of legal frameworks in Europe

Due to the negative impact of the emissions of nitrogen oxides, sulfur oxides as well as heavy metals from fossil-fueled power plants, legal regulations have been implemented and limiting values for the emissions set. However, the regulations and frameworks in Europe and the US regarding the pollutants differ.

Due to the direct effects of the pollutants like acid rain, smog or respiratory problems, quite early in the 1970s, regulations like the "Bundesimmissionsschutzgesetz" [18] were set in force in Germany in order to directly reduce the most relevant pollutants. The legal frameworks are supplemented by administrative regulations like the "Technische Anleitung zur Reinhaltung der Luft" (TA Luft), which is was recently revised in the issue of 2021 [19]. Regarding the emissions from coal-fired power plants and the emissions from waste incineration plants, there are regulations set in the 13th and 17th "Verordnung zur Durchführung des Bundes-Immissionsschutzgesetzes" [20], [21]. The limiting values are given in mass concentrations in STP and refer to a certain residual oxygen content. In table 1-1 and table 1-2, an overview of limiting values for existing, old coal-fired power plants and waste incineration plants is given. The limiting values for new coal-fired power plants according to the recently revised legislation are lower. Especially for lignite-fired power plants, slightly higher limiting values apply, when the mercury content in fuel is higher than 0,1 mg/kg.

Table 1-1: Limiting values for nitrogen oxides according to German legislation

	Averaging interval	**Thermal input (in MW)**	**Fuel**	**13th BImSchV [20] in mg/m³ (O_2 reference: 6%)**	**17th BImSchV [21] in mg/m³ (O_2 reference: 11%)**
Nitrogen oxides (calculated as NO_2)	Half hour	50-100	lignite / hard coal	600	
		100-300	lignite / hard coal	400	
		> 300	lignite / hard coal	400	
		> 50	waste		150
	Daily	50-100	lignite / hard coal	300	
		100-300	lignite / hard coal	200	
		> 300	lignite	200	
			hard coal	200/150*	
		> 50	waste		400
	Yearly	50-100	lignite / hard coal	250	
		100-300	lignite / hard coal	180/100*	
		> 300	lignite	175/100*	
			hard coal	150/100*	
		> 50	waste		100

* existing plants with commissioning between 7th of January 2014 an 18th of August 2021

Table 1-2: Limiting values for mercury according to German legislation

	Averaging interval	**Thermal input (in MW)**	**Fuel**	**13th BImSchV [20] in mg/m³ (O_2 reference: 6%)**	**17th BImSchV [21] in mg/m³ (O_2 reference: 11%)**
Mercury	Half hour	> 50	hard coal/ lignite/	0.04	0.05
		> 50	waste		0.03
	Daily	> 50	hard coal/ lignite/	0.02	
		> 50			0.03
	Yearly	50-300	lignite	0.01	
			hard coal	0.005	
		> 300	lignite	0.005/0.004**	
			hard coal	0.004/0.003**	
		> 50	waste		0.01

** lower value effective from 15th of July 2025

While the continuous measurement of nitrogen oxides and the delivery of half-hour average values is obligatory for coal-fired power plants, the continuous measurement of mercury concentrations at the stack can be avoided, when other methods e.g. fuel analyses show, that the emissions will be lower than 50% of the limiting values and discontinuously/yearly measurements prove that the emissions are well under the limiting values listed above [20]. In waste incineration plants or plants with co-combustion of waste, it has to be shown that the values measured at the stack only reach 20% of the limiting value in order to forgo continuous mercury measurements.

In recent years, German environmental legislation has mostly been influenced by the legislation of the European Union, which sets standards for the whole Community to be fulfilled by all of their member states. An important directive in this process was the Large Combustion Plant Directive (Directive 2001/80/EC) [22], setting the first regulations on trace element emissions. In 2005, the EU published a Strategy on Mercury [23], a first initiative to reduce the use of mercury in industry. In this document, coal combustion was identified as a main source of mercury release.

The approach of the European Union and its legislation was driven quite early by providing information on best available techniques (BAT) to reduce emissions, which set the basis for the limiting values which have to be adhered to. The first BAT documents for large combustion plants [24] had been published under the legal basis of the Integrated Pollution Prevention and Control Guidance (IVU-RL) [25]. The revision process of these documents started under the framework of the Industrial Emissions Directive (2010/75/EU) [26], which set the basis for new best available technique reference documents (BREF) for different industrial fields. The new BREF document for large combustion plants (LCP-BREF) includes emission bandwidths for mercury as shown in table 1-3:

Table 1-3: Emission bandwidths (yearly average) for mercury in the LCP BREF [27]

Fuel	**Power**	**Emission limits**	
	Firing thermal capacity (in MW)	New plants (in µg/m³)	Existing plants (in µg/m³)
Hard coal	< 300	< 1-3	< 1-9
	> 300	< 1-2	< 1-4
Lignite	< 300	< 1-5	< 1-10
	> 300	< 1-4	< 1-7

Plant operators had to comply with these values by 2021 at the latest.

1.2.2 Air quality regulations in the US

The legal framework in the US follows a slightly different approach compared to the EU. The first limits for emissions to the environment came with the Clean Air Act (CAA) of 1970. In the 1990s, amendments to the CAA were made [28] and the regulation started to be based on the best demonstrated control technologies called “reasonably available control technology” (RACT) or “maximum achievable control technologies” (MACT). These also included emission regulation on NO_x emissions, especially during the summertime, the so-called “ozone season”. The individual federal states can set their own limiting values regarding emissions while implementing and executing the regulations of the EPA (United States Environmental Protection Agency).

However, the regulation on coal-fired power plants started in 2000, when the EPA started to establish emission standards which are technologically based. The best-performing 12% of the existing plants set the benchmark for the limiting values [29]. The regulations on mercury started with the Clean Air Mercury Rule (CAMR) in 2005 [30], which introduced a nationwide cap and trade program for mercury emissions in the US to be started in 2010. In the same year, the Clean Air Interstate Rule (CAIR) [31] addressed SO_x and NO_x emissions in the power sector, which for the first time set the requirement to install SCR DeNOx catalysts and wet flue gas desulfurization plants. However, the CAMR was vacated by court in 2008. In 2012, the Mercury and Air Toxic Standards (MATS) replaced the CAMR, setting the strictest emission limits in the world for mercury emissions to the air [32]. It was revised in certain points in 2015, especially taking into account the impracticably low values for mercury emissions of newly built power plants [33]. The Supreme Court of the US decided to stop the MATS rule in June 2015 since the EPA had not considered the costs. These documents on the costs were submitted in spring 2016, showing that the effects for the environment and health are higher than the costs for industry, so the MATS remain in place. In addition to the MATS, each federal state can set individual limiting values for mercury emissions. The current MATS limits are given referring to the thermal input or output as well as to the electrical output as a 30-day rolling average and are shown in table 1-4:

Table 1-4: Emission limits for mercury into to the atmosphere according to the MATS

Fuel	**Emission limits**			
	New plants	Existing plants		
	Ref. to output (in lb/GWh)	Ref. to input (in lb/TBtu)	Ref. to output (in lb/GWh)	Calculated mass concentrations (in µg/m³) according to [34]
Hard coal > 8300 Btu/lb	0.003	1.2	0.013	2.2
Lignite < 8300 Btu/lb	0.04	4.0	0.04	5.4

For the conversion of the MATS limiting values to mass concentrations, the European standard conditions and the efficiency of the plant have to be considered besides the conversion of the units to the SI system [34]. The precise conversion leads to slightly different values compared to the values published before (hard coal: 1.4 µg/m³ and lignite: 4.7 µg/m³ [29]). The differences in conversion result amongst others from the higher efficiency of the German power plants considered by [34] which was not considered in the earlier published values. As measurement methods for the supervision of the limiting values, continuous mercury monitors as well as discontinuous sorbent trap measurements are accepted.

1.2.3 Global efforts to reduce mercury emissions from power plants

Since mercury is a pollutant of global concern as shown in figure 1-3, there is a global initiative to reduce mercury emissions to the atmosphere, which is led by the United Nations Environment Programme (UNEP). Similar to the United Nations Framework Convention on Climate Change (UNFCC), the initiative on mercury aimed at a globally binding agreement within a top-down approach [35]. This initiative sets binding targets on emission reduction. After only four years of negotiations, the Minamata Convention on Mercury was signed by governments in 2013 as a legally binding multilateral environmental agreement (after ratification by at least 50 states, which was fulfilled in 2017) [36]. The development of this initiative also includes a technical review on BAT and a process optimization guidance document (POG) on easily finding strategies for Hg emissions reduction [37].

2 Fundamentals of flue gas cleaning systems

2.1 Origin and formation of pollutants

Within the process of coal combustion and emissions control, various chemical reactions take place in the flue gas pathway – from the formation of the substances in the boiler up to their destruction or removal in the air pollution control devices. In this chapter, the most relevant chemical compounds from the perspective of the selective catalytic reduction (SCR) catalyst are named and discussed.

2.1.1 Nitrogen in coal and NO_x formation

In technical combustions of solid fuels like coal with low excess air, the most relevant nitrogen oxide species is nitrogen oxide (NO), which together with nitrogen dioxide (NO_2) is summarized as NO_x. There is a thermodynamic equilibrium between nitrogen oxide and nitrogen dioxide (NO_2) according to:

$$NO + \frac{1}{2}O_2 \leftrightarrow NO_2 \qquad \text{equation 2-1}$$

At higher temperatures, the chemical equilibrium is on the left side. Thus, in the flue gas pathway of coal-fired power plants, there is only 5% NO_2 [38]. However, because nitrogen oxide is oxidized to nitrogen dioxide when emitted to the atmosphere, emissions are always calculated as nitrogen dioxide.

The formation of nitrogen oxide in technical combustions can be described by three mechanisms: thermal, prompt, and fuel NO_x.

Thermal NO_x is formed during combustion at temperatures above 1,000°C due to partial oxidation of molecular nitrogen contained in the combustion air. The detailed reaction mechanism was first described by Zeldovich [39] in 1946. Due to the strong threefold bonding of the nitrogen molecule, high activation energy is needed for the reaction according to equation 2-2 and equation 2-3:

$$N_2 + O \leftrightarrow NO + N \qquad \text{equation 2-2}$$

$$N + O_2 \leftrightarrow NO + O \qquad \text{equation 2-3}$$

The formed oxygen radical itself can oxidize a nitrogen molecule again if the energy is available. Thus, the reaction rate increases exponentially at higher temperatures [38]. Fuel-lean conditions promote the formation of thermal NO_x.

Prompt NO_x is formed by radical reactions in the fuel-rich flame front. The mechanism was firstly described by Fenimore [40] in the 1970s with an intermediate step with a cyanide compound (HCN) determining the reaction rate. However, recent studies and compilations by Glarborg [41] confirmed an NCN as the intermediate step resulting from the attack of CH radical into the N_2 triple bond (as shown in simplified form in equation 2-4). The NCN radical is afterwards further oxidized to nitrogen oxide or N_2.

$$CH + N_2 \leftrightarrow NCN + H \qquad \text{equation 2-4}$$

The formation of prompt NO_x occurs under fuel-rich conditions.

Fuel NO_x represents the third NO_x pathway. Nitrogen is contained in the organic matter of the fuel. It is the most relevant source of nitrogen oxides in solid-fuel-fired systems [42]. In table 2-1, the nitrogen content of various fuels is listed, which varies within a certain range depending on the origin of the fuel.

Table 2-1: Average nitrogen content of various fuels [42], [44]

Fuel		**Nitrogen content (in wt.-%, dry)**
Bituminous coal	low sulfur	1.50
	medium sulfur	1.66
	high sulfur	1.07
Subbituminous coal		0.95
Lignite		0.96
Peat		0.5-2.5
Wood		0.03-1.0
Straw		0.3-1.5
Sewage sludge		2.5-6.5
Meat and bone meal		8.7

Part of the complex nitrogen compounds are volatilized during combustion, and in this process the fuel nitrogen is separated from char and volatiles [42]. The nitrogen compounds are subsequently reduced to simple amines and cyanides, which can be further oxidized to nitrogen oxide [43].

Figure 2-1 shows the partitioning of the NO_x species in coal-fired combustion. It can be seen that at lower combustion temperatures fuel NO_x forms the greatest share of the NO_x pathways. At higher combustion temperatures, thermal NO_x gains in importance. This means that the reduction of combustion temperature by measures in firing system technology can only reduce NO_x formation to a certain extent.

For the NO_x reduction in industrial processes, primary measures like fuel- or air-staging by the application of low-NOx burners and secondary measures like selective catalytic reduction (SCR) and selective non-catalytic reduction (SNCR) are applied.

Selective catalytic reduction includes a catalytically active material installed in the flue gas pathway. This will be discussed in the following chapters in detail.

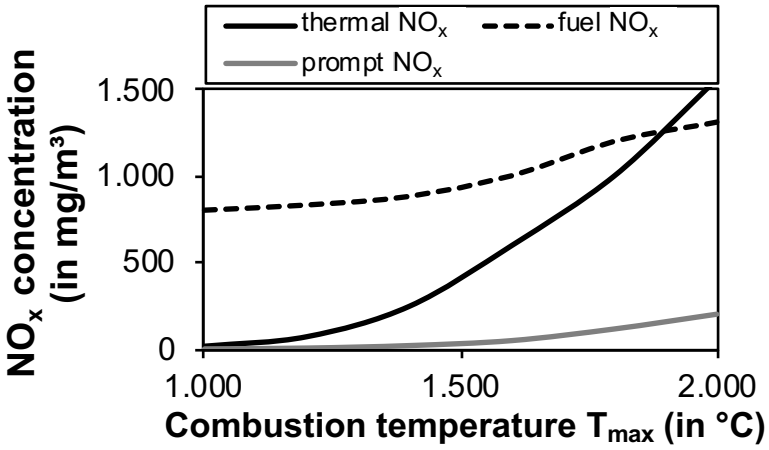

Figure 2-1: NO_x formation in coal-fired power plants over the combustion temperature. Adapted from [38]

The selective non-catalytic reduction requires a specific temperature window of 850 to 1,000°C [4]. At higher temperatures, additional NO is formed, while at lower temperatures, high ammonia (NH_3) slip occurs, meaning that ammonia, which has not reacted with nitrogen oxides, is released. Thus, in practical application, a good mixing of the reagent with the flue gas within the right temperature window during the reaction time is required [45]. The reaction with urea as the reducing agent proceeds according to:

$$H_2NCONH_2 + 2NO + \frac{1}{2}O_2 \rightarrow 2N_2 + CO_2 + 2H_2O \qquad \text{equation 2-5}$$

There are various other partly proprietary reducing agents available. Online temperature measurements combined with computational fluid dynamics (CFD) calculations as well as specifically designed grid of injection nozzles ensure an injection of the reducing agent in the appropriate temperature range. This can lead to more than 50% NO_x reduction and low ammonia slip at low costs [46]. This process is very common in waste incineration or cement plants. However, high NO_x reduction at low NH_3 slip can only be achieved by means of SCR. Thus, almost all hard coal-fired power plants and an increasing share of cement plants have SCR systems installed to achieve low NO_x emissions.

2.1.2 Sulfur in coal and SO_2 formation

Sulfur is also a part of the fuel matrix. It is found inorganically bound for example as pyrite (FeS) and gypsum ($CaSO_4$), organically bound, or sometimes as elemental sulfur. The typical overall sulfur content of various fuels is listed in table 2-2.

Within the thermochemical conversion of the fuel, the sulfur is almost totally oxidized to sulfur dioxide within an exothermic reaction according to equation 2-6 [48]. The oxidation

reaction of sulfur dioxide is assumed to be quite fast, so the SO_2 concentration in flue gas can be calculated by equilibrium calculations [49].

Table 2-2: Typical sulfur content of various fuels ([44], [47] and own analyses)

Fuel		**Sulfur content (in wt.-%, dry)**
Bituminous coal	low sulfur	1.04
	medium sulfur	3.08
	high sulfur	7.40
	El Cerrejón (CO)	0.64
	Kleinkopje	1.60
Subbituminous coal		0.79
Lignite	Lusatian	1.46
	Greek	0.63
Wood		0.02 - 0.05
Straw		0.1 - 0.3
Sewage sludge		3.0
Meat and bone meal		0.56

$$S + O_2 \rightarrow SO_2 \qquad \text{equation 2-6}$$

Sulfur dioxide forms sulfurous acid (H_2SO_3) when it is dissolved in water at lower flue gas temperatures.

Sulfur trioxide (SO_3) is formed during combustion at temperatures above 1,400°C in the flame by direct reaction with atomic oxygen according to equation 2-7. However, it dissociates to SO_2 or is subsequently reduced and thus there is only a little amount left downstream of the burner.

$$SO_2 + O + M \rightarrow SO_3 + M \qquad \text{equation 2-7}$$

During the cooling down of the flue gas, heterogeneous SO_3 formation takes place in the economizer. At temperatures between 420 and 600°C, SO_2 is oxidized by molecular oxygen catalyzed by iron oxides, which are contained in the fly ash [49]. Overall, the conversion of SO_2 to SO_3 in the boiler to downstream of the economizer is about 0.8 to 1.6% for bituminous and 0.05 to 0.1% for subbituminous coals [50].

Besides the previously discussed environmental effects of sulfur oxides, the formation of sulfur trioxide also has negative effects on plant operation. Due to the high hygroscopy, SO_3 absorbs water vapor of the flue gas and forms sulfuric acid according to:

$$SO_3 + H_2O \rightarrow H_2SO_4 \qquad \text{equation 2-8}$$

There is an equilibrium between sulfuric acid and SO_3 in flue gas, depending on temperature and moisture content as shown in figure 2-2.

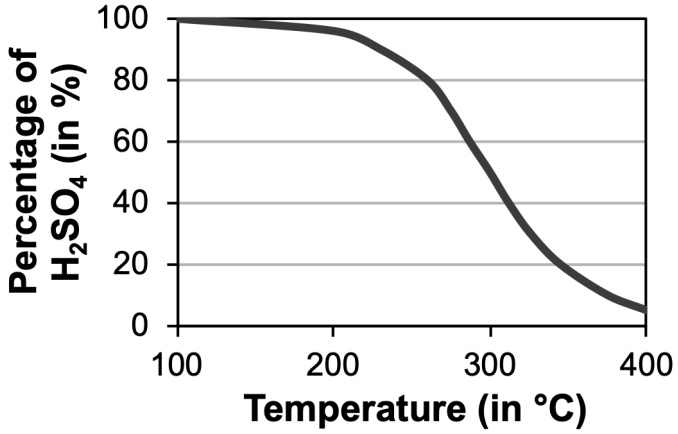

Figure 2-2: Equilibrium of sulfuric acid (H_2SO_4) and SO_3 at 8% H_2O. Adapted from [51].

At lower temperatures of the air preheater, condensation of the gaseous sulfuric acid occurs, which leads to corrosion. Since at temperatures above 100°C only the acid condensates, it is pure sulfuric acid causing the damage. The acid dew point is dependent on the partial pressure of SO_3 and H_2O in flue gas and can be calculated by formulas for example given by experimental correlations of Zarenezhad [52] and Okkes [53]. The acid dew point of H_2SO_4 in the flue gas of coal-fired power plants is typically in the range of 100 to 155°C. Concentrations of H_2SO_4 in the flue gas higher than 10 ppm can lead to an increased opacity of the emission plume, the so-called “blue plume” [54]. This is caused since fine acid aerosol particles are not removed from the flue gas in wet FGD units. Wet FGD units form the state-of-the-art process for SO_2 removal in coal-fired power plants. Their detailed chemical mechanisms will be explained in section 2.1.4, when discussing the behavior of mercury in power plants.

2.1.3 Halogens in coal

Halogens, namely fluorine (F), chlorine (Cl), bromine (Br) and iodine (I), are contained in the fuel as trace or minor elements [55]. The halogens mainly occur as water-soluble salts in the environment and are thus accumulated in seawater, which contains 19 g/l chlorine on average [56]. Volcanic activities are another source of halogens.

The accumulation of halogens in the fuel takes place via the water pathway by adsorbing the halogens from the liquid. Thus, coals from areas next to the sea show higher halogen contents. In general, the halogen content of coals increases with coal rank and depth, because the salinity of formation waters increases with depth [29]. However, the concentration of the single halogen in fuel varies as well. Yudovich and Ketris calculated average values for chlorine in lignite of 120±20 mg/kg and 340±40 mg/kg [56]. In table 2-3, values of the bromine and chlorine content of selected fuels are listed.

Table 2-3: Halogen content of various fuels ([57], [58] and own analyses)

Fuel		**Chlorine content (in mg/kg, maf)**	**Bromine content (in mg/kg, maf)**
Bituminous coal	Pennsylvania (United States)	1193	47
	Utah (United States)	193	2.6
	El Cerrejón (Columbia)	250	< 100
Subbituminous coal	Colorado (United States)	254	1.6
Lignite	Texas (United States)	111	3
Wood pellets		100-2,000	5
Straw		4,000-8,000	-
Sewage sludge		1,511	54
Meat and bone meal		6,200	12
Algae Monodus		856	534

Despite a great variation of halogen content even within a coal reservoir, the numbers confirm the correlation of halogen content with coal rank. According to Wang [59], Chinese coals have much lower average chlorine levels than US coals. Typically, the bromine content is about 1-4 wt.-% of the chlorine content. Analyses of US coals have shown a ratio of Br/Cl = 0.02 [60]. However, in certain coal reservoirs or fuels, much higher amounts of bromine are found.

2.1.4 Mercury in fuel and its behavior in the flue gas pathway

As a naturally occurring trace element, mercury is part of the upper continental earth's crust with average concentrations of about 56 ppb [61]. Due to natural uptake processes of plants during their lifetime and – in the case of coal – the carbonization process, it is part of the fuels. The association of mercury with the organic matter of the fuel is traced back to an adsorption on carbon and is much lower than the association with the inorganic part in chemical compounds [62]. The inorganic part of mercury, mainly the iron disulfide compounds (e.g. pyrite, marcasite), host most of the mercury in form of a solid solution [29]. Kolker [63] found a tendency that low-rank coals have a greater proportion of organic-bound mercury. In table 2-4, typical concentrations of mercury in fuels prior to any processing are listed.

Mercury concentration varies greatly even in the same coal reservoir. The US COALQUAL database [57] lists variations in mercury concentration within a reservoir in the order of magnitude of the average values because the database represents the entire thickness of a coal bed [29]. Although detailed analyses of mercury concentration in coal are not available for all countries worldwide, it can be concluded that the distribution of mercury is more site specific. For example, the review by Dai et al. [64] showed an average of 0.16 mg/kg Hg of 1,666 samples of Chinese coals, which is similar to the value for US coals compiled by the US Geological Survey. Secondary fuels also contain mercury. However, the average mercury content in sewage sludge has decreased during the last years due to

less mercury utilization in industry and in products. Other fossil fuels like crude oil or crude natural gas contain mercury as shown in table 2-4. However, a separation of mercury within the production and upgrading process ensures that the mercury content in the final product is insignificant.

Table 2-4: Typical concentrations of mercury in various (crude) fuels ([57], [65], [66], [67] and own analyses)

Fuel		**Mercury content (in mg/kg, maf)**
Bituminous coal	Pennsylvania (United States)	0.32
	Utah (United States)	0.18
	Donetsk (Ukraine)	< 10
	El Cerrejón (Colombia)	0.065
Subbituminous coal	Colorado (United States)	0.11
	Alaska (United States)	0.027
Lignite	Texas (United States)	0.38
Wood chips		0.0015
Solid waste		2-10
Sewage sludge		1.1
Meat and bone meal		0.007
Straw		0.03
Crude oil (US)		0.0073
Crude natural gas (DE, crude)		1.3

For the utilization of coal in combustion processes, a separation of the mercury-rich fraction (pyrite) by density classification can theoretically lead to 37% lower mercury in the process [68]. Wichlinski [69] identified a thermal coal treatment process at temperatures below 380°C at which 90% of mercury was removed from coal at only 8% loss of thermal energy. Nevertheless, such methods are not an option for large-scale industrial processes due to the high energy loss in the pre-treatment process.

The simplified typical behavior of mercury in the flue gas pathway of coal-fired power plants is depicted in figure 2-3. Independent of its form and type of occurrence in the coal, mercury is completely released from the fuel at combustion temperatures of around 1,000°C. According to Fahlke [70], the volatilization can be considered as evaporation, although the boiling points of the mercury compounds differ (e.g. Hg0: 357°C, $HgCl_2$: 302°C, HgS: 584°C). Independent of the partly oxidizing or reducing conditions during combustion, mercury is always present as elemental mercury (Hg^0) vapor at temperatures above 700°C, as at these temperatures there are no oxidation reactions taking place. This can also be shown by thermodynamic equilibrium calculations of the mercury species in flue gas as shown in [71].

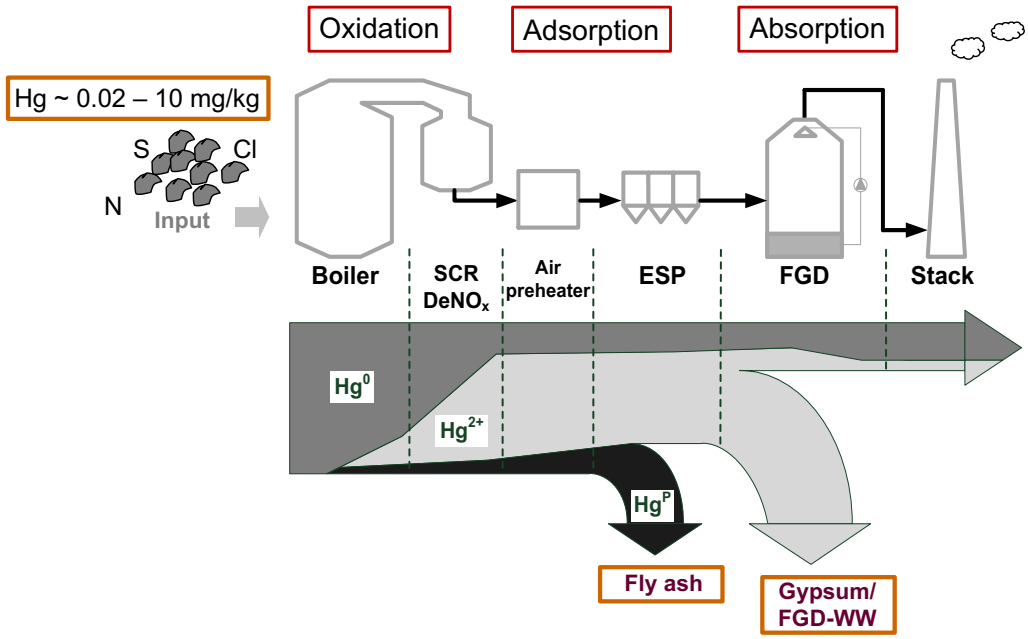

Figure 2-3: Mercury behavior in coal-fired power plants with SCR, ESP and wet FGD unit (figure modified from [72])

Boiler

When the flue gas cools down while passing the heat exchangers in the **boiler** (see figure 2-3), transformation and oxidation of the elemental mercury starts to take place. In flue gases with halogens released from the fuel, e.g. chlorine, bromine, iodine, the mercury halides (e.g. $HgCl_2$) are the dominating Hg species besides elemental mercury. Various authors have studied and published research on homogeneous mercury oxidation reactions [70], [71], [73], [74]. Homogeneous gas phase mercury oxidation reactions and gas-phase sub-reactions can be described as follows, whereas various other homogeneous reactions might take place as described in [66].

$$2Hg + 4HCl + O_2 \leftrightarrow 2HgCl_2 + 2H_2O \qquad \text{equation 2-9}$$

$$4HCl + O_2 \leftrightarrow 2Cl_2 + 2H_2O \qquad \text{equation 2-10}$$

$$Hg + Cl_2 \leftrightarrow HgCl_2 \qquad \text{equation 2-11}$$

$$Cl_2 + SO_2 + H_2O \leftrightarrow SO_3 + 2HCl \qquad \text{equation 2-12}$$

The chlorine-Deacon reaction as shown in equation 2-9 and equation 2-10 forms one possible reaction pathway, and is thermodynamically favored at lower temperatures. However, the reactions with other halogens are more favored at higher temperatures, for example the bromine-Deacon-reaction (with the same stoichiometry as the aforementioned reactions, but with bromine instead of chlorine). As described by Griffin [75], there is also a possibility of the consumption of halogens by reaction with SO_2 (equation 2-12), called the chlorine-Griffin-reaction. This reaction is thermodynamically

more favored with chlorine than with bromine [60]; thus, adding calcium bromide to the fuel can lead to a much more increased homogeneous mercury oxidation [60], [76].

SCR DeNOx

Further mercury oxidation takes place according to the previously described reactions or various other pathways heterogeneously at the **high-dust SCR catalyst**, which forms the core part of this work and will be discussed later in 2.2.6 in detail. As shown in figure 2-3, SCR catalysts in hard-coal-fired power plants are installed directly downstream of the economizer in the so-called high-dust configuration. In lignite-fired power plants, there are usually no installations of SCR catalysts [77]. Tests in the 1980s have shown that in the case of lignite power plants, significant plugging and erosion occurs at the catalyst. In parallel, combustion optimization measures had proven to be sufficient to meet the limiting values of NOx emissions in these plants. During lignite combustion, there is lower NO_x formation due to reduced combustion temperature [78]. The phenomenon of Hg oxidation at SCR catalysts was first described and discussed by Gutberlet [79] and further researched for example by Hocquel [66], Thorwarth [80] and Madsen [81] in recent years.

Air preheater

During cooling down of the flue gas in the **air preheater** and the flue gas pathway downstream of the SCR catalyst, flue gas and fly ash are in intense contact. The specific surface area of fly ash can vary from 170 to 1,000 m^2/g [82] while unburned carbon (coke) has an approximately tenfold higher surface area than the mineral matter. Due to pore condensation on the surface of fly ash particles, mercury is adsorbed on the particles and **particulate-bound mercury** is formed. Significant mercury adsorption can be found in the temperature range of 130-170°C and below [80], while at temperatures above 300°C, the adsorption equilibrium is totally on the side of the gas phase. On the surface of the particles, oxidation can take place as well, which leads to further adsorption of Hg^0 on particles. Thus, gas-phase mercury concentration decreases while preferentially oxidized mercury is removed from the flue gas [83]. In the literature, it is consistently reported that highest mercury removal is found with fly ashes with high carbon content [29], [83], [84]. In the research of Jäger [83], a reducing effect of the alkaline earth oxides on oxidized mercury was also found.

ESP

The separation of particulates from flue gas is carried out by **electrostatic precipitators (ESP)** or baghouse filters. In the latter, the fly ash is captured in a mesh formed as cylindrical bags. Due to gravitational or electrostatic forces or diffusion, the particles are bound on the mesh in the form of surface filtration. When the filter cake is built up, the pressure drop increases and the filter cake is cleaned by pressure surges. Due to their relatively high pressure drop of 8 to 15 mbar, baghouse filters are not very common in coal-fired power plants [85], since modern ESPs show almost the same separation

efficiency as with fly ash [86]. In ESPs, a corona discharge of 10-80 kV negatively charges the fly ash particles, which are then deposited on positively charged metal plates downstream [4]. The fly ash is then periodically removed from the plates by vibration and transported to the bunker. The pressure drop of the ESP is much smaller than the pressure drop of the baghouse filter, since the flue gas flows through the filter without any interaction with the filter material. However, very fine particles which show relatively high mercury content due to their high surface area can pass through the ESP.

FGD

The **FGD** unit is primarily installed for the removal of sulfur dioxide from the flue gas. The most common method for pulverized coal-fired power plants is the wet limestone scrubber [87]. Aside from this, there are other methods like dry desulfurization, in which dry alkaline-based sorbents are added to the flue gas stream, or the semi-dry method, in which an aqueous suspension of sodium or calcium-based compounds is sprayed in the flue gas stream [4]. However, due to the high pressure drop of the downstream baghouse filter and the higher costs of the sorbents, these methods are preferentially applied in waste incineration plants.

As feed in the wet FGD unit, usually limestone ($CaCO_3$) is added in the scrubber process as a wet suspension which is sprayed in the flue gas stream countercurrently. The SO_2 contained in the flue gas is first physically absorbed in the slurry and thus removed from the flue gas. Sulfurous acid is formed and the pH value of the slurry decreases. Under forced oxidation by aeration of the slurry sump, the sulfite (SO_3^{2-}) is oxidized to sulfate (SO_4^{2-}) and by reaction with dissolved Ca^{2+} ions of the ground limestone, gypsum ($CaSO_4 \cdot 2H_2O$) is formed, which is then separated from the slurry [88]. In equation 2-13, the overall reaction is shown:

$$2CaCO_3 + 2SO_2 + O_2 + 4H_2O \leftrightarrow 2[CaSO_4 \cdot 2H_2O] + 2CO_2 \qquad \text{equation 2-13}$$

By adding new limestone and the continuous absorption of SO_2, the equilibrium of the pH is adjusted in the slurry [4]. The wet flue gas desulfurization is either built as a single-loop scrubber with only one sump or as a dual-loop scrubber in which the reactions take place in two separate sumps: the quencher and the absorber [89].

The gypsum formed in the process is, in contrast to the product of the dry or semi-dry methods, a saleable by-product. Thus, in hard-coal-fired power plants, the solid fraction is separated from the slurry and the wastewater is treated in a special wastewater treatment step. In lignite-fired plants, the effluent slurry of the FGD unit can be mixed with fly ash since this fly ash is deposited on the mining site. The synthetic gypsum of hard-coal-fired power plants has the same properties as naturally occurring gypsum and is used, after some drying and calcination steps, in the construction industry, especially for gypsum cardboards [90].

Various measurements in full-scale plants as well as research within the past years have shown mercury removal in the wet FGD unit [66], [79], [88], [89], [91]. In general, this can be traced back to the water solubility of the oxidized mercury ($HgCl_2$: 66 g/l, other oxidized mercury species show lower values). However, even elemental mercury can be partially absorbed in solutions with zero mercury content, despite its very low water solubility of $6x10^{-5}$ g/l [92]. The equilibrium between gas phase and liquid phase can be described by Henry's law, which also includes a temperature dependency.

After physical absorption of Hg^{2+} in the slurry, the chemical redox reactions and complexations lead to the retention of mercury in the slurry. Halogens like chlorine, bromine and iodine that are occurring in the flue gas show very high water solubility and are quantitatively removed from flue gas. The influences and interactions of halogen ligands on mercury complexation and retention were extensively described by Bittig [93]. Furthermore, due to the absorption of SO_2, the pH of the scrubber varies from the droplets to the total sump. The aeration of the scrubber sump to oxidize the sulfite to sulfate leads to a change in the oxidation reduction potential (ORP). Unfavorable changes in ORP can lead to a release of mercury, the so-called "re-emission of mercury". The importance of the role of S(IV) species (mainly SO_3^{2-}) in the mercury chemistry of FGD slurry was studied by Heidel [91]. While low concentrations of SO_3^{2-} lead to low re-emission by the formation of sulfitomercurate(II)-complexes, a high concentration of SO_3^{2-} in the slurry leads to high Hg re-emission due to the reducing effect of this anion on dissolved Hg species in the slurry.

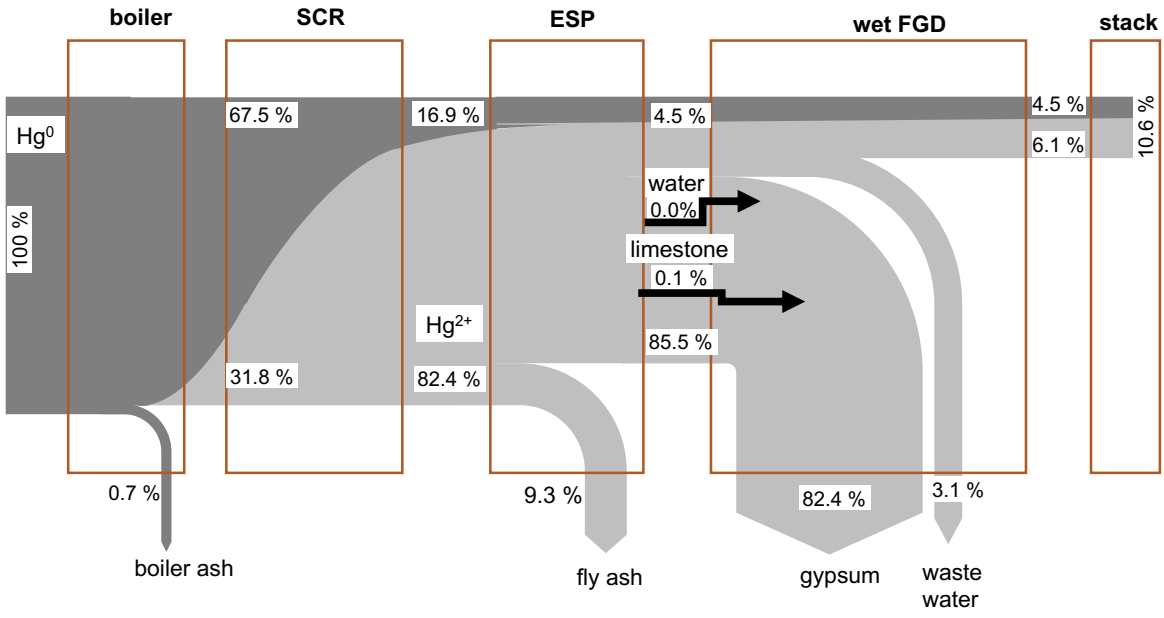

Figure 2-4: Percentage distribution of the mercury streams within a 920 MW hard-coal-fired power plant in Germany (derived from data included in [94])

The mercury complexation in slurry and its redox-chemistry also determines the partitioning of mercury between the gypsum and the wastewater. The aim of the co-

benefit approach for mercury emission reduction is to produce nearly mercury-free gypsum and concentrate the mercury in a small fraction of wastewater slurry for deposition.

In the Sankey diagram in figure 2-4, the percentage distribution of mercury within a 920 MW coal-fired power plant in Germany measured in 2012 is shown. It clearly shows the behavior of mercury discussed in this chapter. Downstream of the SCR, over 80% of the mercury is in oxidized form. Comprising about 10% of the total mercury, mainly oxidized mercury is removed in the ESP. In the wet FGD unit, due to the operating conditions during these measurements, more than 80% of mercury input is removed from the flue gas. The highest share of mercury in the slurry is found in the gypsum, meaning that in this case according to the co-benefit approach there is some need for optimization in mercury partitioning in the FGD. Finally, about 10% of the total mercury is emitted at the stack.

2.2 Fundamentals of the application of SCR catalysts

2.2.1 The SCR reactor within the flue gas pathway

The most common arrangement of the SCR catalyst within the flue gas pathway is the high-dust configuration [77], in which the SCR reactor is located directly downstream of the economizer and upstream of the air preheater with a vertical flow from up to down. The optimal temperature range for the SCR reaction is 330 to 410°C. However, the high fly ash content may lead to catalyst erosion, which can be counteracted by an increase of the catalyst's pitch and the wall thickness. Typical channel widths are in the range of 6-7 mm. Since this configuration is the most common in power plant application [95], the discussion about SCR reactors in the following chapters will be about this type of catalyst installation.

Another possible installation of the SCR reactor is the "low-dust" configuration downstream of the ESP (figure 2-5). Since the flue gas is no longer dust-loaded, the catalyst's channels are smaller and their lifetime is typically higher due to much lower erosion. Typical channel widths for low dust configuration are 3-4 mm [96]. However, due to lower temperatures, in this section of the flue gas pathway, the reaction rate is lower and problems with catalyst deactivation by ammonium sulfates could occur.

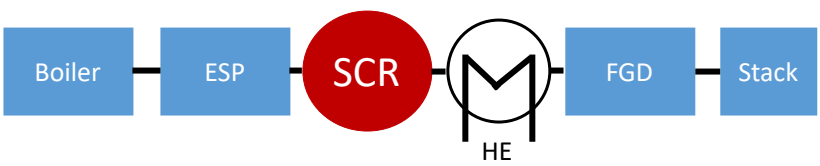

Figure 2-5: Low-dust configuration of the SCR (HE – heat exchanger)

The third technically relevant configuration of the SCR reactor within the flue gas pathway is the “tail-end” configuration. This configuration is very common in waste incineration plants, but it is also applied in coal-fired power plants in which an installation of the SCR in high-dust configuration was not possible. The channel width is normally smaller than 4 mm [95] since the flue gas after the FGD unit is dust free. This can also reduce the space required for the catalyst. A further advantage is that there are no catalyst poisons in the flue gas, since they have already been removed upstream of the catalyst using ESP and wet FGD unit. This is the main reason why this type of configuration is very common in waste incineration plants. As shown in figure 2-6, a heat exchanger downstream of the FGD unit transfers the heat of the flue gas upstream of the SCR to the flue gas downstream of the FGD unit. Finally, a reheater (RH) upstream of the SCR reactor operated by steam or natural gas is required which compensates the terminal temperature difference of the heat exchanger to the operating temperature of the catalyst [97]. The operating temperature of tail-end SCR catalysts is generally < 300°C. The efficiency of the plant is lower compared to plants with a high-dust arrangement.

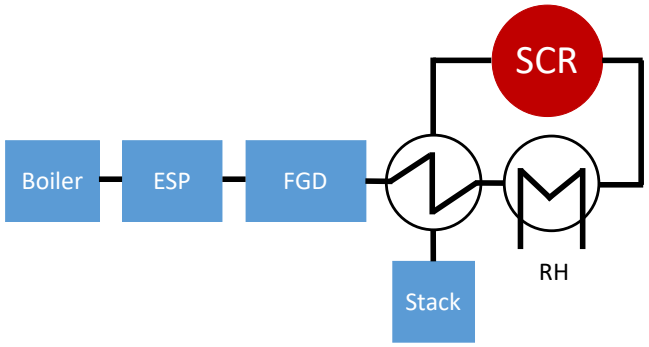

Figure 2-6: Tail-end configuration of the SCR (RH – reheater)

The setup of an SCR reactor, which is the same for all above-mentioned arrangements, is shown in figure 2-7. The catalyst monolith or catalyst element in the case of honeycombs or the catalyst boxes in the case of plate-type catalysts are installed in catalyst modules of typically 2 m by 1 m which are then arranged in layers with sealing between each module and the reactor wall.

Honeycomb catalysts

Honeycomb catalysts are homogeneously extruded ceramic monoliths. To produce honeycomb catalysts, the raw material (metal oxides) and water are mixed in their exact ratio and kneaded to get a well-defined ceramic mass, which is then extruded by special tools, giving the typical honeycomb shape and defining the geometrical properties. A drying and calcining step leads to the formation of the final ceramic structure and defines the inner structures and pores of the material. Special thermal and chemical treatment of the inlet section can be carried out to make it more resistant against erosion (front edge hardening). The whole monolith of honeycomb catalysts is catalytically active. The

monoliths typically have a dimension of 150 x 150 mm and a length of up to 1,300 mm [77] and are directly placed in the catalyst module forming one layer.

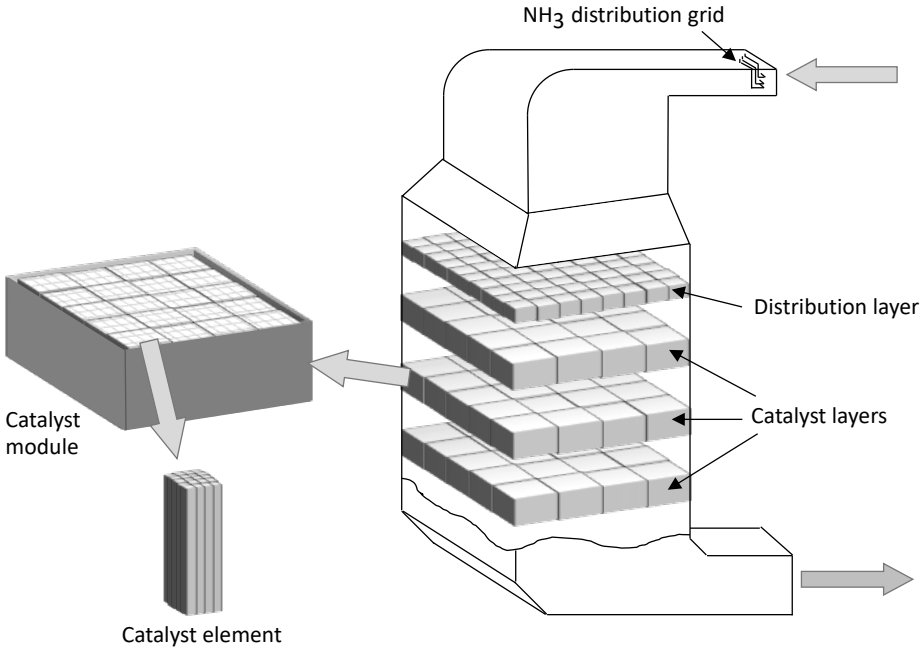

Figure 2-7: Setup of an SCR reactor (modified from [98])

Plate-type catalyst

A mesh of steel forms the base of a plate-type catalyst. The ceramic mass is produced similar to the honeycomb ceramic mass and then applied and rolled on the steel mesh. The channel width is defined by bends in the plate, the notches. About 72 to 82 plates with a width of 450 mm are placed in baskets [77]. Sixteen of these baskets are placed in the module, forming two half-layers.

Corrugated or triangle-shaped catalysts

Corrugated or triangle-shaped catalysts are a further catalyst type. They are a corrugated or triangle-shaped carrier made of paperboard on which the ceramic material is evenly distributed. Due to the weak erosion resistance, these catalysts are mostly applied in low-dust environments.

2.2.2 Chemical composition of the catalyst

For the application in coal-fired power plants, different catalyst types have been tested. Noble metal catalysts were considered for NO_x reduction [99], but since they have low selectivity, oxidize ammonia and are very sensitive regarding poisoning, they have not been further researched or applied for SCR application in power plants [96]. Zeolites like the ZSM-5 (zeolithe socony mobil-5) can also be applied for NH_3 SCR, because they have high stability at higher temperatures up to 600°C. Currently, they are especially applied in

gas-fired power plants as well as for mobile sources, since they show very high activity [96], [99].

Today, metal oxide catalysts with titania as base material (TiO_2) form the state of the art for NO_x reduction in power plant application. Titania in its anatase form with 70-90 wt.-% leads to a large surface area of 50-60 m^2/g [100]. Furthermore, anatase acts as "activating support", leading to higher activity of the active components like vanadium(V) oxide compared to other support materials [95]. Anatase is converted at temperatures higher than 600°C into rutile, which forms the more stable crystalline form of titania, but shows less surface area.

Vanadium, or more precisely vanadium(V) oxide (*vanadia,* V_2O_5), forms the main active component of the catalyst. For power plant applications, the vanadates are homogeneously distributed over the ceramic mass in concentrations of about 0.3 to 2 wt.-%. Together with the TiO_2, monomeric Lewis acid or polymeric Brønsted acid sites are formed. The superior performance of the TiO_2-V_2O_5 system can be traced back to crystallographic similarities between the anatase TiO_2 and V_2O_5. The similarities lead to an electromagnetic interaction because the valence-conduction band gap of the TiO_2 is next to the d-orbital of the vanadium centers [101]. At very low concentrations, vanadate is present as isolated monomeric vanadyl species (V=O), which forms Lewis acid sites. Increasing the vanadate mass concentration homogeneously leads to the formation of polymeric vanadate, higher acidity and thus increased DeNOx activity. An ideal monolayer of vanadate shows the highest activity [102]. A further increase of *vanadia* in the catalyst leads to the formation of amorphous V_2O_5 or crystalline V_2O_5 with no further increase in activity. Limitations in the *vanadia* content of the catalyst are given by the undesired side reaction of SO_2/SO_3 conversion. That is why SCR reactors in power plants with low sulfur fuels like biomass are equipped with SCR catalysts with higher *vanadia* content.

In SCR catalysts, the promoters tungsten(VI) oxide (WO_3) or molybdenum(VI) oxide (MoO_3) are added in a weight-percent range of 5-10% to the ceramic mass. Typical SCR DeNOx catalysts are often denoted as V_2O_5-WO_3/TiO_2 catalysts. The promoters lead to increased acidity and thus increased activity of the catalyst. They increase the thermal and mechanical stability of the catalyst, leading to a broader temperature window for application. Furthermore, the SO_2/SO_3 conversion can be suppressed by these promoters [98]. It has been discussed in the literature that MoO_3 as promoter leads to more resistance against poisoning by arsenic [103], [104], [105]. Lange [106] explained that SCR catalysts containing MoO_3 show smaller pores compared to WO_3 catalysts and these smaller pores lead to lower penetration of the As_2O_3 molecule in the catalyst pores. A drawback of the use of MoO_3 is the lower selectivity of the catalyst, meaning that N_2O could be formed, e.g. according to equation 2-14.

$$4NO + 4\mathrm{NH_3} + 3O_2 \leftrightarrow 4N_2O + 6H_2O \qquad \text{equation 2-14}$$

As a support for its mechanical structure, glass fibers (mainly containing SiO_2, Al_2O_3) are added to the ceramic mass. With plate catalysts, a lower amount of silica fibers is needed due to the support of the stainless-steel mesh.

In chemical analysis of SCR catalysts (e.g. X-ray fluorescence analysis (XRF)), a significant amount of SO_4^{2-} can be found (up to 3 wt.-%) in standard high-dust applications. The catalyst accumulates sulfates from the flue gas on its surface at the active sites. The Lewis acid sites on titania are enhanced and Brønsted acid sites are formed, leading to an increase in activity and increased NO_x removal efficiency [107], [108].

2.2.3 The importance of mass transfer in the reactions in the catalyst

Prior to looking at the reactions at the active sites in detail, the mass transfer of the reactants from the gas phase to the active sites has to be considered with these heterogeneously catalyzed reactions. In figure 2-8, the flow within a channel is shown figuratively:

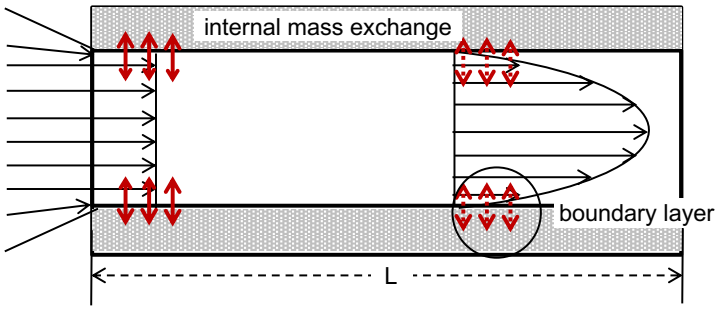

Figure 2-8: Mass exchange within a catalyst's channel (symbolized by the red arrows)

In the inlet zone (on the left side of the diagram), flue gas enters the channel, but the flow profile is not yet fully developed. There is mass exchange from the bulk phase to the surface of the catalyst due to convection and diffusion. Thus, this zone is in practice also called the "turbulent" inlet zone [77] symbolized by solid red arrows, despite the Reynolds number being lower than 2,300. Downstream of the inlet zone, the laminar flow profile has been fully developed. In this profile, mass exchange is only due to diffusion, being limited when compared to convection shown by dashed arrows. Therefore, the rate of NO_x reduction is much greater in the inlet zone of the catalyst. The mass exchange can be described by film- or boundary-layer diffusion models. The external mass transfer coefficient (in m/s) in a rectangular duct can be described by the Hawthorn correlation as proposed by Beeckman [109]:

$$k_{m,NO} = \frac{D_{NO}}{2R_{hyd}} B \left(1 + 0.095 \frac{2R_{hyd}}{L} Re\, Sc_{NO}\right)^{0.45} \qquad \text{equation 2-15}$$

The external mass transfer coefficient $k_{m,NO}$ is thus dependent of the molecular diffusion coefficient D_{NO}, a channel shape factor B, the hydraulic radius R_{hyd}, the length of the catalyst L and the Reynolds and Schmidt numbers.

This correlation enables the comparison of different catalyst geometries and reactor operating parameters related to the mass exchange in the catalyst. According to Jung [110], the entrance length of the flow in a catalyst channel is proportional to:

$$L_E \sim \frac{D_{\mathrm{hyd}}}{L} Re \qquad \text{equation 2-16}$$

Since after this entrance length the flow is developed and the mass transfer lower, the layer arrangement of the catalyst as described in section 2.2.1 has the benefit of increased mass transfer within each catalyst layer. Several smaller layers show higher NO_x reduction than one long layer of the same total length.

When the reactants have passed the so-called boundary layer, they can react on the surface of the catalyst or they penetrate deeper into the catalyst's wall. On their way through the catalyst's inner pore system, complex mechanisms of adsorption, reaction and desorption take place, which will be described later. Thus, the catalyst's pore system is of great importance. This can be described by the Brunauer-Emmett-Teller (BET) analysis of the surface area or the Barrett, Joyner, Halenda pore size distribution (BJH). However, compared to the external mass transfer through the boundary layer, the internal mass transfer by pore diffusion is faster [100].

2.2.4 Mechanisms of NO_x reduction at SCR catalysts

In the reduction of NO_x, which is mainly nitrogen monoxide in the case of coal-fired power plants, ammonia plays a key role, forming nitrogen (N_2) and water (H_2O). The main overall reactions can be summarized as [95]:

$$4NO + 4NH_3 + O_2 \rightarrow 4N_2 + 6H_2O \qquad \text{equation 2-17}$$

$$6NO + 4NH_3 \rightarrow 5N_2 + 6H_2O \qquad \text{equation 2-18}$$

$$6NO_2 + 8NH_3 \rightarrow 7N_2 + 12H_2O \qquad \text{equation 2-19}$$

$$NO + NO_2 + 2NH_3 \rightarrow 2N_2 + 3H_2O \qquad \text{equation 2-20}$$

Reaction equation 2-17 is the most important standard SCR-reaction, taking place at temperatures of high-dust SCR catalyst installations with excess oxygen (O_2), while reaction equation 2-18, which is without oxygen, is quite slow. Reaction equation 2-20 is the so-called "fast SCR reaction", which is relatively fast under ideal conditions without oxygen. However, the regeneration of the active sites needs oxygen, and without oxygen the overall reaction over a long period of time is quite slow. In coal-fired power plant

application, reactions with nitrogen dioxide play a minor role, since the share of NO_2 in total NO_x is below 5% [95].

The detailed mechanism of NO_x reduction has been the subject of intense research within the last 40 years [111]. One of the discussed mechanisms was a Langmuir-Hinshelwood-type mechanism proposed by Takagi [112] in the early state of research. However, the reaction mechanism follows an Eley-Rideal-type mechanism, which was first identified by Inomata [113]. The reaction steps include a strong adsorption of the gaseous ammonia on the active *vanadia* sites of the catalyst, followed by a reaction of a second reactant directly from the gas phase (nitrogen oxide), which might only be weakly adsorbed. Studies carried out with the method of isotopic labelling, e.g. by Janssen [114] and Ozkan [115], confirmed the reaction type and, furthermore, added a redox cycle to the reaction, which explains the formation of the by-products. The commonly accepted reaction cycle as published by Topsøe [116] is shown in figure 2-9.

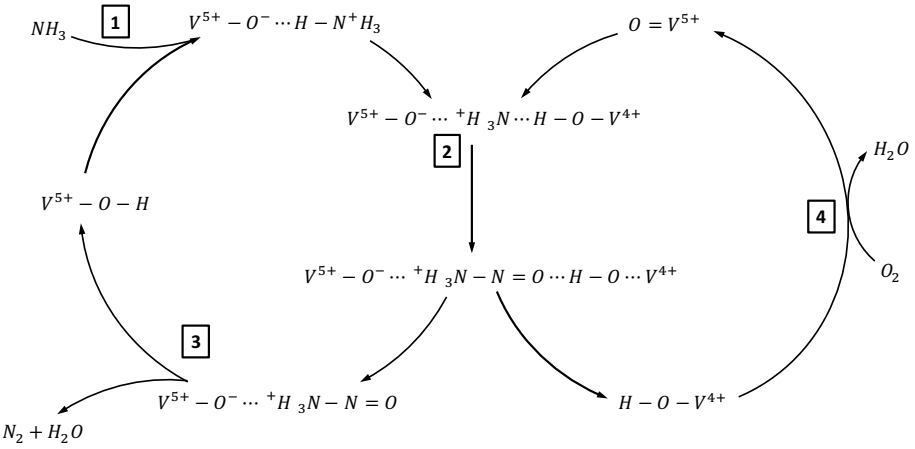

Figure 2-9: Eley-Rideal mechanism of the DeNOx reaction according to Topsøe [116]

The first step is the adsorption of ammonia on V^{5+}-OH or Brønsted acid sites (1). Subsequently, gaseous or weakly adsorbed NO reacts with the active site, which was activated by the V^{5+}=O group (2). Afterwards, this intermediate complex decomposes and N_2 and H_2O are released (3). To complete the cycle and to return to its original state, the V^{4+}-OH has to be oxidized by flue gas oxygen to V^{5+}=O (4). The last step is the rate limiting reaction. However, since in coal-fired power plant flue gases there is enough oxygen present (> 3% oxygen) downstream of the boiler, steps 1-3 determine the turnover of the reaction.

The NO_x reduction at the SCR catalyst is strongly dependent on the temperature. This temperature dependency is mainly determined by the chemical composition of the catalyst. Figure 2-10 shows the typical temperature dependency of the DeNOx reaction with standard V_2O_5-WO_3/TiO_2 catalysts. The maximum achievable NO_x reduction takes place between 370 and 390°C at this type [111], [117], which is also the most typical operating temperature of standard high-dust SCR reactors. When other materials are

applied in the catalyst, the temperature range is shifted. For example, when the base material is zeolite, the shift is to higher temperatures, or when metal oxides like cerium oxides or tungsten oxides are applied, to lower temperatures [118].

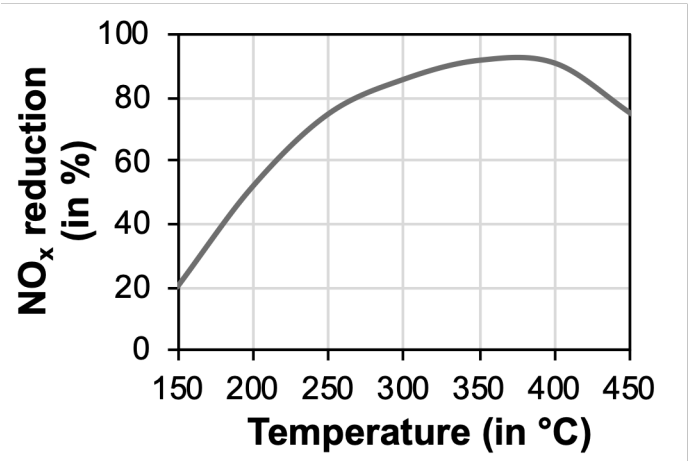

Figure 2-10: NO_x reduction over temperature [[4], modified]

At higher temperatures, side reactions take place and the selectivity of the DeNOx process is reduced. The most relevant reactions at higher temperatures related to NO_x/NH_3 are ammonia oxidation and the formation of nitrous oxide.

$$4NH_3 + 3O_2 \rightarrow 2N_2 + 6H_2O \qquad \text{equation 2-21}$$

$$4NH_3 + 5O_2 \rightarrow 4NO + 6H_2O \qquad \text{equation 2-22}$$

$$2NH_3 + 2O_2 \rightarrow N_2O + 3H_2O \qquad \text{equation 2-23}$$

Ammonia oxidation leads to lower NO_x reduction due to less ammonia available and can even lead to an increase in NO_x concentrations. N_2O formation has to be avoided since it has a high global warming potential.

The kinetics of the NO_x reduction can be described as a first-order reaction regarding NO_x concentration and zero order in NH_3 when $NH_3/NO > 1$ [119]. Furthermore, under typical power plant conditions, the reaction is of zero order regarding H_2O and O_2 [119], [120]. Thus, the turnover can be described with the reaction rate equation for first-order reactions:

$$-\frac{d\,\beta_{\mathrm{NO}}}{dt} = k \cdot \beta_{\mathrm{NO}} \qquad \text{equation 2-24}$$

From this, the activity constant K in m/h, the so-called DeNOx activity, can be derived:

$$K_{\mathrm{NOx}} = -AV \cdot ln(1 - \eta(\propto)) \qquad \text{equation 2-25}$$

In this equation, the parameters are calculated as:

$$AV = \frac{\dot{V}_{\text{wet}}}{S_C} \quad \text{with} \quad S_{\text{C}} = 2 \cdot (a_{\text{ch}} + b_{\text{ch}}) \cdot L \cdot n \qquad \text{equation 2-26}$$

$$\eta(\alpha) = \frac{\beta_{\text{in}}(NO_x) - \beta_{\text{out}}(NO_{\text{x}})}{\beta_{\text{in}}(NO_{\text{x}})} \quad \text{with} \quad \propto = \frac{\beta_{\text{in}}(NH_3)}{\beta_{\text{in}}(NO)} \qquad \text{equation 2-27}$$

A more detailed description of the formulas and further relevant calculations is presented in section 3.8.

The activation energy of the DeNOx reaction changes through the application of a heterogeneous catalyst compared to the homogeneous gas phase reaction, for example with the SNCR process from 350 kJ/mol to about 20 to 150 kJ/mol [120]. Since the standard DeNOx reaction is very fast under power plant conditions, the reaction only takes place in the first 50 µm of depth on the catalyst's surface [100].

2.2.5 SO_2/SO_3 conversion over SCR catalysts

In the past, the most relevant side reaction for high-dust SCR application was the SO_2/SO_3 conversion, meaning the oxidation of SO_2 present in the flue gas to SO_3 according to:

$$SO_2 + {}^1/_2 O_2 \rightarrow SO_3 \qquad \text{equation 2-28}$$

Sulfuric acid is formed at temperatures below 400°C together with the water vapor from the flue gas due to the strong hygroscopy of SO_3 [121].

$$SO_3 + H_2O \rightarrow H_2SO_4 \qquad \text{equation 2-29}$$

Together with free burnt lime (CaO) in the fly ash, a layer of gypsum may be formed on the catalyst's surface, blocking the access of the reactants to the active sites. Furthermore, with excess ammonia, ammonium sulfate and ammonium bisulfate can be formed in the flue gas:

$$NH_3 + SO_3 + H_2O \rightarrow NH_4HSO_4 \qquad \text{equation 2-30}$$

$$2NH_3 + SO_3 + H_2O \rightarrow (NH_4)_2SO_4 \qquad \text{equation 2-31}$$

This formation takes place directly in the catalyst channels, leading to a blocking of the fine porous system of the catalyst, resulting in lower NO_x reduction [77]. Due to capillary force, the condensation in the catalyst porous system takes place even at temperatures above the atmospheric dew point. Thus, this is a factor determining the minimum operating temperature of a catalyst. If a catalyst is heated up to temperatures above 320°C, the ammonium salt deactivation can be removed. Furthermore, SO_3 or ammonia sulfates may lead to corrosion and plugging problems in equipment downstream of the SCR like the air preheater. Thus, the SO_2/SO_3 conversion of a catalyst has to be low.

The SO_2/SO_3 conversion is relatively slow, in comparison to the DeNOx reaction. The mechanism is a Mars-Maessen/Mars-van-Krevelen mechanism according to the following equations as published by Svachula [122]:

$$(V_{2\_}SO_3)_{ox} + SO_2 \rightarrow (V_{2\_}SO_{3\_}SO_2)_{ox} \qquad \text{equation 2-32}$$

$$(V_{2\_}SO_{3\_}SO_2)_{\mathrm{ox}} \rightarrow (V_{2\_}SO_3)_{\mathrm{red}} + SO_3 \qquad \text{equation 2-33}$$

$$(V_{2\_}SO_3)_{\mathrm{red}} + {}^1/_2\, O_2 \rightarrow (V_{2\_}SO_3)_{\mathrm{ox}} \qquad \text{equation 2-34}$$

First, SO_2 is adsorbed from the gas phase at the active *vanadia* site. The second step is quite slow and includes a reduction of the *vanadia* site and the release of SO_3. The re-oxidation of the *vanadia* site takes place using the lattice oxygen and is the slowest step in the cycle. This mechanism explains the long conditioning time needed of new catalysts that is the time to reach steady-state SO_2/SO_3 conversion [122], [123].

Another reaction mechanism of the SO_2/SO_3 conversion was proposed by Dunn [124]. It consists of an adsorption of SO_2 on the active sites, which is the V-O carrier material followed by an oxidation to SO_3, which is then released. The relatively low conversion rate is explained by the stronger adsorption of the product SO_3 than the reagent SO_2 on the active sites.

2.2.6 Mercury oxidation over SCR catalysts

In addition to the homogeneous mercury oxidation, previously discussed in subsection 2.1.4, there is the heterogeneous mercury oxidation at SCR catalysts. Since the chemical equilibrium is on the side of the oxidized mercury – as shown by equilibrium calculations based on the minimization of Gibbs energy, for example by Gutberlet [79], Martel [71] and Stolle [125] – and due to the fact that the reaction is limited by reaction kinetics, a catalyst may help to run the reaction almost completely under flue gas conditions.

Various reaction pathways have been discussed in recent years in the literature:

1. The Deacon reaction

The heterogeneous Deacon reaction can be catalyzed by metal oxides at lower temperatures. This mechanism was proposed by Gutberlet [79] as an explanation for the measured Hg oxidation.

According to the Deacon reaction [126], molecular chlorine can be formed out of hydrogen chloride (HCl) when a copper catalyst is present. The reaction at the metal oxide takes place according to the reactions as shown in equation 2-35 and equation 2-36:

$$MeO_{\frac{x}{2}} + xHCl \rightarrow MeCl_x + \frac{x}{2}H_2O \qquad \text{equation 2-35}$$

$$MeCl_x + \frac{x}{4}O_2 \rightarrow MeO_{\frac{x}{2}} + \frac{x}{2}Cl_2$$ equation 2-36

Reaction equation 2-35 shows the adsorption of HCl on the metal oxide and reaction equation 2-36 the oxidation of the metal-chloride and formation of Cl_2. Subsequently, Hg^0 is oxidized by molecular chlorine (equation 2-11), which is quite a fast reaction. Hisham [127] showed that the reaction could take place similarly with various other metal oxides like manganese oxide (MnO_2) or vanadium oxide (V_2O_5), but copper oxide is the only one with a complete Hg oxidation cycle at temperatures below 700 K. When SO_2 is present in the flue gas, the previously formed Cl_2 can be reduced by the so-called Griffin-reaction (as described in section 2.1.4), which has a strong negative free Gibbs enthalpy over the whole temperature range [60].

2. The Langmuir-Hinshelwood mechanism

The Langmuir-Hinshelwood mechanism includes first an adsorption of Hg and HCl on the catalyst sites and then a reaction of these substances on the catalyst as shown in simplified form in equation 2-37. This means that the catalyst material has to adsorb both substances. Eom [128] proposed this type of reaction mechanism as an explanation for his finding that several layers of mercury are adsorbed on the catalyst.

$$Hg^0_{\text{ads}} + 2HCl_{\text{ads}} + \frac{1}{2}O_{2,\text{ads}} \rightarrow HgCl_{2,\text{des}} + H_2O_{\text{des}}$$ equation 2-37

3. The Eley-Rideal mechanism

The Eley-Rideal mechanism describes a reaction in which one reactant is adsorbed on the catalyst and further reacts with another gaseous or only weakly adsorbed reactant. While some publications claim that HCl is adsorbed and mercury reacts from the gas phase [129], others found in their research and models that mercury adsorbs on the surface and it is HCl which comes from the gas phase [130].

$$HCl_{\text{g}} \rightarrow HCl_{\text{ads}}$$ equation 2-38

$$Hg^0_{\text{g}} + 2HCl_{\text{ads}} + \frac{1}{2}O_{2,\text{g}} \rightarrow HgCl_{2,\text{des}} + H_2O_{\text{des}}$$ equation 2-39

$$Hg_g \rightarrow Hg_{\text{ads}}$$ equation 2-40

$$Hg^0_{\text{ads}} + 2HCl_{\text{g}} + \frac{1}{2}O_{2,\text{g}} \rightarrow HgCl_{2,\text{des}} + H_2O_{\text{des}}$$ equation 2-41

While both Eley-Rideal mechanisms consider the lower Hg oxidation with increasing NH_3/NO ratio – in the first reaction by the competition of NH_3 with HCl, in the second by the competition of NH_3 with mercury – the first reaction mechanism does not take into account the Hg adsorption on the catalyst and the conditioning of the catalyst as reported for example by [66].

4. Mars-Maessen or Mars-van-Krevelen mechanism

This mechanism includes an intermediate, binary mercury oxide (HgO) in the cycle, which is formed by the reaction of adsorbed elemental mercury and the metal oxide of the catalyst. The mechanism was first discussed by Gutberlet [79] and Granite [131] and can be written as:

$$Hg_{\mathrm{g}} + metal\ oxide\ surface \rightarrow Hg_{\mathrm{ads}} \qquad \text{equation 2-42}$$

$$Hg_{\mathrm{ads}} + M_xO_y \rightarrow HgO_{\mathrm{ads}} + M_xO_{y-1} \qquad \text{equation 2-43}$$

$$HgO_{\mathrm{ads}} + 2HCl \rightarrow HgCl_2 + H_2O \qquad \text{equation 2-44}$$

$$M_xO_{y-1} + \tfrac{1}{2}O_2 \rightarrow M_xO_y \qquad \text{equation 2-45}$$

The intermediate mercury oxide then reacts with flue gas HCl forming the mercury(II) chloride, which is volatile and thus released to the gas phase. The oxygen in the reaction cycle comes from the metal oxide lattice, which is independently re-oxidized by flue gas oxygen. This is also in line with the observation of mercury oxidation in the absence of oxygen due to the oxygen storage capacity of the catalyst.

These various reaction pathways are currently still under discussion and no mechanism has been definitely confirmed [125], [132], [133].

2.3 Research on influences on mercury oxidation over SCR catalysts

While the precise mechanism for mercury oxidation is still under discussion, various effects and influences on Hg oxidation have been researched in the past decades.

Flue gas halogen content

The dependency of the Hg oxidation on the halogen content is apparent from the reaction equation. However, in the flue gas, HCl is always present in superstoichiometric ratios, as can be derived from table 2-3 and table 2-4. Stolle [125], Usberti [133], Madsen [81], Kamata [134] and many others showed an increase in Hg oxidation by increasing HCl content in the range of practical relevance for coal-fired power plants. However, since most of these studies were laboratory tests under different catalyst operating conditions, the extent and slope of Hg oxidation dependency on the HCl content varies greatly. This leads to the conclusion that there is a limitation due to internal mass transfer. The important role of oxygen in the Hg oxidation reaction was pointed out by Li et al. [135] in experiments with halogens and oxygen. Without oxygen in the flue gas, independently of the HCl content in flue gas, only insignificant Hg oxidation was measured. This was

explained by the re-oxidation of the catalyst's lattice, which was assumed to play an important role in the oxidation of Hg^0.

The superior performance of Hg bromination compared to Hg chlorination was pointed out by Vosteen [60] and researched by Stolle [125]. A tenfold lower concentration of bromine led to the same mercury oxidation compared to chlorine. However, as shown in table 2-3, the bromine content of the fuel is normally only about 1% of the chlorine content. This was explained by the bromine-Deacon equilibrium in combination with the bromine-Griffin reaction, which both point more strongly to the side of molecular bromine (Br_2) and subsequently $HgBr_2$ under SCR flue gas conditions due to their strongly negative free Gibbs enthalpy.

Nitrogen oxide

There are only a few studies on the single effect of nitrogen oxide on Hg oxidation, since, due to the NO_x reduction, both NO_x and NH_3 are present. Tong [136] and Stolle [125] found a slightly positive effect of nitrogen oxide (NO) on mercury oxidation. The effect was explained by the partial oxidation of NO to NO_2 in the flue gas, which could act as oxidizer.

Ammonia

Various literature has shown a strong inhibition of the Hg oxidation by ammonia ([80], [81], [125]). This was explained by the competitive adsorption of ammonia and HCl on the active sites as well as by the reduction of already formed $HgCl_2$ by ammonia according to:

$$3HgCl_2 + 2NH_3 \rightarrow 3Hg + N_2 + 6HCl \qquad \text{equation 2-46}$$

Stolle [137] described an "induced mercury reduction" in a combined reaction involving NO and $HgCl_2$:

$$6NO + 6NH_3 + 3HgCl_2 \rightarrow 6N_2 + 3Hg^0 + 6HCl + 6H_2O \qquad \text{equation 2-47}$$

This leads to the model prospect which was discussed by Thorwarth [80], that there is an ammonia-rich NO_x reduction zone in the SCR reactor in which there is virtually no effective mercury oxidation. This is followed by an NH_3-poor zone in which only Hg oxidation takes place. According to this, shortening the NO_x reduction zone, which is for example possible by increasing the external mass transfer, would lead to higher mercury oxidation.

Sulfur dioxide

Ambiguous effects of SO_2 on Hg oxidation are discussed in the literature. While Stolle [125] found a decrease of Hg oxidation with increasing SO_2 concentration, which was explained by the chlorine-Griffin reaction, Li [135] found an increase of oxidized mercury when SO_2 and O_2 are present in the flue gas. In bench-scale studies, Zhuang [138] found a

mitigation effect of SO_2 and SO_3 on mercury oxidation and explained the effect by competition of HCl and these acid gases for the same active sites. In another study, Li et al. [139] found a promoting effect of SO_2 at low concentrations while at higher concentrations, SO_2 had an inhibitive effect on Hg oxidation.

2.4 Material research to improve Hg oxidation over SCR catalysts

In order to achieve higher mercury oxidation than with standard catalysts, various materials have been researched in the past decade.

As reported by Dranga [140], Stolle [125] and Hocquel [66], the V_2O_5 content of an SCR catalyst greatly influences mercury oxidation. An almost linear dependency could be derived by Stolle. In another work, Stolle [141] tested various metal oxides impregnated on standard SCR DeNOx catalysts in concentrations of 2-3 wt.-% in flue gas atmosphere with and without SO_2. In this study, CuO and Cr_2O_3 showed superior Hg oxidation with little or no influence on DeNOx activity.

Hocquel [66] tested the effect of various metal oxides of "standard" SCR catalysts as pure material powders and found significant Hg oxidation only for V_2O_5, while MoO_3, WoO_3, SiO_2 and TiO_2 (rutile) did not have an effect on Hg oxidation.

Research on various TiO_2-supported metal oxides (Cr_2O_3, V_2O_5, Mn_2O_3, Fe_2O_3, CuO, MoO_3, NiO) was carried out by Kamata [142]. A correlation between Hg oxidation and NO_x reduction and an inhibition of Hg oxidation by ammonia was found. The Hg oxidation followed the order MoO_3~V_2O_5>Cr_2O_3>Mn_2O_3>Fe_2O_3>CuO>NiO.

The effect of MnO_x on alumina was studied by Qiao [143]. The catalysts showed an Hg adsorption effect when no HCl/Cl_2 was present in the flue gas and could be regenerated by rinsing with the respective halogen. Further research on V_2O_5-MoO_3/TiO_2 catalysts showed that adding molybdenum to the catalyst leads to higher Hg oxidation compared to commercial titanium-vanadium-tungsten catalysts [144]. Furthermore, it was assumed in this publication that the Hg oxidation follows a Mars-Maessen mechanism.

Various catalyst materials for the oxidation of mercury were reviewed and discussed by Presto [145]. Iron oxides were found to catalyze the oxidation of Hg^0. But while α-Fe_2O_3 did not have an effect on Hg oxidation, γ-Fe_2O_3 increased the extent of Hg oxidation. As other metal or metal oxides with potential for Hg oxidation, copper oxide (CuO) as well as noble metals (gold, silver, palladium, platinum) have been identified, of which some showed high Hg oxidation also in power plant application. For example, a test in a coal-fired power plant over ten months showed an Hg oxidation rate of over 80% for palladium.

The application of ruthenium (Ru) in SCR catalysts to boost Hg oxidation was described in [146]. Standard SCR catalysts were modified with Ru and combinations of Ru and Mo in order to produce an “SCR-plus” catalyst. The combination of Ru with Mo helped to reduce the amount of the precious metal Ru and the tolerance regarding to SO_2 was increased.

A review by Dranga [140] discussed developments for Hg oxidation catalysts. In the review paper, the positive effect of CuO catalysts was confirmed under various test conditions and, for the first time, nano CuO was mentioned as being used for catalytic Hg oxidation. As another group, MnO_x catalysts were discussed, which showed up to 90% Hg oxidation, while some papers claimed a high Hg sorption capacity. Due to their high oxygen storage capacity, CeO_2 indicated to have high Hg oxidation potential in some experiments.

Mitsubishi Hitachi Power Systems is following a different approach for increasing the Hg oxidation at SCR catalysts. Instead of the application of different metal oxides with the aim of increasing the Hg oxidation, the so-called TRAC® catalyst includes a high amount of active components, e.g. vanadium, which is selectively deactivated with an α-component to be inactively related to SO_2/SO_3 conversion [147].

2.5 Objective and scope of the work

The general problem of comparing catalyst developments in the literature is the lack of a standard setup and standardized test procedure in the respective research. Some catalysts are tested as powders or coarse particles in laboratory setups, but at different space velocities, gas compositions and mass transfers than in full-scale power plant application, not reflecting their real application and shape as honeycombs or plates. These studies give a first insight into promising materials, but the application is often questionable since there is still a big step from the laboratory experiment to the full-scale SCR catalyst from the manufacturing side as well as from the chemical and mass transfer side. Regarding the test conditions and procedure, the guideline of the technical association of the large-scale power plant operators, VGB guideline S-302-00-2013-04-DE [123], gives information related to DeNOx activity as well as SO_2/SO_3 conversion measurements. In the US, the American Electric Power Research Institute (EPRI) has published a similar guideline on DeNOx activity and SO_2/SO_3 conversion testing which was revised in 2018 [148]. The first guideline on mercury oxidation testing was published by EPRI in 2015 [149]. These standards form an internationally accepted base for catalyst characterization, which also formed the base for the catalyst test within this work.

As it could be seen in the literature study, many academic works only cover the Hg oxidation in their research, not taking into account the other side reactions of SCR catalysts. Thus, this work focuses on three main points:

1. Research on the individual reactions over the catalysts
2. The interaction of the reactions over the catalysts
3. Effect of new catalyst compositions on the three most relevant reactions: DeNOx activity, Hg oxidation and SO_2/SO_3 conversion

By doing so, for the first time a holistic view on new Hg oxidation catalysts is given, allowing a complete insight into the reactions at SCR catalysts in the industrially relevant range under industrially relevant test conditions.

2.6 Already published parts of the work during its genesis

During the genesis of this work, some of the results were already published by the author as principal author. In order to make these publications identifiable, they are listed and named here.

The first experiments with the newly developed SCR catalysts and the effects on the SO_2/SO_3 conversion were presented at a conference followed by a journal publication [150]. The first important discoveries on catalyst development were summarized in the final report of the DENOPT project (Optimisation of SCR DeNOx catalyst performance related to deactivation and mercury oxidation) [151]. Within the DEVCAT project (Development of high-performance SCR catalysts related to different fuel types), results on geometrical influences were published at a conference followed by a journal publication [152]. Further important results on new catalyst developments were included in the final report of the DEVCAT project [94]. In various conference contributions, selected results of this project or summaries were disseminated [150], [154], [155]. Additionally, the behavior of mercury in the lab-scale firing system was presented at conferences [156], [157] followed by a journal publication [84]. Furthermore, aspects of mercury oxidation at SCR catalysts which were undertaken following special regeneration procedures were discussed in a journal publication [158].

All the aforementioned publications were prepared and submitted by the author. The experiments which were used as a basis for the publications were planned by the author and conducted partly with the support of the co-authors listed in the references/literature. The main scientific conclusions were derived by the author and fruitful discussions with the co-authors helped to state the conclusions more precisely.

3 Experimental methods and equipment for catalyst evaluation

In this chapter, the relevant experimental methods for catalyst characterization are described. Many of the methods are new and were first researched, developed and applied in the framework of this work. The description of the methods helps in understanding the subsequent discussion and interpretation of the conducted experiments described in the chapters 4 and 5.

3.1 Analytical methods

3.1.1 Chemical and physical catalyst characterization

All catalysts, except one plate-type catalyst in section 4.9, were produced in close cooperation with the author by IBIDEN Porzellanfabrik Frauenthal GmbH in their full-size geometrical shape. Following the production, the samples were analyzed for their chemical and sometimes physical characteristics, which led to the respective given chemical composition. “Chemical characteristics” means the analysis of the chemical composition, which is carried out by means of X-ray fluorescence spectrometry (XRF) or by inductively coupled plasma optical emission spectroscopy (ICP-OES). A further but very specific method is scanning electron microscopy (SEM) coupled with energy disperse X-ray spectroscopy (EDX).

X-ray fluorescence spectrometry (XRF) is the most common method of performing chemical elemental analyses on SCR catalyst samples and thus the only method which is discussed here. Each catalyst sample is characterized by a bulk analysis of a homogenized finely ground catalyst material as well as by a surface analysis, which gives only a snapshot of the surface. XRF relies on the principle that atoms can release characteristic X-rays as a result of electrons transferring from higher energy orbital levels to lower energy orbital levels. Prior to this release of radiation, the electrons are lifted in the higher energy orbital levels by excitation of the sample by polychromatic X-ray radiation. Each element will produce these X-rays with strengths characteristic to that particular element. Thus, elemental species can be determined by measuring the emitted X-ray strength. Quantitative determination is made by counting the number of X-rays of any particular strength. The number is proportional to the concentration of the element. In one scan, the presence of elements can be detected starting roughly at atomic number 9 (sodium) to 92 (uranium). The result is usually given for each element in its oxide form

with the highest oxidation state. XRF data is very lab specific and includes the instrument properties, calibration and sample preparation.

The “physical characteristics” of the catalyst refer mainly to the geometrical properties of the fine pore system. The pore system of a catalyst serves as support for the active catalyst compounds like vanadium. A change in the surface area or an enlargement of pore sizes will change the catalyst activity significantly. The surface area is determined by means of the Brunauer-Emmett-Teller (BET) method [159] mentioned in subsection 2.2.3. The Barrett, Joyner and Halenda (BJH) method [160] is used to determine pore volume, pore radius and pore size distribution. These values assist in the explanation of changes in the catalyst activity. The BET method relies on gaseous adsorbents to determine the total surface area of a solid sample. Preferred test methods are single- or multi-point nitrogen adsorption or mercury porosimetry. Especially for determining the BJH pore size distribution, a multi-point adsorption and desorption curve is recorded and evaluated according to the method. By determining the amount of nitrogen gas adsorbed onto internal and external surfaces of catalysts at a specific temperature, the total surface area of a catalyst sample and the pore size distribution can be determined. Careful outgassing of the sample is required and testing occurs under highly controlled pressure and temperature conditions.

3.1.2 Measurement of mercury gas phase concentrations

The measurement of mercury gas phase concentrations is conducted either continuously or discontinuously. The focus of mercury measurement in this study is the continuous Hg measurement, since continuous mercury monitors are the state of the art for mercury measurements in the lab and give an instantaneous response to concentration changes.

The continuous Hg measurement is carried out by a cold vapor atomic absorption (CVAA) monitor with Zeeman background correction. Most tests in this work were carried out using the Hg2010 monitor (Semtech AB, Sweden), although some tests were carried out with the successor of this monitor, called Hg2020 (Semtech AB, Sweden), or with the RA915 AMFG (Lumex, Russia). In these monitors, a UV lamp with a wavelength of 253.7 nm shines through a measurement cell with defined length, which is flown through by measurement gas. The concentration is calculated according to the Lambert-Beer law. An auto-zero valve enables a regular determination of the zero value for calibration. The Zeeman background correction ensures that only mercury is measured by the analyzer and that the background gases (e.g. SO_2) are removed from the signal. A strong magnetic field influences the UV lamp periodically, which leads to a split in the wavelength of the emitted light. While mercury is in the cell which only absorbs UV light at the definite wavelength of 253.7 nm, the background gases absorb over a wide range. The mercury concentration can be calculated from the difference of these two signals.

By means of CVAA, only elemental mercury (Hg^0) can be detected, while other mercury compounds (e.g. $HgCl_2$) do not absorb UV light in the applied range. Thus, an upstream wet chemical reduction unit reduces all oxidized mercury, allowing the analyzer to measure total mercury (Hg^{tot}) as Hg^0. In the framework of this work, tin(II) chloride solution is used as reducing agent, which reacts with Hg^{2+} according to equation 3-1, in which the oxidation numbers are additionally symbolized:

$$Hg^{2+}Cl_2 + Sn^{2+}Cl_2 \rightarrow Hg^0 + Sn^{4+}Cl_4 \qquad \text{equation 3-1}$$

Due to the low solubility of the tin compounds in water, 37 vol.-% HCl is added. The $SnCl_2$ solution is directly added at the hot sampling site to the flue gas by a T-piece. All tubing material is made of Perfluoroalkoxy alkane (PFA). A glass-made reduction loop ensures an intense contact between flue gas and reduction agent. In a flue gas cooler operated at 3°C, liquid and gas are cooled down and separated. A water trap ensures that no water droplets are transferred to the analyzer, where the flue gas is analyzed in the measurement cell. A pump installed downstream sucks the flue gas through the system. By measuring temperature and pressure, the concentration is referred to standard conditions (0°C, 1013 mbar).

Since the analyzer with the upstream wet chemical reduction unit only measures Hg^{tot}, for measuring speciation a special setup is necessary. One could just bypass the reduction unit for measuring only Hg^0, but in the framework of this work, speciation was carried out by an anion ion exchanger resin. The Dowex® 1x8 resin as described by Metzger and Braun [161] selectively adsorbs $HgCl_2$. By pre-treatment with HCl solution, the commercial Dowex® resin, which is a polystyrol resin with trimethyl ammonium as functional group, is activated and converted to its chlorine form in order to be able to capture $HgCl_2$ as chloromercurate complexes. More than 97% efficiency of adsorption was measured in the temperature range of 110°C to 140°C and an adsorption capacity of about 20 mg/g resin was detected. For the measurement of Hg^0, about 500 mg of resin is fixed in a glass tube by quartz wool and installed just upstream of the T-piece at the sampling point. An electrical heat jacket ensures that the required temperature range is kept. Since all other mercury compounds and especially Hg^0 passes the adsorber, Hg^{2+} concentration is then calculated according to:

$$\beta_{Hg^{2+}} = \beta_{Hg^{tot}} - \beta_{Hg^0} \qquad \text{equation 3-2}$$

The concentrations are measured continuously. Under steady state conditions, either total or elemental mercury is measured. Thus, the applied mercury speciation method is quasi-continuous. By measuring the oxygen concentration downstream of the pump of the Hg analyzer, a continuous leak check is carried out.

3.1.3 Determination of SO_2/SO_3 conversion

For the determination of the SO_2/SO_3 conversion, the SO_3 concentration is measured discontinuously according to the VDI method 2462 Bl. 2 [162]. In this controlled condensation method, sulfur trioxide is condensed as sulfuric acid aerosols in a glass condenser since due to the equilibrium of SO_3 and H_2SO_4, as shown in figure 2-2, SO_3 is present as an H_2SO_4 aerosol in flue gases when water vapor is present. For the measurements, a slip stream of the flue gas is sucked through the condenser, which is a glass coil. For the measurements in synthetic flue gas, the condenser is directly connected to the sampling port and for the measurements in real flue gas, the flue gas is filtered by a probe filled with quartz wool in order to hold back the fly ash. In contrast to the VDI method, the glass coil is placed in a water bath on a temperature-controlled heating plate and heated up to 85°C. This temperature is above the water dew point and well below the acid dew point of sulfuric acid. When ammonia is present in the experiments, the temperature of the water bath is increased to 95°C in order to avoid the depositing of ammonia sulfites, which would lead to biased results.

The gas flow and gas volume which is sucked through the coil is measured by a gas meter. After the measurement, the coil is rinsed with a defined amount of deionized water, which is then analyzed by titration with barium perchlorate solution and thorin indicator for the sulfate (SO_4^{2-}) concentration. From the sulfate concentration, the SO_3 concentration can be determined by considering the measured standardized gas volume. Finally, the SO_2/SO_3 conversion is calculated, taking into account the measured SO_2 inlet concentration.

3.1.4 Discontinuous measurement of HCl and NH_3 slip

The concentration of hydrogen chloride (but in some experiments also HBr) and the ammonia concentration downstream of the catalyst, the so-called ammonia slip, is measured discontinuously in order to check the desired concentrations. The measurements were carried out according to DIN EN 1911 (HCl) [163] and VDI 3878 (NH_3) [164]. For the measurement in real flue gases on the lab-scale firing system, the flue gas is filtered in situ by a quartz wool filter. The measurements for HCl and NH_3 are carried out by absorption of the specific components in an absorption solution in wash bottles and by determining the flue gas volume at STP which was sucked through the wash bottles. While for HCl deionized water is used as absorption solution, for NH_3 a sulfuric acid solution of 0.1 mol/l is applied. The solutions are subsequently analyzed for their concentrations (HCl: ion chromatography, NH_3 analyzed as NH_4^+: photometry).

3.1.5 Proof of molecular chlorine (Cl_2) in flue gas

The measurement and proof of molecular chlorine (Cl_2) in flue gas is carried out indirectly, since a direct measurement according to DIN EN 1911 [163] as described in subsection

3.1.4 would result only in a sum of HCl and Cl_2. Thus, a selective method is developed, showing only the molecular halogen concentration. The method is derived from the iodometry titration. Potassium iodide solution is filled in wash bottles. A sample flow is bubbled through the wash bottles and the gas volume is determined. If molecular chlorine is contained in the flue gas, the following oxidation reaction takes place:

$$2\,KI + Cl_2 \rightarrow 2\,KCl + I_2 \qquad \text{equation 3-3}$$

When the measurement is finished, starch solution is added and at a soft acidic pH value and the solution turns blue. With titration with sodium thiosulfate, the color disappears at the equivalence point, since the solved iodine is consumed according to the following equation:

$$I_2 + 2\,S_2O_3^{2-} \rightarrow 2\,I^- + S_4O_6^{2-} \qquad \text{equation 3-4}$$

The amount of consumed sodium thiosulfate solution with a known concentration which is consumed in the reaction is directly equivalent to the amount of Cl_2.

3.1.6 Continuous flue gas analysis – DeNOx activity and SO_2 measurement

NO_x reduction and DeNOx activity are determined by continuous flue gas analysis. The concentration of nitrogen monoxide (NO) is measured either upstream and downstream of the catalyst, or downstream of the catalyst with and without ammonia by non-dispersive infrared light absorption (NDIR). The SO_2 concentration is measured downstream of the catalyst by non-dispersive ultraviolet light absorption (NDUV). Ahead of the analyzer, the flue gas is cooled down in a flue gas cooler. A paramagnetic oxygen analyzer is installed downstream in order to measure the oxygen concentration and for continuous leak check.

3.2 Setup for test of single metal oxides and transition tests

Single metal oxides are tested in a specially designed micro-reactor in order to identify their effect on mercury. The reactor is made of borosilicate glass and constructed as shown in figure 3-1.

The test rig consists of a gas preheating and conditioning unit in which flue gas is mixed by adding HCl solution and Hg^0 to compressed air. Liquid Hg^0 is kept in a vessel placed in a water bath. Due to its vapor pressure, elemental mercury is continuously in the gas phase over the liquid mercury droplet. By purging the gas phase with nitrogen, mercury is carried over to the main gas stream. The mercury concentration can be adjusted by varying the temperature of the water bath in which the vessel containing mercury is

placed. The temperature of the preheating unit can be adjusted in order to reach the desired temperature. The temperature of the reactor containing the metal oxide or catalyst which is installed downstream of the preheating zone can furthermore be adjusted in order to keep the flue gas temperature constant.

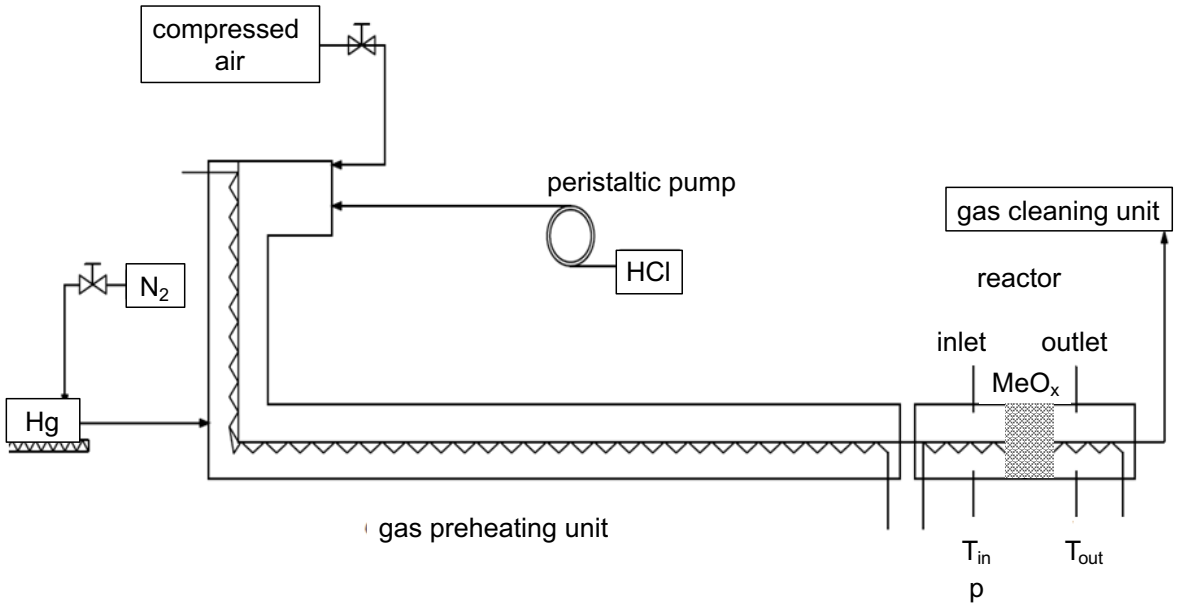

Figure 3-1: Setup for testing of single metal oxides

Temperature measurements (K-type thermocouples) upstream and downstream of the sample ensure a very narrow temperature gradient over the sample. The sample (mostly powder) is fixed and evenly distributed on pure silica wool. An empty reactor test showed that there is no influence on the Hg oxidation resulting from the silica wool.

3.3 Laboratory micro-reactor for catalyst testing

The setup of the laboratory micro-reactor for catalyst testing is similar to the previously described arrangement, but more inspired by the descriptions of micro-reactor tests in VGB S-302 [123]. A schematic of the setup is shown in figure 3-2. The reactor as well as the preheating zone are placed in a semi-muffle furnace. All parts which are in contact with the flue gas are made of borosilicate glass. All gases (N_2, O_2, CO_2, NO, SO_2) except ammonia and mercury are mixed prior to entering the oven. The main gas for the measurements is a premixed synthetic flue gas consisting of oxygen (3.5 vol.-%), carbon dioxide (15 vol.-%) and the remainder nitrogen. All gases are dosed by thermal mass flow controllers. No SO_3 was dosed during the experiments and it was furthermore checked from time to time that the SO_3 inlet concentration is zero. Water as well as halogens in the form of HCl/HBr solution are dosed to the flue gas by adding the solution by peristaltic pumps into the hot zone of the oven, where it is instantaneously evaporated. The exact mass flow is measured and adjusted by placing the bottle on a balance and

determining the change of weight per time interval. Mercury is added, as previously described, just upstream of the catalyst in order to minimize any homogeneous reactions in the pre-mixed zone. In experiments with ammonia, mercury is added at the same position to the main gas stream as well.

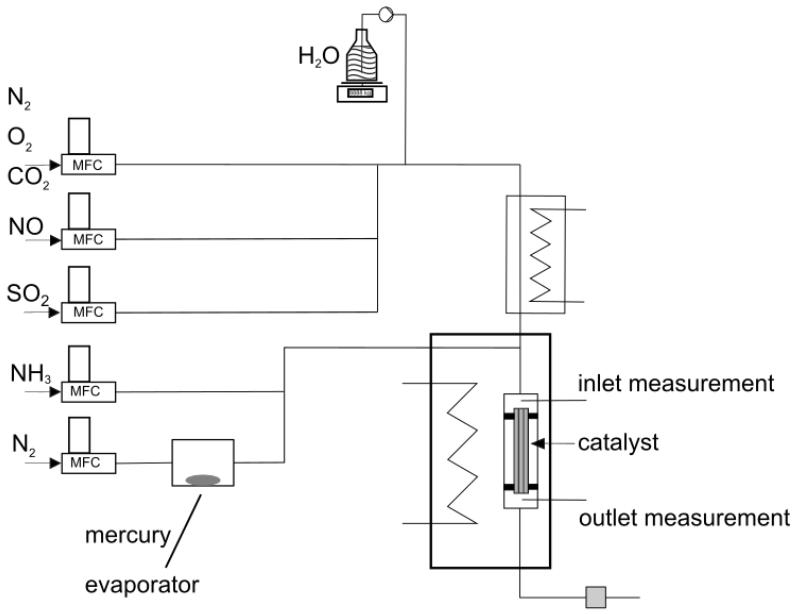

Figure 3-2: Setup of the laboratory micro-reactor

The catalyst is fixed in a glass tube as shown in figure 3-3 and figure 3-4. The distance between the outer wall of the catalyst and the inner wall of the catalyst holder is filled with glass wool in order to avoid the bypassing of flue gas. For the plate catalysts, a special borosilicate glass plate holder keeps a defined clear width and pitch (at identical plate thickness) of the catalyst (figure 3-4). Unlike the catalyst dimensions for micro-reactor testing described in VGB S-302 [123], the length of the samples is increased to about 200 mm and carefully adjusted to meet the desired area velocity (equation 2-26), while keeping the linear velocity constant. A longer sample length leads to an increased share of laminar flow zone of the catalyst, which slightly more reflects the conditions in field application.

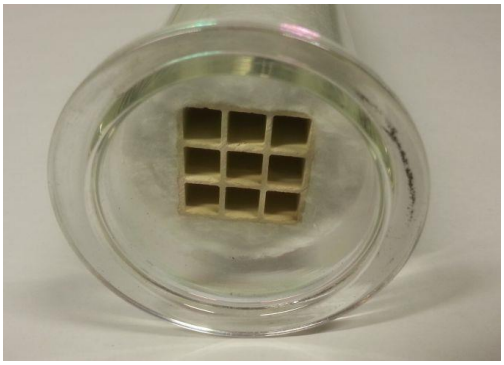

Figure 3-3: Honeycomb catalyst installed in a catalyst holder

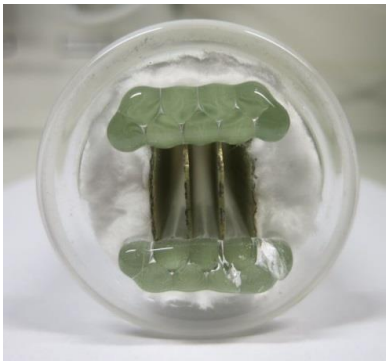

Figure 3-4: Plate catalyst installed in a catalyst holder

The measurement of mercury species is carried out directly upstream and downstream of the catalyst reactor (distance: 50 mm). Prior to starting the determination of the Hg oxidation, the stability criterion has to be fulfilled. In addition to a stable mercury concentration and a stable HCl dosing, the total mercury concentration at the inlet (Hg_{in}^{tot}) and the outlet (Hg_{out}^{tot}) has to be the same, in order to reflect steady state operation and to ensure that no adsorption or desorption is taking place. A deviation of the inlet and outlet mercury concentration of $\pm$ 5% is accepted.

For the measurement of the SO_2/SO_3 conversion, a conditioning of 72 hours in flue gas is done as proposed in VGB S-302 [123]. The stable value is reached when the values of the SO_2/SO_3 conversion measurements fluctuate around a mean value and no trend is visible.

A downstream wet scrubber and an activated charcoal adsorber ensure that no mercury or acid gases are discharged from the experiment.

3.4 Setup of the lab-scale firing system

The lab-scale firing system represents a 600 MW_{el} coal-fired power plant equipped with air pollution control devices scaled down by a factor of approximately 1:1,000,000. Its setup is shown in figure 3-5. It is equipped with the most relevant components of the flue gas pathway of the full-scale plant: combustion chamber, cooling zone (representing the heat exchanger), SCR reactor, electrostatic precipitator, wet flue gas desulfurization and finally an induced draft (ID) fan. The fuel (coal, biomass, and a fuel mixture of coal and biomass) is fed to the burner by a dosing feeder, where it is mixed with combustion air and blown into the combustion chamber. The combustion chamber is a drop tube furnace and is constructed out of an electrically heated highly heat-resisting steel tube of 1,500 mm length. The temperature of the combustion chamber is adjusted to 1,100°C. The combustion air is electrically preheated. The fuel flow rates of the test rig range between 0.15 and 0.45 kg/h, which is equal to a thermal output of about 2 kW.

After the combustion chamber, flue gas is cooled down in an electrically heated cooling section in order to get a smooth decrease in temperature down to the desired operating temperature of the catalyst. Directly downstream of the combustion chamber, additional gases or liquids (like HCl solution) are added in order to adjust the concentrations. Upstream of the SCR catalyst section, ammonia can be added by a spray nozzle and the differential pressure over the catalyst is monitored. At sampling ports upstream and downstream of the SCR reactor the concentrations of the flue gas components are measured.

The catalyst section consists of an electrically heated glass tube which is isolated to ensure a maximum temperature drop over the catalyst of less than 5 K. The application of glass ensures that there is no interference of mercury with the reactor wall, which would

lead to biased measurements. In the catalyst reactor, SCR DeNOx honeycomb catalysts with 3 x 3 channels (at a pitch of 7 mm) can be installed due to the dimensions of the catalyst holder. The length of the reactor is 1 m. During the experiments, the length of the catalyst is adjusted on the cross-sectional dimensions of the catalyst in order to carry out the measurements with all catalysts at a constant area velocity (AV).

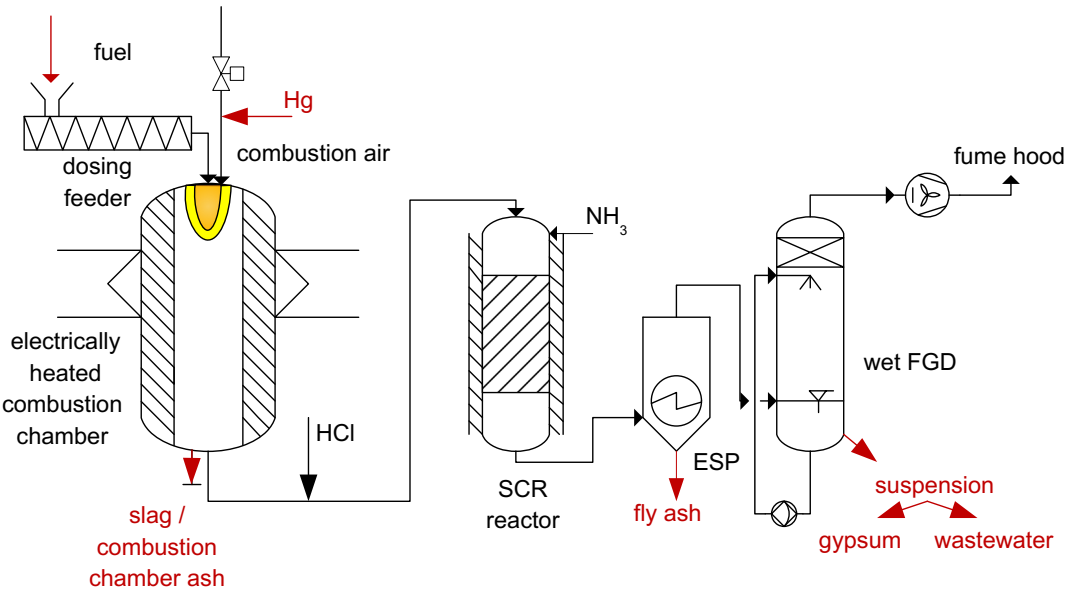

Figure 3-5: Setup of the lab-scale firing system

Downstream of the catalyst section, the flue gas cools further down and enters the electrically heated electrostatic precipitator (ESP, Delta-Profimat®, Haereus Electro-Nite). A spray electrode directly in the center of the flue gas flow charges the particles. Then, particles deposit on the stainless-steel deposition foil and can be collected. Glass wool at the outlet of the filter ensures that fine fly ash particles are also removed from the flue gas before entering the wet flue gas desulfurization unit.

Furthermore, a wet flue gas desulfurization unit fully constructed of glass is integrated in the flue gas pathway downstream of the ESP. It is designed as a single-loop FGD unit with an external sump. The separation of the absorber and the sump enables detailed research in the two relevant sections of an FGD unit. Relevant parameters, such as pH value, oxidation reduction potential (ORP) and temperature, are measured in the external sump as well as in the small sump of the absorber. The pH in the FGD unit is adjusted by dosing of limestone slurry. Aeration of the external sump is carried out by pure oxygen due to the scale of the setup. The external and absorber sumps are heated to adjust a defined slurry temperature. During the experiments, the FGD unit was operated under stationary conditions. A demister after the absorber minimizes the loss of water in the absorber. Finally, an ID fan is installed in the flue gas path which sucks the flue gas through the plant directed at the fume hood.

3.5 The bench-scale reactor for industrial catalyst tests

While the laboratory micro-reactor described in section 3.3 is partly used in industry for catalyst testing especially for production quality assurance and quality control as well as for research purposes, the testing of SCR catalysts in the lab-scale firing system described in section 3.4 is unique in the framework of this work. The most commonly used method and state-of-the-art for industrial catalyst testing is the so-called bench-scale catalyst test in the bench reactor. This is a setup for catalyst tests in their original full-scale sample cross section of 150 mm x 150 mm and their full-scale length as described in the VGB S-302 [123] and EPRI Testing Protocol 3002013048 [148]. The flue gas in these tests is synthetically mixed but the test condition, meaning the flue gas flow in the catalyst's channels and the flue gas composition is representative to field conditions [148]. The setup is not discussed in any further detail here, since the results of tests in the bench-scale reactor are only interpreted in section 4.4.

3.6 Test conditions of micro-reactor tests

The general test conditions for the determination of NO_x activity, SO_2/SO_3 conversion and Hg oxidation in synthetic flue gas in micro-reactor tests can be summarized as shown in table 3-1 and table 3-2.

Table 3-1: Test conditions for catalyst tests for DeNOx activity and SO_2/SO_3 conversion

		Range	**Setpoint activity (in m/h, STP, dry)**	**Setpoint SO_2/SO_3 conversion (in %)**
NO	mg/m^3 (STP, dry)	0-600	500	-
NH_3/NO ratio	-	0-1.2	1.2	-
SO_2	mg/m^3 (STP, dry)	0-5.000	1.500	
O_2	%	3-5	4	
H_2O	%	7-10	7	
N_2	%	balance	balance	
T	°C	380	380	
AV*	m/h (STP, dry)	approx. 27	approx. 27	
LV	m/s (STP, dry)	1	1	
Clear width HC	mm	variable	6.2 (standard), as listed	
Clear width PT	mm	-	5	
Length*	mm	160-300	approx. 200	
Channels*	pc.	2x2 or 3x3	3x3	

*: depending on the catalyst type; HC: honeycomb; PT: plate

The test conditions are adjusted in a way to represent the flue gas of a coal-fired power plant, or a power plant with co-combustion of secondary fuels like sewage sludge or meat and bone meal, or a power plant with biomass (wood) combustion. Coal and co-combustion differ only in their halogen content.

Table 3-2: Test conditions for Hg oxidation testing

		Range	Setpoint Hg oxidation (in %)
NO	mg/m^3 (STP, dry)	0-600	-
NH_3/NO ratio	-	0-1.2	-
SO_2	mg/m^3 (STP, dry)	0-1.500	-
O_2	%	4	4
H_2O	%	7	7
N_2	%	balance	balance
HCl	mg/m^3 (STP, dry)	0-150	10; 50; 100; (150)
$Hg_{el./ox}$	$\mu g/m^3$ (STP, dry)	50	50
T	°C	350-400	380
AV*	m/h (STP, dry)	approx. 27	approx. 27
LV	m/s (STP, dry)	1	1
Clear width HC	mm	variable	6.2 (standard), as listed
Clear width PT	mm	-	5
Length*	mm	160-300	approx. 200
Channels*	pc.	3x3; 2x2	3x3

*: depending on the catalyst type; HC: honeycomb; PT: plate

3.7 Operating conditions of lab-scale firing system for catalyst tests

The lab-scale firing system was fired with different fuels in order to research the reactions at different real flue gas atmospheres: coal (“100C”), natural, non-torrefied biomass (unspecified wood, “100B”) and a mixture of torrefied biomass and coal with a percentage of 80% coal and 20% biomass (“80C/20B”). The ultimate and proximate analysis as well as the chlorine and mercury content of the fuels are listed in table 3-3.

The coal is a typical coal from El Cerrejón, Colombia, characterized by moderate sulfur content and relatively high ash content. Biomass is finely ground wood pellets. The “80C/20B” mixture is a commercial fuel mixture of a coal different to El Cerrejón and torrefied biomass originating from Norway. This 80C/20B mixture forms a typical flue gas for co-combustion since the chlorine content is increased by a factor of five, which results in this case possibly from the different coal. Since the biomass (“100B”) has a lower calorific value, in order to reach the similar flue gas composition, the mass flow of the biomass is increased. Furthermore, the mercury concentration in the flue gas is increased by adding elemental mercury by an evaporator as described above in section 3.3, in order to reduce the bias of the measurement.

In table 3-4, the standard test conditions for the measurements at the lab-scale firing system are listed. These form the basis for further variations in flue gas composition.

Table 3-3: Properties of the fuels fired in the lab-scale firing system

Sample	**Unit**	**Coal - ("100C")**	**Biomass - ("100B")**	**Mixture - ("80C/20B")**
Proximate analysis				
Volatiles (N_2+900°C)	%, dry	30.6	77.1	40.6
Ash (O_2+550°C)	%, dry	13.2	1.3	8.9
Ultimate analysis				
Carbon (C)	%, dry	70.0	52.5	68.4
Hydrogen (H)	%, dry	4.4	5.9	5.2
Nitrogen (N)	%, dry	1.55	n.d. < 0.3	1.2
Sulfur (S)	%, dry	0.652	0.104	0.454
Mercury (Hg)	mg/kg, maf	0.085	0.025	0.052
Chlorine	mg/kg, maf	120	130	570
Physical/chemical properties				
Net calorific value	J/g, dry	27,614	19,665	27,049

Compared to the micro-reactor test conditions, the catalyst measurements in the lab-scale firing system are aiming at the application in the real flue gas atmosphere. The linear velocity is slightly increased in the tests in the lab-scale firing system and the area velocity is decreased compared to the tests in the micro-reactor in synthetic flue gas since the length of the sample is longer.

Due to problems with the adjustment of the dosing feeder, a precise variation of the fuel mass flow was not possible. Thus, the dosing feeder is fixed to a narrow range, the mass flow is determined, and the shortfall of the desired flue gas flow rate is added by synthetic flue gas (15% CO_2, 3.5% O_2 in N_2 as used in the micro-reactor tests).

When experiments with ammonium chloride are carried out, for ammonium chloride (NH_4Cl), the ammonium chloride ratio with the NH_3 resulting from NH_4Cl (equivalent to the NH_3/NO ratio when ammonia is applied as reducing agent) is applied as given in table 3-4.

Table 3-4: Test conditions for catalyst test on the lab-scale firing system

Parameter	**Unit**	**Standard**	**Minimum**	**Maximum**
Catalyst temperature	°C	380	320	420
Flue gas flow	m³/h (STP, wet)	2.05	1.9	2.4
Fuel mass flow	kg/h	0.230	0.210	0.250
Area velocity (AV)	m/h (STP, wet)	13	11	15
Linear velocity (LV)	m/s (STP, wet)	1.7	1.3	1.9
NH_3/NO ratio	-	1.2	0	1.2
Additional HCl	mg/m³ (STP, dry)	0	0	100
Ammonium chloride to NO ratio (NH_3 (from NH_4Cl) / NO)	-	0.5	0.5	0.8
Mercury (Hg)	µg/m³ (STP, dry)	50	-	-

3.8 Characteristic numbers for catalyst tests

Some catalyst-specific parameters need to be defined in order to understand the test conditions and the results. First of all, the geometry of honeycomb SCR catalysts for power plant application can be described by the clear width, the wall thickness and the length. More common is also the expression “pitch”, which is equal to one clear width and one wall thickness. The channels are of quadratic shape.

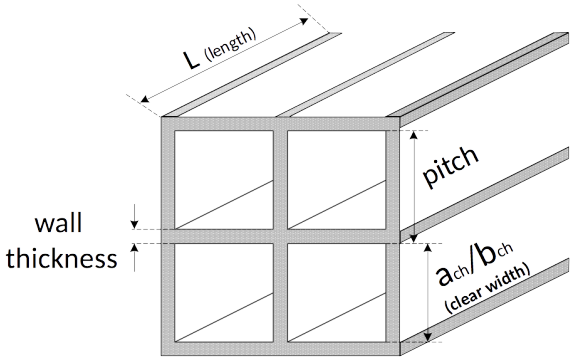

Figure 3-6: Geometrical characteristics of a honeycomb SCR catalyst

The geometric measures are listed in table 3-5 and include the linear velocity (LV), which describes the velocity of the flow through the catalyst. The area velocity (AV) describes the ratio between the volumetric flow and the contact area. Additionally, their relevant surface areas A_{ch} and S_C are listed. The calculated parameters and results are listed in table 3-6.

Table 3-5: Geometric measures at SCR catalysts

Measure	Unit	Calculation	
Linear velocity	$\frac{\mathrm{m}}{\mathrm{s}}$ (STP, wet)	$LV = \frac{\dot{V}_{\mathrm{wet}}}{A_{\mathrm{ch}}}$	equation 3-5
Area velocity	$\frac{\mathrm{m}}{\mathrm{h}}$ (STP, wet)	$AV = \frac{\dot{V}_{\mathrm{wet}}}{S_C}$	equation 3-6
$A_{ch,\ honeycomb}$	m^2	$A_{\mathrm{ch}} = a_{\mathrm{ch}} \cdot b_{\mathrm{ch}} \cdot n$	equation 3-7
S_C	m^2	$S_{\mathrm{C}} = 2 \cdot (a_{\mathrm{ch}} + b_{\mathrm{ch}}) \cdot L \cdot n$	equation 3-8

The calculated measures for NO_x reduction, SO_2/SO_3 conversion and Hg oxidation reflect the change of the respective flue gas component over the catalyst. When calculating the SO_2/SO_3 conversion with mass concentrations as given in equation 3-12, the different molar mass of SO_2 and SO_3 has to be considered. This ratio equals 0.8.

From the NO_x reduction, the DeNOx activity can be derived by the first-order approach [120]. Similarly, the SO_2/SO_3 conversion coefficient can also be calculated, since, according to Svachula [122] and Dunn [165], in the range of practical relevance, the rate is

of first order with respect to sulfur dioxide. Finally, an Hg oxidation coefficient can also be derived for the Hg oxidation and calculated according to a first-order approach at constant given hydrogen halide content since, with respect to the Hg concentration, the Hg oxidation follows a first-order reaction [125].

Table 3-6: Calculated parameters and results of SCR catalyst tests

Measure	**Unit**	**Calculation**	
NH_3/NO ratio	-	$\propto = \frac{\beta_{\mathrm{in}}(NH_3)}{\beta_{\mathrm{in}}(NO)}$	equation 3-9
NO_x reduction	%	$\eta(\alpha) = \frac{\beta_{\mathrm{in}}(NO_x) - \beta_{\mathrm{out}}(NO_{\mathrm{x}})}{\beta_{\mathrm{in}}(NO_{\mathrm{x}})} \cdot 100\%$	equation 3-10
DeNOx activity	$\frac{\mathrm{m}}{\mathrm{h}}$	$K_{\mathrm{NOx}}(\alpha) = -AV \cdot ln\,(1 - \eta(\alpha))$	equation 3-11
SO_2/SO_3 conversion	%	$\kappa_{23} = \frac{\beta_{\mathrm{out}}(SO_3) - \beta_{\mathrm{in}}(SO_3)}{\beta_{\mathrm{in}}(SO_2)} \cdot \frac{M_{\mathrm{SO_2}}}{M_{\mathrm{SO_3}}} \cdot 100\%$	equation 3-12
SO_2/SO_3 conversion coefficient	$\frac{\mathrm{m}}{\mathrm{h}}$	$K_{23} = -AV \cdot ln\,(1 - \kappa_{23})$	equation 3-13
SO_2/SO_3 reaction rate constant	$\frac{1}{s}$	$k_{23} = -\frac{\dot{V}_{\mathrm{dry(p,T)}}}{V_{\mathrm{C}}} \cdot ln\,(1 - \kappa_{23})$	equation 3-14
Hg oxidation	%	$\kappa_{\mathrm{Hg^0/Hg^{2+}}} = \frac{\beta_{\mathrm{out}}(Hg^{2+}) - \beta_{\mathrm{in}}(Hg^{2+})}{\beta_{\mathrm{in}}(Hg^0)} \cdot 100\%$	equation 3-15
Hg oxidation coefficient	$\frac{\mathrm{m}}{\mathrm{h}}$	$K_{\mathrm{Hg}} = -AV \cdot ln\,(1 - \kappa_{\mathrm{Hg^0/Hg^{2+}}})$	equation 3-16
Performance indicator	$\frac{\mathrm{m}}{\mathrm{h}}$	$P_3 = \frac{K_{\mathrm{NO_x}} \cdot K_{\mathrm{Hg}}}{K_{23}}$	equation 3-17

In order to compare the catalysts, a “performance indicator” P3 (equation 3-17) in m/h is introduced which reflects the desired performance of an optimized SCR catalyst, meaning the highest value shows the best-performing catalyst. P3 is calculated under the setpoint test conditions listed above in table 3-1 and table 3-2. The indicator is only valid for tests carried out under the same test conditions, since for example the SO_2/SO_3 conversion is especially sensitive to temperature changes.

4 Results and discussion for synthetic flue gas in micro-reactors

4.1 Catalytic effect of various metal oxides as powders on Hg oxidation

In order to identify the metal oxides which have an effect on the Hg oxidation, the single metal oxides are tested in the reactor setup as described in section 3.2. The approach is directly derived from the experiments carried out by Hocquel [66] and helps to find possible new materials for SCR catalyst production and to identify the active compounds. For the tests, 100 mg of new, powdered metal oxide is placed on silica wool in the reactor. Tests with pure silica showed no effect on the Hg species distribution. The temperature is set to 380°C, flow rate is kept at 10 l/min in order to keep the space velocity constant and the HCl concentration is varied between 100 mg/m^3 and 500 mg/m^3. Mercury concentration is kept at 100 µg/m^3, which is present as 99% elemental mercury. The metal oxides which are tested are listed in table 4-1. Additionally, an SCR catalyst is ground to the same particle size as the other powders.

Table 4-1: Characteristics of tested metal oxides

Material	**Molar mass (in g/mol)**	**Density (in kg/m^3)**	**Crystal structure**	**Assay/purity (in %)**
TiO_2 (anatase)	79.89	4.23	tetragonal	>99
V_2O_5	181.88	3.36	orthorombic	99
MoO_3	143.94	4.69	orthorombic	99.9
MnO_2	86.93	5.03	cubic	99.9
Mn_3O_4 (chunks)	157.87	4.50	cubic	99
La_2O_3	325.81	6.51	hexagonal	99
SCR catalyst (0.55% V_2O_5, 5.4% WO_3, 78.7% TiO_2)	-	-	-	100

The TiO_2, V_2O_5 and MoO_3 form base materials of SCR catalysts. Manganese oxides (MnO_2 and Mn_3O_4) are used in many applications as catalysts and were also reported to be active for Hg oxidation [166]. Lanthanum oxide (La_2O_3) as one transition metal representative is tested as a new material, since it was previously tested for NO_x reduction and it was claimed that it has more oxidative catalytic activity [167]. The results of the tests are shown in figure 4-1.

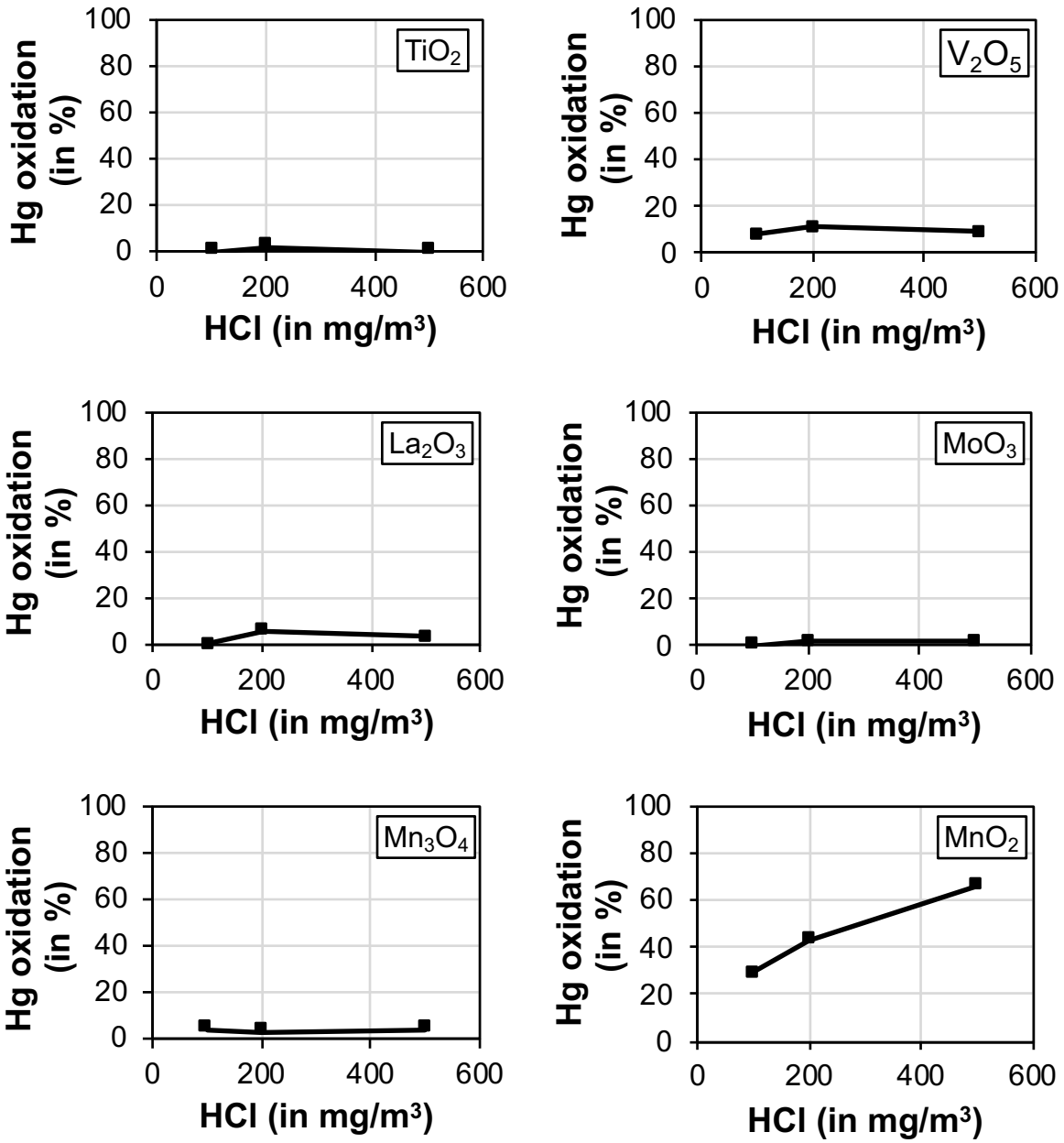

Figure 4-1: Oxidation of Hg^0 to Hg^{2+} at 100 mg of various metal oxides at 380°C

In general, the measured Hg oxidation of the single metal oxides is quite low. As comparison and reference, Hg oxidation of 100 mg of ground standard SCR catalyst is shown in figure 4-2. For the pure anatase (TiO_2), there is no Hg oxidation measured, which is in accordance with the measurements of Hocquel [66] and Thorwarth [80]. For V_2O_5, an Hg oxidation is clearly measured compared to the other metal oxides tested, which confirms the positive effect of *vanadia* on Hg oxidation as discussed for example by Stolle [125] and which will be discussed later in more detail. Lanthanum oxide was researched in the literature as a possible SCR catalyst and Jiang [168] claimed to have found great synergy for Hg oxidation when La_2O_3-TiO_2 is tested with NO and HCl in

parallel. However, there was no potential for Hg oxidation detected under the chosen test conditions, so this metal oxide is no longer researched. A reason could be that in this test compared to the tests carried out by Jiang, no nitrogen oxide was present and the described mechanism could not take place. Furthermore, in contrast to the current test, a La_2O_3-TiO_2 catalyst was tested with possible synergy between these metal oxides.

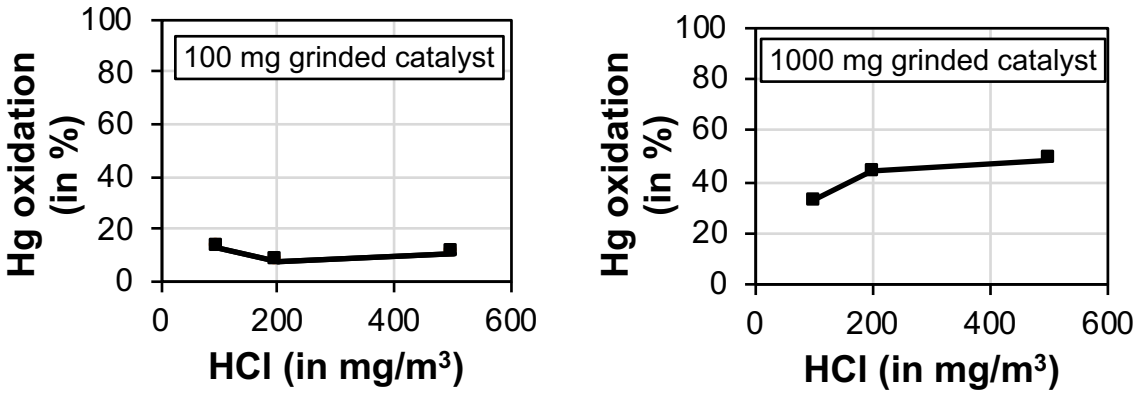

Figure 4-2: Hg oxidation of 100 mg and 1,000 mg powdered and ground standard SCR catalyst

Molybdenum as a single metal oxide does not show a net overall Hg oxidation in the tested range. Hocquel [66] found a reduction of $HgCl_2$ with molybdenum oxide, so formed $HgCl_2$ is possibly instantaneously reduced and no net oxidation is measured.

For the manganese oxides, there is an ambiguous result. While for Mn_3O_4 there is almost no Hg oxidation, the MnO_2 shows the highest result of the tested metal oxides. Since for Mn_3O_4 compared to the other materials, 1.6 mm chunks are used and not a fine powder, the surface area is much lower and thus the area velocity is higher, resulting in lower Hg oxidation. For pure MnO_2, there is a strong increase of Hg oxidation with increasing HCl content. The relatively high Hg oxidation potential is confirmed in figure 4-3, in which the dependency on catalyst operating temperature is studied.

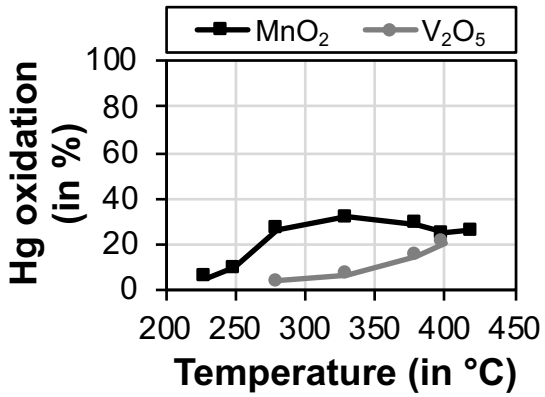

Figure 4-3: Hg oxidation of 100 mg pure MnO_2 and 100 mg pure V_2O_5 over temperature (at 100 mg/m³ HCl)

The Hg oxidation increases with increasing temperature up to a maximum at 330°C. From this point on, the Hg oxidation decreases slightly until a minimum at about 400°C is

reached. This trend indicates an adsorption of mercury on the MnO_2 as one step in the Hg oxidation process. Since the adsorption is lower at higher temperatures there is less Hg oxidation under these conditions. Below 300°C, the activation energy is too low for the complete reaction to take place and thus the overall Hg oxidation decreases. The hypothesis of the reaction based on an adsorption mechanism is further supported by various works on manganese oxides, e.g. by Qiao [143]. In his work, the reaction pathway was further explained as a Mars-van-Krevelen mechanism in which Hg^0 is adsorbed on the MnO_2/alumina sites. Similar to the results above, in this study the favorable adsorption temperature was determined to be at 327°C. The application as a sorbent was also discussed by Pavlish [166], stating a comparable catalytic activity to activated carbon. Furthermore, high potential for mercury adsorption was researched by Wiatros-Motyka [169], indicating a dependency between manganese oxide content and Hg capture with co-precipitated manganese oxides sorbents. A further explanation for the lower Hg oxidation measured at a temperature of 400°C is given by the research of Takenami [170], who found in temperature programmed desorption experiments (TPD) with MnO_2 a desorption peak at about 400°C, confirming that in this temperature range the desorption of mercury dominates and there is no Hg oxidation.

Another possible pathway of Hg oxidation on manganese oxides is the Deacon-reaction, as discussed in subsection 2.2.6. Besides copper and iron, manganese oxides are supposed to be good catalysts for the formation of Cl_2 from HCl [171]. However, the measured temperature dependency is not typical for the Deacon-reaction since the turnover decreases below 330°C. Hisham [127] studied the thermochemical parameters of the Deacon-reaction of several main group and transition metals. The exothermic metal chlorination step is followed by a slow endothermic oxidation step. For MnO_2, the exothermic adsorption step was determined by Hisham to be -131 kJ/mol and the decomposition of the manganese oxychloride ($MnOCl_2$) was determined to be 117.3 kJ/mol. Thus, the overall reaction takes place since the net reaction enthalpy is negative and the total reaction is exothermic. In this study by Hisham, a release of Cl_2 was measured when pure MnO_2 is exposed to flue gas with HCl.

The finely ground SCR catalyst (figure 4-2) shows, compared to the other tested pure metal oxides, a relatively high Hg oxidation. The catalyst reflects a state-of-the-art “standard” SCR composition, as shown in table 4-1. This means that the absolute amount of V_2O_5 in this sample was only 0.55 mg, which is about 180-fold lower than the amount of the pure V_2O_5 shown above. For comparison, 1,000 mg SCR catalyst is tested, reflecting a tenfold higher amount of V_2O_5 than the test before. It can be clearly seen despite the low amount of the previously tested single active metal oxide component (V_2O_5) that the Hg oxidation is comparably much higher. This can be traced back to the interactions and transfers which took place in the calcined SCR catalyst. So it is not only the V_2O_5 which is active in Hg oxidation, but even more so the connection with TiO_2 anatase, which binds the vanadate in a large surface area [100].

4.2 Mercury adsorption at SCR catalysts

The subsequent results were all gained at SCR catalysts produced either in lab-scale or technical scale, meaning that these results reflect the reaction of the total SCR catalyst which was produced as or similar to standard SCR catalysts. All tests were carried out on samples of full catalysts or technical-scale honeycomb catalysts, keeping their original shape. The first two catalysts studied can be characterized as listed in table 4-2.

Table 4-2: Characterization of catalyst A and catalyst B

	Unit	Catalyst	
		A	B
$TiO_{2\ (bulk)}$	wt.-%	79.6	76.1
$SiO_{2\ (bulk)}$	wt.-%	9.0	11.2
$WO_{3\ (bulk)}$	wt.-%	5.2	5.5
$V_2O_{5\ (bulk)}$	wt.-%	0.5	0.5
BET surface area	m^2/g	53.5	57.4
Average pore size	nm	15.2	14.2

In figure 4-4, the desorption curve of two catalysts (3x3 channels) after adsorption in HCl-free flue gas atmosphere is shown (3.5% O_2, 15% CO_2, 50 µg/m^3 Hg, 380°C). The release of Hg was triggered by the addition of 100 mg/m^3 HCl to the flue gas at the marked point. Additionally, the Hg dosing was switched off in order to get a zero baseline.

Both catalysts A and B adsorb significant amounts of mercury during exposure for one week in halogen-free flue gas atmosphere. After about 20 minutes in flue gas with HCl, all mercury which was previously adsorbed is desorbed from the catalyst. Even though both catalysts were exposed for the same time to Hg and there was the same HCl flue gas concentration during desorption, a difference in desorbed Hg was found.

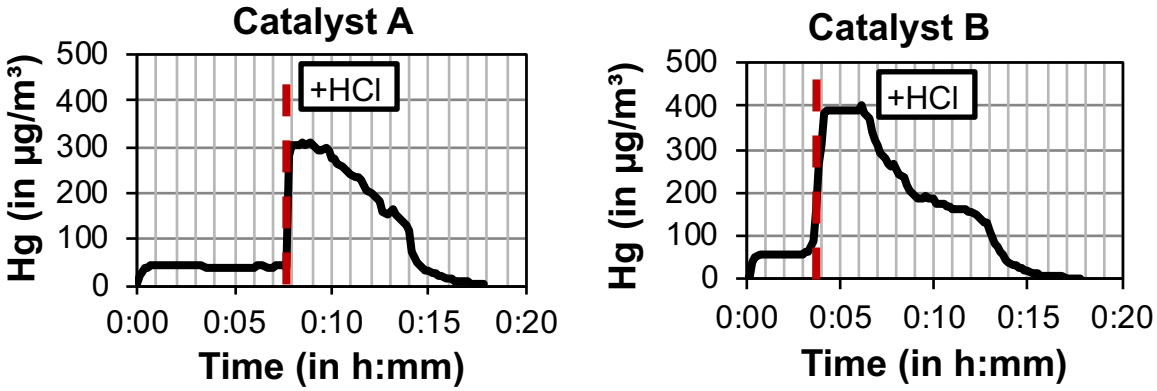

Figure 4-4: Desorption of mercury from two SCR catalysts after Hg adsorption without HCl

Catalyst B adsorbs significantly more mercury than catalyst A. In the case of catalyst B, the analyzer reaches its limit of 400 µg/m³ during minute 4 and minute 6 of the experiment, meaning that the upper part of the curve is cut out and the amount of desorbed Hg is even higher than the curve shows. Since the chemical composition of both catalysts is identical, especially of the active materials V_2O_5, WO_3, the difference can be traced back to the different TiO_2 support material used in these catalysts. This also has a small effect on the BET surface area and the BJH pore size distribution as shown in the smaller average pore size. It is assumed that the higher surface area leads to more adsorption sites.

In figure 4-4, the signal shows only total mercury (Hg^{tot}); however, speciation measurements showed that more than 90% of the released mercury is Hg^{2+}. This was also found by Hocquel [66]. Thus, the observation indicates a possible reaction step of the Hg oxidation, since an adsorption of Hg^0 can be clearly measured. The model of the pure Deacon-reaction as discussed by Gutberlet [79] does not include an Hg adsorption step, meaning that the Hg only reacts in the gas phase with Cl_2, which cannot be confirmed by this result.

In order to research this step in more detail, further experiments are carried out on the adsorption of mercury on various SCR catalysts. Figure 4-5 shows an adsorption and desorption curve for a 2 by 2 channel sample cut out of catalyst C, a standard high-dust SCR catalyst (as shown in table 4-3) which is quite similar to catalyst A. Since catalyst C has a standard formulation and can be considered a state-of-the-art SCR catalyst, it is taken as the reference in the following sections.

Table 4-3: Characteristics of catalyst C

	Unit	Catalyst C
TiO_2 (bulk)	wt.-%	78.7
SiO_2 (bulk)	wt.-%	9.5
WO_3 (bulk)	wt.-%	5.4
V_2O_5 (bulk)	wt.-%	0.6
BET surface area	m^2/g	63.0
Average pore size	nm	14.6

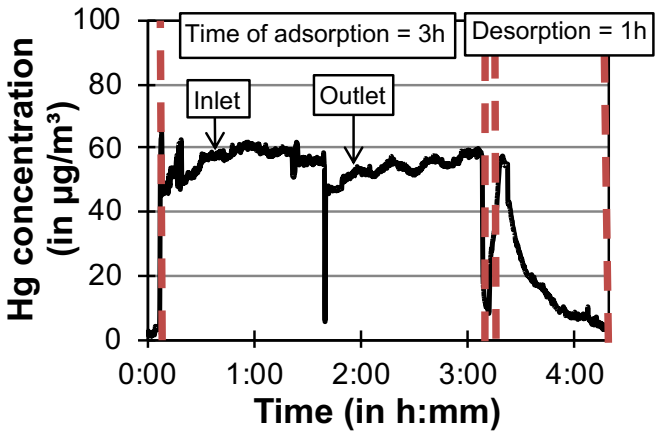

Figure 4-5: Adsorption and desorption of Hg at catalyst C

The measurement of the inlet concentration shows a value of approximately 58 µg/m³, while the measurement at the outlet shows after 1:40 h a concentration of approximately 48 µg/m³ and reaches the inlet concentration after 3:00 h, meaning that equilibrium is reached. Then the Hg dosing is switched off (at 3:08 h) and desorption is initiated by adding 250 mg/m³ HCl to the flue gas. The release of mercury in the form of $HgCl_2$ takes place instantaneously and is finished within one hour. By integrating the Hg concentration over time during desorption (equation 4-1) and multiplying the number with desorption time and the flue gas flow rate (equation 4-2), the mass of mercury which was previously adsorbed on the catalyst is calculated.

$$\overline{\beta_{\mathrm{Hg}}} = \frac{1}{t}\int_0^t \beta_{\mathrm{Hg}}(t)dt \qquad \text{equation 4-1}$$

$$m_{\mathrm{Hg}} = \overline{\beta_{\mathrm{Hg}}} \cdot t \cdot \dot{V}_{\mathrm{dry}} \qquad \text{equation 4-2}$$

This experiment shows a desorbed Hg mass of 10.5 µg Hg in the case of catalyst C, which can be considered as the adsorbed Hg mass. Based on this experiment, further standardized tests were conducted in which adsorption and desorption are carried out in the same time frame at the same sample geometry (surface area) as well as flue gas composition. When varying the HCl content in the flue gas during desorption, the results in table 4-4 are obtained.

Table 4-4: Desorbed Hg at different HCl contents during desorption

HCl flue gas content	(in mg/m³)	150	250	500
Desorbed Hg mass	(in µg)	8.1	9.6±1	10.5±1

These results indicate that the flue gas HCl content during the desorption does not have an effect on the desorbed Hg mass (which was previously adsorbed). Higher HCl concentrations lead to a higher desorption rate, meaning a more instantaneous release of Hg. At lower concentrations of HCl, the release of Hg from the catalyst is more distributed over the time of desorption. Differences in desorbed Hg mass can be explained by an incomplete desorption after one hour of desorption time and by temperature fluctuations during adsorption. Thus, the HCl concentration of these batch tests is set to 500 mg/m³ for the following tests. The role of temperature on Hg adsorption is shown in figure 4-6 by comparing the mass of desorbed Hg at different adsorption temperatures, when desorbing the Hg by a flue gas with catalyst C with 3x3 channels.

The highest mass of desorbed Hg, which is equal to the adsorbed Hg, is reached at 320°C, while higher temperatures of the catalyst result in lower adsorption. These results give a further indication on mechanistic aspects of the Hg oxidation. At lower temperatures, the Hg adsorption is higher. This is in line with various results on Hg oxidation published for example by [125], [130] and [172] showing higher values at lower flue gas temperatures.

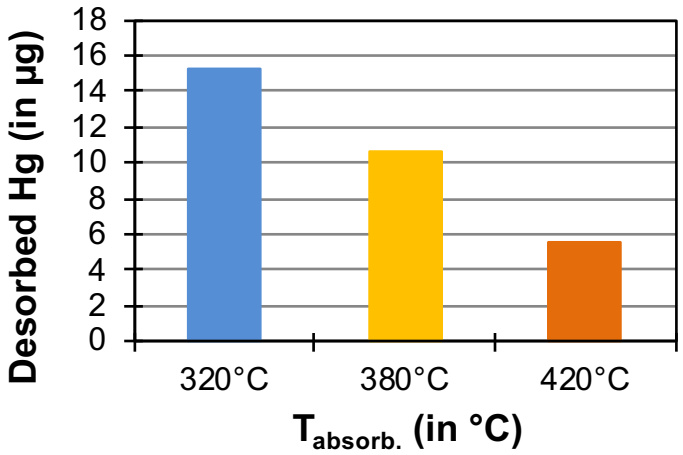

Figure 4-6: Mass of Hg at different adsorption temperatures with a 3x3 channel sample of catalyst C

In table 4-5, the catalysts tested in the standardized three-hour adsorption and one-hour desorption test at 380°C are listed. They can be characterized by variations in chemical composition as well as in BET surface area.

Table 4-5: Catalysts tested in the standardized adsorption/desorption test

	Unit	Catalyst					
		D	E	F	G	H	I
$TiO_{2\ (bulk)}$	wt.-%	78.1	83.9	78.3	79.4	76.9	78.7
$SiO_{2\ (bulk)}$	wt.-%	8.8	8.4	8.3	7.2	14.2	10.3
$WO_{3\ (bulk)}$	wt.-%	5.4	0.04	6.2	10.9	1.1	0.7
$V_2O_{5\ (bulk)}$	wt.-%	1.6	0.1	0.1	0.2	0.5	0.7
Other $_{(bulk)}$	wt.-%	-	-	1.2 MnO_2	0.3 Pd	-	4.7 MoO_3
BET surface area	m^2/g	47.5	-	-	-	80.4	50.4
Average pore size	nm	18.2	-	-	-	11.9	15.1

The results in figure 4-7 show a strong difference between the various catalysts. Compared to the reference catalyst C, catalyst D with higher *vanadia* content shows a higher Hg adsorption while catalyst E, which contains almost zero *vanadia*, adsorbs only half the amount of Hg. This confirms the results of Hocquel [66] and Straube [173], who found a similar correlation of mercury adsorption with increasing *vanadia* content.

Catalyst F has a totally different chemical composition compared to the other catalysts with only traces of *vanadia*, but instead it contains MnO_2. The traces of *vanadia* of 0.1 wt.-% result from traces in the production process. It seems that MnO_2 does not adsorb Hg at the high-dust operating temperature of 380°C. In this case, the Hg oxidation cannot be described with an Hg adsorption step. According to the literature, the adsorption of mercury on manganese oxides takes place at very much lower temperatures [169], which indicates that any measured Hg oxidation on this catalyst would follow a different mechanism compared to the other catalysts.

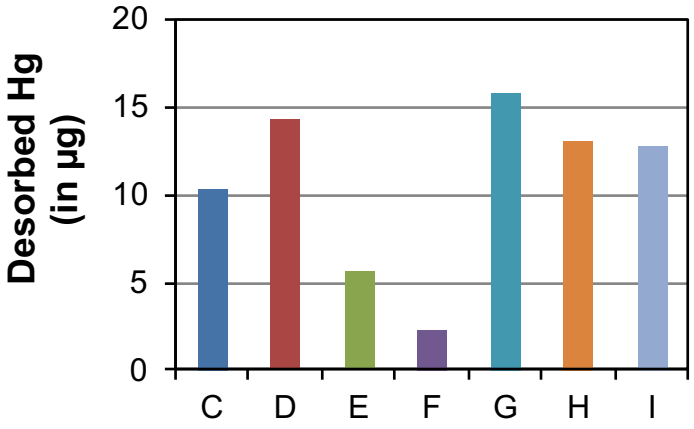

Figure 4-7: Desorbed Hg at various tested catalysts during standardized adsorption/desorption test

The highest Hg adsorption and release was found with catalyst G. Compared to the other catalysts, catalyst G contains palladium (Pd), which was previously determined by Granite [174] to be one of the strongest adsorbents for mercury. Furthermore, Poulston [175] found that with the researched noble metals palladium and platinum (Pt), Hg adsorption and Hg oxidation increase with increased Pd loading. It was also found in this work that the support of the noble metal plays an important role in Hg adsorption, which also confirms the general importance of the adsorption step in Hg oxidation, as already pointed out in section 4.1.

Catalyst H was modified by different support and base material, namely a special blend of titania and silica, which led to an increase in surface area and shows higher Hg adsorption compared to the reference catalyst C. In tests of nano-sized V_2O_5/TiO_2 catalysts, Lee [176] found that catalysts with the highest surface area have the highest reactivity for the removal of Hg^0 in the form of adsorption compared to impregnated or conventional SCR catalysts.

Compared to the reference catalyst C, with catalyst I slightly higher adsorption is measured. However, in this case, the surface area is lower. The difference in this case is explained by a higher *vanadia* content in connection with the molybdenum content of the catalyst. MoO_3 seems to be more actively related to Hg oxidation compared to WO_3.

The Hg adsorption and desorption is further studied as shown in figure 4-8 and figure 4-9. In figure 4-8, the Hg adsorption and desorption of catalyst C is shown as well as the temperature during this process. At 2:30, the measurement of the Hg concentration is switched to the outlet of the catalyst. After the Hg dosing is switched off at 3:00, the temperature of the catalyst is increased from 320°C to 380°C. There is no release of Hg due to the change of temperature since the outlet measurement shows no change of Hg concentration during heating up. The following desorption (not shown in the diagram) is similar to the previous tests without the preheating step.

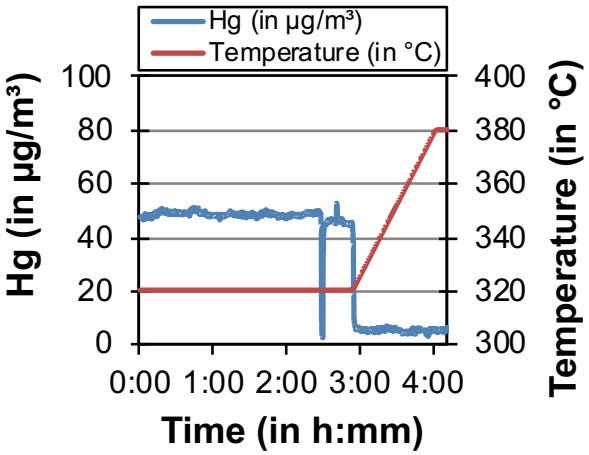

Figure 4-8: Increase of temperature prior to desorption with catalyst C

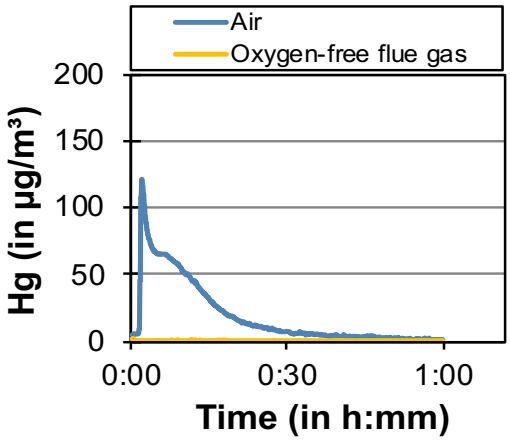

Figure 4-9: Desorption after adsorption in flue gas with/without oxygen with catalyst C

From the results, it can be concluded that the adsorption of Hg^0 is not due to physisorption but is due to chemisorption, since the additional energy brought into the catalyst by heating up does not have an effect on the adsorbed Hg^0. Straube [173] determined an isosteric heat of adsorption of 61.1 kJ/mol for Hg^0, indicating the chemisorptive type of adsorption. For $HgCl_2$, a very much lower value of 16.7 kJ/mol is given. Comparing these numbers with the typical values for physisorption and chemisorption clearly shows that the adsorption of $HgCl_2$ is of typical physisorptive nature since the heat of adsorption is lower than 40 kJ/mol. Thus, $HgCl_2$ is easily released from the active sites on the catalysts after its formation. In general, for chemisorption, the heat of adsorption for chemical reactions is comparable with the reaction enthalpy [177].

In figure 4-9, the desorption curve of catalyst C is shown during the standard procedure and when the adsorption was carried out under oxygen-free atmosphere. From these results it can be concluded that the adsorption necessarily needs oxygen to take place despite the oxygen-rich surface of the metal oxide catalyst. This is an indication of a Mars-van-Krevelen reaction type with the intermediate product HgO adsorbed on the surface of the catalyst. The possible pathway could take place as shown in equation 2-42 to equation 2-45.

Due to the lack of oxygen during the adsorption phase, it is assumed that most of the active sites of the studied catalyst C were in the reduced state and thus no adsorption could take place during the experiment and no desorption can be measured.

4.3 Mercury oxidation of reference catalyst C and chemically comparable catalysts

Reference catalyst C is researched in the present section in more detail. The research is carried out in the laboratory micro-reactor as described in section 3.3. In addition to the Hg oxidation of the reference, this evaluation includes a discussion of further catalysts with identical chemical composition but different geometry.

4.3.1 Dependency of Hg oxidation on HCl content

In figure 4-10, the Hg oxidation of catalyst C at different HCl concentrations is shown. There is a strong increase in Hg oxidation with increasing HCl content until an HCl concentration of about 50 mg/m³ is reached. Then it flattens out after reaching its maximum of about 30% at 380°C. When the test is carried out at 350°C, the shape of the curve stays the same; however, the oxidation is about 10% (absolute) higher at each of the measured HCl concentrations.

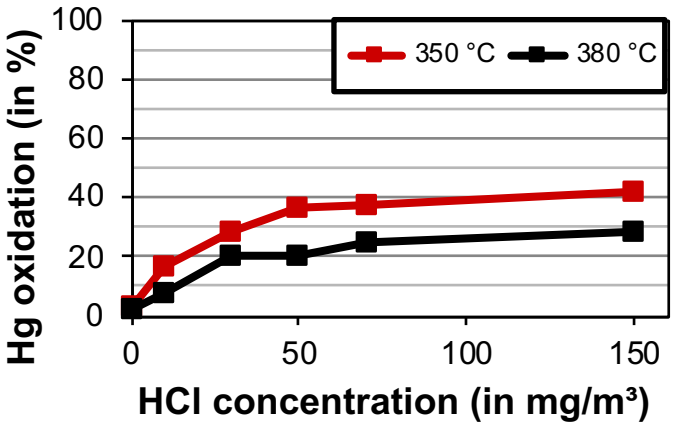

Figure 4-10: Hg oxidation over HCl concentration with catalyst C at different temperatures

Despite lower mercury flue gas concentrations in some orders of magnitude compared to the flue gas HCl concentration ($ß_{HCl}/ß_{Hg} \cong 1{,}000$), there is a dependency on the HCl content. The studied range of HCl concentration covers almost the whole concentration range of flue gas in full-scale power plants, which is strongly dependent on the origin of the coal. As discussed in subsection 2.1.3, Kolker [63] presented a range of 10-5,000 mg Cl/kg coal, resulting in flue gas concentrations of about 1-500 mg HCl/m³. However, most of the coals fired in boilers globally have a low Cl content, resulting in flue gas HCl concentrations lower than 100 mg/m³. It is commonly accepted that HCl plays an important role in mercury oxidation ([66], [129], [142], [178]), but no evidence has been given why such an abundance of HCl is needed, even if there are no other possibly disturbing flue gas components involved. The strong dependency of mercury oxidation on flue gas HCl content was also studied by Hocquel [66]. Stolle [125] also showed a great influence of flue gas HCl content on mercury oxidation in the range covered by the

presented experiments. The curves seem to approach exponentially the maximum Hg oxidation with saturation between 50 and 150 mg/m³ HCl. In the previously discussed model of Hg adsorption on the active sites, the HCl concentration or the partial pressure of HCl is the crucial step in the reaction to $HgCl_2$. Presumably, only at higher partial HCl pressures does enough HCl reach the active sites in order to react with adsorbed mercury. Thus, due to the relatively low reaction rate of the Hg oxidation, the adsorption isotherms become visible under the applied test conditions.

4.3.2 Effect of changes in flue gas flow rate

A change in test conditions, in this case the flow of the synthetic flue gas, is shown in figure 4-11. The characteristic numbers are the linear velocity (LV) and the area velocity (AV) as defined in table 3-5 and calculated at STP. The characteristic numbers are starting from the "standard" test point as listed in table 3-1 and increased and decreased by 50%. Furthermore, the tests are carried out at different HCl concentrations. While for the lower velocity the curve looks similar to the reference point, there is almost no Hg oxidation measured at LV=1.5 m/s, which is equal to a real velocity in the channels of 3.6 m/s and a residence time of 0.06 seconds. Due to their definition, AV and LV are linked to each other at the same catalyst geometry, meaning that increasing the flow rate is associated with a higher AV and a lower overall residence time. This indicates that the residence time is too low for the Hg oxidation to take place at this sample. If the Hg oxidation is expressed as Hg oxidation coefficient K_{Hg} as noted in section 3.8, the values for the test points at 150 mg/m³ HCl are quite similar for LV=0.5 m/s and LV=1.0 m/s (K_{Hg}=9.3 m/h and K_{Hg}=9.6 m/h, respectively). However, this first-order approach for the calculation of the Hg oxidation coefficient is not valid for the results measured for LV=1.5 m/s. According to this approach, the Hg oxidation should be 20.6% at the selected comparison point of maximum Hg oxidation, so it seems that this approach might not be valid in the whole range of operating/test conditions and a double-check at selected supporting points is necessary.

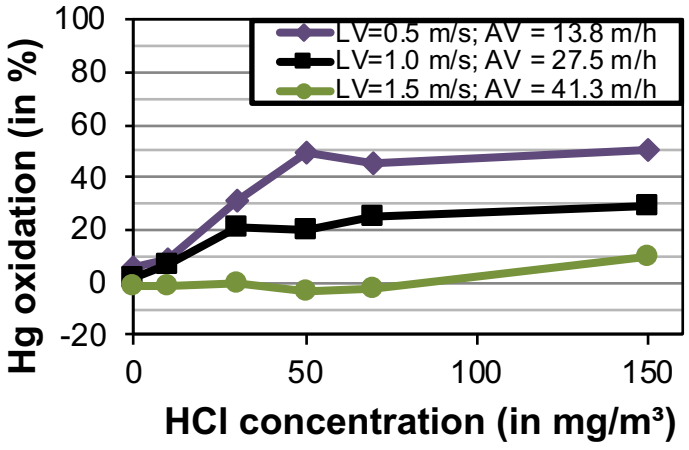

Figure 4-11: Effect of altered flue gas velocities on Hg oxidation

4.3.3 Effect of Hg concentration on Hg oxidation

The measurement of the Hg oxidation at different Hg concentrations is shown in figure 4-12. This study is carried out with a different catalyst than catalyst C (catalyst AJ, which is introduced later); thus, the overall Hg oxidation is higher than the previously discussed results. The Hg oxidation is almost constant at 57% from 230 µg/m³ Hg to 25 µg/m³ Hg.

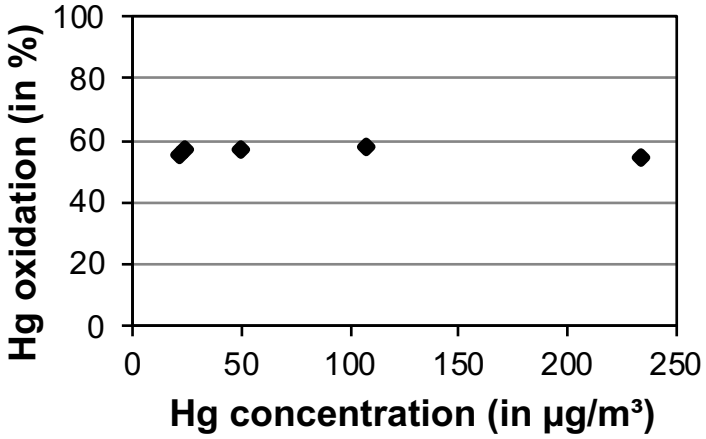

Figure 4-12: Effect of varied Hg concentration on Hg oxidation at the standard test conditions (see table 3-2)

Thus, an Hg concentration of 50 µg/m³ is chosen for the tests, being a compromise between accuracy and real Hg flue gas concentrations as discussed in section 2.1.4. From the results it can furthermore be concluded that the reaction of Hg oxidation (given in percent as defined in equation 3-15) is of first reaction order regarding the Hg concentration. The reaction rate of Hg is dependent on the Hg concentration with higher turnover at higher Hg concentrations. At higher inlet Hg^0 concentrations, a higher amount of Hg^{2+} is present at the outlet of the catalyst, which leads to an overall calculated constant percentage Hg oxidation. This is in line with the observations of Stolle [125] and Usberti [133]. However, Usberti et al. explained the fact by a surface chlorination of the active sites, which makes the Hg oxidation independent of the concentration of mercury.

4.3.4 Effect of temperature on Hg oxidation

As shown in figure 4-10, there is a dependency of the Hg oxidation on the flue gas temperature. The test series carried out at 350°C shows significantly higher Hg oxidation than the measurements at 380°C. The general trend of increasing Hg oxidation with lower temperature was previously also discussed amongst others by Rallo [179], who measured a strong increase of Hg oxidation from 400°C down to 300°C in a technical-scale test rig in a real flue gas atmosphere. This trend was only confirmed for low HCl concentrations by Usberti [133] in laboratory and modelling studies. In the study conducted by Usberti, it was found that the temperature dependency of the Hg oxidation is dependent on the HCl content. While at HCl concentrations as low as 2.5 ppm there is a decrease in Hg oxidation with increasing temperature, at 10 ppm HCl the Hg oxidation stays almost

constant from 400°C to 300°C and at 50 ppm HCl even a decrease of Hg oxidation was measured, reducing the temperature from 400°C to 250°C. Comparing these results with results from Rallo and figure 4-10, a contradiction is found, which can partly be explained by the low chlorine content of the fired El Cerrejón coal in the experiments of Rallo. In Schwämmle [158], almost no change in Hg oxidation at 50 ppm HCl, or with some catalysts even a lower Hg oxidation was measured. In addition, it was shown that the increase in Hg oxidation with decreasing temperature is significant only at HCl concentrations as low as 10 ppm HCl. Especially at test points with NO and NH_3, the effect of temperature becomes obvious. Summarizing the results presented here together with the discussed results from the literature, it can be concluded that the Hg oxidation increases with lower temperature, with a stronger tendency at low HCl concentrations.

This conclusion can be explained by the thermodynamic equilibrium of Hg species with temperature as discussed for example by [66] and [133], showing the shift to Hg^{2+} at lower temperatures. Furthermore, as discussed in section 4.2, the Hg adsorption on catalytic material is more favored at lower temperatures than at 400°C. As a third point, the real residence time of the flue gas in the catalyst's channel is higher at lower temperatures. This can be calculated by the ideal gas law, since the tests points for the flow rate of the results presented in figure 4-10 as well as in [158] are set based on STP conditions, meaning the gas flow is kept constant.

4.4 Effect of catalyst wall thickness on Hg oxidation, DeNOx activity and SO_2/SO_3 conversion

In this section, catalysts of the same chemical composition as the previously discussed reference catalyst C are researched and discussed. They all show the same chemical composition with small deviations due to production as well as analytical considerations. Also, from the physical point of view, their BET surface area as well as their pore size distribution can be considered as equal. The catalysts differ in their pitch as well as their wall thickness (see section 3.8 for further information), as shown in table 4-6. These values show the actually measured values and differ slightly from the initially planned even values (e.g. 8.2 mm) due to production issues, since the samples are cut out from full-size monoliths.

The catalysts listed in table 4-6 including catalyst C reflect the whole range of catalysts for coal-fired power plant application. The Hg oxidation of these catalysts depending on the flue gas HCl content and tested under the coal combustion flue gas test conditions as listed in table 3-2 is shown in figure 4-13. There is a general trend of increasing Hg oxidation with increasing wall thickness and pitch. This is a first indication for a relatively slow reaction and a reaction in the bulk of the catalyst.

Table 4-6: Geometrical measures of tested catalysts

	Unit	Catalyst				
		C	J	L	M	N
Pitch	mm	7.05	5.95	8.25	9.2	9.7
Clear width	mm	6.2	5.10	7.25	8.0	8.3
Wall thickness	mm	0.85	0.80	1.0	1.2	1.4

In order to classify the results in more detail, the other reactions in the catalyst are tested in the same reactor under the same conditions as listed in table 3-1. The results are presented in figure 4-14. In contrast to the previously discussed results for Hg oxidation, there is no visible increase. On the contrary, there is even a slight decrease of NO_x activity with increasing pitch. While catalysts C and J show activities (with SO_2) well above 40 m/h, catalysts L and M only show values of about 40 m/h. This is furthermore confirmed when looking at figure 4-15. This diagram shows the result of the test of the catalysts in full-scale size in the bench reactor under full-scale flow and full-scale flue gas conditions as described in subsection 3.5. The results are given here supplemental.

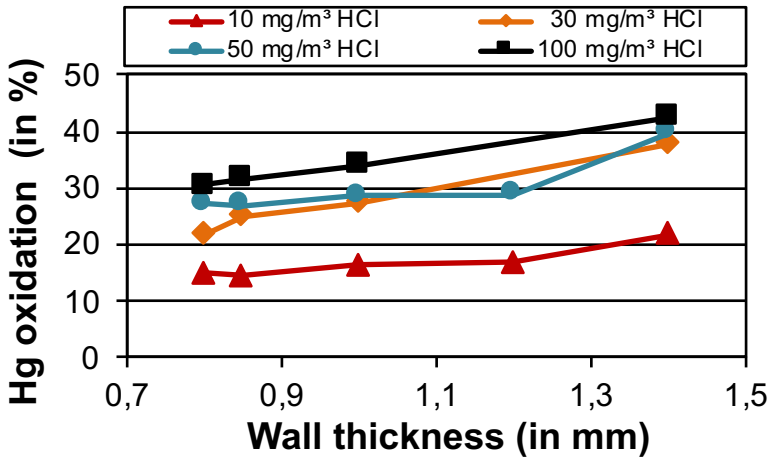

Figure 4-13: Hg oxidation in catalysts with different wall thicknesses at the standard test conditions (as listed in table 3-2)

Comparing the results for catalyst C in the two tests (micro-reactor and bench-scale reactor), the absolute values of the DeNOx activity are more or less the same. A value of DeNOx activity of 40 m/h is representative for standard commercial honeycomb catalysts [77]. Slightly higher values of the micro-reactor tests can be traced back to the higher NH_3/NO ratio of 1.2 in the micro-reactor tests, compared to 1.0 in the bench-scale reactor rests.

The high velocity of the surface reaction can be seen in figure 4-15 in the test results of bench-scale testing. With increasing clear width, the limitation of the mass transfer becomes more visible. With increased pitch, which is associated with the clear width, the DeNOx activity decreases. As explained in subsection 2.2.3, the reaction over the catalyst is a product of external mass transfer to the catalyst's surface, the internal mass transfer

from the surface to the respective active site and back to the surface and finally the chemical reaction at the active site. According to Beck [100], only the outer 50 µm of the catalyst wall contribute to the NO_x reduction.

In this test series, the external mass transfer is influenced and varied, which especially has an effect on the reaction rate in the laminar flow zone of the catalyst, in which mass transfer takes place only by diffusion. In the turbulent zone of the catalyst, the mass transfer is higher and both advection and diffusion play a role. However, due to different dimensions/lengths of the micro-reactor samples (figure 4-14) vs. bench-reactor samples (figure 4-15), the share of the "turbulent" inlet zone is higher in the micro-reactor samples compared to the bench reactor samples, which are much longer. This can also be expressed by the diameter/length ratio, which for the micro-reactor samples is 0.03 and thus much higher than for the bench-scale reactor samples (between 0.005 and 0.008). This explains why for the micro-reactor samples the effect of external mass transfer is almost not visible under the chosen test conditions. The effect of external mass transfer on the reactions in the SCR catalyst channels was also discussed and confirmed by [109], [119], [180], [181].

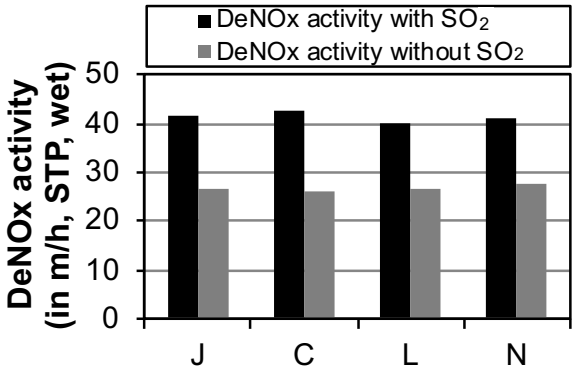

Figure 4-14: DeNOx activity of selected catalysts with different pitch measured in the micro-reactor

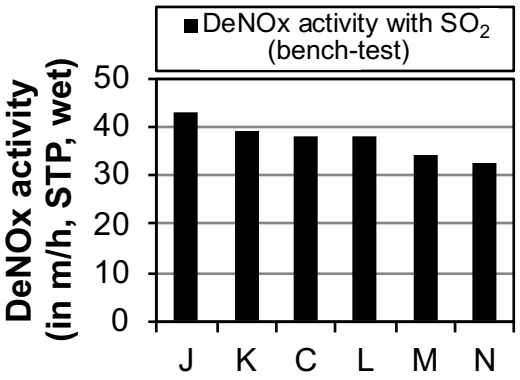

Figure 4-15: DeNOx activity of selected catalysts with increasing pitch tested in the bench-scale reactor

An example of a typical reaction taking place in the catalyst's bulk can be seen in figure 4-16 and figure 4-17. The results of micro-reactor measurements clearly show a direct correlation between the wall thickness and the SO_2/SO_3 conversion. With increasing wall thickness, meaning more catalytically active material of the fully extruded honeycomb, the SO_2/SO_3 conversion increases. Since thicker catalyst walls mean more material, the SO_2/SO_3 conversion is plotted over the weight per channel in figure 4-17 in order to refer to all tested catalysts on the same mass basis, as catalyst N was tested only with two channels due to reactor size. This correlation confirms the previously mentioned assumption that the SO_2/SO_3 conversion is a reaction with quite slow reaction kinetics and taking place in the whole bulk of the catalyst, meaning that SO_2 penetrates deeply into the microporous system of the catalyst wall. So, the picture is directly the opposite of

the previously discussed NO_x reduction, which is limited by external mass transfer and diffusion. A linear dependency of the SO_2/SO_3 conversion was also found by Svachula [119]. As discussed by Dunn [124], the low turnover frequency is caused by inefficient adsorption of SO_2 on the acidic surface *vanadia* species.

At this point, supplemental information is given from bench-scale reactor test results (not shown here). The tests of these catalysts in the bench-scale reactor showed the same trend. When comparing the SO_2/SO_3 conversion in percent per kg of catalytically active catalyst material measured in these supplemental bench-scale tests an almost constant value was found for all tested catalysts. Since the honeycomb catalysts have the same outer dimensions of 150 mm x 150 mm and approximately the same length, the weight of the samples is different when the thickness is increased. As a consequence, when comparing catalysts of different chemical compositions, the wall thickness has to be kept constant.

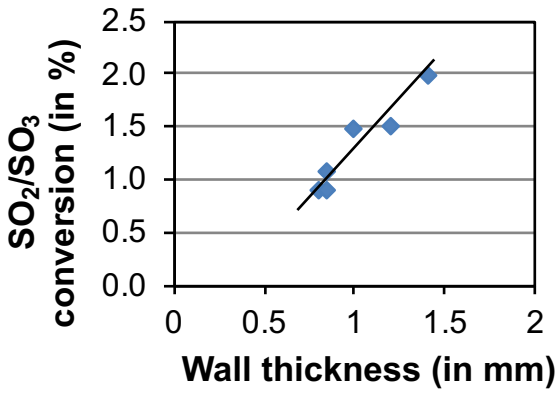

Figure 4-16: SO_2/SO_3 conversion of catalysts with different wall thicknesses measured in the micro-reactor

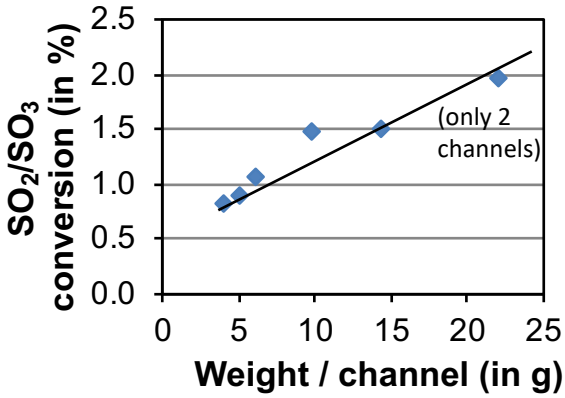

Figure 4-17: SO_2/SO_3 conversion of catalysts with different weights/channel

Comparing the results for the full-scale monoliths of catalyst C measured in the supplemental bench-scale tests with the results from the micro-reactor (figure 4-16), a difference becomes obvious. This can be traced back to the different flue gas temperatures. The flue gas temperature of the micro-reactor tests for SO_2/SO_3 conversion was about 14 Kelvin higher than initially planned. This can be seen in figure 8-1 in the annex, which shows the repetition of the experiment with catalyst C. The error can be traced back to an error in temperature measurement. The correlation presented in the annex in figure 8-1 shows the result after adjustment of the temperature measurement. The results are then in line with the bench-test results. The temperature dependency of the SO_2/SO_3 conversion will be discussed in detail later on in subsection 4.6.3.4.

Further tests on the dependency of the Hg oxidation on the wall thickness are carried out with catalysts O and P. In figure 4-18, the Hg oxidation of the two catalysts with different wall thicknesses is shown. It can be clearly seen that catalyst P with the thicker wall has a higher Hg oxidation. The variation presented here is carried out by keeping the pitch

constant at different wall thicknesses. This causes a difference in clear width. However, this difference is only 6% (increase of wall thickness: +57%), while the resulting relative increase in Hg oxidation is about 25% at all test points. Of course, there is a contribution of the smaller clear width due to increased mass transfer. However, as can be seen over the whole range of tests, the difference in Hg oxidation is significantly higher than the change in clear width. It can finally be concluded that there is an influence of the catalyst's wall thickness on the Hg oxidation.

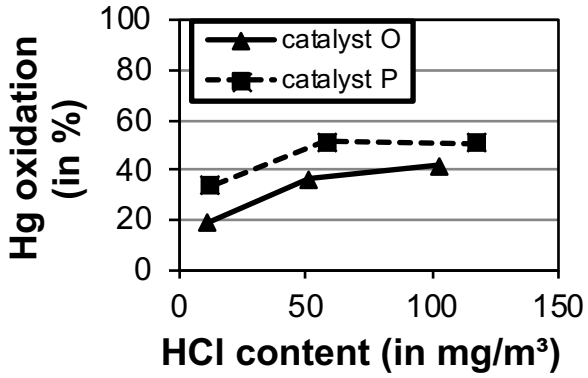

Figure 4-18: Hg oxidation dependent on wall thickness with catalysts O and P

Table 4-7: Geometrical characteristics of catalyst O and catalyst P

	Unit	Catalyst	
		O	P
Pitch	mm	7.0	7.0
Clear width	mm	6.3	5.9
Wall thickness	mm	0.7	1.1

When the performance indicator presented in section 3.8 is applied on the experimental outcome discussed above, the numbers in table 4-8 can be calculated. Differences of the given P3 value to the given numbers are attributed to rounding differences, especially at K_{23}, since the value is given to two decimal points. As discussed above, for catalyst C (and all other catalysts within this specific test series) an erroneous SO_2/SO_3 conversion was measured. The result within this specific test series cannot be taken into account for further discussion and thus the reference catalyst C is marked as C* in the table below.

Table 4-8: Performance indicator of tested catalysts in this section

Catalyst	C*	J	L	N	O	P
K_{NOx} (in m/h)	42.7	41.8	40.1	40.9	47.2	51.3
K_{Hg} (in m/h)	10.5	10.0	11.5	15.2	15.4	19.4
K_{23} (in m/h)	0.29	0.25	0.41	0.59	0.07	0.16
P3 (in m/h)	1,538	1,680	1,129	1,051	9,778	6,039

From the first test series (catalysts C*, J, L, N), catalyst J shows the best result, followed by catalyst C*, which is taken as the reference. However, it has to be mentioned that the results when comparing the result for catalysts O and P cannot be compared directly to the other catalysts since the SO_2/SO_3 conversion in this series was measured in a different way (not according to the method described in section 3.1.3), which leads to extremely high values for P3. Thus, the performance indicator P3 can only be applied when comparing two catalysts at the same test rig tested under the same test conditions. P3

thus forms a relative measure and indicator. An adjustment between different test rigs or test conditions could be carried out by introducing a correction factor for each of the three parameters in order to refer the results to the same baseline. For example, when a round robin test showed for K_{NOx} for lab A a 10% higher result than the average, the K_{NOx} value for another sample measured by lab A could be corrected by 10% in order to have a common basis for the calculated P3.

4.5 Single-reactions over newly developed SCR catalysts – first-generation catalysts

The development and improvement of SCR catalysts related to the desired property "Hg oxidation" forms the central part of this work. In order to achieve this aim, the understanding of the physical and chemical interaction is important as well as the dedicated modification of catalysts to increase the Hg oxidation compared to the state-of-the-art catalysts. The selection of the materials is carried out based on the literature study. Additional metal oxides are systematically added to the catalyst matrix. If not stated otherwise, the metal oxides are implemented during the kneading process. Thus, they can be considered as homogeneously distributed over the catalyst without any surface effect. All tests related to interactions and tests of newly developed catalysts related to increased Hg oxidation are carried out with catalysts with the same geometry as the reference catalyst C, being a typical 7 mm pitch honeycomb. In addition to the focus on Hg oxidation, two further important reactions at the SCR catalyst, NO reduction and SO_2/SO_3 conversion, are discussed in the context.

4.5.1 Hg oxidation

In a first step, the three metal oxides copper oxide, iron oxide and manganese oxide are added to the catalyst's bulk directly during the production process. The metal oxide concentrations of this first test series are quite low and vanadium was added in addition to the metal oxides in order to increase the Hg oxidation. The chemical composition of the catalysts naming the relevant metal oxides is listed in table 4-9. For copper oxide two different compositions are tested, with catalyst Q having double the amount of CuO compared to catalyst R. The results of the Hg oxidation measurements at these catalysts as single-reaction tests with 150 mg/m^3 HCl in flue gas are shown in figure 4-19.

All new catalysts except catalyst E show higher Hg oxidation compared to the reference catalyst C. Since there is, as previously discussed in section 4.2, almost no active component in catalyst E, the overall Hg oxidation is quite poor. The highest Hg oxidation is measured with catalyst Q. Despite the quite low amount of copper oxide, the Hg oxidation is almost doubled. Even reducing the amount of copper oxide to half of the value (catalyst R) only leads to a decrease of Hg oxidation of less than 10% (absolute).

Table 4-9: Chemical composition (bulk) of first-generation metal oxide test catalysts

	Unit	Catalyst			
		Q	R	S	T
$TiO_{2\ (bulk)}$	wt.-%	78.5	78.8	78.4	79.1
$SiO_{2\ (bulk)}$	wt.-%	9.0	9.1	9.1	8.6
$WO_{3\ (bulk)}$	wt.-%	5.3	5.3	5.3	5.3
$V_2O_{5\ (bulk)}$	wt.-%	0.6	0.6	0.7	0.7
Other $_{(bulk)}$	wt.-%	0.8 CuO	0.4 CuO	1.0 Fe_2O_3	1.6 MnO_2

A reason for this superior performance of the catalysts with additional copper might be the Deacon-reaction as discussed in subsection 2.2.6. Copper is a superior catalyst for the production of chlorine according to the Deacon-process [127].

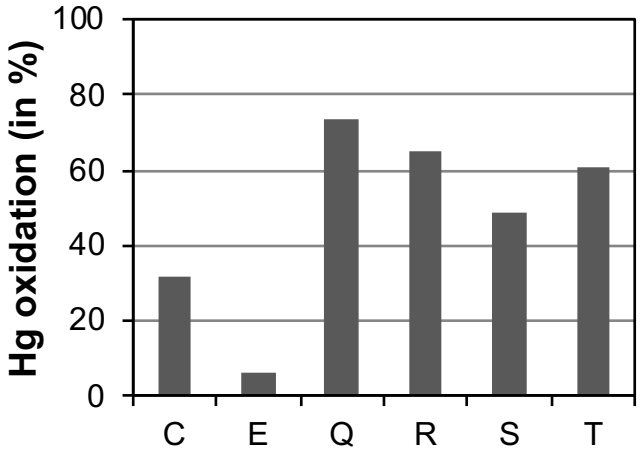

Figure 4-19: Hg oxidation of the first generation of catalysts with added metal oxide tested in the micro-reactor

As discussed in Hisham [127], the process includes first a chlorination of the copper oxide followed by an oxidation step and the forming of molecular chlorine, which then reacts in the gas phase with mercury. However, this is in conflict with the adsorption behavior of mercury on the catalyst discussed in section 4.2 and could only be explained by a Langmuir-Hinshelwood or Mars-Maessen-type mechanism, in which both reactants are (weakly) adsorbed at the catalyst [145]. Especially the Mars-Maessen-type mechanism can explain why the catalysts exhibit some Hg oxidation in the single-digit range when tested in flue gas without HCl. There is a certain oxygen and chloride storage capacity of the catalyst leading to some minor Hg oxidation compared to tests with flue gas HCl. The formation of mercury oxide (HgO) is a possible reaction to be mentioned in this context and which is an intermediate step of the Mars-Maessen-type mechanisms, as explained in section 2.2.6. However, when talking about Hg oxidation in the framework of coal-fired power plants, the intermediate step and especially HgO is not understood as “Hg oxidation” or “oxidized Hg-species” in the narrower sense.

For the catalyst with iron addition in the bulk, an increase in Hg oxidation of about 50% is measured, confirming the positive effect of iron-oxide on Hg oxidation. In this case, the

iron oxide is added in the whole catalyst's bulk and not only present on the surface, which would confirm the effect of the catalyst wall discussed in section 4.4. However, since fly ash contains significant amounts of iron oxides, it can be assumed that this could lead to increased Hg oxidation during operation due to the incorporation of fine porous iron oxides in the porous system of the catalyst. For the oxidative properties of the SCR catalyst related to iron, differences between the iron-lattice modifications α-Fe (hematite) and γ-Fe (maghemite) are also discussed in the case of Hg oxidation, with γ-Fe having much better Hg oxidation behavior than hematite [166], [182]. However, the technique of X-ray diffraction (XRD) was not applied on the catalysts to further distinguish the Fe-modifications really present in the catalysts.

The addition of manganese leads to a doubled Hg oxidation compared to the reference. Furthermore, in tests without any HCl and with low amounts of HCl, the Hg oxidation is still high. This is especially favorable for power plants utilizing coal with low chlorine content. Also manganese, as stated in [171], is a suitable catalyst for the Deacon-process.

4.5.2 DeNOx activity

The DeNOx activity of the first-generation Hg oxidation catalysts is shown in figure 4-20.

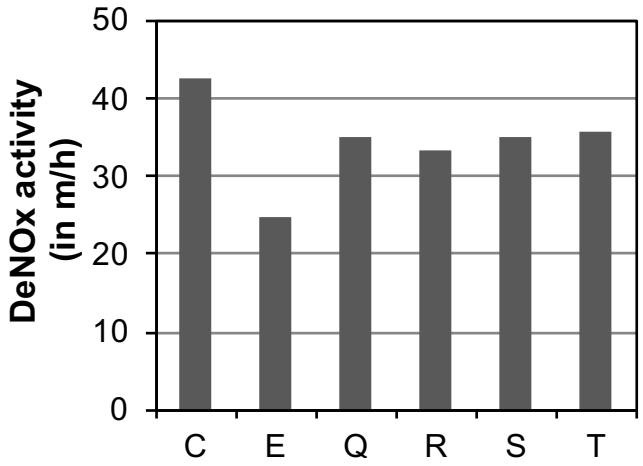

Figure 4-20: DeNOx activity of the first generation of catalysts with added metal oxide

While the activity is tremendously lower but still significantly present for catalyst E with zero vanadium, the NO_x activity is also lower at the other catalysts with added metal oxide, with almost no difference between the metal oxides when vanadium is present.

This can be explained by the dominant influence of vanadium. But for catalyst E without vanadium, the DeNOx activity is related to the TiO_2 structure. Even on the pure anatase surface, acidic centers are formed when SO_2 is present in the flue gas. On these acidic centers, the redox cycle can take place as discussed in subsection 2.2.4.

4.5.3 SO_2/SO_3 conversion

As can be seen in figure 4-21, the formation of surface sulfates is only weak in catalyst E, resulting in a low SO_2/SO_3 conversion coefficient. Also, for the reference catalyst C, the SO_2/SO_3 conversion is quite low, which correlates more or less with the low result for the Hg oxidation. All of the new first-generation Hg oxidation catalysts show a tremendously higher SO_2/SO_3 conversion. With catalysts Q and R, the reduction of the copper content can be directly seen, indicating the superior SO_2 oxidation of the added copper, which can partly be correlated with the Hg oxidation. However, the reduction of about 20% is not in line with the reduction of copper in the catalyst of 50%. Also, catalyst S with iron addition showed higher SO_2 oxidation, indicating the promoting effect of iron on SO_2/SO_3 conversion. Only manganese seems to not be very active related to SO_2 oxidation and thus a good choice for an Hg oxidation catalyst.

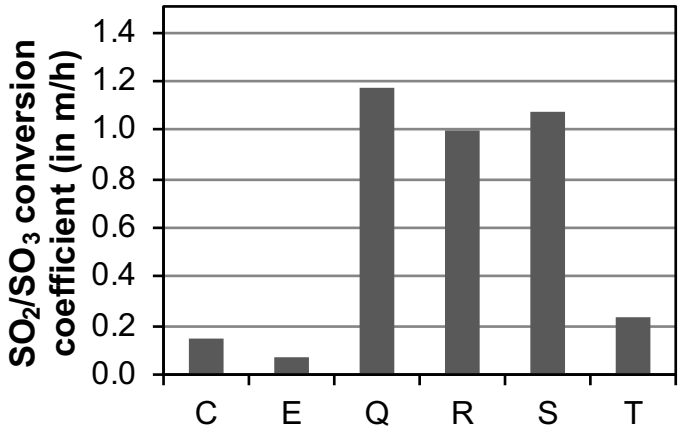

Figure 4-21: SO_2/SO_3 conversion of the first generation of catalysts with added metal oxide

4.5.4 First-generation material test – summary

All the results of these first-generation catalysts with new metal oxides as well as the performance indicator P3 are listed in table 4-10. The result shows that catalyst C and catalyst T are the best-performing catalysts. While copper and iron oxides are good for the promotion of the Hg oxidation, these metal oxides promote the SO_2/SO_3 conversion even more strongly, making these catalysts almost unusable in industrial application. Only manganese oxide seems to be a promoter only in the case of Hg oxidation. However, as stated and discussed amongst others by Zhao [189], Kijlstra [183] and Li [184], manganese oxides face deactivation by the formation of thermally stable manganese sulfates, which would then reduce the activity of the catalyst. However, the SO_2 poisoning could not be detected in these tests since all were carried out as single-reaction relatively short-term tests, meaning that no SO_2 was present in the Hg oxidation tests. While there are possible ways discussed in the literature to avoid sulfur poisoning of manganese oxide catalysts, the result for catalyst T is not as attractive as the performance indicator indicates in this case, since the tests on Hg oxidation were carried out without the addition of SO_2.

Table 4-10: Performance indicator P3 for the first-generation catalyst with new metal oxides

Catalyst	C	E	Q	R	S	T
K_{NOx} (in m/h)	42.7	24.9	35.2	33.4	35.0	35.7
K_{Hg} (in m/h)	10.5	1.9	36.9	29.1	18.5	25.8
K_{23} (in m/h)	0.15	0.07	1.17	1.00	1.07	0.23
P3 (in m/h)	3,006	698	1,111	978	603	3,976

4.6 Single-reactions over newly developed SCR catalysts – effects of the promoter WO_3, active component V_2O_5 and metal oxide application

In order to further verify the previous findings and the effect of the newly introduced metal oxides, further catalyst tests are carried out and at one single metal oxide catalyst the SO_2/SO_3 conversion is studied in more detail. The catalysts' compositions are shown in table 4-11.

Table 4-11: Chemical composition (bulk) of dedicated modified first-generation metal oxide test catalysts

	Unit	Catalyst								
		U	V	W	X	Y	Z	AA	AB	AC
TiO_2 (bulk)	wt.-%	77.0	77.0	78.2	78.1	72.5	83.2	83.1	84.0	83.0
SiO_2 (bulk)	wt.-%	9.4	9.5	8.8	8.9	9.7	8.2	8.2	7.4	8.3
WO_3 (bulk)	wt.-%	6.0	6.0	6.0	6.1	9.8	0.9	0.9	0.9	0.9
V_2O_5 (bulk)	wt.-%	0.1	0.1	0.6 (impr.)	0.8 (impr.)	2.1	0.6	0.6	0.6	0.6
Other (bulk)	wt.-%	0.9 CuO	1.0 Fe_2O_3	-	-	-	1.0 CuO	1.1 Fe_2O_3	1.3 MnO_2	1.0 CeO_2

The first type of catalysts can be characterized as *vanadia*-free catalysts with new metal oxides (catalysts U, V, F (see table 4-5). The second type of catalysts are those with *vanadia* impregnation (impr., catalysts W, X) and with increased *vanadia* content (catalyst Y). Impregnation is an alternative to the kneading process for the application of the active sites and carried out by dedicated dipping of the produced honeycomb catalyst in a prepared vanadate solution. The third type of catalyst can be described as support (tungsten)-free (catalysts Z, AA, AB), meaning that in these catalysts, tungsten was not added as "support". Finally, in these first-generation catalysts, cerium is introduced in one catalyst (catalyst AC).

4.6.1 Hg oxidation

Comparing the results of the single-reaction Hg oxidation at 150 mg/m^3 HCl as shown in figure 4-22 with the results of the previous section, the promoting effect of *vanadia* (V_2O_5) on the Hg oxidation in catalysts with new metal oxides is visible. Catalysts U, V and F show lower Hg oxidation than the corresponding catalysts with vanadium, namely catalysts Q, S and T (catalyst U corresponds to Q, V to S and F to T). However, the new metal oxides compensate for the absence of *vanadia* to a great extent. While for catalyst E without any active material addition an Hg oxidation of <10% was measured in figure 4-19, for all new metal oxides an Hg oxidation of >40% was measured. The effectiveness of Hg oxidation of these new metal oxides was unchanged without *vanadia*. Copper is still the most powerful catalyst tested under these conditions.

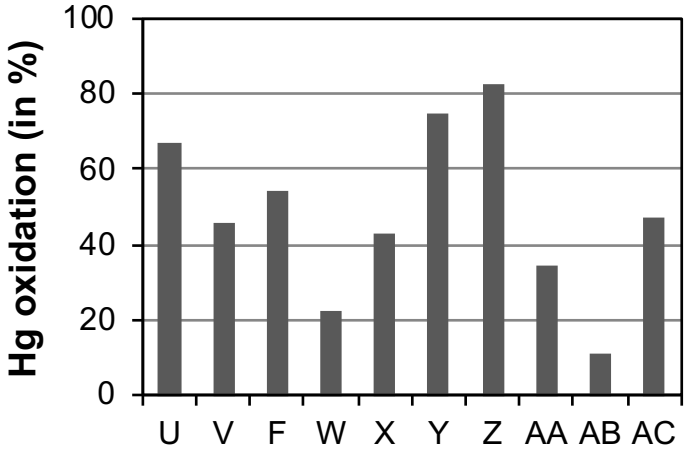

Figure 4-22: Hg oxidation of modified first-generation SCR catalysts

For the catalysts without tungsten oxide, the picture is not that clear from the results. Hg oxidation is higher for catalyst Z than for catalyst Q despite them being identical except of the lack of tungsten oxide in catalyst Z. This difference in Hg oxidation can be explained by the suppression of the properties of the catalyst by tungsten which lead to a high Hg oxidation rate as it is described for tungsten in case of the SO_2/SO_3 conversion [96]. For catalysts AA and AB, the absence of tungsten has a negative effect on the Hg oxidation performance, which can be explained by the various oxidation states of the two metals, which form the right structure for the superior Hg oxidation properties of the catalysts only in combination with TiO_2/WO_3.

Catalyst Y, which has four times higher *vanadia* content compared to catalyst C and also a slightly increased tungsten content, shows more than doubled Hg oxidation. This confirms the positive effect of *vanadia* on the Hg oxidation. The effect of the method of *vanadia* application in TiO_2/WO_3 catalysts can be seen with catalysts W and X when comparing the results with catalyst C. Since the composition of catalyst W is the same as for catalyst C, the form or application of *vanadia* on the catalyst plays a crucial role. The impregnation on the catalyst surface on the one hand leads to the intended bulk V_2O_5 concentration,

but on the other hand, the Hg oxidation is lower. This is a further indication of the importance of the catalyst's bulk for Hg oxidation, as explained in section 4.4, since impregnation does not lead to such an intense mixture of the metal oxides prior to calcination, compared to the mixing and kneading during the production of a homogeneously extruded honeycomb. The impregnation as applied at this catalyst usually only affects the surface of the catalyst. Nevertheless, as can be seen in catalyst X, even with impregnation, the Hg oxidation can be increased by higher concentrations of *vanadia*. Thus, it was found that the homogeneous application of new metal oxides generally shows better results.

As a new support and catalyst material, the application of cerium in a full-scale honeycomb catalyst is tested for the first time to enhance Hg oxidation in the almost tungsten-free catalyst. As can be seen with catalyst AC, the application is successful and a higher Hg oxidation is achieved. Cerium seems to better support Hg oxidation than tungsten. This can be explained by the ability to store and release oxygen due to the redox shift between Ce^{4+} and Ce^{3+} [185]. The synergistic effect of cerium with vanadium was similarly found by Zhao [185], which makes this rare earth element interesting for further study. The oxygen storage capacity as well as the synergistic effect of cerium indicate a Mars-Maessen reaction type for the Hg oxidation.

4.6.2 DeNOx activity

The strong effect of *vanadia* on DeNOx activity can be seen in figure 4-23. The two catalysts U and V, both without *vanadia*, show significantly lower DeNOx activity compared to the – aside from the *vanadia* content – identical catalysts Q and R.

The decrease is quite in line with the previously discussed reduction of the Hg oxidation at these catalysts. Due to the higher *vanadia* content, DeNOx activity is slightly increased with catalyst Y compared to catalyst C. The addition of cerium in the catalyst matrix of catalyst AC does not have a negative effect on the activity. The result is in line with the previously discussed catalyst of the first generation.

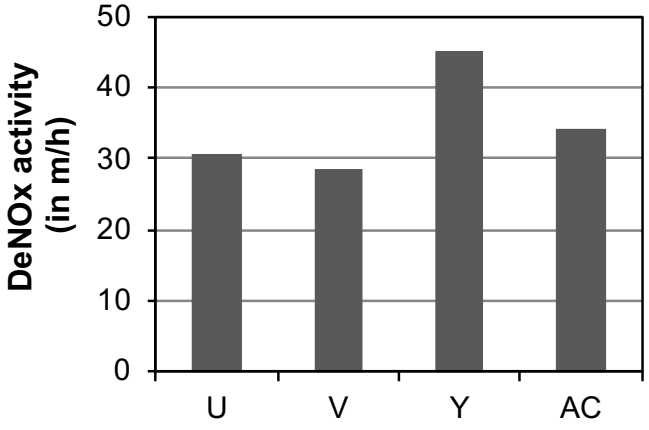

Figure 4-23: DeNOx activity of selected modified first-generation SCR catalysts

4.6.3 SO_2/SO_3 conversion

The SO_2/SO_3 conversion coefficient of the modified first-generation SCR catalysts is listed in figure 4-24. The strong positive effect of *vanadia* can be seen comparing catalysts U, V, F with the corresponding catalysts R, S, T in the previous section. The lack of *vanadia* in catalysts U, V and F leads to a lower SO_2/SO_3 conversion, which is not distinctive from the catalyst with additional manganese (catalyst F). Comparing catalyst W with the reference catalyst C shows more or less the same value for the SO_2/SO_3 conversion. The effect of impregnation is more visible with catalyst X, which was impregnated to achieve a higher V_2O_5 content of the catalyst compared to catalyst C. The corresponding homogeneously extruded honeycomb with the same chemical composition shows significantly higher SO_2/SO_3 conversion. An impregnation as with catalysts W and X delivers the *vanadia* primarily on the surface of the catalytic structure and thus the deeper inner structure is not active in SO_2 oxidation. An even higher *vanadia* content as found in catalyst Y leads then to more than doubled SO_2/SO_3 conversion, since in this homogeneously extruded honeycomb the whole catalyst's bulk is active and SO_2/SO_3 conversion takes place in the whole bulk.

The promoting effect of WO_3, meaning amongst others the suppression of the SO_2/SO_3 conversion by adding the metal oxide, as described in the literature for example by Forzatti [96], can be seen neither in catalyst Z nor in catalyst AA. Both show lower SO_2/SO_3 conversion without tungsten. The effect of the promoter tungsten can only be seen at the manganese-impregnated catalyst AB. Different findings confirming the results of catalysts Z and AA were obtained by Morikawa [186] and Dunn [124]. They explained these findings with the fact that the vanadium and tungsten active sites act independently without any synergistic interactions in the ternary catalysts, meaning that vanadium and tungsten contribute equally to the SO_2/SO_3 conversion and the result for the ternary catalyst is simply the sum of the corresponding binary active sites.

Despite the good properties related to Hg oxidation, the SO_2/SO_3 conversion of catalyst AC stays low, showing in fact almost the lowest conversion in this series. In three-way catalysts, cerium can be added to trap small amounts of SO_2 under fuel-lean conditions in the form of stable sulfates [187]. However, in the standardized SO_2/SO_3 conversion testing as carried out here, the result is an equilibrium state, showing that the cerium catalyst is also capable of releasing the formed SO_3.

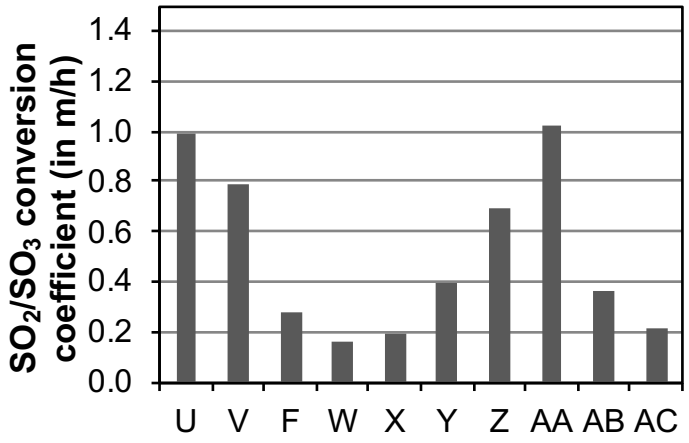

Figure 4-24: SO_2/SO_3 conversion coefficient of modified first-generation SCR catalysts

4.6.3.1 Effect of SO_2 concentration on SO_2/SO_3 conversion

Since for the newly developed catalysts of the first generation, the SO_2/SO_3 conversion is much higher than the reference, further experiments are carried out in order to further understand the dependencies of the SO_2/SO_3 conversion on the operating conditions and possible areas of operation. This section and the following subsections until 4.6.3.4 are mainly extracted from [150]. The SO_2/SO_3 conversion and the SO_3 concentration downstream of the catalyst over the SO_2 concentration is shown in figure 4-25. The measurements are carried out at 380°C, 5% O_2 and a water content of 10% in the flue gas.

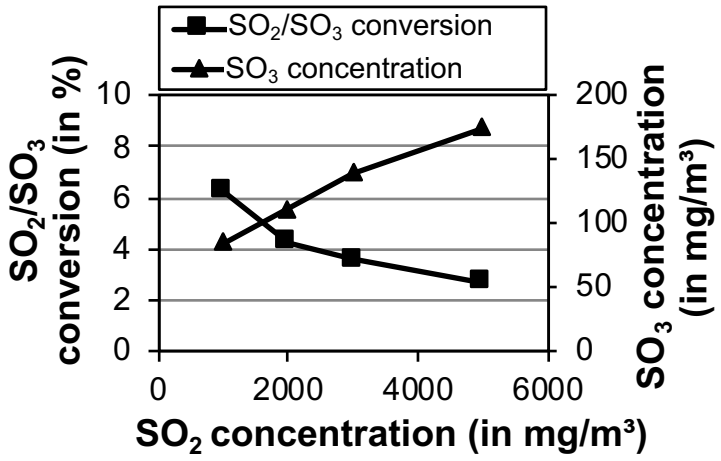

Figure 4-25: SO_2/SO_3 conversion of catalyst U over SO_2 concentration

The SO_3 concentration is increased when the SO_2 concentration is increased, but there is a non-linear tendency. There seems to be a saturation point of the curve at higher SO_2 concentrations. This is clearly visible in the curves of the SO_2/SO_3 conversion. At very low concentrations, the conversion is very high and becomes lower at higher SO_2 concentrations. These results also lead to the conclusion that the reaction order in the observed concentration range is a pseudo-first-order reaction because there is a dependency, but not a linear one, of the SO_3 concentration on the SO_2 concentration [150]. Compared to SO_2, there is a great abundance of oxygen present (about 0.2 vol.%

SO_2 vs. 5 vol.% oxygen). Thus, the oxygen concentration is not the limiting factor in the reaction and can be considered as constant. The limiting factor in the reaction of SO_2 to SO_3 is the availability of active sites. At low SO_2 concentrations, there are numerous free active sites available and the reaction takes place at the sites on the surface (when not occupied by ammonia). At higher SO_2 concentrations, more SO_2 molecules enter the catalyst bulk and more and more active sites become occupied. According to Svachula [122], the reaction rate of the SO_2 conversion is much smaller than the diffusion rate of the educts SO_2 and O_2 and the product SO_3 through the catalyst volume. Thus, if more and more active sites are occupied because of the low reaction rate, no more reactions can take place and less SO_3 is produced.

4.6.3.2 Effect of residence time

To get a better insight into the reaction rate, experiments with different gas velocities are carried out. Therefore, tests at linear velocities of 0.3-1.5 m/s (wet, STP) resulting in area velocities of 8-41 m/h (wet, STP) were performed as shown in figure 4-26. It has to be noted that the figure shows the residence time at STP and the real gas velocity is much higher due to higher gas volume because of the higher gas temperature. The residence time is therefore again lower.

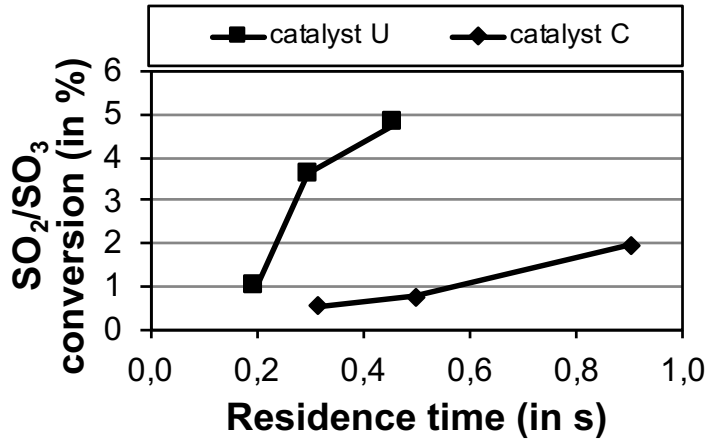

Figure 4-26: SO_2/SO_3 conversion of catalyst C and catalyst U at different residence times in the catalyst

Both curves have a positive slope. The SO_2/SO_3 conversion in percent increases with increasing residence time. The slope is steeper at the Cu-containing catalyst, whereas the curve becomes flat with a residence time of more than 0.3 s. With catalyst C, there is only a slight increase in the SO_2/SO_3 conversion, since this catalyst formulation is already optimized for low SO_2/SO_3 conversion. The difference of the slope of the curves can be explained with a higher conversion of the Cu-containing catalyst compared to the reference catalyst because of a change in the catalytic active sites. These results can also be linked with the results of the concentration-dependency measurements of the previous section. A high residence time means that there is a lot of time for the reaction of SO_2 to SO_3 on the catalyst. At shorter residence times (meaning also higher area velocities), most of the SO_2/SO_3 molecules just pass the catalyst without any reaction

because the available active sites are already occupied by other SO_2/SO_3 molecules, which are currently oxidized or on their way to the surface of the catalyst. For the construction, calculation and operation of an SCR unit, the residence time is an important factor. Lower gas velocities or higher residence times will yield higher SO_2/SO_3 conversion rates and possibly cause problems downstream of the reactor.

4.6.3.3 Effect of water content

Since various fuels and combustion conditions lead to different water contents in flue gas, the effect on the SO_2/SO_3 conversion over the catalyst is evaluated with catalyst C and catalyst U. Measurements at different moisture contents between 0.7 vol.% and 10.2 vol.% were performed as shown in figure 4-27. The measurement of the SO_2/SO_3 conversion in dry flue gas is not possible as described in [162], because in the condenser, sulfuric acid aerosols are precipitated by inertial force at a temperature of about 90°C. To form sulfuric acid aerosols out of SO_3, the presence of water is necessary. Due to the high hygroscopicity and the very low SO_3 content, only a small amount of water is needed. Therefore, measurements with water contents at about 0.7 vol.-% as the lowest possible values were performed.

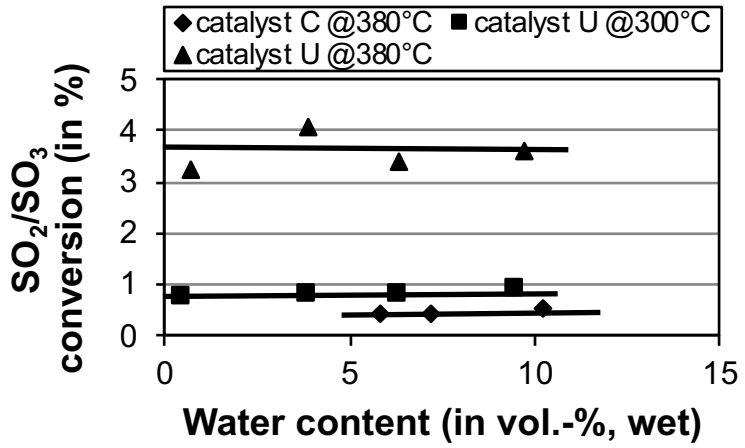

Figure 4-27: Effect of water content on SO_2/SO_3 conversion with catalyst C and catalyst U

According to these results, no dependency of the SO_2/SO_3 conversion on the water content is visible in the observed range. Variations of the measured value can be explained by errors in the measurement, so all measurements show comparable values and confirm the results of Svachula et al. [122] and Dunn et al. [124]. Svachula found that in the range of practical interest (water content between 5 and 15 vol.-%), there is no dependency on the water content. However, it is likely that water, due to its polarity, interacts with the catalyst's surface. The results presented here confirm that the reaction of the SO_2/SO_3 conversion is of zeroth order regarding the water content. This could be explained by the fact that water does not play a role in the formation cycle of SO_3 at the active sites and water content is always very high in flue gas compared to SO_2. Again, as discussed before, catalyst U shows higher SO_2/SO_3 conversion compared to catalyst C, even when catalyst U is tested only at a flue gas temperature as low as 300 °C.

4.6.3.4 Effect of temperature

The effect of temperature on the SO_2/SO_3 conversion is additionally studied with catalyst C and catalyst U in order to get a deeper insight. The tests are carried out at 10 vol.-% water content while all other conditions are kept as before. Both catalysts show an exponential increase of SO_2/SO_3 conversion with temperature as already mentioned in section 4.4 and shown in figure 4-28. The slope is much higher at the Cu-containing catalyst U compared to catalyst C. The reaction kinetics of the SO_2/SO_3 conversion can be described by either the Arrhenius equation or the Eyring equation. The Eyring equation gives an accurate correlation between temperature and reaction rate. In contrast to the Arrhenius equation, which is based on empirical studies, the Eyring equation is based on the thermodynamic theory of transition state and can be applied on two phase reactions. The derivation can be found in [188]. In its linear form, the Eyring equation can be expressed as shown in equation 4-3, in which the SO_2/SO_3 reaction rate constant k_{23} (in 1/s) is calculated according to equation 3-14.

$$\ln\frac{k_{23}}{T} = \frac{\Delta H}{\tilde{R}}\cdot\frac{1}{T} + \ln\frac{k_{\mathrm{Bo}}}{h} + \frac{\Delta S}{\tilde{R}} \qquad \text{equation 4-3}$$

The further parameters and constants in the equation are the absolute temperature T (in Kelvin), the universal gas constant $\tilde{R}$ (in J/(mol·K)), the Boltzmann constant k_{Bo} (in J/K) and the Planck constant h (in J/s). By plotting the temperature-corrected reaction rate constant over the reciprocal of the temperature, the activation enthalpy (ΔH) and the activation entropy (ΔS) can be determined. The plot of the measurements of catalysts C and U is shown in figure 4-29. The distribution of points of the Cu-containing catalyst U can be described by two separate straight lines with an intersection point at about 350°C. With catalyst C, such a characteristic knee of the curve is not visible. This may be because of the very low SO_2/SO_3 conversion of this catalyst. The characteristic knee was also described by Svachula [122].

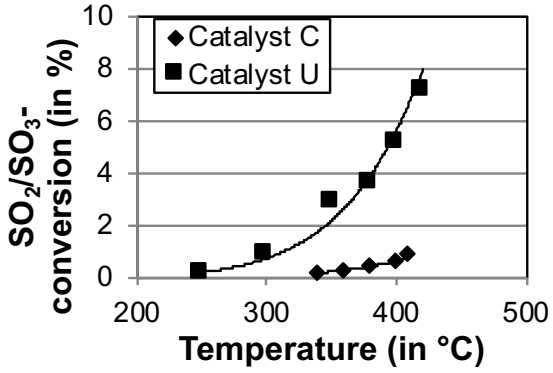

Figure 4-28: Temperature dependency of the SO_2/SO_3 conversion with catalysts C and U

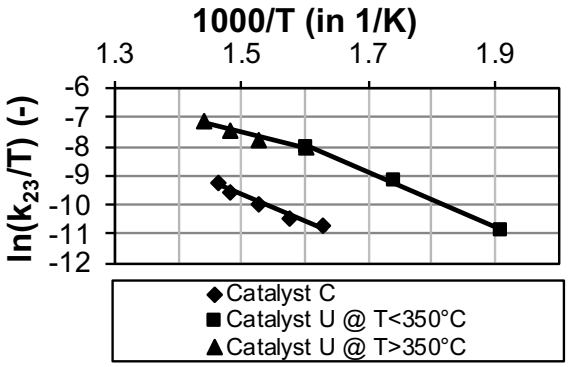

Figure 4-29: Eyring diagram of the SO_2/SO_3 conversion with catalysts C and U

The result shows that there are possibly different reaction pathways responsible for the SO_2/SO_3 conversion at different temperature ranges and this convex curve for catalyst U is also evidence of a catalyzed reaction. According to the linear form of the Eyring equation (equation 4-3), the activation enthalpy and activation entropy are calculated. The results are shown in table 4-12.

Table 4-12: Calculated activation enthalpy and entropy

Catalyst	Temperature range [°C]	ΔH [kJ/mol]	ΔS [J/(mol·K)]
C	340-410	76	-164
U	250-350	78	-138
U	350-420	47	-189

While slower reaction rates can be seen at higher activation enthalpies or energies, fast reaction rates are characterized by respectively lower values of activation enthalpy. That means that catalyst U, with copper added, at low temperatures and catalyst C at the whole temperature range both show relatively moderate SO_2/SO_3 conversion because of the similar activation enthalpy. The reaction in catalyst U at higher temperatures is different because of the comparably low reaction enthalpy. Thus, more SO_3 is produced at higher temperatures. An indicator for different reaction pathways is also the difference in the activation entropy, which is an indicator of the degree of order in the transition state.

Differences in the reaction enthalpy and the overall SO_2/SO_3 conversion at different catalysts and temperatures can be attributed to different catalytic active sites at different temperatures and different catalyst compositions. Dimeric vanadyl sulfates have been identified as the active sites for SO_2/SO_3 conversion on standard commercial TiO_2/WO_3-V_2O_5 catalysts [122]. The adsorption of sulfur dioxide on the vanadium-oxygen metal support bonds has been proposed [124], resulting in (V^{5+})-SO_2 adsorption states or (V^{3+})-SO_3 adsorption states. When the V^{5+}-O-SO_2 or M-O-SO_2 bond is loosened, SO_3 is formed. Regeneration of the active site takes place by re-oxidation by oxygen. A reaction mechanism for NO reduction over copper- and manganese-based catalysts has been proposed by Centi [97] which is different to the reaction mechanism over *vanadia*–titania-based catalysts. Possibly, the buildup and depletion of sulfates at the catalyst is favored at Cu-surface sites. Due to the fact that the Cu-containing catalyst is based on a TiO_2/WO_3 catalyst, a mixture of reaction pathways are possibly acting together or influenced by each other in different ways at different temperatures.

Compared to the activation energy of the DeNOx reaction, which was determined by Svachula et al. [119] to be about 21 kJ/mol, the activation energy (activation enthalpy) of the SO_2/SO_3 conversion is much higher. The process of SO_2 oxidation is kinetically controlled and the DeNOx reaction is controlled by diffusion. This means that the DeNOx reaction is preferred at the prevailing temperatures in the catalyst. The results presented here show the situation as it is in the last layer of a power plant's DeNOx reactor, where

almost all ammonia is consumed. Thus, the results show the maximum SO_2/SO_3 conversion. The SO_2/SO_3 conversion in the flue gas of power plants with ammonia present will be lower than the values discussed here due to the inhibition by ammonia. A further evaluation is presented in subsection 4.10.8.

As already discussed in section 4.4, the process of SO_2 oxidation at SCR catalysts is kinetically controlled. This means, that the due to the slow reaction velocity, SO_2 can diffuse through the whole catalyst volume and does not react directly on the surface. The whole volume of the catalyst and not just the surface can be considered as the place of the reaction. Regarding the SO_2/SO_3 conversion at these newly developed catalysts, the wall thickness could be reduced. This would lead to lower SO_2/SO_3 conversion without affecting the DeNOx reaction, which is, because of the limited diffusion, a surface reaction. However, in parallel, the Hg oxidation would be reduced. But other effects like long-term catalyst stability and erosion resistance also have to be considered. An installation of catalyst U at lower temperatures or when Ca-rich fly ash is present to react with SO_3 could also be a possible application.

4.6.4 Summary of the test series

The performance indicator P3 is also calculated for this test series, as shown in table 4-13. Since not all parameters are determined for all catalysts, P3 can only be given for a selection. The introduction of the new metal oxides without *vanadia* cannot be considered as effective. Compared to catalyst C, the increase of the *vanadia* content (combined with higher tungsten) seems a way to increase the overall performance (as shown with catalyst Y). The result of catalyst AC with cerium seems to be promising, but needs further optimization.

Table 4-13: Performance indicator P3 for the catalysts with different active components

Catalyst	C	U	V	Y	AC
K_{NOx} (in m/h)	42.7	30.6	28.4	45.1	34.3
K_{Hg} (in m/h)	10.5	30.5	17.0	38.0	17.6
K_{23} (in m/h)	0.15	0.99	0.79	0.40	0.22
P3 (in m/h)	3,006	946	612	4282	2787

4.7 Single-reactions over newly developed SCR catalysts – effects of varied titania oxide powder

For the production of SCR catalysts, a specific TiO_2 powder is applied. In the case of catalyst C, it is a certain grade. However, there are various other powders on the market with specific grades from different suppliers. Some of them have higher surface areas and particle sizes down to nanometer range. These powders, sometimes with nanoparticles

included, were applied on catalysts H, AD, AE and AF and compared to catalyst C. The composition of catalysts AD, AE and AF, which have not been discussed before, is shown in table 4-14. At some of these catalysts, the silica content is increased. This is due to the TiO_2 powder being doped with SiO_2 powder, not due to an increased silica content due to glass fibers, which is normally the source of the SiO_2 content in SCR catalysts.

Table 4-14: Composition of catalysts with certain TiO_2 base materials

	Unit	Catalyst		
		AD	AE	AF
$TiO_{2\ (bulk)}$	wt.-%	71.9	76.9	75.6
$SiO_{2\ (bulk)}$	wt.-%	14.9	10.5	11.5
$WO_{3\ (bulk)}$	wt.-%	5.6	5.8	5.3
$V_2O_{5\ (bulk)}$	wt.-%	0.4	0.5	0.4
BET surface area	m^2/g	75.5	59.0	67.9
Average pore size	nm	12.2	14.4	13.6

4.7.1 Hg oxidation

The Hg oxidation of these modified catalysts is shown in figure 4-30 at three different HCl concentrations. The strong influence of HCl concentration on Hg oxidation as discussed in subsection 4.3.1 is also present here.

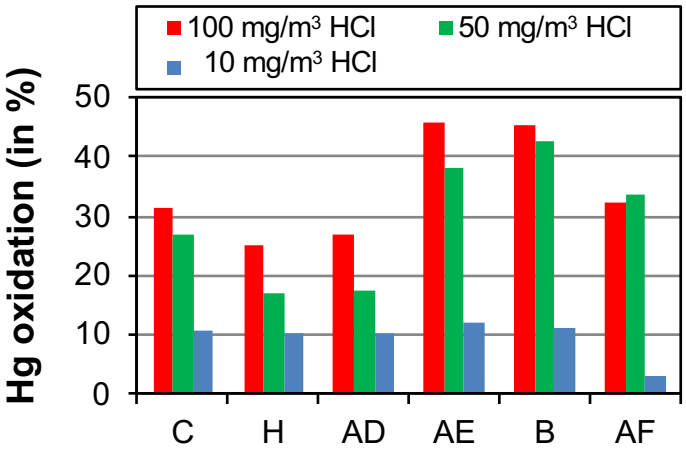

Figure 4-30: Hg oxidation of SCR catalysts with various TiO_2 base materials at different HCl concentrations

While at high HCl contents, the Hg oxidation is higher for some of the new catalysts compared to the reference, the Hg oxidation is only slightly increased at 10 mg/m^3 HCl for catalysts AE and B, while for catalyst AF it is lower. For the Si-containing catalysts, the result can be explained by a diluting effect. The silica powder in the catalyst bulk is not active in terms of Hg oxidation and interrupts the active V-TiO_2 bonding, thus behaving differently to the separate, almost pure SiO_2 glass fibers. The silica addition leads to a higher surface area, as can be seen in the BET surface area; however, the Hg oxidation

stays low. This is a further indicator that the Hg oxidation is not only a pure surface reaction. Assuming a pure surface reaction, the result should be higher with increased surface area. An interesting effect can be seen at the two best-performing catalysts within this series, catalysts AE and B. At these catalysts, for the first time TiO_2 in a special nano-grade was applied. However, this didn't result in a higher surface area in the final product and thus a higher Hg oxidation. Contrariwise, the surface area stayed the same as with catalyst C, but the influence on the internal V-TiO_2 bonds related to Hg oxidation was significant. Possibly, the nano-grade powder supports the structure formation during kneading and calcination during the production process, in order for *vanadia* and titania oxide to be more evenly distributed in the inner surface of the catalyst.

4.7.2 DeNOx activity

The DeNOx activity is not significantly influenced by the variation of the TiO_2 base material, as can be seen in figure 4-31. The silica in the base material on the one hand leads to an increased surface area, which should favor the DeNOx activity, but on the other hand, the surface area is possibly slightly disturbed by the addition of silica. Thus, the surface is not that active in terms of NO_x reduction. This can be compensated by the addition of WO_3, as shown with catalyst AD.

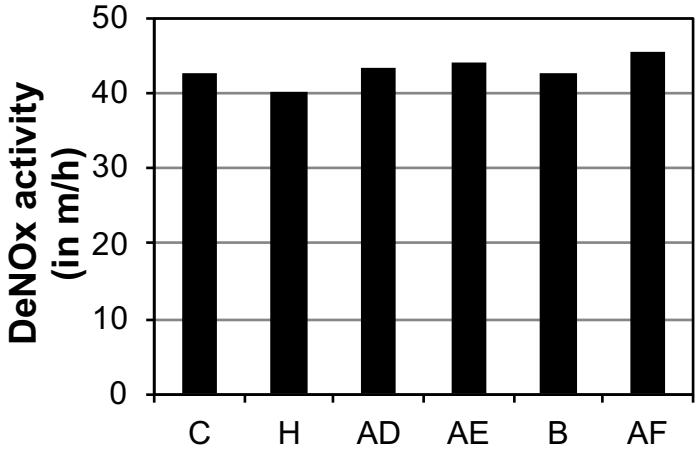

Figure 4-31: DeNOx activity of SCR catalysts with various TiO_2 base materials

4.7.3 SO_2/SO_3 conversion

The main advantage and benefit of the different TiO_2 base materials compared to the conventional catalyst C is the lower SO_2/SO_3 conversion. As can be seen in figure 4-32, the SO_2/SO_3 conversion of these new catalysts is almost half of catalyst C, which can partly be explained by the diluting effect of SiO_2. Furthermore, the applied nano-grade TiO_2 seems to contribute less to the SO_2/SO_3 conversion than the conventional catalyst base material.

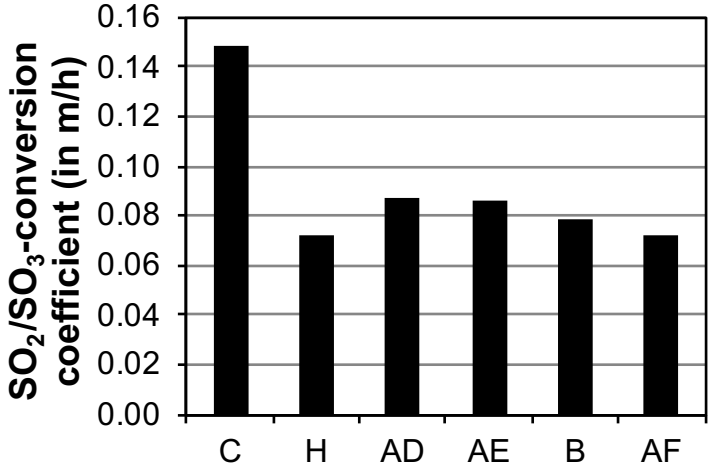

Figure 4-32: SO_2/SO_3 conversion of SCR catalysts with various TiO_2 base materials

4.7.4 Summary of the test series

Finally, the performance indicator P3 is calculated from this test series as listed in table 4-15. The highest values are reached for catalysts AE and B. However, due to the low SO_2/SO_3 conversion, all catalysts in this series with a modified TiO_2 base material show better values than the conventional catalyst C. Thus, from these first results, it can already be concluded that this test was successful. A lower Hg oxidation of these catalysts can possibly be compensated by a higher *vanadia* content, as shown in section 4.6.1 comparing catalyst W and catalyst X. However, this method of improvement of the catalyst's performance is strongly driven by the price of the respective TiO_2 base material, since TiO_2, with a share of 70 to 80 wt.-%, forms the main ingredient in SCR catalysts.

Table 4-15: Performance indicator P3 for the catalyst with different TiO_2 base materials

Catalyst	C	H	AD	AE	B	AF
K_{NOx} (in m/h)	42.7	40.0	43.4	44.2	42.5	45.4
K_{Hg} (in m/h)	10.5	7.9	8.7	16.8	16.6	10.8
K_{23} (in m/h)	0.15	0.07	0.09	0.09	0.08	0.07
P3 (in m/h)	3,006	4,378	4,289	8,639	9,006	6,749

4.8 Single-reactions over newly developed SCR catalysts – effects of molybdenum and cerium

At these second-generation SCR catalysts, previously discovered positive effects on the performance of SCR catalysts are studied in detail. A positive effect of molybdenum was seen in section 4.2, and is here directly compared to tungsten. Cerium was discussed for the first time in section 4.6 and is researched in more detail in this section. The properties of these catalysts are listed in table 4-16.

Table 4-16: Chemical composition (bulk) of modified second-generation metal oxide catalysts

	Unit	Catalyst						
		AG	I	AH	AI	AJ	AK	AL
$TiO_{2\ (bulk)}$	wt.-%	79.5	78.7	75.0	77.9	77.3	60.3	60.7
$SiO_{2\ (bulk)}$	wt.-%	9.0	10.3	11.0	10.0	10.3	13.4	13.3
$WO_{3\ (bulk)}$	wt.-%	5.4	0.7	3.5	0.7	0.8	5.1	5.1
$V_2O_{5\ (bulk)}$	wt.-%	0.5	0.7	0.6	0.7	0.7	-	-
Other (bulk)	wt.-%	-	4.7 MoO_3	4.6 MoO_3	6.0 MoO_3	5.8 MoO_3	14.0 CeO_2	14.0 CeO_2
BET surface area	m^2/g	50.4	50.4	52.8	57.3	65.6	99.4	107.7
Average pore size	nm	15.1	15.1	14.2	14.5	12.4	9.1	8.2

4.8.1 Hg oxidation

The Hg oxidation of the second-generation SCR catalysts is shown in figure 4-33. Compared to the previously discussed state-of-the-art catalyst C, all of these new formulations show an increase in Hg oxidation. The lowest result is measured with catalyst AG, which in fact shows the same chemical composition as catalyst C. The difference can be traced back to a different TiO_2 powder used for the production of catalyst AG. In catalyst I, instead of WO_3, MoO_3 was applied, with the remaining composition the same as in catalyst C. As already found and discussed in section 4.7, the molybdenum catalysts show higher Hg oxidation. In [144], these findings were confirmed and explained by the superior ability of molybdenum to contribute to the re-oxidation of vanadium from V^{3+} to V^{5+}. Furthermore, the findings were confirmed in an actual flue gas atmosphere [189]. In a few other publications ([125], [133], [142]), V_2O_5-MoO_3/TiO_2 catalysts were researched, but not in a direct comparison to WO_3 catalysts.

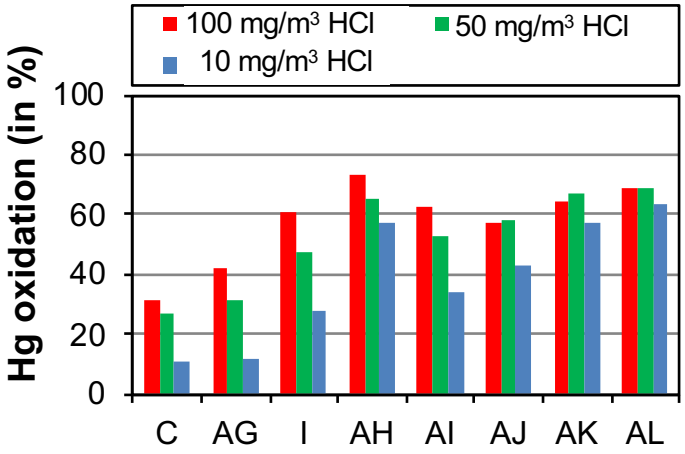

Figure 4-33: Hg oxidation of second-generation SCR catalysts

Catalysts AK and AL, with cerium as a new material but without vanadium, show very high Hg oxidation under these standard test conditions, which can be traced back to the superior oxidation properties of the cerium as discussed in subsection 4.6.1. Especially at low HCl concentration, the Hg oxidation stays high at more than 90% of its value at 100 mg/m^3 test point, while it is only one third at the standard commercial catalyst C. The superior properties of catalyst AL become obvious when reducing the HCl concentration further below 10 mg/m^3. Even at HCl concentrations of 2.7 mg/m^3, as shown in the annex in figure 8-2, the Hg oxidation is higher than in catalyst C with 100 mg/m^3 HCl, which confirms the superior redox properties of cerium. Overall, compared to the result in the previous section, the result of the catalysts in this section is slightly higher, which is due to the higher amount of cerium, but there is no *vanadia* applied to the two catalysts AK and AL. Possibly, the Hg oxidation can further be increased by adding a low amount of *vanadia* to these catalysts with high cerium content. Of all researched catalysts, these catalysts with the addition of cerium show the highest surface area and smallest pores. Thus, the increase of Hg oxidation could be explained by the increased surface area, but the relative increase of Hg oxidation, compared to the other catalysts, is not linear to the increase in surface area, especially comparing catalysts AH and AL. In [190], also no significant influence of the BET surface area on the catalytic performance was found at CeO_2-WO_3/TiO_2 nanocomposite catalysts. However, the slight increase of Hg oxidation between catalysts AK and AL must be traced back to the surface area, since both catalysts have the same chemical composition. The dedicated modification between these two catalysts was carried out by variations in calcining temperature, which determines the inner pore formation. The effect can also be seen with catalysts AI and AJ, which show the same chemical composition but varied calcining procedures. However, summarizing the discussion, the redox properties of the chemical composition of the catalyst are more important than its inner surface area. This is especially the case considering that fine pores can be easily and quickly plugged by fly ash.

4.8.2 DeNOx activity

The DeNOx activity of the tested second-generation catalysts is similar to catalyst C as shown in figure 4-34, except for catalysts AK and AL. This can be explained by the more or less similar surface chemistry of the catalysts. Neither WO_3 nor MoO_3 have any negative influence on the DeNOx activity. Both are stabilizers and promoters for the TiO_2 structure and hinder the transformation of TiO_2 anatase to rutile at higher temperatures [111]. Different to the previously shown result of catalyst AC, the two catalysts with cerium show a significantly lower DeNOx activity. This can be explained by the absence of *vanadia* in these catalysts. The synergistic redox cycle with Ce^{4+} and V^{4+} therefore cannot take place as it would greatly improve the NO_x reduction over V_2O_5-WO_3/TiO_2-CeO_2 catalysts as discussed in [191]. CeO_2 is not as active in NO_x reduction as V_2O5 or V_2O_5-CeO_2, which is in contrast to the results of Chen [192], who found enhanced DeNOx

activity of the CeO_2-WO_3/TiO_2 catalyst over a wide range of operating temperatures. However, the tests in [192] were carried out with catalyst powder and not homogeneously extruded honeycombs. As already discussed above, the addition of vanadium would possibly increase the DeNOx activity. The slight difference of the DeNOx activity of catalysts AK and AL can be traced back to the slightly higher surface area of catalyst AL, which has a positive effect on the available active sites on the surface.

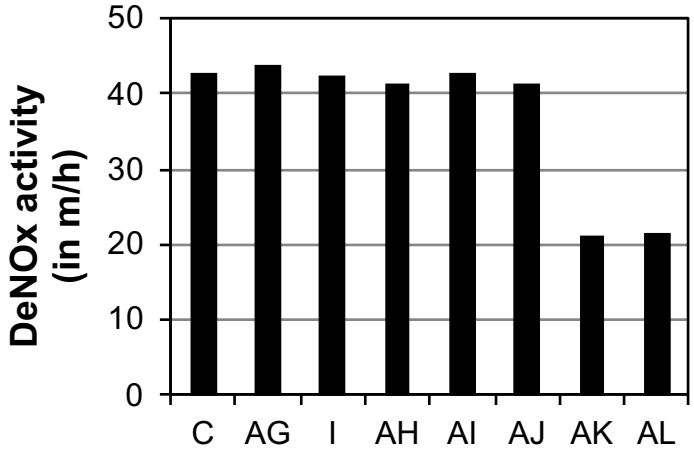

Figure 4-34: DeNOx activity of second-generation SCR catalysts

4.8.3 SO_2/SO_3 conversion

The nano-material catalysts and the catalysts with cerium added show in figure 4-35 lower SO_2/SO_3 conversion. This confirms the previously discussed finding that the SO_2/SO_3 conversion is independent of the catalyst's surface and preferentially takes place in the catalyst's bulk. A change in surface area has only a minor influence on the conversion rate and conversion coefficient, as can be seen with catalyst AI compared to AJ and catalyst AK compared to AL. The direct comparison of WO_3 vs. MoO_3 does not show a direct advantage of MoO_3 related to SO_2/SO_3 oxidation, comparing catalyst AG and catalyst I.

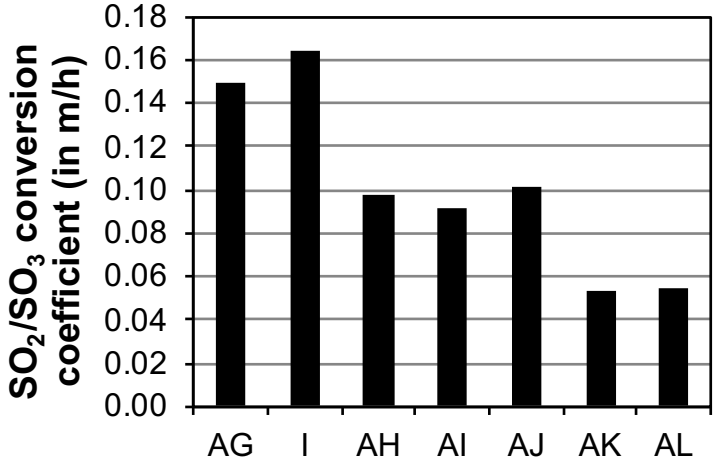

Figure 4-35: SO_2/SO_3 conversion of second-generation SCR catalysts

The result is superimposed by an increased *vanadia* content of catalyst I. A slight increase in V_2O_5 could lead to an increased SO_2/SO_3 conversion. This result furthermore confirms the results of Morikawa [186], who did not find any difference in SO_2/SO_3 conversion when comparing V_2O_5-WO_3/TiO_2 vs. V_2O_5-MoO_3/TiO_2. Additionally, Dunn [193] measured the same turnover frequencies (number of SO_2 molecules oxidized per surface *vanadia* site per second) for both molybdenum- and tungsten-oxide catalysts, and found them to be lower than the values measured over the catalysts without any promoter.

4.8.4 Summary of the test series

As summary of this section, the performance indicator P3 is calculated and listed in table 4-17. As can be seen, the catalysts of this section show the highest performance indicator of the tested catalysts.

Table 4-17: Performance indicator P3 of the catalysts with molybdenum and cerium

Catalyst	C	AG	I	AH	AI	AJ	AK	AL
K_{NOx} (in m/h)	42.7	43.7	42.4	41.4	42.7	41.4	21.1	21.7
K_{Hg} (in m/h)	10.5	15.1	25.8	36.1	27.2	23.3	28.1	32.3
K_{23} (in m/h)	0.15	0.15	0.16	0.10	0.09	0.10	0.05	0.06
P3 (in m/h)	3,006	4,436	6,643	15,405	12,677	9,566	11,119	12,686

Especially catalysts AH, AI and AL show very high values for P3, which are up to five times higher than the value determined for catalyst C in subsection 4.5.4. This demonstrates the successful development of these catalysts, which was carried out as a final step by modifications in the TiO_2 base material quality, modifications of the promoter as well as the discovery of the superior properties of a newly introduced metal oxide. However, it has to be kept in mind that the P3 indicator weights all three reactions equally, which is not the case for all high-dust applications. When looking at the P3 indicator in the case of catalysts AK and AL, the conclusion could be misleading, especially if the Hg oxidation and SO_2/SO_3 conversion is not required for the catalyst application, for example at low catalyst operating temperatures or with secondary Hg reduction measures.

4.9 Single-reactions over plate-type catalysts

The second type of SCR catalyst with a high market share are plate-type catalysts as introduced in subsection 2.2.1. Especially in high-dust applications, when the fly ash content is very high or even erosive, plate-type catalysts might be advantageous compared to honeycomb catalysts. While the absolute numbers of the relevant test conditions area velocity and linear velocity are the same as for the honeycomb catalyst tests, the setup, due to the use of a catalyst holder, is slightly different and a direct comparison of honeycomb vs. plate is not possible in the framework of these

measurements. Thus, the plate catalysts as listed in table 4-18 are discussed separately from the honeycomb catalysts.

They can be characterized by catalysts with WO_3 support (catalyst AM) or with MoO_3 support (catalyst AN). Both catalysts have slightly higher vanadium content as at the studied honeycomb catalysts (e.g. catalyst I). As seen at the honeycombs, the ceramic mass of catalyst AN with molybdenum support shows a higher surface area. Catalyst AO has a special composition. In this catalyst, the *vanadia* content is tremendously increased and it seems to be poisoned by a high phosphor content.

Table 4-18: Chemical composition (bulk) of plate-type catalysts

	Unit	**Catalyst**		
		AM	**AN**	**AO**
$TiO_{2\ (bulk)}$	wt.-%	76.2	77.1	73.7
$SiO_{2\ (bulk)}$	wt.-%	11.0	12.9	14.2
$WO_{3\ (bulk)}$	wt.-%	5.2	1.0	0.0
$V_2O_{5\ (bulk)}$	wt.-%	0.8	0.7	3.3
Other $_{(bulk)}$	wt.-%	-	2.4 MoO_3	3.3 MoO_3, 2.6 P_2O_5
BET surface area	m^2/g	71.4	89.8	-
Average pore size	nm	13.6	11.0	-

4.9.1 Hg oxidation

All plate-type SCR catalysts show a relatively high Hg oxidation, as presented in figure 4-36. However, the result is partly caused by the relatively low clear width of the plate-type catalyst setup compared to the honeycomb catalysts as shown in figure 3-3, figure 3-4 and table 3-1. This results in a higher mass transfer to the catalyst's surface. Furthermore, just from visible inspection, the surface of plate-type catalysts has in general more surface disturbances like small cracks than honeycomb catalysts. These lead to further increased mass transfer due to small micro-turbulent zones in the catalyst, disturbing the laminar flow through the channel. Thus, higher Hg oxidation is measured with catalyst AN in comparison to honeycomb catalyst I with almost the same composition. In this plate catalyst composition, the previously found advantage of the molybdenum catalyst compared to the tungsten catalyst is not visible. Both catalysts show the same Hg oxidation result. The highest absolute result on all tests so far is reached for catalyst AO. Especially at very low HCl levels, the Hg oxidation stays high. The increase of Hg oxidation with lower HCl content shown in figure 4-36 can possibly be traced back to measurement errors and cannot be explained by any chemical or mechanistic reasons.

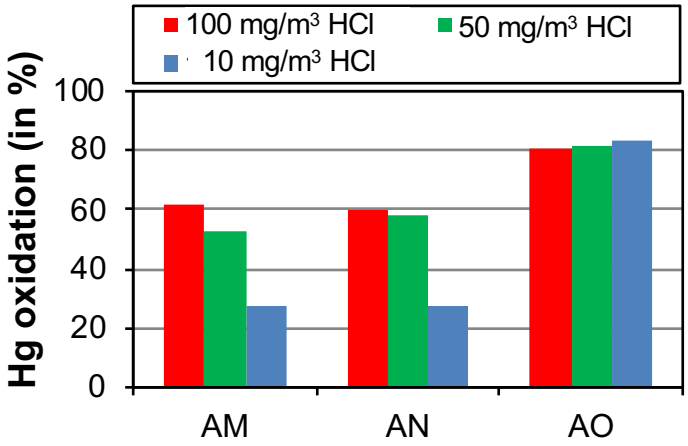

Figure 4-36: Hg oxidation of plate-type catalysts

The high Hg oxidation can be explained by the high *vanadia* content of the catalyst. As previously discussed in section 4.1 and as shown for example by Stolle [Stolle 2014], there is a strong influence of *vanadia* on Hg oxidation. Stolle measured an Hg oxidation of about 80% at a catalyst with about 2.5% V_2O_5, which is similar to the values measured here. The phosphorus in this catalyst seems not to decrease and deactivate the catalyst, which is different to the results presented in [152]. There, the effect of catalyst deactivation by phosphorus in the range of catalyst AO was synthetically applied on a new SCR catalyst with *vanadia* content comparable to catalyst C. The results showed significantly lower DeNOx activity and SO_2/SO_3 conversion but also significantly lower Hg oxidation. Possibly, in catalyst AO the phosphorus is applied in a special way as discussed for example in [194], or the tremendously increased *vanadia* content together with WO_3/MoO_3 pushes the Hg oxidation in catalyst AO. In the reaction model discussed by Neidig [194] for the TRAC® catalyst, a catalyst promoted with high Hg oxidation, high DeNOx activity and low SO_2/SO_3 conversion, a proprietary, not further specified α-component on the activated TiO_2 hinders SO_2 from reacting on the catalyst.

4.9.2 DeNOx activity

In figure 4-37, the DeNOx activity of the plate-type catalysts is shown. There is no big difference between the measured catalysts. All show high DeNOx activities, which are higher than the values measured for the honeycombs, which can be explained by some advantages in mass transfer under the chosen test conditions as discussed above. Slightly higher values for the catalyst AN vs. AM confirm the superior performance of the combination of WO_3 and MoO_3 in this catalyst also for the DeNOx activity, which causes or is supported by the higher surface area, which is crucial for the DeNOx activity taking place on the surface. The high value of AO can be explained by the higher *vanadia* content, providing more active surface sites for DeNOx activity.

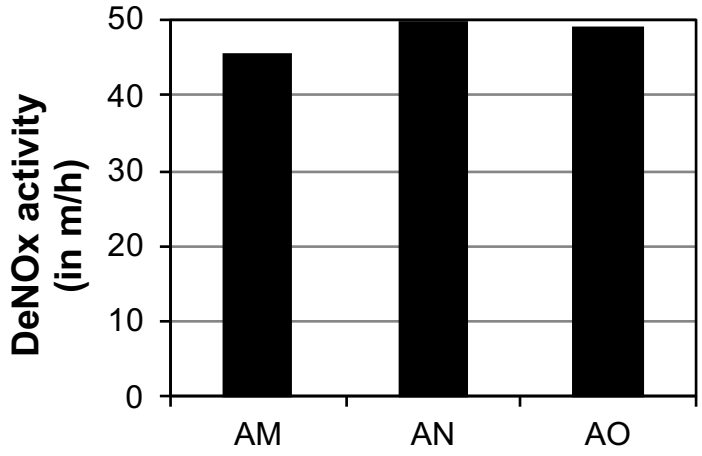

Figure 4-37: DeNOx activity of plate-type catalysts

4.9.3 SO_2/SO_3 conversion

The result for the SO_2/SO_3 conversion as presented in figure 4-38 also shows an advantage for catalyst AN under the chosen test conditions. Catalyst AM shows a significantly higher value of the SO_2/SO_3 conversion coefficient.

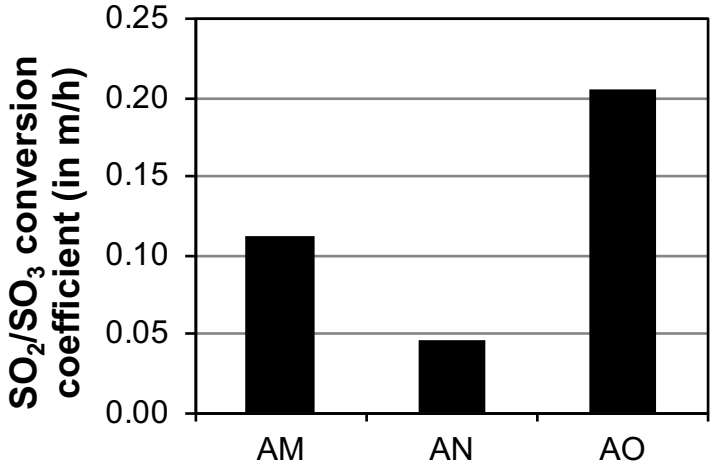

Figure 4-38: SO_2/SO_3 conversion of plate-type catalysts

The highest value is measured with catalyst AO. This can be explained by the very high *vanadia* content, which is tremendously higher than at the other catalysts. The suppression of the SO_2/SO_3 conversion by the α-component as discussed in Neidig [194] is only partially successful. The measured value is lower than the assumed value for the *vanadia* content in a "standard" catalyst, but it is still higher than at the two other plate-type catalysts.

4.9.4 Summary of the test series

Overall, the discussed values are also reflected in the calculated P3 value, as shown in table 4-19. The highest value is calculated for catalyst AN, indicating the best overall

performance under the chosen test conditions. It seems that in contrast to the properties discussed by Neidig [194], the catalyst AO has some advantages related to Hg oxidation, but also some significant disadvantages related to SO_2/SO_3 conversion, which makes this catalyst more ideal at lower flue gas temperatures and very low HCl content, in which low SO_2 concentration is present or no problems associated with SO_3 are expected.

Table 4-19: Performance indicator P3 of the plate-type catalysts

Catalyst	AM	AN	AO
K_{NOx} (in m/h)	45.6	49.7	49.1
K_{Hg} (in m/h)	26.5	25.1	45.0
K_{23} (in m/h)	0.11	0.05	0.21
P3 (in m/h)	10,763	27,379	10,763

4.10 Interaction mechanisms and influences on the reactions over SCR catalysts

The outcomes presented in the previous sections reflect the result of a standardized testing and catalyst screening under constant operating conditions, which is a good tool for catalyst characterization. However, in order to understand the behavior in the power plant installation, further experiments are carried out in which at selected catalysts the flue gas composition is varied.

4.10.1 Effect of SO_2 on NO_x activity

The NO_x reduction is the most important reaction at SCR catalysts. The test conditions for NO_x activity measurement include, as stated in section 3.6, sulfur dioxide (SO_2). The effect of SO_2 on the NO_x activity is discussed here. In figure 4-39, the NO_x activity over NH_3/NO ratio is shown for two fresh catalysts C and L, and for those two catalysts C and L that were previously exposed to SO_2 and thus conditioned before the test.

Both catalysts show a similar curve with slightly lower values for catalyst L. The result at the NH_3/NO ratio of 1.2 was previously shown in figure 4-14. The almost linear behavior of the curve is due to the DeNOx reaction, being a 1:1 reaction of NH_3 and NO under coal combustion conditions. The curve flattens out when the NH_3/NO ratio is >1 and NH_3 is present in excess.

While these slightly lower values for catalyst L can be explained by the different pitches of the catalysts as discussed in section 4.4, the differences between the solid and dashed lines directly reflect the influence of the SO_2. During exposure in flue gas with SO_2, the catalyst accumulates the SO_2 and surface sulfates are formed as discussed in subsection 2.2.2. These surface sulfates lead to increased surface acidity and thus an additional

anchor for the base ammonia. As a result, the DeNOx activity is increased and is significantly higher at fully conditioned catalysts than at fresh catalysts. A conditioning time of several days is necessary to achieve stable surface sulfates and the maximum extent of DeNOx activity in laboratory-scale and technical-scale tests [123].

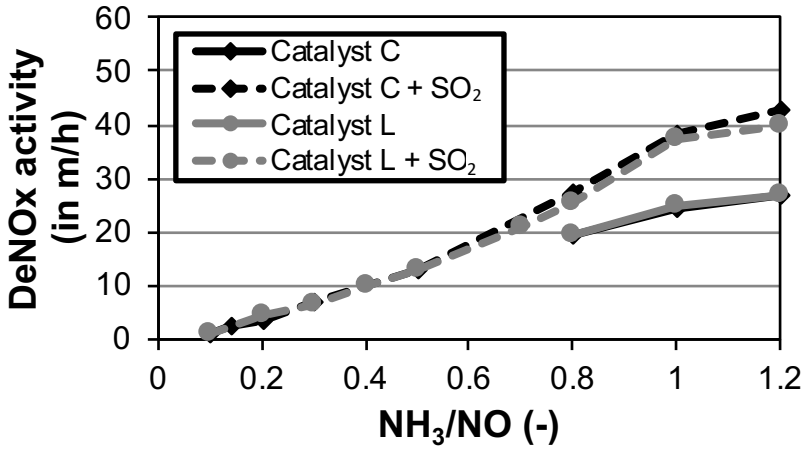

Figure 4-39: Effect of SO_2 on DeNOx activity studied with catalyst C and catalyst L

4.10.2 Effect of SO_2 and NO on Hg oxidation

All previous Hg oxidation screening and comparison tests were carried out without SO_2 and without NO. In the previous subsections, the effect of sulfation on DeNOx activity could be seen. Thus, in the following, Hg oxidation tests are carried out under SO_2 and NO atmosphere. Some 1,500 mg/m^3 SO_2 and 500 mg/m^3 NO are adjusted in addition to 50 µg/m^3 Hg and 50 mg/m^3 HCl. In figure 4-40, the results are shown for selected catalysts.

For the standard catalyst C and for catalyst H, a significant increase of the Hg oxidation is measured when NO and SO_2 are added. It seems that for the new catalyst AI, there is no difference, while there is a difference for AJ. There is possibly an error in the measurement of the tests since no other explanation can be given here. For the new catalyst AL with the addition of cerium, the Hg oxidation drops significantly.

At first glance, this measured increase in Hg oxidation with NO/SO_2 is in contrast to most of the published literature, e.g. the findings of Stolle [125] mentioned in section 2.3. Stolle discusses a negative influence of SO_2 on the Hg oxidation at SCR catalysts. However, most of the literature discusses the gas phase reactions, e.g. the Griffin-reaction, which consumes formed molecular chlorine in a reaction with SO_2, not taking mechanistic aspects in the catalyst into account. Li [135] measured the same effect as presented here. According to this result, it is assumed that the sulfation of the catalyst leads to an activation of the active sites as seen for the DeNOx activity also related to Hg adsorption. Since the new catalyst formulations are already quite active related to Hg oxidation, the benefit due to sulfation is smaller. In catalyst AL, unfortunately the active sites in the new

formulation with cerium are possibly deactivated when SO_2 is added due to the formation of cerium sulfates as discussed in the literature, e.g. in [195].

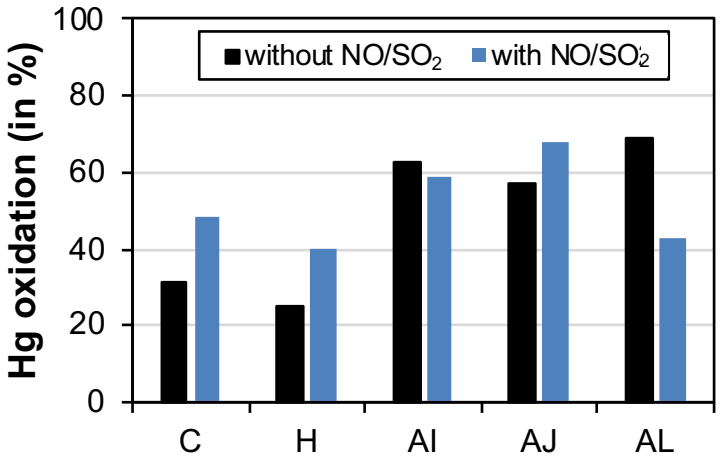

Figure 4-40: Effect of SO_2/NO on Hg oxidation at various SCR catalysts

4.10.3 Effect of parallel DeNOx reaction on Hg oxidation

Since the SCR catalysts are installed for NO_x reduction in flue gas in power plants, the influence of a parallel NO_x reduction over the catalysts on Hg oxidation is studied. It is commonly accepted that NO_x reduction takes place preferentially. According to the model by Thorwarth [80], the SCR catalyst can be divided into two zones, the first being a NO_x reduction zone, followed by an Hg oxidation zone. This was also researched by full-scale measurements of Gutberlet [79]. In figure 4-41, the effect of increasing the NH_3/NO ratio with catalyst L and catalyst C is shown. Starting from the point to the left with zero NH_3, which was discussed in the previous section, the injection of NH_3 is increased until the Hg oxidation is lower than 10%.

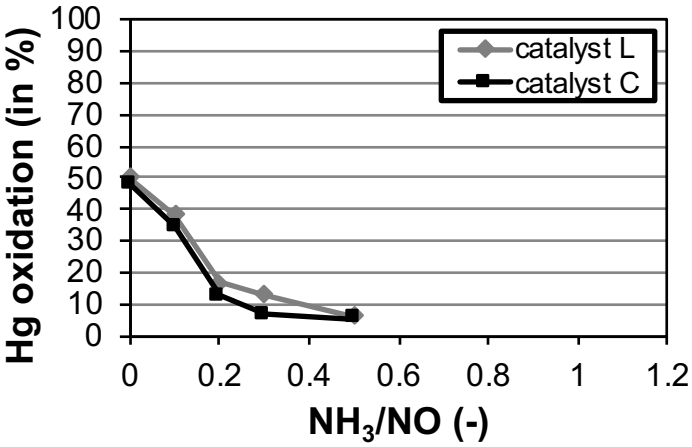

Figure 4-41: Effect of parallel DeNOx reaction on Hg oxidation at conventional catalysts (50 mg/m³ HCl, 1,500 mg/m³ SO_2, 500 mg/m³ NO)

In this measurement, catalyst L with an increased pitch and wall thickness shows slightly higher results compared to catalyst C with 7 mm pitch. The curves for some of the new SCR catalysts are shown in figure 4-42. Due to the previously described effect of SO_2, the curve for catalysts AJ and AL are shown with and without the addition of SO_2.

In all of the curves, there is a strong inhibiting effect of the parallel proceeding DeNOx reaction measured under the chosen test conditions. Only for catalyst AJ (w/o SO_2) is the inhibition less compared to the other catalysts and even at an NH_3/NO ratio of 0.8, there is still 40% Hg oxidation.

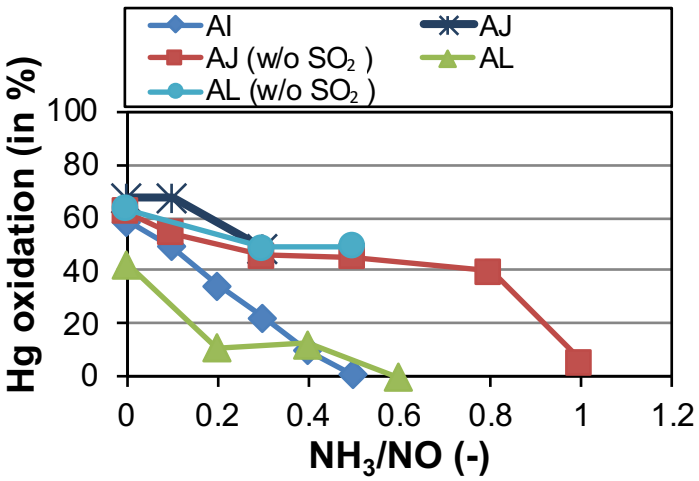

Figure 4-42: Effect of parallel DeNOx reaction on Hg oxidation at the newly developed SCR catalysts AI, AJ and AL with and without SO_2 (50 mg/m³ HCl, 1,500 mg/m³ SO_2, 500 mg/m³ NO)

The effect of the inhibition by ammonia can be explained by a preferential adsorption of ammonia on the active acid sites compared to mercury, which is possibly only weakly adsorbed. Since the DeNOx reaction can be described as an Eley-Rideal mechanism [116] and since the Hg oxidation seems to also be of that type or a Mars-Maessen type, this assumption can describe the measured phenomenon very well. Due to the relatively high area velocity in the catalyst in the experiment, there is no space and time left for the Hg oxidation reaction. This result confirms the previously mentioned zones, e.g. in [80], for the DeNOx reaction and Hg oxidation, meaning that at these conventional SCR catalysts, there is a need for a specific (additional) Hg oxidation layer where no ammonia is left.

It also has to be borne in mind that the result measured here is only a sum of the back and forth reaction, meaning it reflects not only the Hg oxidation but also a possible Hg reduction in flue gas, either in the gas phase or in the catalyst. The numbers represent the net sum of the two reactions. Within this work, the focus is set on Hg oxidation, meaning the oxidation of elemental mercury. Studying the addition of only oxidized mercury would present the share of the back reaction. As also described by Hocquel [66] and Thorwarth [80], there is directly a reduction of already formed $HgCl_2$ in the flue gas, reducing the net percentage of oxidized mercury. A possible back reaction with ammonia as discussed for example by Stolle [125] can be written as:

$$6NO + 6NH_3 + 3HgCl_2 \rightarrow 6N_2 + 3Hg^0 + 6HCl + 6H_2O$$ equation 4-4

Madsen [81] discussed an additional reaction equation, which has an even greater negative reaction enthalpy compared to reaction equation 4-4:

$$6NH_3 + 3HgCl_2 + 3O_2 \rightarrow 3N_2 + 3Hg^0 + 6HCl + 6H_2O$$ equation 4-5

Both reactions are strongly favored under the high-dust SCR operating conditions. Thus, there is a relevant contribution of these reactions to the net Hg oxidation over the catalyst, which is the sum of the Hg oxidation according to the reactions discussed in section 2.2.6 and the reduction of already formed $HgCl_2$ described in the reactions.

Since most of the new catalysts show higher overall Hg oxidation in the presence of NH_3, this is traced back to the higher Hg oxidation at a NH_3/NO ratio of 0, at which the test series started. The higher Hg oxidation at a NH_3/NO ratio of 0 can be explained by a small partial oxidation of NO to NO_2, which acts as an oxidizer. The above-mentioned reactions in the gas phase are also assumed to be first order, meaning a higher Hg reduction when the Hg^{2+} concentration is higher. Since the Hg oxidation in catalyst AJ is overall higher, the lower calcining temperature at this catalyst led to the formation of different active sites, as discussed for example by Kobayashi [196], which are not that sensitive to occupation by ammonia compared to the standard ones, e.g. in catalyst C. This makes catalyst AJ also suitable for installation in the first layer of a full-scale reactor, which implies some benefits regarding the overall Hg oxidation compared to a standard SCR catalyst as catalyst C. A similar catalyst and approach was discussed by Bertole [197], who showed the benefit of an advanced catalyst compared to a traditional catalyst. With catalyst AL, the effect of NH_3 in the absence of SO_2 seemed to be the same as in catalyst AJ. However, with the addition of SO_2, these additional active sites were blocked and the Hg oxidation drops significantly when ammonia is added. This sulfur poisoning puts the result of section 4.8 into perspective, leading to the conclusion that currently only an installation in very low sulfur applications would be good for the application of catalyst AL. There is a need to further develop catalyst AL in order to be more sulfur resistant. Possible approaches are discussed in [198].

4.10.4 Effect of CO on Hg oxidation

Carbon monoxide (CO) as a product of incomplete combustion is also present in the flue gas of coal-fired power plants. Depending on the degree of combustion optimization, the concentration can be up to 200 mg/m³ for large combustion plants according to [20]. In figure 4-43, the Hg oxidation with varied flue gas CO content is shown with catalyst C. There is a strong and significant inhibition of Hg oxidation due to CO in the flue gas. The pre-conditioned, meaning previously sulfated catalyst C, shows at zero CO a result between the results presented in figure 4-30 and in figure 4-40, which can be explained by the NO- and SO_2-free flue gas and the previous sulfation of the catalyst.

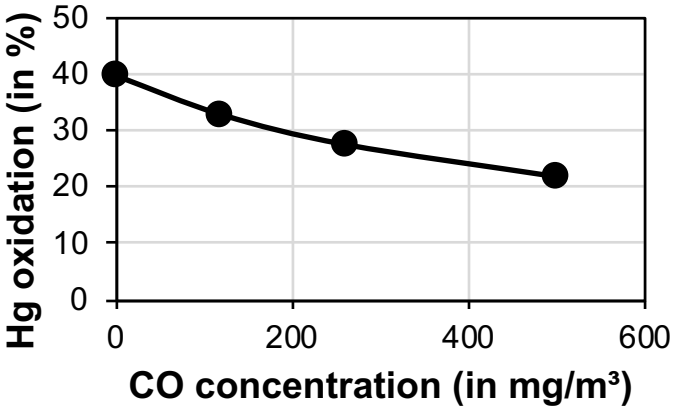

Figure 4-43: Hg oxidation with varied CO concentration in flue gas (standard conditions, 100 mg/m³ HCl)

When the CO concentration is further increased, the Hg oxidation is further lowered until at 500 mg/m³ CO only half of the initial Hg oxidation is measured. This can be explained by the reducing reactions of carbon monoxide with oxidized mercury as shown in equation 4-6.

$$CO + HgCl_2 + H_2O \rightarrow CO_2 + Hg^0 + 2\,HCl \qquad \text{equation 4-6}$$

This was also measured by Tong [136] and Bertole [197]. The results presented here reflect more the lower HCl result in [197], which might be explained by a relatively high area velocity of the standard conditions in this work compared to the test conditions of [197]. Furthermore, Presto [Presto 2006] discussed the formation of carbonyl chlorides, reducing the availability of chlorine for Hg oxidation. In full-scale application when CO is present, the overall net Hg oxidation will be lower compared to laboratory experiments. However, regarding the NO_x reduction in power plants at V_2O_5-WO_3/TiO_2 catalysts under excess oxygen, carbon monoxide does not serve as a reducing agent for nitrogen oxides. High amounts of carbon monoxide in flue gas are frequently associated with a bad burnout in the combustion zone, which leads to higher carbon levels in the ash and lower plant efficiency. Since unburned carbon is quite an effective mercury sorbent [29], plants with very high carbon monoxide higher than previously discussed and bad burnout will probably not have noteworthy mercury emissions at the stack.

4.10.5 Effect of oxygen content on Hg oxidation

In figure 4-44, the Hg oxidation of catalysts AP and AQ is shown with varied oxygen contents. The measurement was carried out at a very low HCl concentration of 5 mg/m³, reflecting a lack of HCl. Curves of other catalysts with more or less the same chemical composition with increased *vanadia* content show the same shape. Similar to the behavior with HCl, which has an effect on the turnover in the catalyst despite its vast excess, there is also the dependency of the oxygen content of the flue gas. This can be seen in the overall reaction equation as shown in equation 2-9. It was found that oxygen

plays a role in the Hg oxidation reaction. This is in contrast to the results of Li [135] and Madsen [81], who both found no effect of oxygen on Hg oxidation at concentrations higher than 4% O_2. In the results presented here, there is an increase in Hg oxidation measured over the whole range of oxygen content, which is in line with the results by [197]. For the catalyst AP, there is a continuous increase of the Hg oxidation with increasing oxygen content, while for catalyst AQ a saturation point is approached.

There are two ways how oxygen could interact in the Hg oxidation reaction: First, directly in the reaction. Possible pathways, like the Deacon-reaction or Eley-Rideal reaction, were discussed in section 2.2.6. Second, in the re-oxidation step of the active sites, which is especially included in the Mars-Maessen reaction. The new catalyst formulations show a huge oxygen storage capacity due to modified active sites of the catalyst. Especially in the case of cerium oxide, there is some kind of oxygen reserve in the event of a lack of oxygen.

Table 4-20: Chemical composition of catalyst AP and AQ

	Unit	Catalyst	
		AP	AQ
$TiO_{2\ (bulk)}$	wt.-%	80.0	70.0
$SiO_{2\ (bulk)}$	wt.-%	6.1	11.6
$WO_{3\ (bulk)}$	wt.-%	7.7	7.6
$V_2O_{5\ (bulk)}$	wt.-%	0.4	2.0

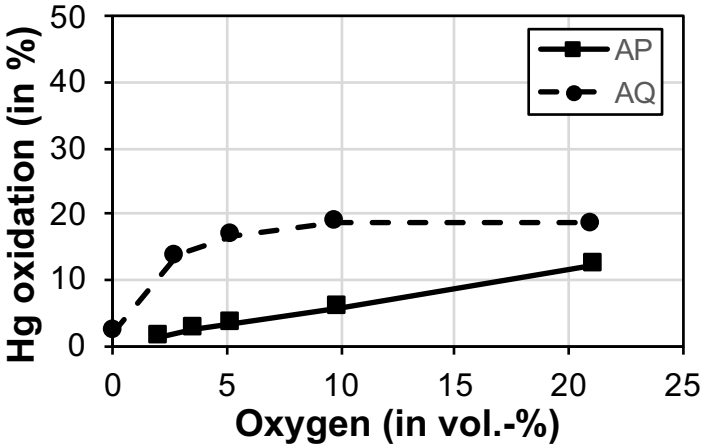

Figure 4-44: Hg oxidation of catalysts AP and AQ measured at varied oxygen content (HCl: 5 mg/m^3)

The oxygen storage capacity can be seen with catalyst AQ, a “standard” catalyst with increased *vanadia* content, which shows over several hours some Hg oxidation even with no oxygen present. For the DeNOx activity and the SO_2/SO_3 conversion, over a certain threshold of about 1%, there is no effect of oxygen measured [119]. The measured dependency for the Hg oxidation reaction from the oxygen content is also a further indicator for a reaction in the bulk since due to the increased partial pressure of oxygen deeper pores are re-oxidized and can take part in further reactions. This can be seen comparing catalysts AP and AQ. While for catalyst AQ enough re-oxidized active sites are available and the low HCl content in the experiment is the limiting factor, in catalyst AP with increased oxygen content, more and more re-oxidized active sites are available.

4.10.6 Effect of different halogens on Hg oxidation with the addition of SO_2

As discussed in subsection 2.1.3, chlorine is not the only halogen present in coal. Bromine is also present, which as discussed in subsection 2.1.4 has an effect on the chemical equilibrium in flue gas. In order to study the effect on the Hg oxidation over the catalyst under the chosen test conditions, various halogen combinations in flue gas are tested. All the tests are carried out with catalyst AI and are shown in figure 4-45. The curve with 50 mg/m^3 HCl represents the reference curve as already shown in figure 4-42. For the measurements of the dashed curve, as halogen 0.5 mg/m^3 HBr is present in the synthetic flue gas. The pointed curve is gained by adding a halogen concentration of 0.15 mg/m^3 HBr and 50 mg/m^3 HCl, representing the bromine to chlorine ratio as it is found in brown wood pellets as listed in the reference discussed in table 2-3.

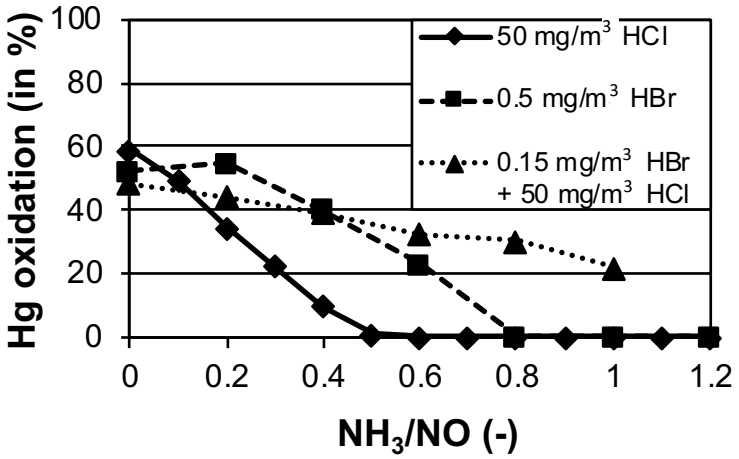

Figure 4-45: Effect of different halogen concentrations in flue gas on Hg oxidation with varied NH_3/NO ratios (with the addition of SO_2)

As can be seen in the diagram, the 100-fold lower bromine concentration in flue gas is even more powerful regarding Hg oxidation than the chlorine. From equilibrium calculations, as shown for example in [60], it can be seen that the chemical equilibrium is more on the side of the oxidized Hg species in the case of bromine than it is for chlorine. This brings to mind the bromine-Deacon and bromine-Griffin-reactions, as discussed in section 2.1.4. Since these tests presented here are carried out with the addition of SO_2, the bromine-Griffin-reaction (equation 2-12) would mean a possible consumption of molecular halogen.

According to theoretical equilibrium calculations [60], chlorine is more consumed than the molecular bromine, leading to higher Hg oxidation due to the availability of the highly active Br_2. However, the Deacon reaction is only one of the discussed reaction pathways, as reviewed in section 2.2.6. Assuming a pure Deacon-reaction, this would not include any of the aspects discussed in the previous sections, especially the adsorption of mercury (e.g. as shown in section 4.2). It is therefore assumed that the catalyst supports the shift

to reach equilibrium in the case of $HgBr_2$ more than in the case of $HgCl_2$. The shift towards $HgBr_2$ is inhibited by ammonia to a lower extent. An even more reduced bromine concentration in combination with chlorine results in a similar Hg oxidation at low NH_3/NO ratios as with the higher bromine concentration. It seems that there is a threshold of bromine concentration similar to the dependency on HCl content described in subsection 4.3.1, but on a very much lower concentration level. The combination of the two halogens leads to a benefit at high NH_3/NO ratios. These two halogens possibly interact and displace ammonia from the active sites, leading to an overall increased Hg oxidation.

The Br/Cl ratio of 0.3%, which is applied in this test simulating wood pellets, reflects a standard or even low bromine ratio of coal, as can be seen in table 2-3 and is discussed by [199]. As described by Vosteen [199], the native Br content in US coals is about 1-4% of their native chlorine content. Concluding the results presented here, the Hg oxidation is highly favored at SCR catalysts when there is a small bromine content in coal, which is normally naturally occurring or can be achieved by dedicated blending of coals from different origins.

4.10.7 Halogen transformation over SCR catalysts and effect of direct molecular halogen addition

As discussed in the previous section and in subsection 2.2.6, molecular halogen might play a role at SCR catalysts in the framework of the Deacon-reaction. A prerequisite and important step in Hg oxidation according to the Deacon mechanism would be the formation of molecular chlorine in the catalyst. As described in section 3.1.5, a method is developed selectively measuring the molecular halogen. The test is carried out with catalyst C and an HCl solution is added upstream of the catalyst in a concentration which could theoretically result in 1,181 mg/m³ Cl_2 in the flue gas (80% turnover of 1,476 mg/m³ according to equilibrium at 380°C). It is repeated, denoted by “test 1” and “test 2”. Flue gas is collected over several hours. The result is presented in figure 4-46.

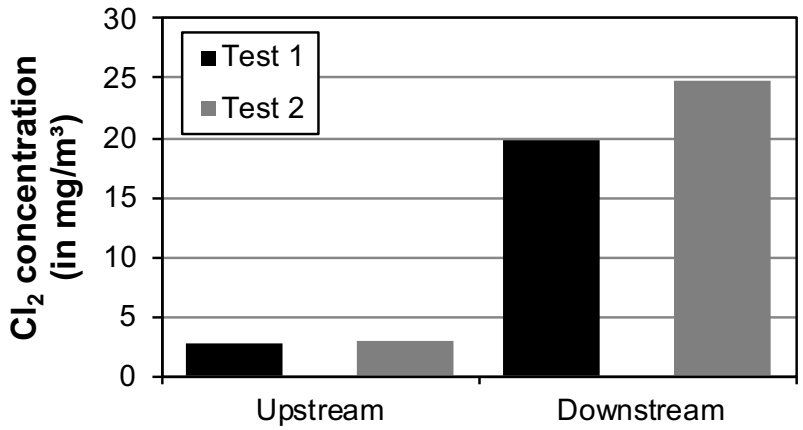

Figure 4-46: Result of selective Cl_2 measurement upstream and downstream of catalyst C at 380°C

The test indicates an increase in molecular chlorine over the catalyst. This is an indicator for the Deacon reaction taking place in the catalyst. Looking at the overall numbers of molecular chlorine measured, the overall turnover of HCl according to equation 2-10 is quite low, less than 3%. Comparing the pure amount of Cl_2 molecules measured in the experiment with the Hg concentration applied in the tests for Hg oxidation, the measured Cl_2 concentration is higher and would theoretically be sufficient for a complete oxidation of elemental mercury downstream of the catalyst according to equation 2-11.

The results confirm the laboratory results of Gutberlet [79], who also found chlorine when different DeNOx catalysts are exposed to a mixture of hydrogen chloride and air. However, the formation of molecular chlorine is only the first step in the Hg oxidation. For the second step, according to equation 2-11, the molecules present in very low concentration in the flue gas must meet the reaction partner. The effect of Cl_2 vs. HCl is presented in figure 4-47. In this experiment, the Hg oxidation test is carried out as in the experiments discussed previously but with the addition of Cl_2 instead of adding HCl upstream of the catalyst. In the diagram, the oxidized Hg is shown upstream and downstream of the catalyst in both experiments. It has to be mentioned here, that the share of Hg^{2+} upstream of the catalyst as shown in this diagram was only in this experiment so high. In the "standardized" screening tests of Hg oxidation as discussed previously, the Hg^{2+} upstream of the catalyst was always < 5%.

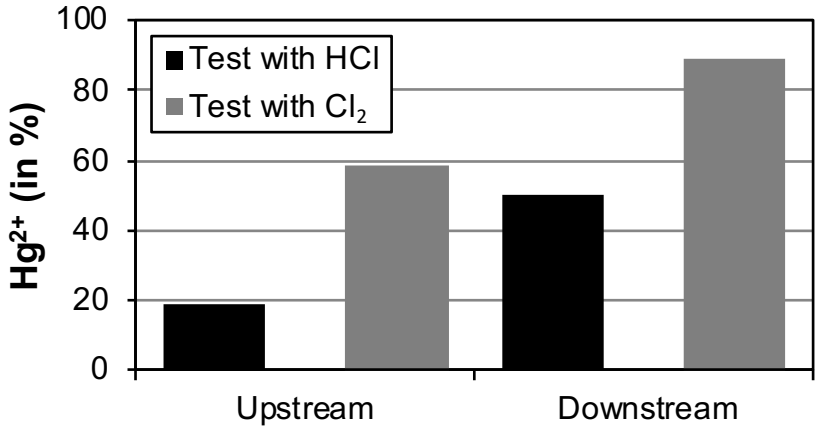

Figure 4-47: Oxidized Hg upstream and downstream of catalyst C when carrying out the standardized test with HCl in comparison to direct Cl_2 addition (both: 100 mg/m^3) at a temperature of 380°C

The results clearly indicate the advantage and the faster reaction kinetics of the reaction of mercury with molecular chlorine in comparison to the hydrogen chloride. As published by Seigneur [200], the reaction rate is three magnitudes higher for Cl_2.

There is a large share of oxidized mercury already upstream of the catalyst with Cl_2 added, indicating the homogeneous nature of the Hg oxidation with Cl_2. Over the catalyst, there is a further increase in oxidized Hg, which might possibly be favored by the catalyst. However, since compared to the reactor diameter the channels of the catalyst are quite narrow, the flow especially at the inlet of the catalyst becomes turbulent, leading to a

further increase in the homogeneous reaction, since the probability of the two reaction partners meeting in the gas phase is increased. Thus, there is no clear indication of the heterogeneous benefit when Cl_2 is added upstream of the catalyst.

4.10.8 Inhibition of SO_2/SO_3 conversion by ammonia

Not only is the oxidation of Hg influenced by the addition of other flue gas components, but also the conversion of SO_2/SO_3. The most relevant flue gas component which has not so far been discussed is ammonia. The results of the SO_2/SO_3 conversion in the previous sections represent the last layer of a large SCR reactor in which there is no ammonia present, since it was consumed already in the upstream layers. The diagram in figure 4-48 shows decreasing SO_2/SO_3 conversion with increasing NH_3/NO ratio, covering almost the whole range of NH_3/NO ratio of a full-scale power plant. In parallel, the DeNOx activity increases until the stoichiometric ratio of $NH_3/NO = 1$ is reached.

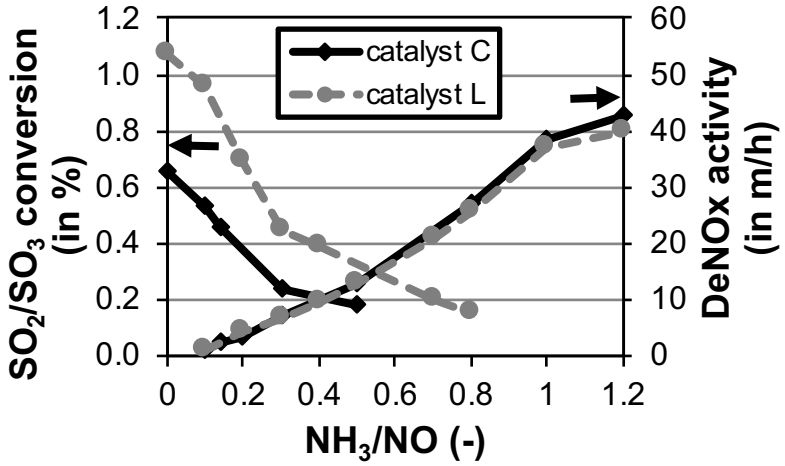

Figure 4-48: SO_2/SO_3 conversion with increasing NH_3/NO ratio with catalysts C and L

The SO_2/SO_3 conversion of catalyst C at $NH_3/NO = 0$ in these results is slightly higher than the result for catalyst C as presented in section 4.5.3 as SO_2/SO_3 conversion coefficient or in figure 8-1 in the annex (κ_{23} = 0.54 %). This can be explained by the oxidation of SO_2 by nitrogen oxide [201]. Similar to the Hg oxidation, the SO_2/SO_3 conversion decreases when the NH_3/NO ratio is increased. Due to the relatively high area velocity, the decrease is quite strong, meaning that the SO_2/SO_3 conversion is only one third of the starting value at a NH_3/NO ratio of 0.4.

For catalyst L, the shape of the curve is similar, with a higher starting value due to the wall thickness as described in section 4.4. The results support more the strong exponential decrease of the SO_2/SO_3 conversion as described by Svachula [119] than the results of Orsenigo [201], who found only a slight decrease of the SO_2/SO_3 conversion, with a strong decrease around $NH_3/NO = 1$, leading to two different regimes for $NH_3/NO < 1$ and $NH_3/NO > 1$. The mechanism can be explained by the occupation of the active sites with

ammonia, which are then blocked for the reaction with SO_2. Since the catalysts are able to accumulate both ammonia and SO_2, it can be seen that the adsorption of ammonia is also strongly favored compared to sulfur dioxide, as it was shown in section 4.10.3.

The DeNOx activity as shown in figure 4-48 increases linearly with increasing NH_3/NO ratio as it is expected until the stoichiometric ratio of NH_3/NO = 1 is reached. A further increase of the NH_3/NO ratio leads only to a slight increase of the activity due to a better distribution of NH_3 over the small sample in the micro-reactor test. Thus, the DeNOx activity was determined at a NH_3/NO ratio of 1.2 in the previous sections, reflecting the maximum DeNOx activity of the respective samples.

In figure 4-49, the SO_2/SO_3 conversion of two of the new catalysts with increased Hg oxidation performance is shown with and without the addition of NH_3. This reflects a last-layer (NH_3/NO ratio α = 0) and middle-layer approach (NH_3/NO ratio α = 0.3) of a full-scale unit. Due to the experience in the previous tests with catalyst C, this middle-layer test point was chosen in order to measure any SO_2/SO_3 conversion, which might be the case in the first layer with a higher NH_3/NO ratio.

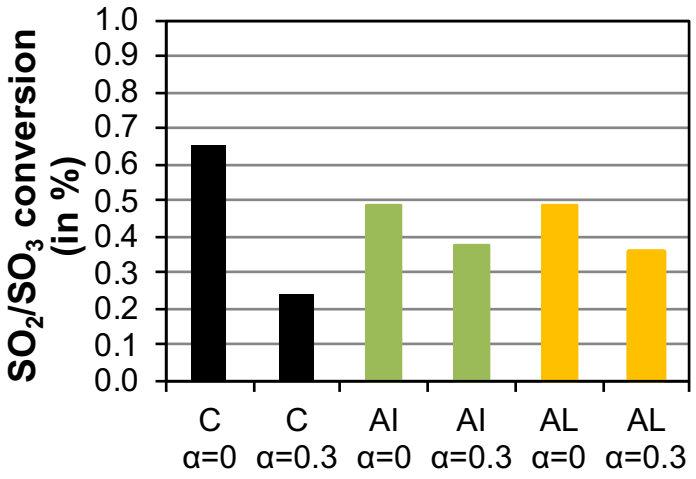

Figure 4-49: SO_2/SO_3 conversion of new SCR catalysts with/without the addition of NH_3

The result shows for catalysts AI and AL an increased SO_2/SO_3 conversion at NH_3/NO = 0, compared to the results presented in section 4.8.3 (as SO_2/SO_3 conversion coefficient), supporting the previously described promoting effect of nitrogen oxide on SO_2/SO_3 conversion.

Nevertheless, the SO_2/SO_3 conversion remains lower for these new catalyst formulations compared to the standard catalyst C. For catalyst AL, the promotional effect of Ce^{3+} on the SO_2/SO_3 conversion as described in [140] could not be measured. On the other hand, the observed deactivation of the catalyst by SO_2 (when measuring the Hg oxidation in section 4.10.2) could not be seen when measuring the SO_2/SO_3 conversion. Since the SO_2/SO_3 conversion measurement takes place over several hours up to days, it can be confirmed

that the catalyst is still moderately active related to SO_2/SO_3 conversion. However, obviously the inhibition of the SO_2/SO_3 conversion of the new catalysts by ammonia (at the measured point $NH_3/NO = 0.3$) is less distinct than for the standard catalyst, which confirms the good oxidative properties of the catalysts even under inhibiting conditions.

5 Results and discussion for real flue gas in the lab-scale firing system

Following on from the measurements for synthetic flue gas as described in chapter 4, in this chapter, measurements in real flue gas atmosphere of a lab-scale firing system as described in section 3.4 are carried out and discussed. This is directly linked to the previously discussed catalyst test and completes the catalyst tests related to their application in real flue gas atmosphere.

The lab-scale firing system is operated continuously for several hours under the conditions presented in section 3.7 in order to carry out the catalyst tests. The flue gas composition under ideal operation is shown for coal in figure 5-1 and for the 80C/20B mixture of a different coal and biomass in figure 5-2.

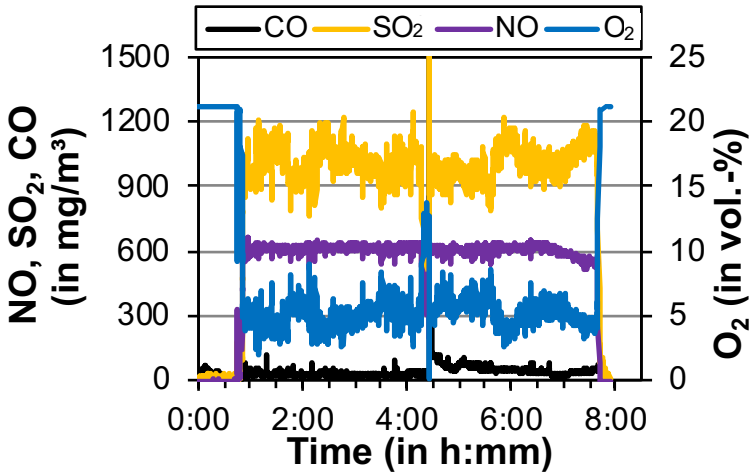

Figure 5-1: Flue gas composition when burning 100% coal

For the fired hard coal, an SO_2 concentration of about 1,000 mg/m^3 is measured. The NO concentration (only measured and given as nitrogen monoxide) is 600 mg/m^3; CO is during most of the time lower than 50 mg/m^3.

For the combustion of the 80C/20B mixture, the SO_2 concentration is lower at about 700 mg/m^3 due to lower sulfur content in fuel. There is a slightly higher NO concentration with the biomass co-combustion, which could be explained by increased thermal NO_x formation since the fuel-nitrogen content is in fact lower in the fuel mixture. The CO concentration is higher and slightly below 200 mg/m^3. This is explained by the burnout, which is slightly worse due to the increased particle size of the biomass. The residence time in the drop-tube furnace is not enough for a complete burnout of the biomass particles.

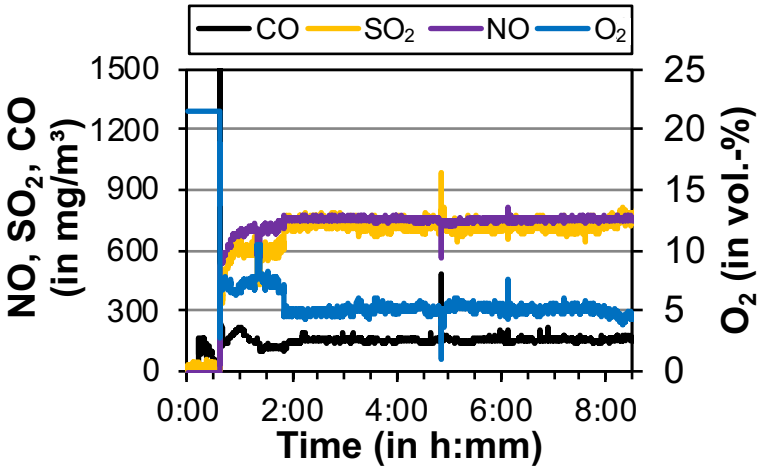

Figure 5-2: Flue gas composition when burning 80% coal/20% biomass

5.1 DeNOx activity measured in real flue gas atmosphere

The DeNOx activity is determined at the standard test point as listed in table 3-4 for catalyst C. In combination with the NO_x reduction measurement, the NH_3 slip is measured, which should be directly linked to the DeNOx activity. The measurements should under ideal conditions theoretically result in a closed mass balance (NH_3 slip in percent $(\alpha-\eta)/\alpha$), see equation 3-9 and equation 3-10). The tests are carried out at different flue gas temperatures and NH_3/NO ratios and are shown in figure 5-3 and figure 5-4.

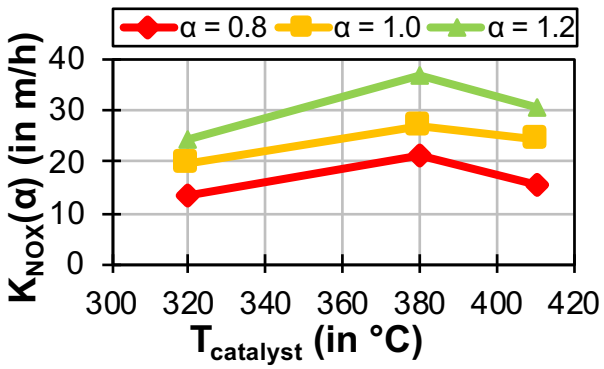

Figure 5-3: DeNOx activity of catalyst C at different temperatures tested under various NH_3/NO ratios (α)

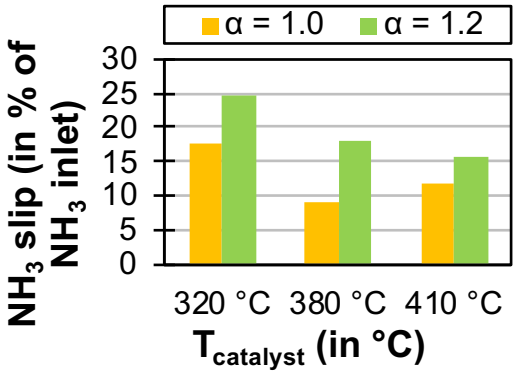

Figure 5-4: NH_3 slip given in percent of the inlet NH_3 concentration

The DeNOx activity shows a maximum at 380°C, with lower values at 320 and 410°C. This is a common standard high-dust SCR phenomenon as described for example in [202] and [203] and is also reflected in the NH_3 slip values. However, at 410°C, the results indicate lower DeNOx activity and NH_3 slip, which would lead to the conclusion that part of the ammonia is oxidized and thus higher NO and lower NH_3 values are present. According to

the literature [104], the ammonia oxidation only starts at 400°C and should be suppressed by WO_3, which is included in catalyst C. Another reason for the lower NH_3 slip for α=1.2 at 410°C as shown in figure 5-4 compared to the value at 380°C could be the NH_3 measurement, which showed the lowest recovery in view of the theoretical value. The general temperature behavior can be explained by the NH_3 adsorption on the surface of the catalyst, which is lower at higher temperatures. At lower temperatures, the adsorption is favored, but on the other hand there is a lack of reaction energy for the full DeNOx reaction to take place at this standard formulation of catalyst C. Thus, for low temperature, e.g. in low-dust or tail-end applications, totally different catalyst formulations with higher active material content are used, which further lowers the activation energy of the DeNOx reaction.

The experiments in the lab-scale firing system were planned to be carried out at NH_3/NO ratios of 0.8, 1.0 and 1.2. However, the NO_x concentration in the flue gas of the lab-scale firing system fluctuates at the catalyst inlet and unlike in full-scale power plants, the NH_3 is not adjusted automatically in the lab-scale firing system. Thus, after the experiment, the actual NH_3/NO ratio is calculated and the DeNOx activity in figure 5-5 shown over the actual NH_3/NO ratio. It can be seen that catalyst Y shows slightly higher NO_x activity than catalyst C. This also reflects the results discussed in section 4.6. The difference between these catalysts is not that high and the additional *vanadia* content of catalyst Y does not show any benefit at the standard temperature of 380°C. Both catalysts were measured with the same ammonia injection grid of the lab-scale firing system. However, although the system was previously optimized, the DeNOx activity still increases with NH_3/NO ratios higher than one. This is an indicator that additional NH_3 brings further benefits due to a possibly uneven distribution of ammonia over the catalyst's channels.

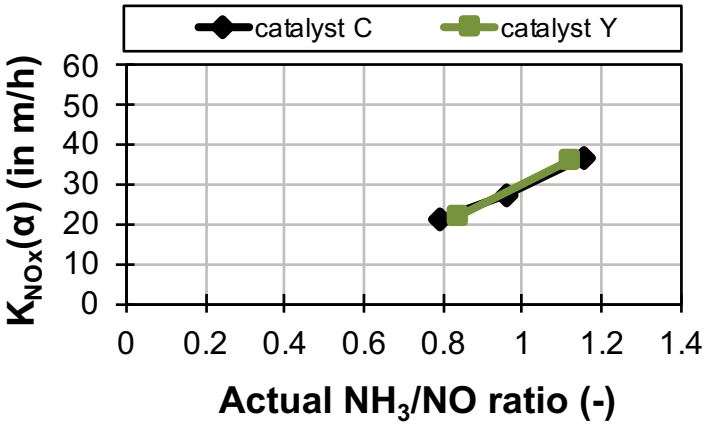

Figure 5-5: DeNOx activity measured in real flue gas (coal combustion) with catalyst C and catalyst Y at 380°C

Figure 5-6 shows the variation of the area velocity with catalyst C measured at two different NH_3/NO ratios. There is a clear trend of increasing DeNOx activity with increasing area velocity at both measured NH_3/NO ratios. Thus, the DeNOx activity is not

constant at varying area velocities, as also shown by Hilber [203]. As discussed in section 2.2.3, the external mass transfer increases with the velocity in the channels. The lower turnover due to reduced residence time by increased area velocity (at constant catalyst geometry) is compensated by the increased mass transfer. The longer catalyst samples tested in the lab-scale firing system and the lower AV during the tests enable the observation of this effect, which could not be seen during the micro-reactor tests, e.g. in section 4.4.

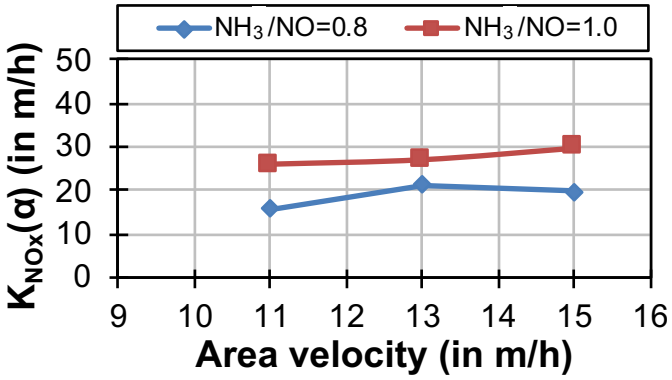

Figure 5-6: Effect of the variation of the area velocity (AV) on the DeNOx activity with catalyst C tested at 380°C

The DeNOx activity is furthermore measured with different fuels as shown in figure 5-7. In addition to the tests with coal, measurements with biomass and biomass-coal mixture are carried out as shown in figure 5-7. The differences in DeNOx activity in the diagram can be explained by mathematical reasons of the calculation of the DeNOx activity in combination with measurement errors. The logarithm in the DeNOx activity calculation (equation 3-11) trends towards infinity when 1 - η approaches zero at high NO_x reduction. Thus, relatively small changes in NO_x reduction of about 1% (abs.) lead to a change in DeNOx activity of 2-3 m/h. A direct influence on the DeNOx activity resulting from the fuel can be excluded.

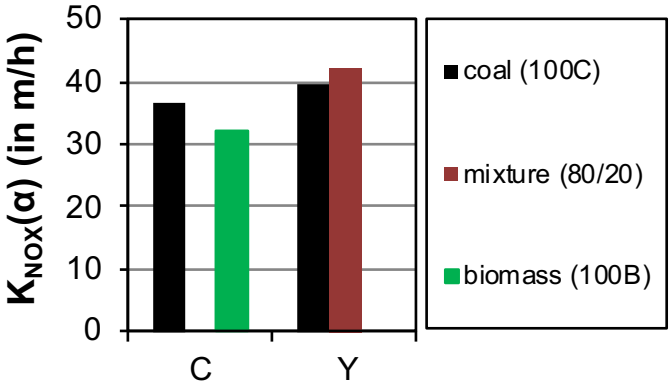

Figure 5-7: DeNOx activity measured at the two catalysts C and Y under different flue gas atmospheres

The fuels coal, biomass and the mixture simulating co-combustion result in different raw NO_x concentrations due to the primary NO_x formation (fuel NO_x and thermal NO_x). While for biomass the nitrogen oxide concentration (NO) is only about 200 mg/m^3 (STP, dry), the mixture results in a NO concentration of as high as 800 mg/m^3 (STP, dry). When adding ammonia in a NH_3/NO ratio of 1.2, concentrations below 25 mg/m^3 are measured. As discussed by Nova [95] on the basis of results generated in synthetic flue gas atmosphere, there is no influence of the nitrogen oxide concentration on the NO_x reduction (NO_x reduction is of first-order kinetics regarding NO_x concentration). However, small changes in NO_x concentration measurement in the range of 25 mg/m^3 NO result in big changes in DeNOx activity as discussed above.

The experiment reflects only a short-term test of the catalyst's behavior in flue gas generated by combustion of different fuels over several hours or days. The long-term behavior and catalyst deactivation can be different in the atmosphere of different fuels due to catalyst deactivation. Especially in flue gas of biomass combustion or co-combustion, under high-dust catalyst conditions significant sodium and potassium aerosol concentrations are found, which will over long periods of time like several thousands of hours result in severe catalyst deactivation. Beck [100] discussed the catalyst deactivation by phosphorus from the co-combustion of sewage sludge and meat and bone meal, which takes place by the penetration in the surface of gaseous phosphorous, leading to a chemical deactivation of the active sites. Furthermore, the co-combustion of phosphorous and alkalis containing fuels like biomass results in sometimes very fine ash particles < 1 µm, which lead to a blocking or masking of the porous system. Zheng [204] found a chemical deactivation in SCR catalysts in a combined heat and power plant firing straw and wood, which was explained by the reaction of the Brønsted acid sites of the catalyst with potassium compounds originating from the fuel.

5.2 SO_2/SO_3 conversion studies in the real flue gas atmosphere

In addition to the DeNOx activity, as with the micro-reactor studies in chapter 4, the SO_2/SO_3 conversion is measured at selected catalysts C and Y, in order to follow a holistic approach covering all relevant parameters for application.

The influence of temperature studied on the lab-scale test rig in comparison to the micro-reactor result is shown in figure 5-8. The SO_2/SO_3 conversion of catalysts C and Y are measured in real flue gas atmosphere and compared to the result presented in subsection 4.6.3 which was measured in the micro-reactor test. It has to be noted that all results are calculated at an AV of 13 m/h in order to have the same area velocity and the same basis for comparison. As already shown in subsection 4.6.3.4 in the micro-reactor, there is also an exponential increase in the SO_2/SO_3 conversion measured in the real flue gas by

increasing temperature. However, comparing catalyst C measured in the lab-scale test rig and on the micro-reactor, a difference can be seen. This can be explained by the fly ash separation during the measurements in the lab-scale test rig. For example, calcium oxide (CaO) reacts with SO_3, forming $CaSO_4$, which is also applied in semi-dry flue gas desulfurization. Extensive studies on interactions of fly ash and filter materials was made in [205], leading to the conclusion that only quartz wool (pure silica) can be applied for fly ash filtration. Glass wool with other constituents like calcium or sodium leads to an additional bias of the results. Another method for sampling with reduced interaction of the SO_3 with fly ash was developed as a titanium probe with electrostatic precipitator in [206] for sampling in the flue gas of a cement plant.

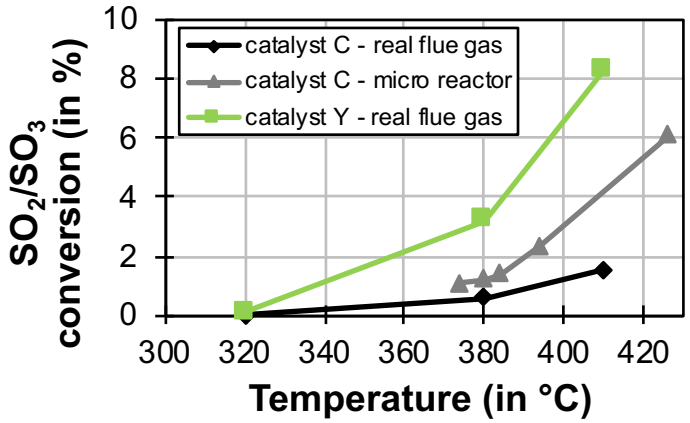

Figure 5-8: SO_2/SO_3 conversion of two different catalysts measured in the real flue gas atmosphere (lab-scale test rig) and (for comparison with catalyst C) in the micro-reactor at different temperatures

In figure 5-8, it can be seen that the SO_2/SO_3 conversion follows an exponential trend, in which for both catalysts around 320°C is the starting temperature of the curve. As discussed in section 4.6.3.4, this behavior can be described by the Arrhenius or the Eyring equation.

Comparing catalyst C with catalyst Y, it becomes obvious also for the measurements in the lab-scale test rig that the higher *vanadia* content of catalyst Y has a strong effect on the SO_2/SO_3 conversion. Tungsten, which is described as a promoter or "support" to suppress the SO_2/SO_3 conversion, is not proportionally varied to the *vanadia* content. It is assumed that a further increase of tungsten or a proportional tungsten content compared to catalyst C does not have a further effect on the SO_2/SO_3 conversion. The effect of the "WO_3 support" is only limited.

The effect of the variation of the area velocity on the SO_2/SO_3 conversion is furthermore determined in the lab-scale test rig. The result is shown in figure 5-9 with catalyst C and catalyst Y. For both catalysts, there is a decrease in SO_2/SO_3 conversion measured when the area velocity is increased. In fact, the variation of the area velocity is at constant catalyst geometries a variation of the residence time, which has already been discussed in section 4.6.3.2. As also shown by Svachula [122], the SO_2/SO_3 conversion is a relatively

slow reaction and thus directly dependent on the residence time. The effect of external and internal mass transfer on the overall conversion can be disregarded and it is only the residence time which determines the turnover. The SO_2/SO_3 conversion coefficient is additionally calculated in figure 5-9, which includes the variation of the flow according to the first-order reaction approach. While the result for catalyst C reflects quite well the approach with a constant or slightly decreasing SO_2/SO_3 conversion coefficient, the result for catalyst Y with an increasing SO_2/SO_3 conversion coefficient cannot be explained and is possibly caused by a too high measurement of the SO_2/SO_3 conversion at higher area velocities. Since the external mass transfer does not have an effect on the slow SO_2/SO_3 conversion, the effect of increased turbulence at the inlet should not have an effect on the result. Again, the effect of *vanadia* on SO_2/SO_3 conversion is quite easily visible comparing catalyst C to catalyst Y. A four-times higher V_2O_5 content leads to a more than four-times higher SO_2/SO_3 conversion, since the effect of the promoter tungsten is only limited and possibly stronger at lower V_2O_5 contents.

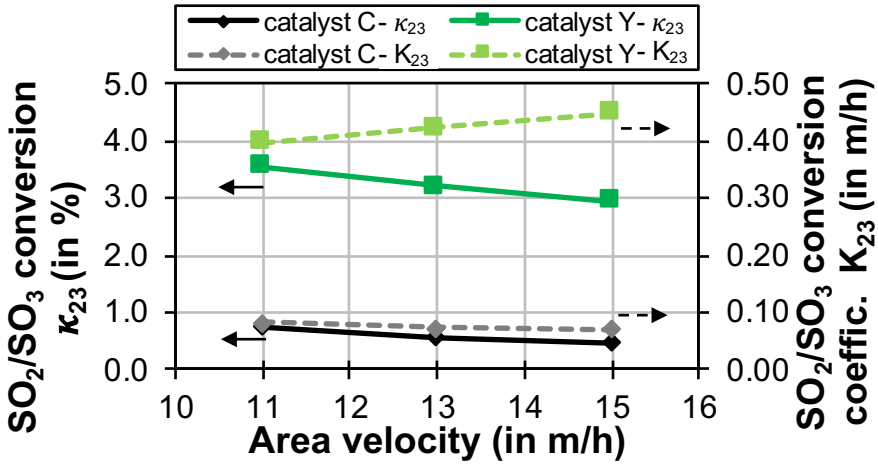

Figure 5-9: Effect of area velocity on SO_2/SO_3 conversion (solid line) and SO_2/SO_3 conversion coefficient (dashed line) with catalyst C and catalyst Y measured at 380°C

5.3 Hg oxidation in real flue gas atmosphere

The oxidation of Hg is studied in the real flue gas atmosphere at various catalysts in order to show the effect of the newly developed catalysts in real flue gas and to mimic their full-scale power plant behavior. Additionally, variations of different parameters are carried out.

5.3.1 Effect of fuel on Hg oxidation

The tests in synthetic flue gas as presented in chapter 4 mimic the different flue gases by the variation of HCl content of the synthetic flue gas. In the lab-scale firing system, various fuels are burned and their effect on Hg oxidation is shown in figure 5-10. The

combustion of the coal (100C), as listed in section 3.7, results in the lowest Hg oxidation, while the combustion of biomass (100B) results in slightly higher Hg oxidation. The highest Hg oxidation is achieved when burning the mixture of coal and biomass (80C/20B). The increase in Hg oxidation can be explained when looking at the HCl content. For 100C, an HCl content of 16.1 mg/m^3 (STP, dry) was measured, for 100B a value of 19.0 mg/m^3 (STP, dry) was determined and the mixture 80C/20B resulted in 69.3 mg/m^3 (STP, dry). Bearing in mind the result presented in figure 4-10, there is a strong increase in Hg oxidation exactly in this range of HCl content.

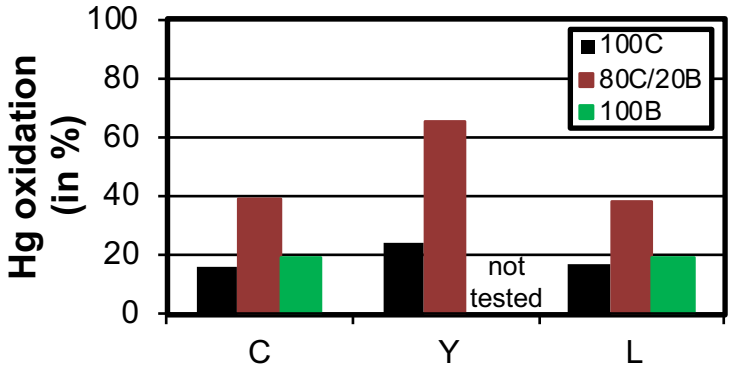

Figure 5-10: Effect of various fuels on Hg oxidation with catalysts C, Y and L

A further increase of the HCl content is simulated by the synthetic addition of HCl to the flue gas resulting from coal combustion as shown in figure 5-11. The black bar reflects the result as shown before and the Hg oxidation with the addition of 100 mg/m^3 HCl is presented in grey. For the combustion of coal, a significant increase in the Hg oxidation can be seen when adding HCl. The value of about 60% is the same value as measured when burning the 80C/20B fuel. This confirms the results discussed above, that an increase in HCl content causes an increase in Hg oxidation also for a real flue gas atmosphere. However, a further increase of the HCl content with catalyst Y when burning 80C/20B does not have an effect on Hg oxidation since the catalyst is already working at its maximum performance.

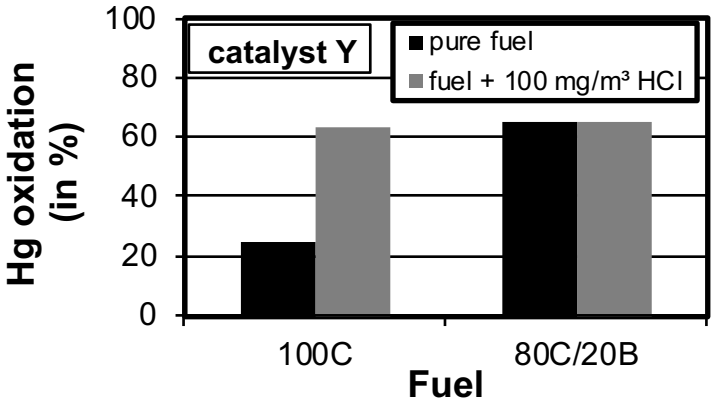

Figure 5-11: Hg oxidation in catalyst Y with increased HCl content in the flue gas

As can be seen in figure 5-1 and figure 5-2, the flue gases when burning these fuels are also different for their SO_2, NO_x and CO content. As shown in section 4.10.2, the flue gas components NO_x and SO_2 do have an effect on the Hg oxidation. However, in the researched range, no effect of the concentration of these flue gas species is found, since the catalysts had been conditioned and operated in the flue gas for several hours in order to have a sulfur equilibrium on the catalysts with additional active sites as described in section 4.10.3.

The absolute Hg oxidation levels measured here are significantly lower compared to the previously discussed results of the micro-reactor tests, even when calculating the Hg oxidation coefficient, which considers the different area velocities in the two reactor designs. In addition to aspects related from mass transfer, meaning a longer laminar zone in the longer samples used in the lab-scale firing system, there is also an aspect from the flue gas composition significantly influencing the Hg oxidation. Looking at figure 4-43, there is a significant influence of the CO concentration on Hg oxidation. During the measurements in the lab-scale firing system, the carbon monoxide content was around 100-200 mg/m^3, as can be seen in figure 5-1 and figure 5-2. This represents optimum operation. Peaks up to 300 mg/m^3 and more were observed due to uneven fuel dosing to the firing system, leading to a local lack of oxygen and incomplete combustion. Thus, considering figure 4-43, the absolute values of the Hg oxidation determined in the lab-scale firing system are about ten percent lower than they would be under ideal conditions, i.e. in a power plant with optimized combustion.

5.3.2 Effect of flue gas temperature on Hg oxidation in real flue gas atmosphere

A first insight into the effect of temperature on Hg oxidation in synthetic flue gas was given in section 4.3.4. Additional experiments are carried out in the real flue gas atmosphere by adjusting the electrical heating of the flue gas duct from the combustion chamber to the SCR reactor as well as the catalyst heating itself. The results of the measurements in real flue gas atmosphere are shown in figure 5-12 for catalyst C (with the addition of HCl) and in figure 5-13 for catalyst Y, both reflecting a high HCl level. The diagrams also include the percentage of Hg^{2+} at the inlet of the catalyst, which is, according to the equation listed in table 3-6, subtracted from the Hg^{2+} at the outlet in order to calculate the Hg oxidation. The general trend of increasing Hg oxidation with decreasing temperature as shown in section 4.3.4 for the synthetic flue gas is confirmed here for a broader range in the real flue gas atmosphere. This is furthermore in line with the tests at plate-type catalysts discussed by [179]. Despite slightly lower HCl content (about 40 mg/m^3 lower) in the flue gas, the Hg oxidation of catalyst Y is at all temperatures higher than for catalyst C, which can be explained by the about four-times higher *vanadia* content of catalyst Y. The general trend of increasing Hg oxidation with lower temperature can be explained by three reasons: First, at the lower temperature,

the real residence time of the flue gas in the catalyst is higher. All numbers given in the test conditions are given at STP and thus the real velocity in the channels is more than two times higher than at STP. A decrease in temperature shifts this to lower velocities and more time for the reaction to take place is available. Second, the adsorption of mercury is more favored at lower temperatures. In an Eley-Rideal reaction model of the Hg oxidation in which mercury is adsorbed on the surface of the catalyst and reacts with HCl from the gas phase or weakly adsorbed, the higher adsorption explains the higher Hg oxidation. This is in line with the Hg adsorption behavior described and studied in section 4.2. As a third reason, the equilibrium of Hg^0/Hg^{2+} lies more on the side of the oxidized species at lower temperatures, as discussed in section 2.1.4. This can be directly seen in the measurements of the Hg^{2+} inlet concentration shown in figure 5-12 and figure 5-13 by the orange points. The Hg^{2+} inlet concentration results from gas-phase reaction of the elemental mercury. Lower temperatures result in a higher share of oxidized mercury during both tests in different flue gases.

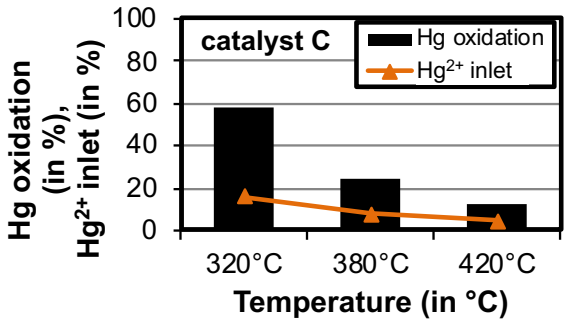

Figure 5-12: Hg oxidation and Hg^{2+} inlet share with varied temperature in catalyst C when burning 100C and adding 100 mg/m³ HCl to the flue gas

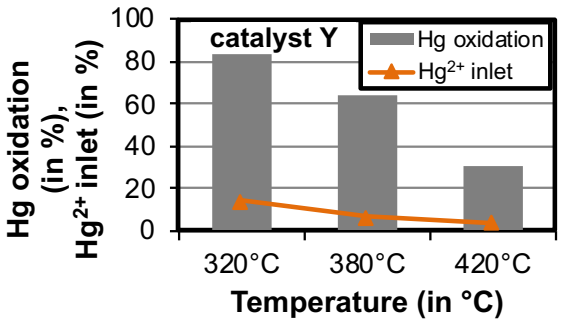

Figure 5-13: Hg oxidation and Hg^{2+} inlet share with varied temperature in catalyst Y when burning 80C/20B fuel

5.3.3 Effect of area velocity on Hg oxidation in real flue gas atmosphere

As discussed in the previous section as one possible reason for the temperature effect on Hg oxidation, an effect of the flue gas flow rate on the Hg oxidation is assumed, also taking into account the results of section 4.3.2. The result of the experiment is presented in figure 5-14 for catalyst Y when firing the 80C/20B fuel mixture, and in figure 5-15 for catalyst L when firing 100% coal. Both measurements are carried out with the addition of 100 mg/m³ HCl in order to carry out both experiments at high HCl concentrations. Additionally, in the diagrams the real residence time of the flue gas in the catalyst channels is calculated as shown by the red line.

For both catalysts (and fuels), there is a continuous decrease in Hg oxidation with increasing flow rate and area velocity. The correlation with the contact time shows that

there is not enough time for the reaction to take place. As pointed out by Niksa [129], the residence time plays an important role in the Hg oxidation. From the results, an Hg oxidation coefficient can be calculated according to the calculation in table 3-6, assuming first-order reaction kinetics with respect to the Hg concentration. While the results of the calculation of the Hg oxidation coefficient for catalyst L with 8.3 m/h, 7.9 m/h and 8.6 m/h show quite a good correlation of these values, the correlation is not that good for catalyst Y with 13.5 m/h, 13.0 m/h and 9.8 m/h. However, this can be explained by the quite low and possibly incorrect result of the point at AV of 14.2 m/h.

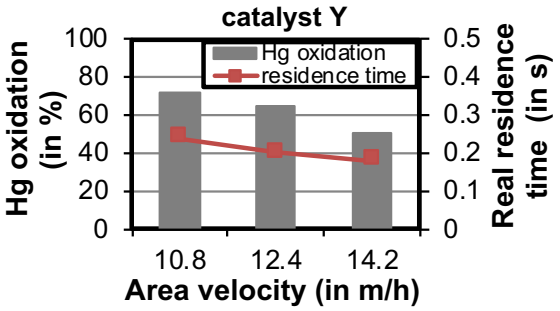

Figure 5-14: Hg oxidation at varied AV in catalyst Y when firing 80C/20B fuel and addition of 100 mg/m^3 HCl

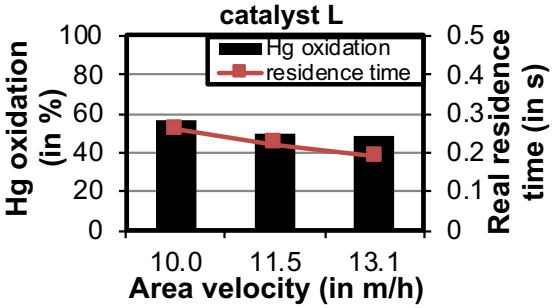

Figure 5-15: Hg oxidation at varied AV in catalyst L when firing 100% coal and addition of 100 mg/m^3 HCl

Summarizing the results of the variation of the flue gas flow over the catalysts also considering the DeNOx activity and SO_2/SO_3 conversion shows that their effect is not that strong compared to the effect of temperature. The variation of temperature includes both a variation in residence time and the kinetics of the reactions. For example, a reduction of temperature from 380°C to 320°C results in an about 10% higher residence time.

According to the results obtained in this study, it can be concluded that related to power plant operation, the quite frequently occurring part load operation and load flexibility also does not have any negative effect on the Hg oxidation on the high-dust SCR. This finding supplements the research carried out by Hilber [203], who already reached this conclusion related to DeNOx activity and SO_2/SO_3 conversion at high-dust SCR catalysts by means of studies of full-size monoliths on a bench-scale reactor.

5.4 Effect of different catalyst types on Hg oxidation in real flue gas atmosphere

In addition to the parameter study, selected new catalysts are measured in the lab-scale firing system for their Hg oxidation when burning coal (100C) and the 80C/20B mixture. The test series is added by the result of catalyst AR, which is in its chemical composition

more or less identical to catalyst H (as shown in table 5-1) with the exception of an increased *vanadia* content of about 0.8 wt.-%, compared to catalyst H with about 0.5 wt.-%. The result is shown in figure 5-16 for 80C/20B fuel and figure 5-17 for 100C.

Table 5-1: Chemical composition of catalyst AR

	Unit	Catalyst AR
$TiO_{2\ (bulk)}$	wt.-%	76.5
$SiO_{2\ (bulk)}$	wt.-%	14.2
$WO_{3\ (bulk)}$	wt.-%	1.2
$V_2O_{5\ (bulk)}$	wt.-%	0.8

Again, the strong effect of HCl on Hg oxidation is obvious when comparing the two results, with different HCl concentrations of 16.1 mg/m³ (STP, dry) for 100B and 69.3 mg/m³ (STP, dry) for 80C/20B as discussed in section 5.3.1. As in the tests in synthetic flue gas, also in the real flue gas atmosphere, the Hg oxidation varies in a wide range depending on the chemical composition of the catalyst. Despite the increased pitch and thus increased clear width of catalyst L compared to catalyst C, the Hg oxidation of catalyst L is the same or even higher than that of catalyst C for both tested fuels. Considering only the mass transfer, a lower Hg oxidation is assumed, as already discussed in the micro-reactor tests in section 4.4. Thus, the effect of wall thickness is confirmed also for real flue gas atmosphere tests, meaning that a thicker wall would be beneficial for Hg oxidation.

The performance of a catalyst with increased *vanadia* content is also quite obvious in the tests in real flue gas atmosphere. The highest Hg oxidation is measured for catalyst Y for both fuels. However, this is, as discussed above, accompanied with the tremendously increased SO_2/SO_3 conversion, which can then cause problems in the air preheater. In plants with already existing SO_3 mitigation technology, like the addition of lime, hydrated lime or trona, such a catalyst might be an easy and cost-effective solution in order to reach a high level of Hg oxidation.

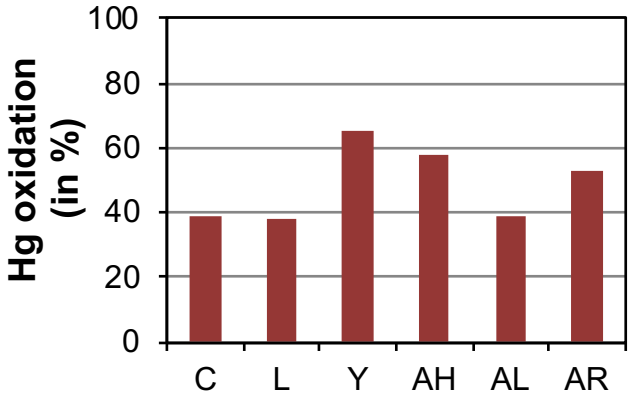

Figure 5-16: Hg oxidation of SCR catalysts tested in the lab-scale firing system in real flue gas atmosphere when burning 80C/20B fuel

The two newly developed catalysts AH and AR follow a different approach with more or less similar results for the Hg oxidation as for catalyst Y. Both catalysts show low SO_2/SO_3 conversion in the micro-reactor tests and an increased Hg oxidation in the real flue gas of

the lab-scale firing system, confirming the successful development also for full-scale application. While for catalyst AR the addition of silica selectively suppressed the activity of the catalyst to oxidize SO_2 to SO_3, the Hg oxidation performance stayed the same. For catalyst AH, the high performance can be explained by the interaction of the molybdenum with the active sites but also with a positive effect of the addition of molybdenum on the pore size of the catalyst. The behavior of catalysts AH and AR when firing coal cannot be explained by overall chemical aspects and flue gas interaction, with the exception of carbon monoxide and its effect on the Hg oxidation as pointed out in section 4.10.4. So, the results are possibly influenced by the high CO content frequently monitored during coal combustion, leading to this “measurement error” compared to not by CO biased measurements and lower Hg oxidation results than expected.

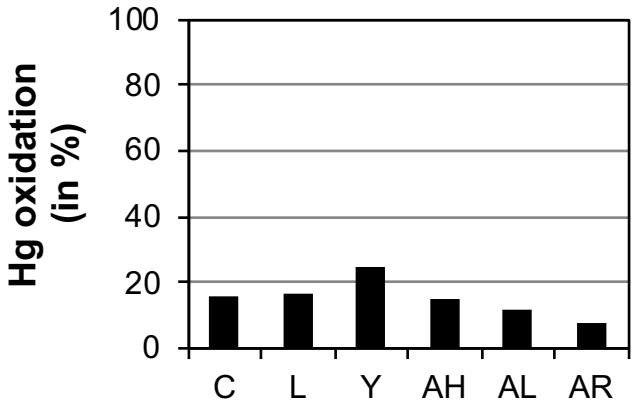

Figure 5-17: Hg oxidation of SCR catalysts tested in the lab-scale firing system in real flue gas atmosphere when burning coal (100C)

Unlike previously assumed and discussed in section 4.10.3 for catalyst AL in synthetic flue gas, in the measurements in real flue gas atmosphere, catalyst AL shows a significantly high Hg oxidation. Perhaps the deactivation of the active sites is not that pronounced. This catalyst without any *vanadia* shows the same Hg oxidation as catalyst C when burning 80C/20B fuel and shows significant Hg oxidation when burning coal. This confirms that cerium is also a powerful catalyst for Hg oxidation in real flue gas atmosphere. As discussed above, the results of coal combustion are influenced by the high CO content in flue gas, leading to an even lower result than with catalyst C.

In figure 5-18, the results of the lab-scale firing system with 80C/20B mixture combustion and the micro-reactor are summarized and compared to catalyst C since the HCl content was not the same in both tests. The results of the micro-reactor tests have been recalculated based on the first-order approach with equation 3-16 at an AV of 13 m/h in order to have the same basis for the comparison. In general, the results for Hg oxidation gained at the lab-scale firing system are lower than at the micro-reactor. One reason is the previously discussed influence of the CO content in the lab-scale firing system. Another reason is of analytical nature. Since the flue gas has to be filtered prior to Hg

speciation, possibly already oxidized mercury is then converted back to elemental mercury. The packed quartz-wool filter accumulates fly ash particles like aluminum oxide and calcium oxide, which were identified by Hocquel [66] to reduce oxidized mercury. Since there is always fly ash present in the flue gas, a measurement without bias is not possible. The application of an electrostatic precipitator in the lab-scale firing system for sampling, as applied for example in [206] for the sampling of SO_3, is not an option, since the corona discharge can lead to the formation of ozone. However, ozone is, like HCl and chlorine, an oxidant for the oxidation of elemental mercury [145] and furthermore known as an important oxidant of elemental mercury in the atmospheric mercury cycle [207].

In figure 5-18, the previously discussed decrease of Hg oxidation of catalyst AL is again visible. While for all other catalysts the difference regarding Hg oxidation between the relative values of micro-reactor and lab-scale firing system is up to 20%, for catalyst AL it is about 50%. This confirms loss in activity of the cerium catalyst when SO_2 is present. However, the Hg oxidation is still on the same level as in catalyst C but with lower SO_2/SO_3 conversion.

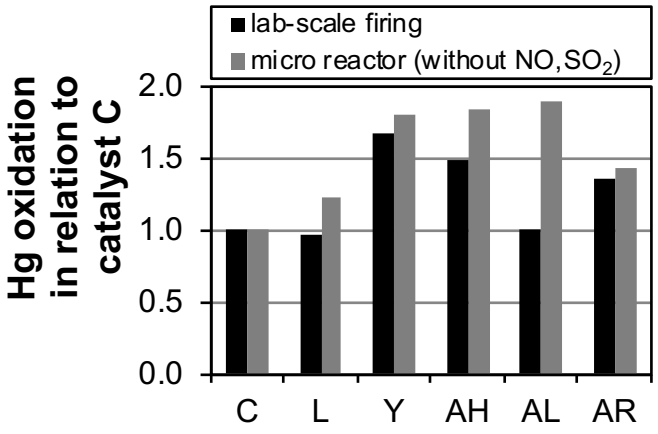

Figure 5-18: Relative comparison of the Hg oxidation measured at the micro-reactor and lab-scale firing system (with 80C/20B fuel)

5.5 Study of parallel NO_x reduction on Hg oxidation in real flue gas atmosphere

As discussed in section 4.10.3, the parallel NO_x reduction has a strong effect on the Hg oxidation and depending on the NH_3/NO ratio and the catalyst type, even almost zero Hg oxidation is measured. The effect in the lab-scale firing system when firing 80C/20B fuel and adding ammonia can be seen in figure 5-19. From about minute 8 to minute 45, the Hg^0 concentration at the outlet of the catalyst is measured. The measurements before minute 8 and after minute 45 show the Hg^{tot} concentration (Hg^0 and Hg^{2+}). Shortly before minute 30, ammonia is added to the flue gas upstream of the catalyst in a ratio to nitrogen oxide of 0.2. While the NO concentration decreases slowly, the Hg^0

concentration increases quite instantaneously with a slightly shorter response time. Due to this effect, the overall Hg oxidation decreases by about 40%.

The slower relative decrease of the nitrogen oxide concentration compared to the increase in Hg^0 concentration in the first minutes after the addition of NH_3 can be explained by the displacement of adsorbed mercury when ammonia is added. This means that first Hg is released from the active sites and then the DeNOx reaction takes place. This confirms the measurements by Thorwarth [80], who also found a release of mercury from the catalyst. Finally, at steady state after minute 36, a NO_x reduction of about 13% is measured. As discussed in section 4.10.3, a reduction of already oxidized mercury could furthermore take place.

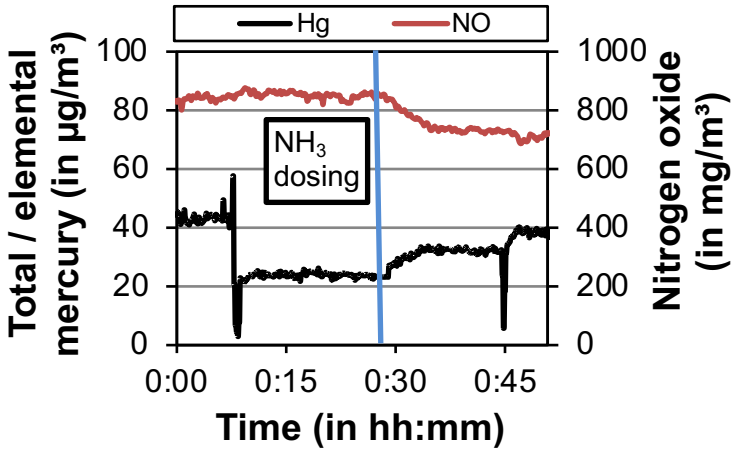

Figure 5-19: Hg and NO concentration measured with catalyst AR when burning 80C/20B fuel and adding NH_3 at a ratio of NH_3/NO=0.2 (starting at the blue vertical line)

In contrast to the results measured at the micro-reactor, a significant Hg oxidation is measured when ammonia is added, which can be explained by the longer catalyst sample. There is therefore enough surface area for Hg oxidation available, which takes place after ammonia is almost fully consumed. The effective area velocity for Hg oxidation is much higher with ammonia than without ammonia since the effective length of the catalyst at which the Hg oxidation could really take place is shorter than the total catalyst length. However, bearing in mind the results of catalyst AJ, the model developed by Thorwarth [80] with discrete zones for NO_x reduction and Hg oxidation cannot be considered valid for all catalysts. Especially at newly developed catalysts, there is possibly a spreading of the active sites between NO_x reduction and Hg oxidation, as both reactions take place simultaneously and not separately. Thus, Thorwarth's model conception has to be revised at least for some of the newly developed catalysts.

5.6 Effect of addition of NH_4Cl on Hg oxidation and DeNOx activity

The strong effect of chlorine on the Hg oxidation was discussed extensively in the previous sections. All results reveal that a high chlorine concentration in the flue gas supports a high Hg oxidation at SCR catalysts. Furthermore, as discussed in Farr [89] and Heidel [91], the high chlorine content in the flue gas, resulting in high chloride levels in the scrubber, leads to a good retention of Hg in the wet FGD unit and as a further benefit to an improved removal of SO_2.

A substance which would increase the flue gas chlorine content by simultaneously providing a reducing agent for the reduction of nitrogen oxide is ammonium chloride (NH_4Cl). This is a transparent crystalline solid substance, which has a good water solubility of 37.2 g NH_4Cl per 100 g H_2O at 20°C [208]. It sublimates at 338°C (with a $\Delta H_{diss.}$= +176.1 kJ/mol) according to:

$$NH_4Cl \rightarrow NH_3 + HCl \qquad \text{equation 5-1}$$

Furthermore, ammonium chloride is less harmful and has a lower safety classification compared to gaseous ammonia or ammonia solution.

For NO_x reduction, ammonia is provided by the decomposition of NH_4Cl and thus lower levels of ammonia are needed. For example, at a nitrogen oxide concentration of 800 mg/m^3 as shown in figure 5-2, an addition of NH_4Cl in order to reach a NH_3/NO ratio of 0.8 leads to an increase in flue gas HCl concentration of 800 mg/m^3. At this HCl concentration, the Hg oxidation is definitely not limited by HCl concentration and a small variation of the concentration does not have any effect on the result.

In figure 5-20, the result of the addition of NH_4Cl at the lab-scale firing system upstream of the SCR reactor is shown in comparison to no addition of NH_4Cl when burning 100% coal (catalyst C) or 80C/20B mixture (catalyst AR). In this experiment, NH_4Cl is added in a calculated NH_3/NO ratio of 0.5 on a mol/mol basis with the NH_3 resulting from the NH_4Cl decomposition. For the addition of ammonia (without NH_4Cl), a nearly stoichiometric reduction of nitrogen oxide is measured, as can be derived from equation 2-17.

The Hg oxidation is measured with an addition of NH_3 slightly lower than shown in figure 5-10, which is caused by the inhibition by ammonia. The addition of NH_4Cl leads only to a substoichiometric NO_x reduction of about 12%. This can be explained by an incomplete decomposition of the NH_4Cl in the experiment or adsorption on fly ash. Despite this incomplete decomposition, significant HCl is still released from the dosed NH_4Cl and thus the measured Hg oxidation is increased despite the availability of ammonia in the flue gas. However, there are still active sites left for Hg oxidation since the available ammonia is instantaneously converted.

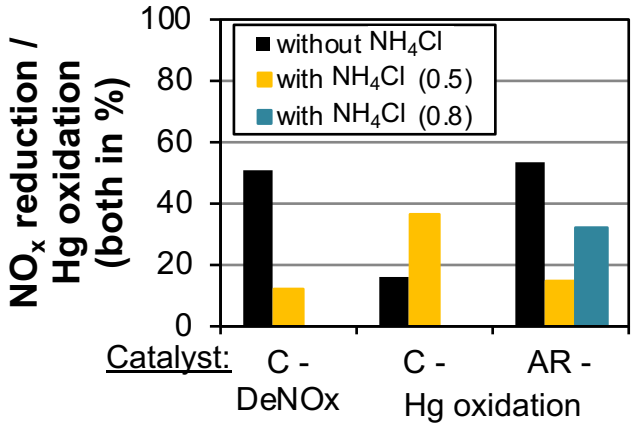

Figure 5-20: Effect of addition of NH_4Cl (in the given ratio) with catalyst C when firing 100% coal and catalyst AR when firing 80C/20B fuel on DeNOx activity (catalyst C) and Hg oxidation compared to the result without addition of NH_4Cl (and in the case of NO_x reduction with addition of NH_3)

A further increased NH_4Cl dosing is studied with catalyst AR when firing 80C/20B fuel. Since this fuel mixture already provides, compared to the used coal, quite a lot of chlorine, the Hg oxidation is significantly higher. However, the adding of NH_4Cl first reduces the Hg oxidation since the active sites are occupied to a certain extent by ammonia. The further increase to a theoretical NH_3/NO ratio of 0.8 increases the Hg oxidation to up to about 33%. This indicates, as discussed before, an incomplete presence of the chlorine contained in the dosed NH_4Cl. A further increase possibly also shifts the equilibrium of Hg^0/Hg^{2+} to the side of the oxidized mercury species, decreasing the reduction of the already oxidized mercury.

A summary of the tests with the addition of NH_4Cl is shown in figure 5-21 (NO_x reduction) and figure 5-22 (Hg oxidation). In contrast to the results presented above, all measurements were carried out with combustion of 80C/20B fuel. Due to an optimized NH_4Cl dosing, higher NO_x reduction is achieved. However, overall the NO_x reduction is still not satisfactory and quite low compared to the adjusted calculated NH_3/NO ratio of 0.5 as described before. The maximum of about 35% is reached with catalyst AL, but considering the discussion above, does not reflect a better performance of the catalyst.

Compared to the results presented above for coal combustion without NO_x reduction as for example shown for catalyst C in figure 5-10, the measurements show a significant increase in Hg oxidation considering the parallel NO_x reduction by ammonia. For catalyst C, the result of the Hg oxidation with the addition of NH_4Cl is even higher than without the addition with the benefit of NO_x reduction. The successful development of the new catalysts is shown with catalyst AH, which already performed quite well in the micro-reactor tests in section 4.8. The addition of molybdenum instead of tungsten has a strong positive effect on the Hg oxidation. For catalyst AL, the lower Hg oxidation can perhaps be explained by the measured higher NO_x reduction and thus a higher ammonia coverage of the catalyst. This catalyst is also special since it does not contain any V_2O_5 active sites and,

as discussed in section 4.10.3, in the presence of SO_2 a significant decrease in Hg oxidation is measured. However, as measured in this test series, there is a significant Hg oxidation present, even at a high NH_3/NO ratio of 0.5. With this result, the applicability of the V_2O_5-free catalyst is further confirmed and the assumed deactivation is not so serious. However, there is still some room for improvement for the AL catalyst.

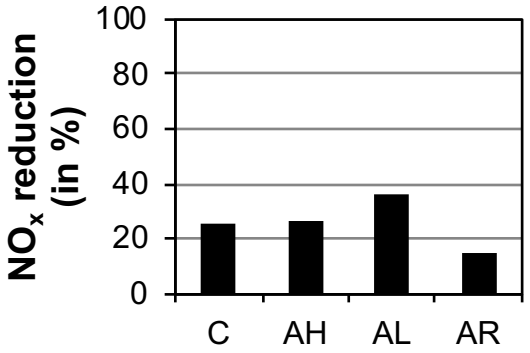

Figure 5-21: NO_x reduction at various catalysts when firing 80C/20B fuel and addition of NH_4Cl (NH_3/NO ratio: 0.5)

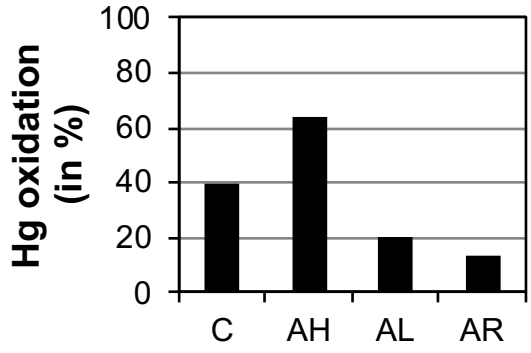

Figure 5-22: Hg oxidation at various catalysts when firing 80C/20B fuel and addition of NH_4Cl (NH_3/NO ratio: 0.5)

The principle of the addition of NH_4Cl for NO_x reduction and Hg oxidation was also researched by Honjo [209] and Okamto [210] in power plant application. Both found an increase in Hg oxidation when adding NH_4Cl due to lower chlorine content of the fuel. In their tests, the DeNOx activity followed directly the adjusted NH_3/NO ratio. Furthermore, in the tests by Okamto, the whole power plant flue gas cleaning system was studied, also considering the ORP in the FGD unit, which plays a crucial role in the Hg removal process in the wet FGD unit [91]. When adding NH_4Cl, the experiments of Okamto in a US power plant showed an oxidized mercury content of over 95% of total mercury downstream of the SCR reactor, which was equipped with a conventional SCR catalyst. A mercury removal rate of over 90% in the air pollution control system was reached [210]. Unfortunately, such an experiment with the addition of NH_4Cl and covering SCR and FGD unit could not be carried out on the lab-scale firing system since the ESP used for fly ash separation probably biases the Hg oxidation and the carbon content in the separated fly ash varies in a broad range [84].

Summarizing the results of this chapter, the phenomena of SCR catalysts discussed in chapter 4 are also observed in real flue gas atmosphere. Thus, the results can in general be transferred from laboratory to real flue gas atmosphere. Different results can be explained for example by the effect of CO on Hg oxidation. Nevertheless, the superior performance of the newly developed SCR catalysts with improved Hg oxidation performance like catalyst AH can be confirmed for tests in real flue gas atmosphere and even with the addition of NH_4Cl.

6 Summary and outlook

SCR catalysts are the state-of-the-art technology for the reduction of NO_x emissions in coal-fired power plants. In the high-dust arrangement, an SCR reactor provides an efficient and flexible method for emission reduction in the power plant process. It has already been found that a high share of oxidized mercury (Hg^{2+}) is a fundamental prerequisite for the efficient removal of mercury in downstream fly ash removal (e.g. ESP) or to a much greater extent in the wet flue gas desulfurization process. In a side reaction, SCR catalysts can contribute to a high share of oxidized mercury in the flue gas by oxidizing the elemental mercury which was previously released in the boiler from the fuel. However, as a further but undesired side reaction, SCR catalysts can oxidize the sulfur dioxide in the flue gas to sulfur trioxide, known as SO_2/SO_3 conversion. In this study, all relevant reactions of SCR catalysts have been researched, with a strong focus on Hg oxidation with modified, newly developed SCR catalysts. The measurements have been carried out not only in laboratory test setups and micro-reactors in synthetic flue gas but also in the real flue gas atmosphere of a lab-scale firing system burning coal and co-firing coal and biomass.

The influence of the interaction of the catalyst matrix and the various metal oxides on Hg oxidation is first shown in powder tests, in which powders of pure metal oxides, partly of compounds of SCR catalysts, have been studied for their Hg oxidation behavior in comparison to a ground/powdered SCR catalyst. The support metal oxides as pure substances like TiO_2 or MoO_3 do not show any Hg oxidation over the researched temperature range. At tests with V_2O_5, Hg oxidation could be measured, confirming its role as an active component in SCR catalysts. Manganese oxide in the form of MnO_2 also shows significant Hg oxidation, being at first sight a promising material for improved Hg oxidation. The importance of testing the complete catalyst matrix in evaluation tests is shown in the superior result of the SCR catalyst powder test compared to the pure metal oxides, showing the interaction effect of the metal oxides within the catalyst matrix.

In a standardized setup and test scheme for the adsorption and desorption of mercury by SCR catalysts, the effect and importance of this reaction step is studied. SCR catalysts directly start Hg adsorption when there is no or only very low halogen component like chlorine or bromine in the flue gas. As soon as the halogen is added to the flue gas, Hg is completely released as HgX_2. In these adsorption and desorption experiments, not only a dependency of the desorbed mercury amount on the surface area is found but also a dependency on the V_2O_5 content of the catalyst. Precious metals like palladium show the highest levels of Hg desorption, while the lowest levels in the studied temperature range are found for manganese oxide, indicating that there are various mechanisms responsible

for the oxidation of Hg with different metal oxides. In standard SCR catalysts with *vanadia*, the mechanism of Hg oxidation might take place via an adsorption step, while in manganese catalysts the Hg oxidation at high temperatures is attributed to the Deacon reaction since no Hg adsorption is found. The Hg adsorption is found to be of a fully chemisorptive nature in the researched high-dust SCR temperature range.

Under the researched flue gas conditions, the HCl content plays an important role, especially with standard SCR catalysts. Between single-digit HCl concentrations and a concentration of 50 mg/m^3, the Hg oxidation increases despite the huge excess of chlorine vs. mercury. This is explained by a deeper penetration of chlorine into the catalyst porous system with increased partial pressure. In contrast to this, the mercury concentration does not have an effect on the oxidation of Hg, which is of first order regarding its concentration.

The effect of temperature on Hg oxidation is ambiguous and also linked to the HCl content. It can be confirmed for low HCl contents that the oxidation of Hg increases with decreasing temperature. However, at high HCl contents of > 50 mg/m^3, the oxidation level of Hg remains constant or even decreases with decreasing temperature in the range relevant for high-dust SCR application. Generally speaking, the effect of temperature on Hg oxidation is more pronounced in situations with a shortage of HCl or when additional stress is put on the Hg oxidation, e.g. due to a parallel reduction in NO_x with occupied active sites been busy by the NO_x reduction reactions.

In order to compare the performance of the SCR catalyst with regard to the desired reactions of NO_x reduction and Hg oxidation and the undesired reaction of SO_2/SO_3 conversion, the performance indicator P3 is introduced that considers the importance of the reactions in high-dust application of the SCR catalyst. The indicator gives the highest number for the -in general- most favorable catalyst, weighting all three reactions equally. Catalyst C with a P3 number of about 3,000 forms the reference for all other catalysts.

The effect of geometrical variations is researched in detail with varied wall thicknesses. Catalysts with increased wall thickness show an increase in Hg oxidation, despite the variation of the cell opening, which should in fact lead to an opposite effect. This indicates that the oxidation of Hg is not a pure surface reaction but also influenced by the catalyst bulk. In contrast, the DeNOx reaction is shown to be a pure surface reaction while the SO_2/SO_3 conversion with varied wall thicknesses gives a clear indication of taking place in the whole bulk of the catalyst.

The application of copper and iron in the catalyst matrix can lead to increased levels of Hg oxidation, but both also boost the SO_2/SO_3 conversion, which results in very low P3 values and makes their high-dust application impossible. However, in the case of Fe_2O_3, which could also result from the fly ash, the accumulation in the catalyst in the right modification (γ-Fe_2O_3) could result in increased Hg oxidation also with increased SO_2/SO_3

conversion rates. The measured positive effect of manganese on the performance of the catalyst has to be regarded with reservations, since the deactivation of manganese by SO_2 needs to be considered.

The method of application of the active material on the catalyst also plays a crucial role for the performance. Catalysts with impregnation of the active component (e.g. V_2O_5) show lower Hg oxidation and also lower SO_2/SO_3 conversion since the impregnation, depending on the method, generally has more of an effect on the surface.

The role of WO_3 as a promoter cannot be confirmed for Hg oxidation and SO_2/SO_3 conversion in connection with the introduction of new metal oxide. There is no significant positive change of these reactions when WO_3 is added. The effect of *vanadia* or other metal oxides is dominating.

The amount of SO_3 formed over the catalyst approaches a maximum with increasing SO_2 concentration due to the availability of the active sites. Thus, the SO_2/SO_3 conversion is dependent on the SO_2 concentration and also on the residence time. The water content does not have an effect on the result. By analyzing the strong exponential increase of the SO_2/SO_3 conversion by thermodynamic considerations, for the newly developed catalyst with copper, two different reaction enthalpies are identified in various temperature ranges, which result from different reaction mechanisms.

Modifications to the TiO_2 base material used for the production of the catalyst also have a significant effect on the performance of the catalyst. However, the application of nano-material does not necessarily result in a higher surface area of the catalyst and thus higher turnover. The higher performance of the catalyst is attributed to the distribution of the active material over the inner surface. Regarding the conversion of SO_2/SO_3, catalysts with the applied nano-grade base material show lower values. An additional lowering of the SO_2/SO_3 conversion rate can be achieved by dedicated adding of SiO_2 to the catalyst's base material, which is inactive with regard to SO_2/SO_3 conversion and dilutes the active sites.

Molybdenum oxide (MoO_3) is a powerful promoter for Hg oxidation, without any negative effect on the DeNOx activity and SO_2/SO_3 conversion. It shows significant benefits compared to WO_3-promoted catalysts due to the ability to contribute to the re-oxidation of vanadium from V^{3+} to V^{5+}. Cerium oxide (CeO_2) in catalysts without any further active component like *vanadia* results in a strong benefit regarding Hg oxidation even at very low HCl concentrations, which can be explained by the much higher BET surface area of these catalysts and additionally by the good oxidation properties of cerium due to the redox shift between Ce^{4+} and Ce^{3+}. However, the catalysts with cerium oxide are less DeNOx-active but on the other hand, they show lower SO_2/SO_3 conversion rates.

The study of three plate-type catalysts shows higher NO_x reduction and Hg oxidation under the same test conditions compared to the honeycomb catalysts due to increased

surface mass transfer at the plates caused by macroscopic and microscopic cracks in the surface of the plate catalyst structure. Molybdenum in the researched plate catalyst does not have that much effect on the Hg oxidation on these plates in comparison to tungsten, but does on the DeNOx activity, which is a result of the increased BET surface area. A possible different approach to catalyst improvement can be seen in the third tested plate catalyst. There, the *vanadia* content is tremendously increased, but it is selectively deactivated by phosphorus, which results in high Hg oxidation, high DeNOx activity and moderately increased SO_2/SO_3 conversion.

There are various effects and mechanisms which influence the reactions over the catalysts. Sulfation of the active sites has a strong positive effect on the DeNOx activity and Hg oxidation, except for the catalyst with CeO_2 as active component. In conventional, state-of-the-art catalysts, the parallel DeNOx activity suppresses the Hg oxidation tremendously with increasing NH_3/NO ratio. Similarly, the SO_2/SO_3 conversion is suppressed. This means that in the first catalyst layer, there is only minor Hg oxidation taking place and the reduction of formed $HgCl_2$ by ammonia could dominate. In the newly developed catalysts, the inhibition is not that distinctive due to different active sites and the Hg oxidation can even take place in the first layer of the SCR reactor. Thus, the benefit of these newly developed SCR catalysts is the higher flexibility in layer arrangement. Carbon monoxide, a product of incomplete combustion present in real flue gas, also has a strong negative effect on the Hg oxidation due to a reduction of the already formed $HgCl_2$. Additionally, there is a slight increase of Hg oxidation with increasing oxygen content in the flue gas, but the catalysts also show some oxygen storage capacity.

It is not only halogen chlorine which plays an important role in Hg oxidation. Bromine is more active even in 100-fold lower concentrations, especially when SO_2 is present in the flue gas. The oxidation of Hg is then also less inhibited by the parallel reduction of NO_x. The mechanistic study on the halogen application clearly shows the superior Hg oxidation of the molecular halogen compared to the hydrogen halide in the homogeneous gas-phase reaction. A benefit of a catalyst when adding the molecular halogen, that is of the heterogeneous way, could not be definitely shown. The formation of molecular chlorine from HCl over the catalyst according to the Deacon-reaction was measured with a conversion rate of less than 2%. However, there are still doubts on the significance of the contribution of this pathway to the overall Hg oxidation.

The results as discussed above are partly verified in real flue gas of coal, biomass and co-combustion. A significant influence of these fuels specifically could not be found in the short-term tests. It is more the flue gas composition that influences the results. The flue gas composition is mainly determined by the fuel composition, as shown in the literature review. For the DeNOx activity, a peak of 380°C is found with a state-of-the-art catalyst, reflecting its design, and the DeNOx activity slightly increases with increasing area velocity. For the conversion of SO_2 to SO_3, the exponential increase with temperature is

also seen in the real flue gas, but the absolute levels are lower due to interaction with fly ash. The strong dependency of the Hg oxidation on the HCl concentration is also measured in the real flue gas, with the highest Hg oxidation measured in the applied co-combustion fuel with the highest chlorine level. The general trend of higher Hg oxidation at lower flue gas temperatures is confirmed along with the influence of the residence time.

The general trend and the above-described performance of the newly developed catalysts related to Hg oxidation are confirmed for the real flue gas atmosphere despite the quite low absolute values. This means that there is no negative influence of real flue gas atmosphere on the newly developed catalysts during short-term tests. Differences between the micro-reactor tests and the tests in real flue gas atmosphere in the lab-scale firing system can be seen in the reference as well as in newly developed catalysts. They can be traced back to exceptionally high CO contents in the flue gas of the lab-scale firing system, which acts as a reducing agent, and interactions of oxidized mercury with fly ash. The influence of the parallel DeNOx reaction on the Hg oxidation is also seen in real flue gas atmosphere, but in the case of the longer samples applied in real flue gas tests, the inhibition is not that pronounced since there is still enough space for Hg oxidation left. Finally, the effect of the application of ammonium chloride (NH_4Cl) on NO_x reduction in combination with an increase in Hg oxidation is shown, forming one further option especially in low-chlorine applications.

Summarizing all results and observations on the mechanistic studies of Hg oxidation in SCR catalysts, it can be concluded that the reaction of the Hg oxidation is of Eley-Rideal or Mars-Maessen type, although the latter with an intermediate HgO form seems to be more probable. This can be justified by the distinct adsorption-desorption behavior of mercury and the effect of the catalyst bulk, which could be seen in the experiments. HCl only seems to play a role as a weakly adsorbed oxidation agent. The frequently discussed Deacon-reaction could play an additional role in the Hg oxidation process, but the major role is attributed to the mechanism discussed above, since the results on the production of molecular chlorine were not that convincing. Through the addition of new metal oxides or modifications to the base material powder, the formation of separate active sites for Hg oxidation and SO_2/SO_3 conversion or a suppression or even selective deactivation of the active sites related to SO_2/SO_3 conversion seems possible, leading to the aim of high DeNOx activity, high Hg oxidation and low SO_2/SO_3 conversion. This is expressed in this work with a high P3 coefficient.

However, the tests presented here reflect short-term laboratory or lab-scale firing system tests with catalyst operation of < 2 weeks. The lifetime of high-dust SCR catalysts is in the range of tens of thousands of hours of operation. It could even be extended by catalyst regeneration with dedicated regeneration steps. Thus, the behavior over at least several thousand hours of operation needs to be tested on the one hand related to the stability

of the active sites of the catalyst and on the other related to the deactivation behavior, which might be different to the standard SCR catalyst. Since regeneration of SCR catalysts is a good method to extend the lifetime, the behavior of the new catalysts with new recipes in regeneration steps like washing is one point to be of future interest. The mechanical stability of the material is also an important aspect to be considered, especially its erosion resistance, since each and every powder and calcination process modification also has an effect on mechanical stability. This is even more important in view of possible new applications of these newly developed SCR catalysts in high-dust applications, for example in lignite-fired power plants or in the high-dust arrangement of a cement kiln. Last but not least, SCR catalyst development and application are also strongly driven by economic aspects, and a tradeoff between catalyst performance and production cost has to be found.

7 Literature

[1] BP statistical review of world energy 2019 https://www.bp.com/content/dam/bp/business-sites/en/global/corporate/pdfs/energy-economics/statistical-review/bp-stats-review-2019-full-report.pdf, accessed: 5/24/2020

[2] IEA, World Energy Outlook 2015, OECD Publishing, Paris, 2015. DOI: http://dx.doi.org/10.1787/weo-2015-en, accessed: 5/24/2020

[3] IEA, World Energy Outlook 2019, OECD Publishing, Paris, 2019. DOI: https://doi.org/10.1787/caf32f3b-en, accessed: 5/24/2020

[4] Baumbach, G.: Luftreinhaltung, Springer-Verlag Berlin Heidelberg, 1994, ISBN: 3-540-56823-0

[5] Umweltbundesamt: Nationale Trendtabellen für die Berichterstattung atmosphärischer Emissionen 1990-2015, Dessau, Januar 2017

[6] AMAP/UNEP: Technical Background Report for the Global Mercury Assessment 2013. Arctic Monitoring and Assessment Program, Oslo, Norway/UNEP Chemicals Branch, Geneva, Switzerland, 2013

[7] Pacyna, E.G., Pacyna, J.M., Steenhuisen, F., Wilson, S.: Global anthropogenic mercury emission inventory 2000, Atm. Environment, 40, 2006, pp. 4048-4063

[8] AMAP/UNEP: Technical Background report to the Global Atmospheric Mercury Assessment, 2008, UNEP Chemical Branch

[9] Ebinghaus, R., Jennings, S., Kock, H., Derwent, R., Manning, A. and Spain, T.: Decreasing trends in total gaseous mercury observations in baseline air at Mace Head, Ireland from 1996 to 2009, Atmospheric Environment, 45, 2011, pp. 3475-3480

[10] Zhang, L., Blanchard, P., Gay, D.A., Prestbo, E.M., Risch, M.R., Johnson, D., Narayan, J., Zsolway, R., Holson, T.M., Miller, E.K., Castro, M.S., Graydon, J.A., St. Louis, V.L.and Dalziel, J.: Estimation of speciated and total mercury dry deposition at monitoring locations in eastern and central North America, Atmospheric Chemistry and Physics, 12, 2012, pp. 4372-4340

[11] Friedli, H.R., A.F. Arellano Jr., F. Geng, C. Cai and L. Pan: Measurements of atmospheric mercury in Shanghai during September 2009, Atmospheric Chemistry and Physics, 11, 2011, pp. 3781-3788

[12] Mergler, D.; Anderson, H. A.; Hing Man Chan, L.: Methylmercury Exposure and Health Effects in Humans: A Worldwide Concern, Ambio, 36 (1), 2007

[13] Dietz, R., Outridge, P.M., Hobson, K.A.: Anthropogenic contributions to mercury levels in present-day Arctic animals-A review, Science of the Total Environment, 407 (24), 2009, p. 6120-6131

[14] Outridge, P M; Hobson, K A; Savelle, J.: Long-term changes of mercury levels in ringed seal (Phoca hispida) from Amundsen Gulf, and beluga (Delphinapterus leucas) from the Beaufort Sea, western Canadian Arctic, The Science of the total environment, 407 (23), 2009, pp. 6044-6051

[15] Muckle, G., Ayotte, P., Dewailly, E., Jacobson, S.W. and Jacobson, J.L.: Determinants of polychlorinated biphenyls and methylmercury exposure in Inuit women of childbearing age, Environ. Health Perspect. 109, 2001, pp. 957–963

[16] Konkel, L.: How brain-damaging mercury puts arctic kids at a risk, National Geographic, 27.03.2015, https://www.nationalgeographic.com/science/article/150327-inuit-mercury-beluga-iq-canada-nunavik-arctic-faroe-islands, accessed: 5/24/2020

[17] Slemr, F., Brenninkmeijer, C.A., Rauthe-Schöch, A., Weigelt, A., Ebinghaus, R., Brunke, E.-G., Martin, L., Spain, T.G. and O'Doherty, S.: El Niño–Southern Oscillation influence on tropospheric mercury concentrations, Geophys. Res. Lett., 43, 2016, doi:10.1002/2016GL067949

[18] Gesetz zum Schutz vor schädlichen Umwelteinwirkungen durch Luftverunreinigungen, Geräuschen, Erschütterungen und ähnlichen Vorgängen (Bundes-Immissionsschutzgesetz), 2015

[19] Bundesministerium für Umwelt, Naturschutz und nukleare Sicherheit: Neufassung der Ersten allgemeine Verwaltungsvorschrift zum Bundes-Immissionsschutzgesetz, 2021

[20] Bundesministerium der Justiz und für Verbraucherschutz: Dreizehnte Verordnung zur Durchführung des Bundes-Immissionsschutzgesetzes (Verordnung über Großfeuerungs-, Gasturbinen- und Verbrennungsmotoranlagen – 13. BimSchV), 6. July 2021

[21] Bundesministerium der Justiz und für Verbraucherschutz: Siebzehnte Verordnung zur Durchführung des Bundes-Immissionsschutzgesetzes (Verordnung über die

Verbrennung und die Mitverbrennung von Abfällen – 17. BimSchV), 02. Mai 2013 revised 6. July 2021

[22] European Commission: Directive 2001/80/EC of the European Parliament and of the Council of 23 October 2001 on the limitation of emissions of certain pollutants into the air from large combustion plants, Official Journal L309, November 2001

[23] European Commission – Directorate-General Environment: Communication from the Commission to the Council and the European Parliament – Community Strategy Concerning Mercury, COM/2005/0020, Brussels, 2005

[24] European Commission: Integrated Pollution Prevention and Control: Reference Document on Best Available Techniques for Large Combustion Plants, July 2006

[25] Rat der Europäischen Union: Richtlinie 96/61/EG über die integrierte Vermeidung und Verminderung der Umweltverschmutzung, September 1996

[26] Rat der Europäischen Union: Richtlinie 2010/75/EU über Industrieemissionen (integrierte Vermeidung und Verminderung von Umweltverschmutzung), Dezember 2010

[27] Beckers, R.: Stand der Arbeiten zur Revision des BVT-Merkblattes Großfeuerungsanlagen und der Vorbereitung seiner nationalen Umsetzung, VDI Wissensforum „Messung und Minderung von Quecksilberemissionen“, April 2016

[28] US Environmental Protection Agency: The Clean Air Act Text https://www.epa.gov/clean-air-act-overview/clean-air-act-text, 1990, accessed: 5/24/2020

[29] Granite, E., Pennline, H., Senior, C.: Mercury Control for Coal-derived gas streams, Wiley-VCH, Weinheim, 2014

[30] US Environmental Protection Agency: The Clean Air Mercury Rule, https://archive.epa.gov/air/mercuryrule/web/html/rule.html, 2005, accessed: 5/24/2020

[31] US Environmental Protection Agency: The Clean Air Interstate Rule https://archive.epa.gov/airmarkets/programs/cair/web/html/index.html, 2005, accessed: 5/24/2020

[32] US Environmental Protection Agency: 40 CFR Parts 60 and 63; National Emission Standards for Hazardous Air Pollutants from Coal and Oil-Fired Electric Utility Steam Generating Units; 02/16/2012; https://www.gpo.gov/fdsys/pkg/FR-2012-02-16/pdf/2012-806.pdf, accessed: 5/24/2020

[33] US Environmental Protection Agency: 80 FR 8441: National Emission Standards for Hazardous Air Pollutants from Coal- and Oil-Fired Electric Utility Steam Generating Units; 02/17/2015; https://www.gpo.gov/fdsys/pkg/FR-2015-02-17/pdf/2015-01699.pdf, accessed: 5/24/2020

[34] Kather, A., Klostermann, M.: Grenzwerte für Quecksilberemissionen aus Kohlekraftwerken, VGB-PowerTech, 12, 2015

[35] UNEP: United Nation's Framework Convention on Climate Change and the Minamata Convention on Mercury: A comparison for the Coal Combustion Sector. UNEP Chemicals Branch, Geneva, Switzerland, 2015

[36] www.mercuryconvention.org, accessed: 2/10/2021

[37] Krishnakumar, B., Niksa, S., Sloss, L., Jozewicz, W., Futsaeter, G.: Process optimization guidance (POG and iPOG) for Mercury Emission Control, Energy and Fuels, 26, 2012

[38] Schrod, M., Semel, J., Steiner, R.: „Verfahren zur Minderung von NOx-Emissionen in Rauchgasen". Chem.-Ing.-Tech., 57, 1985, 9, pp. 717-727

[39] Zeldovich, Y.B.: The oxidation of nitrogen in combustion and explosions. In: Acta Physicochimica USSR, 21, 1946, 4, pp. 577 – 628

[40] Fenimore, C.P.: Formation of nitric oxide in premixed hydrocarbon flames, In: Symposium (International) on Combustion, Elsevier, 13, 1971, pp. 373-380

[41] Glarborg, P., Miller, J.A., Ruscic, B., Klippenstein, S.J.: Modeling Nitrogen Chemistry in Combustion, Progress in Energy and Combustion Science, 67, 2018, pp. 31-68

[42] Glarborg, P., Jenssen, A.D., Johnsson, J.E.: Fuel nitrogen conversion in solid fuel fired systems, Progress in Energy and Combustion Science, 29, 2003, pp. 89-113

[43] Warnatz, J., Maas, U.: Technische Verbrennung, Springer Verlag, Stuttgart, 1993

[44] Moyeda, D.K.: Pulverized Coal-Fired Boilers and Pollution Control, In: Malhotra, R.: Fossil Energy, Springer, New York, 2013

[45] Radojevic, M.: Reduction of nitrogen oxides in flue gases, Environmental Pollution, 102, 1998, pp. 685-689

[46] Schüttenhelm, W., Huber, K., Teuber, Z.: SNCR technology for large scale combustion plants – Operational experiences with commercial installation in a 225 MW_{el} coal-fired boiler, VGB PowerTech, 12, 2013, pp. 71-75

[47] Kaltschmitt, M., Hartmann, H., Hofbauer, H.: Energie aus Biomasse; Springer Berlin Heidelberg, 2009

[48] Joos, F.: Technische Verbrennung – Verbrennungstechnik, Verbrennungsmodellierung, Emissionen. Springer Berlin Heidelberg, 2006

[49] Srivastava, R.K., Miller, C.A, Erickson, C., Jambhekar, R.: Emissions of Sulfur Trioxide from Coal-Fired Power Plants, J. Air & Waste Manage. Assoc., 54, 2004

[50] Monroe, L.: An Updated Method for Estimating Total Sulfuric Acid Emissions from Stationary Power Plants; Research and Environmental Affairs Department, Southern Company Generation and Electricity Marketing: Birmingham, AL, 2001.

[51] Jaworowski, R. J., Mack, S. S.: Evaluation of Methods for Measurement of SO_3/H_2SO_4 in Flue Gas, Journal of the Air Pollution Control Association, 29, 1979, pp. 43-46

[52] Zarenezhad, B.: New correlation predicts flue gas sulfuric acid dewpoints, Oil & Gas Journal, 107, 2009, pp. 60–63

[53] Okkes, A.G.: Get acid dewpoint of flue gas, Hydrocarbon Processing, 7, 1987, pp. 53–55

[54] Walsh, P. M., McCain, J. D., Cushing, K.M.: Evaluation and mitigation of visible acid aerosol plumes from coal fired power plants, Final report, EPA/600/R-06/156, 2006

[55] Zevenhoven, R., Kilpinen, P.: Control of pollutants in flue gases and fuel gases, 3rd edition, 2004, ISBN: 951-22-5527-8

[56] Yudovich, Ya.E, Ketris, M.P.: Chlorine in coal: A review, International Journal of Coal Geology, 67, 2006, pp. 127-144

[57] Palmer, C.A., Oman, C.L., Park, A.J., and Luppens, J.A.: The U.S. Geological Survey coal quality (COALQUAL) database version 3.0: U.S. Geological Survey Data Series 975, 2015

[58] TNO Biomass and Circular Technologies: Phyllis2, database for (treated) biomass, algae feedstocks for biogas production and biochar, https//phyllis.nl, accessed: 5/24/2020

[59] Wang, S., Wu, Y.: Reducing Mercury Emissions from Coal Combustion in the Energy Sector, Mercury Emissions from Coal 7, Glasgow, June 2010

[60] Vosteen, B.W., Hartmann, T.C., Berry, M.S.: Versuche und Betriebserfahrungen mit bromgestützter Quecksilberabscheidung an mehreren US-amerikanischen Kohlekraftwerken, In: Beckmann, M., Hurtado, A.: Kraftwerkstechnik – Band 4, TK-Verlag, Neuruppin, 2012, ISBN: 978-3-935317-87-0

[61] Wedepohl, K.H.: The composition of the continental crust. Geochimica et Cosmochimica Acta, 59, 7, 1995, pp. 1217-1232

[62] US Department of Energy: Toxic Substances from Coal Combustion – A Comprehensive Assessment; Final Report; DOE-Contract No. DE-AC22-95PC95101; July 2001

[63] Kolker, A., Senior, C.L., Quick, J.C.: Mercury in coal and the impact of coal quality on mercury emissions from combustion systems, Appl. Geochemistry, 21, 2006, p. 1821-1836

[64] Dai, S., Ren, D., Chou, C.-L., Finkelman, R.B., Seredin, V.V., and Zhou, Y.: Geochemistry of trace elements in Chinese coals: a review of abundances, genetic types, and impacts on human health and industrial utilization, Int. J. Coal Geol., 94, 2012, 3–21

[65] Köser, H.: Quecksilber in fossilen und nachwachsenden Brennstoffen, VDI-Berichte 2214, 2014

[66] Hocquel, M.: The Behaviour and Fate of Mercury in Coal-Fired Power Plants with Downstream Air Pollution Control Devices, Dissertation, Universität Stuttgart, 2004

[67] Wilhelm, M.S., Liang, L., Cussen, D., Kirchgessner, D. A.: Mercury in Crude Oil Processed in the United States (2004), Env. Sci. & Techn., 41 (13), 2007, pp. 4509-4514

[68] Toole-O'Neil, B., Tewalt, S.J., Finkelman, R.B., Akers, D.J.: Mercury concentration in coal-unraveling the puzzle, Fuel, 78 (1), 1999, pp. 47-54

[69] Wichlinski, M., Kobylecki, R., Bis, Z.: The release of mercury from polish coals during thermal treatment of fuels in a fluidized bed reactor, Fuel Process. Tech., 119, 2014, pp. 92-97

[70] Fahlke, J.: Spurenelementbilanzierungen bei Steinkohlefeuerungen am Beispiel einer Trocken- und einer Schmelzfeuerung unter Berücksichtigung der Rauchgasreinigungsanlagen, Dissertation, Universität Stuttgart, 1994.

[71] Martel, C.: Brennstoff- und lastspezifische Untersuchungen von Schwermetallen in Kohlenstaubfeuerungen, Dissertation, Universität Stuttgart, 2000

[72] Scheffknecht, G., Farr, S., Heidel, B., Schwämmle, T., Brechtel, K.: Quecksilber aus thermischen Kraftwerken: Freisetzungs- und Umwandlungsmechanismen sowie Möglichkeiten zur Minderung, Chemie Ingenieur Technik, 84 (7), 2012, pp. 1041-1051

[73] Hall, B., Schager, P., Lindqvist, O.: Chemical reactions of mercury in combustion flue gases, Water, Air, and Soil Pollution, 56 (3-14), 1991

[74] Schager, P.: The character of mercury in flue gases, PhD thesis, Chalmers University of Technology, Göteborg, 1990

[75] Griffin, R.D.: A new theory of dioxin formation in municipal solid waste combustion, Chemosphere, 15 (9-12), 1982, pp. 1987-1990

[76] Riethmann, T.: Untersuchungen zur Sorption von Quecksilber aus Verbrennungsabgasen und Nebenprodukten in Entschwefelungsanlagen, Shaker Verlag, Aachen, 2013

[77] VGB PowerTech e.V.: Bauart, Betrieb und Wartung von Rauchgasentstickungsanlagen (DeNOx), VGB-Standard S-014-2011-DE, VGB PowerTech Service GmbH, Essen, 2011

[78] König, J., Derichs, W., Hein, K.: Einsatz der SCR-Technik hinter Braunkohlefeuerungen, Komponenten zur Rauchgasreinigung, Oktober 1988

[79] Gutberlet, H., Spiesberger, A., Kastner, F., Tembrink, J.: Zum Verhalten des Spurenelements Quecksilber in Steinkohlefeuerungen mit Rauchgasreinigungsanlagen, VGB Kraftwerkstechnik, 72 (7), 1992

[80] Thorwarth, H.: Trace Element Behaviour in Pulverised Fuel Fired Power Plants – Impacts of Fuels and Emission Control Technologies, Dissertation, Universität Stuttgart, 2007

[81] Madsen, K.: Mercury oxidation over Selective Catalytic Reduction (SCR) Catalysts, Dissertation, Technical University of Denmark, 2011

[82] Ahmaruzzaman, M.: A review on the utilization of fly ash, Progress in Energy and Combustion Science, 36, 2010, pp. 327-363

[83] Jäger, U., Thorwarth, H., Acuna-Caro, C., Scheffknecht, G.: Verhalten von Quecksilber und seinen Verbindungen in staubhaltigen Rauchgasen, Abschlussbericht zum AiF-Forschungsvorhaben Nr. 13 534N, IVD-Berichte, Mai 2006, ISBN 3-928123-56-4

[84] Schwämmle, T., Farr, S., Heidel, B., Scheffknecht, G.: Mass balance of mercury in air pollution control devices while co-firing biomass at a lab-scale firing system, VGB PowerTech, 4, 2014, pp. 57 – 63

[85] Strauß, K.: Kraftwerkstechnik zur Nutzung fossiler, nuklearer und regenerativer Energiequellen, Springer Verlag Berlin, 2009

[86] Heiting, B.: Stand der Technik bei Rauchgasreinigungsanlagen in Großkraftwerken, VGB PowerTech, 6, 2011

[87] VGB PowerTech e.V., „VGB M 419: Merkblatt für Bauart, Betrieb und Wartung von Rauchgasentschwefelungsanlagen (REA)“, VGB Powertech Service GmbH Verlag Techn.-Wiss. Schr., Essen, 2009

[88] Acuña Caro, C.: Chemical Behaviour of Mercury in Wet Flue Gas Desulphurisation Systems, Dissertation, University of Stuttgart, 2015

[89] Farr, S., Heidel, B., Hilber, M. Scheffknecht, G.: Influence of Flue-Gas Components on Mercury Removal and Retention in Dual-Loop Flue-Gas Desulfurization, Energy and Fuels, 29 (7), 2015, pp. 4418 – 4427

[90] Demmich, J.: Qualitätsanforderungen der Gipsindustrie an REA-Gips mit Schwerpunkt Quecksilber, VDI-Wissensforum „Messung und Minderung von Quecksilber-Emissionen“, 15.-16.04.2015, Düsseldorf

[91] Heidel, B.: Wechselwirkungen bei der Abscheidung von Schwefeldioxid und Quecksilber durch nasse Rauchgasentschwefelungsanlagen, Dissertation, University of Stuttgart, 2015

[92] Aylett, B.J.: The Chemistry of Zinc, Cadmium and Mercury. Comprehensive Inorganic Chemistry, Ed. Pergamon Press, 1975, pp. 187-191 and 275-328

[93] Bittig, M.: Zum Einfluss unterschiedlicher Liganden auf die Quecksilberabscheidung in absorptiven Abgasreinigungsstufen, Dissertation, University of Duisburg-Essen, 2010

[94] Schwämmle, T., Heidel, B., Hartung, A., et al.: Development of high performance SCR catalysts related to different fuel types (DEVCAT), Final report, Luxembourg, Publication office of the European Union, 2015, ISBN: 978-92-79-48143-7

[95] Nova, I., Beretta, A., Groppi, G., Lietti, L., Tronconi, E., Forzatti, P.: Monolithic Catalysts for NO_x Removal from Stationary Sources, In: Structured Catalysts and Reactors, CRC Taiylor & Francis, 2005, p. 171-214

[96] Forzatti, P.: Present status and perspectives in de-NO_x SCR catalysis, Appl. Cat. A: General, 222, 2001, pp. 221 – 236

[97] Centi, G., Perathoner, S.: Chapter 1 Introduction: State of the art in the development of catalytic processes for the selective catalytic reduction of NO_x into N_2, In: Studies in Surface Science and Catalysis, 171, 2007, pp. 1-23

[98] Forzatti, P., Lietti, L., Tronconi, E.: Nitrogen oxides removal – industrial, in: Encyclopedia of Catalysis, 1st ed., Horvath, I.T., Ed., Wiley, New York, 2002

[99] Skalska, K., Miller, J.S., Ledakowicz, S.: Trends in NO_x-abatement: A review, Science of the Total Environment, 408, 2010, pp. 3976-3989

[100] Beck, J.: The behavior of Phosphorus Compounds and Their Effect on DeNOx-Catalysts in Coal Fired Power Plants, Dissertation, University of Stuttgart, 2007

[101] Paganini, M.C., Dall'Acqua, L., Giamello, E., Lietti, L., Forzatti, P.: An EPR Study of the Surface Chemistry of the V_2O_5-WO_3/TiO_2 Catalyst: Redox Behaviour and State of V(IV), Journal of Catalysis, 166 (2), 1997, pp. 195–205

[102] Lietti, L., Forzatti, P., Ramis, G.: Potassium doping of vanadia/titania de-Noxing catalysts: Surface characterization and reactivity study, Appl. Cat. B: Environmental, 3, 1993, pp. 13–35

[103] Vogel, D.: Desaktivierungsvorgänge an DeNOx Katalysatoren auf TiO_2/V_2O_5-Basis durch As_2O_3, Dissertation, University of Erlangen, 1989

[104] Chen, J.P., Yang, R.T.: Role of WO_3 in mixed V_2O_5-WO_3/TiO_2 catalysts for selective catalytic reduction of nitric oxide with ammonia, Applied Catalysis A: General; 80 (1), 1992, pp. 135–148

[105] Hilbrig, F., Göbel, H.E., Knözinger, H., Schmelz, H., Langeler, B.: Interaction of arsenious oxide with deNOx catalysts: an X-ray absorption and diffuse reflectance infrared spectroscopy study, J. Catal., 129, 1991, pp. 168–176

[106] Lange, F.: Arsenvergiftung von DeNOx-Katalysatoren, Dissertation, Technische Universität München, 1994

[107] Khodayari, R., Odenbrand, C.U. I.: Regeneration of commercial SCR catalysts by washing and sulphation: effect of sulphate groups on the activity, Appl. Cat. B: Environmental, 33, 2001, pp. 277-291

[108] Baxter, L: Biomass Impacts on SCR Catalyst Performance, Technical Report, IEA Bioenergy Task 32, 2005

[109] Beeckman, J. W., Hegedus, L.L.: Design of Monolith Catalysts for Power Plant NO_x Emission Control, Ind. Eng. Chem. Res., 30 (5), 1991, pp. 969-978

[110] Jung, J., Panagiotidis, Th.: Untersuchungen zur Übertragbarkeit der im Labor- und Technikumsmaßstab bestimmten Eigenschaften von SCR-Wabenkatalysatoren auf großtechnische DENOX-Anlagen, Chemie im Kraftwerk, 1990

[111] Busca, G., Lietti, L., Ramis, G., Berti, F.: Chemical and mechanistic aspects of the selective catalytic reduction of NO_x by ammonia over oxide catalysts: A review, Appl. Cat. B: Environmental, 18, 1998, pp. 1-36

[112] Takagi, M.; Kowai, T.; Soma, M., Onishi, T., Tamaru, K.: The mechanism of the reaction between NO_x and NH_3 on V_2O_5 in the presence of oxygen, J. of Catalysis, 50 (3), 1977, pp. 441-446

[113] Inomata, M., Miyamoto, A., Murakami, Y.: Mechanism of the reaction of NO and NH_3 on vanadium oxide catalyst in the presence of oxygen under the dilute gas condition, J. of Catalysis, 1980, pp. 140-148

[114] Janssen, F.J.J.G., Kerkhof, F.M.G. Van d., Bosch, H., Ross, J.R.H.: Mechanism of the reaction of nitric oxide, ammonia, and oxygen over vanadia catalysts. I. The role of oxygen studied by way of isotopic transients under dilute conditions. J. of Phys. Chem., 91 (23), 1987, pp. 5921-5927

[115] Ozkan, U.S., Cai, Y.P., Kumthekar, M.W.: Investigation of the Reaction Pathways in Selective Catalytic Reduction of NO with NH_3 over V_2O_5 Catalysts: Isotopic Labeling Studies Using $^{18}O_2$, $^{15}NH_3$, ^{15}NO, and $^{15}N^{18}O$, J. of Catalysis, 149 (2),1994, pp. 390-403

[116] Topsøe, N.-Y.: Mechanism of the Selective Catalytic Reduction of Nitric Oxide by Ammonia Elucidated by in Situ On-Line Fourier Transform Infrared Spectroscopy. Science, 265, 1994, pp. 1217-1219

[117] Alemany, L. J., Lietti, L., Ferlazzo, N. et. al.: Reactivity and Physicochemical Characterisation of V_2O_5-WO_3/TiO_2 DeNOx Catalysts; J. of Catalysis, 155, 1995, pp. 117-130

[118] Xu, H., Zhang, Q., Qiu, C., Lin, T., Gong, M., Chen, Y.: Tungsten modified MnOx – CeO_2/ZrO_2 monolith catalysts for selective catalytic reduction of NOx with ammonia, Chem. Eng. Science, 76, 2012, pp. 120-128

[119] Svachula, J., Ferlazzo, N., Forzatti, P., Tronconi, E.: Selective Reduction of NO_x by NH_3 over Honeycomb DeNOxing Catalysts, Ind. Eng. Chem. Res., 32, 1993, pp. 1053-1060

[120] Schneider, G. Lebensdauerprognosen von SCR-Katalysatoren, Dissertation, Universität Stuttgart, 1999

[121] Perujo, P. M.: Condensation of Water Vapor and Acid Mixtures from Exhaust Gases, Institut für Energietechnik, Technische Universität Berlin, Dissertation, November 2004

[122] Svachula, J., Alemany, L.J., Ferlazzo, N., et. al.: Oxidation of SO_2 to SO_3 over Honeycomb DeNOxing Catalysts, Ind. Eng. Chem. Res., 1993, pp. 826-834

[123] VGB PowerTech e.V.: Richtlinie zur Prüfung von DeNOx-Katalysatoren, VGB-Standard VGB-S-302-00-2013-04-DE, VGB PowerTech Service GmbH, Essen, 2013

[124] Dunn, J.P., Stenger, H.G., Wachs, I. E.: Oxidation of sulfur dioxide over supported vanadia catalysts: molecular structure – reactivity relationships and reaction kinetics, Catalysis Today, 51, 1999, pp. 301-318

[125] Stolle, R.: Untersuchung zum Verhalten von Quecksilber in SCR-DeNOx-Anlagen in Kohlekraftwerken. Dissertation, University of Halle-Wittenberg, 2014

[126] Deacon, H.: On Deacon's method of obtaining chlorine, as illustrating some principles of chemical dynamics, J. Chem. Soc., 25, 1872, pp. 725–767

[127] Hisham, M.W.M., Benson, S.W.: Thermochemistry of the Deacon Process, J. Phys. Chem., 99, 1995, pp. 6194-6198

[128] Eom, Y., Ho Jeon, S., An Ngo, T., Kim, J., Gyu Lee, T.: Heterogeneous Mercury Reaction on a Selective Catalytic Reduction (SCR) Catalyst, Catal. Lett., 121, 2008, pp. 119-125

[129] Niksa, S., Fujiwara, N.: A predictive mechanism for mercury oxidation on selective catalytic reduction catalysts under coal-derived flue gas, J. Air & Waste Manage. Assoc., 55, 2005, pp. 1866-1875

[130] Senior, C.L.: Oxidation of Mercury across Selective Catalytic Reduction Catalysts in Coal–Fired Power Plants, J. Air & Waste Manage. Assoc., 56, 2006, pp. 23-31

[131] Granite, E., Pennline, H.,Hargis, R.: Novel sorbents for mercury removal from flue gas, Ind. Eng. Chem. Res., 39, 2000, pp. 1020-1029

[132] Li, H., Wu, C.-Y., Li, Y., Zhang, J.: CeO_2-TiO_2 Catalysts for Catalytic Oxidation of Elemental Mercury in Low-Rank Coal Combustion Flue Gas, Environ. Sci. Technol., 45, 2011, pp. 7394-7400

[133] Usberti, N., Alcove Clave, S., Nash, M., Beretta, A.: Kinetics of Hg0 oxidation over a V_2O_5/MoO_3/TiO_2 catalyst: Experimental and modelling study under DeNOX inactive conditions, Appl. Cat. B.: Environment, 193, 2016, pp. 121-132

[134] Kamata, H., Ueno, S.-i., Naito, T., Yukimura, A.: Mercury Oxidation over the $V_2O_5(WO_3)/TiO_2$ Commercial SCR Catalyst, Ind. Eng. Chem. Res., 47, 2008, pp. 8136-8141

[135] Li, H., Li, Y., Wu, C.-Y.,Zhang, J.: Oxidation and capture of elemental mercury over SiO_2–TiO_2–V_2O_5 catalysts in simulated low-rank coal combustion flue gas. Chemical Eng. J.,169, 2011, pp. 186-193

[136] Tong, G.: Oxidation of mercury during selective catalytic reduction of nitric oxide, Dissertation, University of Alabama at Birmingham, Birmingham, AL, US, 2009

[137] Stolle, R., Köser, H., Gutberlet, H.: Oxidation and reduction of mercury by SCR DeNOx catalysts under flue gas conditions in coal fired power plants. Appl. Cat. B: Environmental, 144, 2014, pp. 486-497

[138] Zhuang, Y., Laumb, J., Liggett, R., Holmes, M., Pavlish, J.: Impacts of acid gases on mercury oxidation across SCR catalyst, Fuel Process. Techn., 88, 2007, pp. 929-934

[139] Li, H., Wu, C.-Y., Li, Y, Li, L, Zhao, Y., Zhang, J.: Impact of SO_2 on elemental mercury oxidation over CeO_2-TiO_2 catalyst, Chem. Eng. J., 219, 2013, pp. 319-326

[140] Dranga, B.-A., Lazar, L., Köser, H.: Oxidation catalysts for elemental mercury in flue gases – a review, Catalysts, 2, 2012, pp. 139-170

[141] Stolle, R., Zeng, K. and Köser, H.: Katalytische Quecksilberoxidation als Vorstufe zur Abscheidung aus Feuerungsabgasen. Abschlussbericht, Martin-Luther-Universität Halle-Wittenberg: Max-Buchner-Forschungsstiftung FKZ: 2717, 2009.

[142] Kamata, H., Ueno, S-i., Sato, N., Naito, T.: Mercury oxidation by hydrochloric acid over TiO_2 supported metal oxide catalysts in coal combustion flue gas, Fuel Processing Technology, 90, 2009, pp. 947-951

[143] Qiao, S., Chen, J., Li, J., Qu, Z., Liu, P., Yan, N., Jia. J.: Adsorption and Catalytic Oxidation of Gaseous Elemental Mercury in Flue Gas over MnOx/Alumina, Ind. Eng. Chem. Res., 48, 2009, pp. 3317–3322

[144] Zhao, B., Liu, X., Zhou, Z., Shao, H., Wang, C., Si, J., Xu, M.: Effect of Molybdenum on Mercury Oxidation by V_2O_5-MoO_3/TiO_2 Catalysts, Chem. Eng. J., 253, 2014, pp. 508-517

[145] Presto, A.A., Granite, E.J.: Survey of Catalysts for the Oxidation of Mercury in Flue Gas, Env. Sci. and Techn., 40, 2006, pp. 5601-5609

[146] Chen, W., Ma, Y., Yan, N., Qu, Z., Yang, S., Xie, J., Guo, Y., Hu, L., Jia, J.: The co-benefit of elemental mercury oxidation and slip ammonia abatement with SCR-plus catalysts, Fuel, 133, 2014, pp. 263-269

[147] Favale, A.C., Nakamoto, T., Kato, Y., Nagai, Y.: Mercury Mitigation Strategy Through The Co-Benefit Of Mercury Oxidation With SCR Catalyst, Power Engineering, 117 (1), 2013, pp. 46-52

[148] Laboratory Testing Protocol for Coal-Fired SCR Catalyst: 3rd Edition. EPRI, Palo Alto, CA: 2018. 3002013048

[149] SCR Catalyst Mercury Oxidation Laboratory Testing Guideline – Industry Version. EPRI, Palo Alto, CA: 2015. 3002005087

[150] Schwaemmle, T., Heidel, B., Brechtel, K., Scheffknecht, G.: Study of the effect of newly developed mercury oxidation catalysts on the DeNOx activity and SO_2–SO_3-conversion, Fuel, 101, 2012, pp. 179-186

[151] Schwämmle, T., Brechtel, K., Salvati, M., Di Blasi, M., Klatt, A., et al: Optimisation of SCR-DeNOx catalyst performance related to deactivation and mercury oxidation (DENOPT), European Comission, Luxembourg, Publication office of the European Union 2013, ISBN: 978-92-79-24936-5

[152] Schwämmle, T., Bertsche, F., Hartung, A., Brandenstein, J., Heidel, B., Scheffknecht, G.: Influence of geometrical parameters of honeycomb commercial SCR-DeNOx-catalysts on DeNOx activity, mercury oxidation and SO_2/SO_3-conversion, Chem. Eng. J., 222, 2013, pp. 274-281

[153] Schwaemmle, T., Hartung, A., Brandenstein, J. et. al: SCR-DeNOx catalyst development towards high-performance catalysts related to different fuel types, MEC9 Mercury Emissions from Coal, May 2012, St. Petersburg, Russia

[154] Schwämmle, T., Heidel, B., Klein, B., Scheffknecht, G.: Beitrag neu entwickelter SCR-DeNOx-Katalysatoren zur Quecksilberminderung in Kraftwerken: Ergebnisse aus dem europäischen Forschungsprojekt „DEVCAT“, 15. VDI Fachkonferenz Messung und Minderung von Quecksilber-Emissionen, April 2015, Düsseldorf, Germany

[155] Schwämmle, T., Heidel, B., Masoomi, I. et. al: Investigating recent innovations in technologies for decreasing mercury content in emissions, ExPPERTS Europe 2015, September 2015, Krakow, Poland

[156] Schwämmle, T., Farr, S., Heidel, B., Scheffnecht, G.: Effect of co-firing of biomass on mercury removal by state of the art air pollution control devices. 3rd IEA CCC Workshop on Cofiring Biomass with Coal, June 2013, Groningen, Netherlands.

[157] Schwämmle, T., Farr, S., Heidel, B., Scheffknecht, G.: Bilanzierung von Quecksilber in der Rauchgasreinigung bei der Mitverbrennung von Biomasse in einer Laborfeuerungsanlage, Chemie im Kraftwerk, Oktober 2013, Leipzig, Germany.

[158] Schwämmle, T., Dux, T., Liu, X., Testing and regeneration of SCR catalysts in View on their Mercury-Oxidation-Potential, VGB-PowerTech, 6, 2018

[159] Brunauer, S., Emmet, P., Teller, E.J.: Adsorption of Gases in Multimolecular Layers, J. Amer. Chem. Soc., 60, 1938, pp. 309-319

[160] Barrett, E.P., Joyner, L.G., Halenda, P.P.: The Determination of Pore Volume and Area Distributions in Porous Substances, I. Computations from Nitrogen Isotherms., J. Amer. Chem. Soc., 73, 1951, pp. 373-380

[161] Metzger M.; Braun H.: In-situ mercury speciation in flue gas by liquid and solid sorption systems, Chemosphere, 16 (4), 1987, pp. 821-832

[162] VDI Guideline 2462 Bl.2: Bestimmung von Schwefeltrioxid in wasserdampfhaltigen Abgasen, Beuth Verlag, Berlin, 11/2011

[163] Deutsches Institut für Normung: DIN EN 1911: Emissionen aus stationären Quellen - Bestimmung der Massenkonzentration von gasförmigen Chloriden, angegeben als HCl – Standardreferenzverfahren, Beuth Verlag, Berlin, 12/2010

[164] VDI guideline 3878: Messen gasförmiger Emissionen - Messen von Ammoniak (und gas- und dampfförmigen Ammoniumverbindungen) - Manuelles Verfahren, Beuth Verlag, Berlin, 09/2017

[165] Dunn, J.P., Koppula, P.R., Stenger, H.G., Wachs, I.E.: Oxidation of sulfur dioxide to sulfur trioxide over supported vanadia catalysts, Appl. Cat. B: Environmental, 19, 1998, pp. 103-117

[166] Pavlish, J.; Sondreal, E.; Mann, M.; Olson, E.; Galbreath, K.; Laudal, D.; Benson, S.: Status review of mercury control options for coal-fired power plants, Fuel Process. Technol., 82 (2-3), 2003, pp. 89-165

[167] Salker, A.V., Weisweiler, W.: Catalytic reduction of NOx by ammonia over nickel and lanthanum supported on zeolite. Ind. J. of Chem., 43a, 2004, pp. 1167-1171

[168] Jiang S., Liu X., Li H., Wang J., Yang Z., Peng H., Shih K.: Synergistic effect of HCl and NO in elemental mercury catalytic oxidation over La_2O_3-TiO_2 catalyst, Fuel, 215, 2018, pp. 232-238

[169] Wiatros-Motyka, M. M., Sun, C-g., Stevens, L. A., Snape, C.E.: High capacity co-precipitated manganese oxides sorbents for oxidative mercury capture, Fuel, 109, 2003, pp. 559-562

[170] Takenami, J., Uddin, A., Sasaoka, E., Shioya, Y., Takase, T.: Removal of Elemental Mercury from Dry Methane Gas with Manganese Oxides, Int. J. of Chem. and Molec. Eng., 3 (8), 2009, pp. 375-379

[171] Zhao, L., Li, C., Zhang, X., Zeng, G., Zhang, J., Xie, Y.: A review on oxidation of elemental mercury from coal-fired flue gas with selective catalytic reduction catalysts, Catal. Sci. Technol., 5, 2015, pp. 3459 – 3472

[172] Jian-rong, L., Chi, H., Xue-song, S., Jin-sheng, C., Xiao-wei, Y., Yuan-jun, Y.: Oxidation efficiency of elemental mercury in flue gas by SCR-De-NOx catalysts, J. of Fuel Chemistry and Techn., 40, 2012, pp. 242-246

[173] Straube, S.: Untersuchungen zum Verhalten von Quecksilber in Reingas-SCR-DeNOx-Anlagen. Dissertation, University of Halle-Wittenberg, 2010

[174] Granite, E.J., Myers, C.R., King, W.P., Stanko, D.C., Pennline, H.W.: Sorbents for mercury capture from fuel gas with application to gasification systems, Industrial and Engineering Chemistry Research, 45 (13), 2006, pp. 4844–4848

[175] Poulston, S., Granite, E.J., Pennline, H.W.,Myers, C.R., Stanko, D.P., Hamilton, H., Rowsell, L.,Smith, A.W.J., Ilkenhans, T., Chu,W.: Metal sorbents for high temperature mercury capture from fuel gas, Fuel, 86 (14), 2007, pp. 2201–2203

[176] Lee, W., Bae, G.-N.: Removal of Elemental Mercury (Hg(0)) by Nanosized V_2O_5/TiO_2 Catalysts. Environ. Sci. Technol., 43, 2009, pp. 1522-1527

[177] Gege, I.: Studien zur Sorption von Quecksilberchlorid an einer metallbeschichteten porösen Keramik. Dissertation, Universität Karlsruhe, 1999

[178] Hong, H.J., Ham, S.W., Kim, M.H. et al.: Characteristics of commercial selective catalytic reduction catalyst for the oxidation of gaseous elemental mercury with respect to reaction conditions, Korean J. of Chem. Eng., 2010, 27, 4, pp. 1117-1122

[179] Rallo, M., Heidel, B., Brechtel, K., Maroto-Valer, M.: Effect of SCR operation variables on mercury speciation, Chem. Eng. J., 198-199, 2012, pp. 87-94

[180] Binder-Begsteiger, I., Herzog, G., Megla, E., Thormann-Rosos, M.: Zur Kinetik der Denox-Reaktion an V_2O_5-WO_3-Wabenkatalysatoren, Chem. Ing. Technik, 1990, 62, pp. 60-61

[181] Tronconi, E., Beretta, A.: The role of inter- and intra-phase mass transfer in the SCR-DeNOx-reaction over catalysts of different shapes, Catal. Today, 52,1992, pp. 249–258

[182] Galbreath, K. C., Zygarlicke C. J., Tibbetts J. E., Schulz R. L., Dunham G. E.: Effects of NO_x, α-Fe_2O_3, γ-Fe_2O_3, and HCl on mercury transformations in a 7-kW coal combustion system, Fuel Process Technol, 2005, 86, 4, pp. 429–448

[183] Kijlstra, W.S., Biervliet, M., Poels, E.K., Bliek, A.: Deactivation by SO_2 of MnO_x/Al_2O_3 catalysts used for the selective catalytic reduction of NO with NH_3 at low temperatures, Appl. Catal. B, 16, 1998, pp. 327–337

[184] Li, H., Wu, C.-W., Li, Y., Li, L., Zhao, Y., Zhang, J.: Role of flue gas components in mercury oxidation over TiO_2 supported MnOx-CeO_2 mixed-oxide at low temperature, J. of Hazardous Materials, 243, 2012, pp. 117-123

[185] Zhao, L., Li, C., Zhang, J., Zhang, X., Zhan, F., Ma, J., Xie, Y., Zeng, G.: Promotional effect of CeO_2 modified support on V_2O_5–WO_3/TiO_2 catalyst for elemental mercury oxidation in simulated coal-fired flue gas, Fuel, 153, 2015, pp. 361-369

[186] Morikawa, S., Yoshida, H., Takahashi, K., Kurita, S.: Improvement of V_2O_5–TiO_2 catalyst for NO_x reduction with NH_3 in flue gases, Chem. Lett., 22, 1981, pp. 251–254

[187] Trovarelli, A.: Catalytic properties of Ceria and CeO_2-containing materials, Catalysis Reviews: Science and Engineering, 38 (4), 1996, pp. 439-520

[188] Winzor, D.J, Jackson, C.M.: Interpretation of the temperature dependence of equilibrium and rate constants, J. Mol. Recognit., 19, 2006, pp. 389–407

[189] Zhao, B., Wei Liu, X, Jian Zhou, Z., Shao, H.-Z., Wang, C., Xu, M.-H.: Mercury oxidized by V_2O_5–MoO_3/TiO_2 under multiple components flue gas: An actual coal-fired power plant test and a laboratory experiment, Fuel Processing Technology, 134, 2015, pp. 198-204

[190] Wan, Q., Duan, L., He, K., Li, J.: Removal of gaseous elemental mercury over a CeO_2–WO_3/TiO_2 nanocomposite in simulated coal-fired flue gas, Chemical Engineering Journal, 170, 2011, pp. 512-517

[191] Chen, C., Cao, Y., Liu, S., Chen, J., Jia, W.: Review on the latest developments in modified vanadium-titanium-based SCR catalysts, Chinese Journal of Catalysis, 39, 2018, pp. 1347-1365

[192] Chen, L., Li, J., Ge, M., Zhu, R.: Enhanced activity of tungsten modified CeO_2/TiO_2 for selective catalytic reduction of NOx with ammonia, Catalysis Today, 153, 2010, pp. 77-83

[193] Dunn, J. P., Stenger, H. G., Wachs, I. E.: Oxidation of SO_2 over Supported Metal Oxide Catalysts, Journal of Catalysis, 181, 1999, pp. 233-243

[194] Neidig, K., Nakamoto, T., Kato, Y., Nagai, Y.: SCR catalyst, A low cost technology for mercury mitigation, Proceedings: Air Quality IX, Arlington, VA, US, October 2013

[195] Ma, Z., Wu, X., Feng, Y., Si, Z., Weng, D., Shi, L.: Low-temperature SCR activity and SO_2 deactivation mechanism of Ce-modified V_2O_5–WO_3/TiO_2 catalyst, Progress in Natural Science: Materials International, 25, 2015, pp. 342–352

[196] Kobayashi, M., Hagi, M.: V_2O_5-WO_3/TiO_2-SiO_2-SO_4^{2-} catalysts: Influence of active components and supports on activities in the selective catalytic reduction of NO by NH3 and in the oxidation of SO_2, Appl. Cat. B: Environmental, 63, 2006, pp. 104–113

[197] Bertole, C.: The SCR Toolbox for Mercury Emission Management. Reinhold NOx-combustion round table, Richmond, VA, US, 2015

[198] Liu, C., Chen, L., Li, J., Ma, L., Arandiyan, H., Du, Y., Xu, J., Hao, J.: Enhancement of Activity and Sulfur Resistance of CeO_2 Supported on TiO_2–SiO_2 for the Selective Catalytic Reduction of NO by NH_3, Environ. Sci. Technol., 46, 2012, pp. 6182−6189

[199] Vosteen, B.: Native Halogens in Coals from US, China, and elsewhere – Low Chlorine Coals Need Bromine Addition for Effective Mercury Capture, MEC7 – Mercury Emissions from Coal, Glasgow, Scotland, June 16-18, 2010

[200] Seigneur, C., Wrobel, J., Constaninou, E.: A Chemical Kinetic Mechanism for Atmospheric Inorganic Mercury. Environmental Science Technology, 28, 1994. pp. 1589-1597

[201] Orsenigo, C., Beretta, A., Forzatti, P., Svachula, J., Tronconi, E., Bregani, F., Baldacci, A.: Theoretical and experimental study of the interaction between NO_x reduction and SO_2 oxidation over DeNOx-SCR catalysts, Catalysis Today, 27, 1996, pp. 15-21

[202] Lietti, L., Nova, I., Ramis, G. et al.: Characterization and Reactivity of V_2O_5-MoO_3/TiO_2 DeNOx SCR catalysts, J. of Catalysis, 187, 1999, pp. 419-435

[203] Hilber, M., Thorwarth, H.: Lab-scale assessment of different parameters influencing the operational behavior of SCR-DeNOx catalysts, VGB Power-Tech, 10, 2012, pp. 69-73

[204] Zheng, Y., Jensen, A.D., Johnsson, J.E.: Deactivation of V_2O_5-WO_3-TiO_2 SCR catalyst at a biomass-fired combined heat and power plant. Appl. Cat. B: Environmental, 60, 2005, pp. 253-264

[205] Spörl, R.: Studies on conversion of SO_2 to SO_3 at a SCR-DeNOx-Catalyst, Diploma Thesis, University of Stuttgart, 2010

[206] Suchak, C.: Ursachen der Niedertemperaturkorrosion im Abgasweg von Zementdrehofenanlagen, Dissertation, Technical University Clausthal, 2014

[207] Hall, B.: The gas phase oxidation of elemental mercury by ozone, Water, Air & Soil Pollution, 80 (1-4), 1995, pp. 301-315

[208] Hollemann, A.F., Wiberg, N.: Lehrbuch der Anorganischen Chemie, 102. Auflage, de Gruyter, Berlin New York, 2007, p. 670

[209] Honjo, S., Iwakura, K., Welliver, B. et al.: MHI Mercury Removal System with NH_4Cl Injection, Power Plant Air Pollutant Control “MEGA” Symposium, Baltimore, MD, 2012

[210] Okamto, T., Nagae, S., Ukai, N. et al.: Mercury Removal Technology demonstration results. VGB PowerTech, 1/2 2013, pp. 87-91

8 Annex

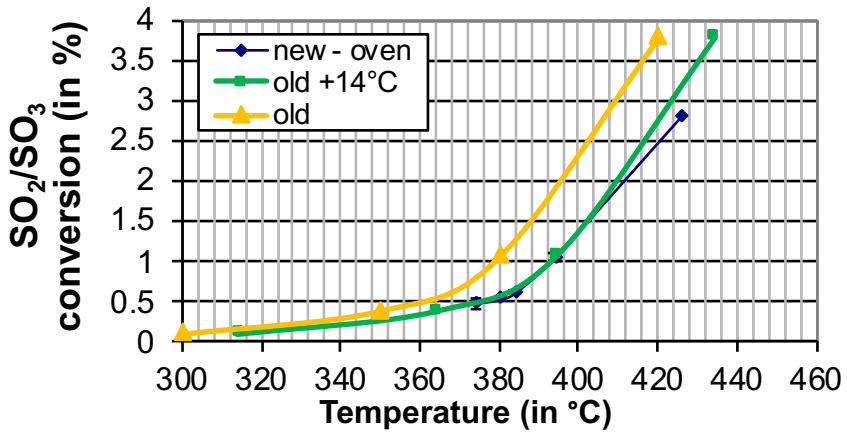

Figure 8-1: Error of the SO_2/SO_3 conversion measurement studied with catalyst C due to erroneous temperature measurement

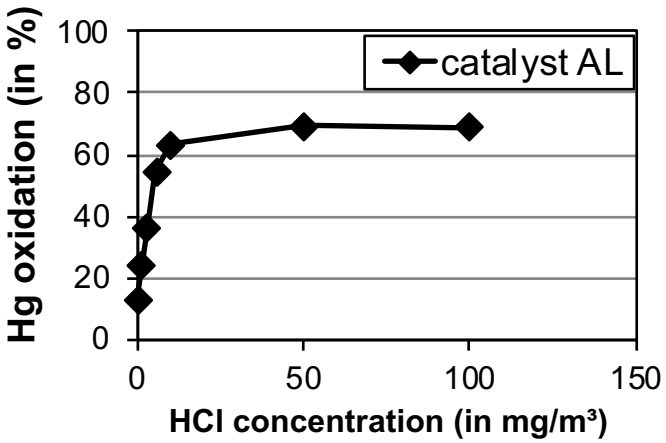

Figure 8-2: Hg oxidation of catalyst AL over the HCl concentration with extended range of research

Table 8-1: Chemical and physical data on the researched catalysts

	unit	A	B	C	D	E	F	G	H	I	J	L	M	N	O	P	Q	R	S	T	U	V
TiO_2	wt.-%	79.6	76.1	78.7	78.1	83.9	78.3	79.4	76.9	78.7	identical to catalyst C						78.5	78.8	78.4	79.1	77.0	77.0
SiO_2		9.0	11.2	9.5	8.8	8.4	8.3	7.2	14.2	10.3							9.0	9.1	9.1	8.6	9.4	9.5
WO_3		5.2	5.5	5.4	5.4	0.0	6.2	10.9	1.1	0.7							5.3	5.3	5.3	5.3	6.0	6.0
MoO_3		-	-	-	-	-	-	-	-	4.7							-	-	-	-	-	-
MnO		-	-	-	-	-	1.2	-	-	-							-	-	-	1.6	-	-
CuO		-	-	-	-	-	-	-	-	-							0.8	0.4	-	-	0.9	-
Fe_2O_3		-	-	-	-	-	-	-	-	-							-	-	1.0	-	-	1.0
CeO_2		-	-	-	-	-	-	-	-	-							-	-	-	-	-	-
Pd		-	-	-	-	-	-	0.3	-	-							-	-	-	-	-	-
P_2O_5		-	-	-	-	-	-	-	-	-							-	-	-	-	-	-
V_2O_5		0.5	0.5	0.6	1.6	0.1	0.1	0.2	0.5	0.7							0.6	0.6	0.7	0.7	0.1	0.1
BET surface area	m^2/g	53.5	57.4	63.0	47.5	-	-	-	80.4	50.4							-	-	-	-	-	-
Average pore size	nm	15.2	14.2	14.6	18.2	-	-	-	11.9	15.1							-	-	-	-	-	-

	unit	W	X	Y	Z	AA	AB	AC	AD	AE	AF	AG	AH	AI	AJ	AK	AL	AM	AN	AO	AP	AQ	AR
TiO_2	wt.-%	78.2	78.1	72.5	83.2	83.1	84.0	83.0	71.9	76.9	75.6	79.5	75.0	77.9	77.3	60.3	60.7	76.2	77.1	73.7	80.0	70.0	76.5
SiO_2		8.8	8.9	9.7	8.2	8.2	7.4	8.3	14.9	10.5	11.5	9.0	11.0	10.0	10.3	13.4	13.3	11.0	12.9	14.2	6.1	11.6	14.2
WO_3		6.0	6.1	9.8	0.9	0.9	0.9	0.9	5.6	5.8	5.3	5.4	3.5	0.7	0.8	5.1	5.1	5.2	1.0	0.0	7.7	7.6	1.2
MoO_3		-	-	-	-	-	-	-	-	-	-	-	4.6	6.0	5.8	-	-	-	2.4	3.3	-	-	-
MnO		-	-	-	-	-	1.3	-	-	-	-	-	-	-	-	-	-	-	-	-	-	-	-
CuO		-	-	-	1.0	-	-	-	-	-	-	-	-	-	-	-	-	-	-	-	-	-	-
Fe_2O_3		-	-	-	-	1.1	-	-	-	-	-	-	-	-	-	-	-	-	-	-	-	-	-
CeO_2		-	-	-	-	-	-	1.0	-	-	-	-	-	-	-	14.0	14.0	-	-	-	-	-	-
Pd		-	-	-	-	-	-	-	-	-	-	-	-	-	-	-	-	-	-	-	-	-	-
P_2O_5		-	-	-	-	-	-	-	-	-	-	-	-	-	-	-	-	-	-	2.6	-	-	-
V_2O_5		0.6	0.8	2.1	0.6	0.6	0.6	0.6	0.4	0.5	0.5	0.5	0.6	0.7	0.7	-	-	0.8	0.7	3.3	0.4	2.0	0.8
BET surface area	m^2/g	-	-	-	-	-	-	-	75.5	59.0	67.9	50.4	52.8	57.3	65.6	99.4	107.7	71.4	89.8	-	-	-	-
Average pore size	nm	-	-	-	-	-	-	-	12.2	14.4	13.6	15.1	14.2	14.5	12.4	9.1	8.2	13.6	11.0	-	-	-	-